University of Strathclyde

Department of Physics

Submitted in partial fulfilment of the requirements for the degree of Doctor of Philosophy

---

Theory of self-organisation in cold atoms

Author:
Enrico Tesio

Supervisor:
Dr. Gordon Robb
Second supervisor:
Prof. Gian-Luca Oppo

March 11, 2014

This thesis is the result of the author's original research. It has been composed by the author and has not been previously submitted for examination which has led to the award of a degree.

SIGNED:

DATE:

Before I came here I was confused about this subject.
Having listened to your lecture I am still confused.
But on a higher level.

ENRICO FERMI

To my family

Contents

Published material

Papers published or submitted to peer-reviewed journals:

- E. Tesio, G.R.M. Robb, G.-L. Oppo, W.J. Firth, P.M. Gomes, T. Ackemann, G. Labeyrie, R. Kaiser, *Self-organisation in cold atomic gases: a synchronisation perspective*, submitted to Roy. Soc. Proc. A (2014)

- E. Tesio, G.R.M. Robb, T. Ackemann, W.J. Firth, and G.-L. Oppo, *Kinetic theory for transverse optomechanical instabilities*, Phys. Rev. Lett. **112**, 043901 (2014)

- G. Labeyrie, E. Tesio, P.M. Gomes, G.-L. Oppo, W.J. Firth, G.R.M. Robb, A.S. Arnold, R. Kaiser, and T. Ackemann, *Optomechanical self-structuring in cold atomic gases*, accepted for publication on Nature Photonics (2014)

- E. Tesio, G.R.M. Robb, T. Ackemann, W.J. Firth, and G.-L. Oppo, *Dissipative solitons in the coupled dynamics of light and cold atoms*, Opt. Exp. **21**, 26144 (2013)

- E. Tesio, G.R.M. Robb, T. Ackemann, W.J. Firth, and G.L.-Oppo, *Spontaneous optomechanical pattern formation in cold atoms*, Phys. Rev. A **86**, 031801(R) (2012)

Contributions to conferences (talks and poster presentations):

- *Opto-mechanical dissipative solitons in cold atoms*, talk at the 'Extreme Nonlinearities and Solitons' (ENOS) Workshop, Weierstrass Institute for Applied Analysis and Stochastics (WIAS), Berlin, 2013
- *Symmetry breaking instabilities in cold atomic gases*, poster presented at the workshop 'From Dynamics to Statistical Mechanics and Back', Max Planck Institute for the Physics of Complex Systems (PKS-MPI), Dresden, 2013
- *Transverse self-structuring in cold atomic gases*, talk at the Collective Scattering of Light (COSCALI) meeting, Naples, 2013
- *Spontaneous Opto-Mechanical Structures in Cold Atomic Gases*, talk at the International Quantum Electronic Conference (IQEC), Munich, 2013
- *Opto-mechanical transverse patterns in cold atomic gases*, talk at the European Optical Society Annual Meeting (EOSAM), Aberdeen (UK), 2012
- *Spatial opto-mechanical structures in cold atomic gases*, poster presented at the Insitute of Physics (IOP) Photon12 conference, Durham (UK), 2012

The following conference presentations are related to the work presented in this thesis, but I did not present them:

- T. Ackemann, *Optomechanical self-organization in cold atomic gases*, talk at the 'Rio de la Plata' Workshop on Lasers Dynamics and Nonlinear Photonics, Montevideo, Uruguay, December $9 - 12$, 2013.

- G.R.M. Robb, *Kinetic model of optomechanical self-structuring in cold atomic gases*, talk at the Physics of Quantum Electronic (PQE) 5−9 January 2014, Snowbird, Utah, USA

- W.J. Firth, *Spontaneous spatial structures in cold atoms due to opto-mechanical coupling*, talk at the XXXIII Dynamics Days Europe, $3 - 7$ June 2013, Madrid, Spain

- W.J. Firth, *Extreme nonlinearity from linear optical scattering in cold atoms*, talk at the 'Extreme Nonlinearities and Solitons' (ENOS) Workshop, Weierstrass Institute for Applied Analysis and Stochastics (WIAS), Berlin, 2013

This work is related to my research activity as a graduate student at the Università degli Studi di Milano, and was published with a double affiliation (Milano/Strathclyde):

- S. Cialdi, D. Brivio, E. Tesio, and M. G. A. Paris, *Nonlocal compensation of pure phase objects with entangled photons*, Phys. Rev. A **84**, 043817 (2011)

Abstract

Since the first realization of a laser source in 1960, tremendous progresses have been made in the theoretical understanding and experimental control of interacting atomic-optical systems. Optical fields can nowadays be used to engineer long-range interactions in cold atomic gases, manipulating the external degrees of freedom of the atoms via optical forces. This opens the possibility for the study of highly controllable and tunable long-range interacting systems, in which a complex dynamics for the motional properties of the gas can arise due to the effective atom-atom coupling induced by the field.

In this thesis the spontaneous emergence of spatial structures in non-equilibrium atom-optical systems is theoretically and numerically investigated, for different geometries and physical configurations. Extending previous research in hot atomic gases, self-organising instabilities involving the external degrees of freedom are studied, and in contrast to other cold-atom spatial instabilities the spontaneous breaking of continuous symmetries is predicted. The main focus of the work presented in this thesis is on dynamical instabilities in cold gases. However, connections are found with other fields of nonlinear physics, such as synchronisation of coupled oscillators and phase transitions in many-body systems. Part of the research presented here has been conducted in the context of a collaboration with the Photonics group at Strathclyde

and the Institut non Linéaire de Nice, in which experimental observations of self-organisation and continuous symmetry breaking were obtained.

Introduction

The spontaneous emergence of order lies at the heart of much of the observed world: we can experience it looking at sand dunes in the desert, or at the clouds every time we are on a plane. We witness (and take part in) a remarkable biological diversity with millions of different species, and our heartbeat is determined by the synchronization of countless pacemaker cells. We can observe entire riverbanks of fireflies flashing in unison, planets forming galaxies, galaxies forming clusters, and our brain itself is a self-organizing system. How can complexity arise spontaneously from the simple laws governing the dynamics of these systems? Should we expect only intelligent systems to be capable of ordered, collective behaviour? As a matter of fact, the answer is no: the interaction between 'simple' and rather unintelligent constituents of a physical system can in fact be responsible for the spontaneous emergence of 'complex' and beautiful spatio-temporal structures.

The study of self-organization has made enormous progresses since the seminal works by Turing [1] and Prigogine [2] in chemical systems, by Haken [3] in optical systems and other pioneers of the field [4]. We have nowadays a quite general framework to understand complexity, and in particular the spontaneous emergence of structures and order. Spatio-temporal structures can emerge in nonlinear systems driven far from equilibrium, when

the homogeneous state loses stability against another state which displays some form of spatio-temporal variation − a pattern − which is maintained stationary by a flux of energy through the system. Over the years a long list of pattern-forming models have been built, ranging from chemical, to fluid-dynamical, and biological [4]. However, very often these systems are not easily controllable experimentally, or they are not describable from first principles; highly controllable and well-understood systems displaying self-organization are precious and rare.

Nonlinear optics proved to be a powerful benchmark for testing pattern-formation models, as it offers great flexibility and an extreme level of control, as well as a well-established microscopic understanding of the underlying dynamics. Typically, optical self-organization experiments are arranged as follows: a relatively intense plane wave beam is shone onto a nonlinear optical material, and feedback is provided by retroreflecting the transmitted beam [5, 6, 7, 8] or via the interaction of two counterpropagating beams [9, 10]. A large variety of nonlinear media has been employed through the years, such as atomic gases [11, 8], Liquid Crystal Light Valves [12, 13], or photorefractive media [14] to name a few. Above a given threshold for the incident power, spatial structures emerge in the plane transverse to the propagation direction of the optical beam(s); this explains why this field of research (particularly active during the 1990s) fell under the name of *transverse nonlinear optics* [15, 16, 17]. Thanks to the high level of experimental control and the detailed theoretical understanding of these systems, the agreement between theoretical/numerical results and the experiments reached an unprecedented level among self-organizing studies. Structures such as hexagons, rolls, squares have been predicted and generated [16],

as well as more exotic ones such as quasi-crystals [18]. Moreover, transverse nonlinear optics is still opening unexplored areas of research, including the implementation of optical fractal patterns [19, 20], or self-organizing arrays of optical vortices [21].

All these studies belong to the realm of nonlinear optics, where the interaction between the optical fields and the medium is mediated by an internal excitation of the medium. This internal excitation is the carrier density in photorefractive media, or (for the case of interest in this thesis) is given by the internal-state populations and coherence of the atoms composing a gas [8]. This means that hexagon formation is realized, for instance, by encoding complementary structures in the medium polarization, which (at the microscopic level) corresponds to the atomic coherence. The external degrees of freedom are untouched by nonlinear optics experiments at room temperature, as even for strong optical gradients optical forces are overwhelmed by thermal effects.
Parallel to the development of transverse nonlinear optics, however, another field of research developed and quickly became an important part of modern science: cold-atoms physics. Evolving from the first realizations of laser cooling in 1978 [22, 23], modern setups are now used everyday in numerous laboratories worldwide that can confine up to $10^{10} - 10^{11}$ (neutral) atoms at extremely low temperatures ($\sim 10\,\mu$K) and high peak densities ($\sim 10^{11}$at/cm^3). Laser cooling and the realization of cold thermal gases has rapidly become a 'standard' procedure, let aside the realization of Bose-Einstein condensates at even lower temperatures and higher densities [24]. Cold atoms offer numerous benefits in terms of reduced Doppler broadening, extremely low speed, and sensitivity to optical forces: dipole traps are in fact

extremely effective in confining atoms for long times in the potential imposed by light fields. Dipole traps nowadays represents a true workhorse for the realization of condensed matter hamiltonians [25, 26], modern studies of quantum computation and information protocols [27], and fundamental studies of nonlinear dynamical systems [28].

Can we bring together this *opto-mechanical* coupling between light and cold atoms and the general ideas of self-organization? In particular, can we investigate self-organizing dynamics in cold atoms where the center of mass of the atoms is affected, and not their internal excitation? The answer to this question is that we can, and there already exist a variety of setups showing self-crystallization and ordering of cold atoms. Since the advent of laser cooling it became clear that atomic motion exerts a back-action on the dynamics of the optical fields: early examples include, for instance, recoil-induced-resonances [29], the Collective Atomic Recoil Laser (CARL) [30, 31, 32, 33], or superradiant Rayleigh scattering [34]. In the presence of feedback, spatial instabilities can be expected for the coupled light-atom dynamics, as the stationary state for the system might not be homogeneous. Generally speaking, cold atoms in optical lattices (and self-organizing optical lattices) received notable interest in recent years as they offer the possibility of emulating magnetism in highly controllable systems (both in terms of classical and quantum spin systems). The realization of complex and tunable many-body interactions is in fact possible in cold atoms, leading for example to the realization of Bose-Hubbard [25] and Dicke hamiltonians [26], or spin-glass behaviour and frustrated interactions [35, 36]. Both classical and quantum phase transitions can be explored using

these many-body cavity quantum electrodynamics setups, giving the possibility of testing fundamental models of magnetism and condensed matter.

Collective Atomic Recoil Lasing

The first proposal for spatial instabilities due to opto-mechanical coupling arose in what has been termed Collective Atomic Recoil Laser (CARL) [30], where a cloud of cold atoms is placed within a bidirectional ring cavity and pumped by one side. A *backscattered* field is generated by the atoms, which counterpropagates with the pump. Interference between the two beams results in a dipole potential which in turns cause the atoms to bunch in its minima, maximizing the Bragg condition for backscattering. A dynamical instability is therefore obtained where the homogeneous state (no backscattered beam, no density modulation) is converted into a patterned state (two counterpropagating beams, $\lambda/2$ modulation of the density) [32, 33]. Moreover, the location of the potential minima along the cavity axis is self-selected, which results in a breaking of a continuous symmetry. CARL essentially realizes the atomic equivalent of a Free Electron Laser (FEL), where the electrons composing a plasma self-bunch and emit coherent radiation (with extreme properties of tunability and power, see [37]). The denomination CARL highlights some of the essential features of all cold atoms self-organizing systems:

- Collective. The self-organization process is essentially a many-body effect, as the atoms composing the gas are coupled in an all-to-all fashion through the optical field.
- Recoil. The fundamental process in the dynamics is the atomic recoil which follows scattering events; in other words,

the interaction involves the motional degrees of freedom of the atoms (and not the internal-state polarization, at least in a fundamental way)

- Lasing. The self-generated radiation (the backscattered beam in this case) is coherent, which means that the self-organization process results in an unconventional form of lasing[1].

Cavity-pump setups

A second setup which gained notable notoriety in the cold-atoms community is what we term here the cavity-pump setup. Originally proposed by Domokos and Ritsch [38] for cold (thermal) atoms, it has been more recently extended to a Bose-Einstein condensate in a series of experiments at ETH [39, 40, 41, 42]. The phenomenology is similar in the two cases, but a simple and insightful analysis [43] shows that in the zero-temperature limit the self-organization process realizes the superradiant quantum phase transition of the Dicke-model hamiltonian. For deep potentials, the dynamics of the system can be mapped into a Bose-Hubbard model, so that the spontaneous emergence of a pattern effectively realizes the celebrated superfluid-to-Mott transition [13].
In the cavity-pump setup, a cloud of cold (or condensed) atoms is placed within a Fabry-Perót cavity, and pumped from the side (transversely to the cavity axis). Some of the pump photons are scattered into the cavity mode by the initially homogeneous cloud, which creates a standing wave $\sim \cos^2 kx$. As in CARL, the atoms bunch into the minima of the corresponding optical potential, which optimizes the Bragg condition and enhances scattering into the cavity mode. As a result of this runaway mechanism, the homogeneous state is unstable (above a critical value for the pump)

[1] Unconventional for atomic systems, but not in plasma/FEL setups.

and is converted into a periodic , wavelength-scale checkerboard pattern [38, 44, 39]. Due to the interference between the pump and the cavity fields not all the potential wells are populated, but the system can self-select whether to occupy the 'odd' or the 'even' wells. This results in a spontaneous breaking of a discrete Z_2 symmetry (which is in fact broken by the Dicke phase transition), and in the superradiant population of the cavity mode. With a view to the pattern-forming dynamics, however, it is important to bear in mind that no continuous symmetry is broken by the system, as the spatial periodicity is determined (as in CARL) by the optical wavelength. Otherwise stated, placing a cavity in the empty space already breaks the translational symmetry, and the cavity-pump self-organization further breaks the discrete Z_2 symmetry. Extending this setup to a multi-mode cavity a continuous symmetry breaking is expected, as the system can choose between a continuum of transverse modes to populate. This in turns has been proposed to realize frustrated interactions and glassiness, as a disordered spin dynamics can effectively be realized using the motional degrees of freedom of the atoms [35, 36].

Counterpropagating beams in an elongated cloud

A third setup that we wish to briefly discuss here has been recently implemented at Duke University in the group led by Daniel J. Gauthier. It consists of an elongated cloud of cold (thermal) atoms, pumped by two counterpropagating beams. This system has been shown to display collective behaviour, and again the superradiant emission of wave-mixing beams was reported [45]. Moreover, the light-atoms interaction leads to an extremely strong $\chi^{(5)}$ nonlinearity at remarkably low light levels [46].

In terms of pattern-forming dynamics, the spontaneous emer-

gence of off-axis sidebands have been reported in [47]. In the near field, this indeed corresponds to the spontaneous emergence of spatial patterns, but the system is quite limited by its small aspect-ratio (the longitudinal dimension is much larger than the transverse one). As can be seen from Ref. [47], in fact, the transverse domain accommodates the fundamental wavenumber but is not capable of resolving higher-order spatial harmonics. These experiments thus show the first realization of a true pattern-forming dynamics due to opto-mechanical coupling, but in a quite small aspect-ratio system, so that the results are hard to interpret and analyse.

What is new in this work?

The expression 'true pattern-forming dynamics due to opto-mechanical coupling' used above means the spontaneous breaking of continuous translational degrees of freedom (unlike in cavity-pump setups), where spatial patterns are encoded in the motional degrees of freedom of the gas, and emerge with self-selected scales and self-selected orientations (unlike in CARL). As in all the systems discussed above, we also expect such an opto-mechanical pattern formation to lead to cooperative behaviour; in the rest of the thesis, a synonym for opto-mechanical pattern formation will be *self-structuring*, emphasizing that spatial structures are realized for the atomic density (and not the internal-state properties as in hot-atoms pattern formation). The work presented in this thesis is concerned with the theoretical and numerical study of cold-atoms setup in which a self-structuring transition can be observed in the plane transverse to the propagation of a single optical beam. Systems of interest for this thesis are those which 'naturally' possess a multi-mode nature (similar to

the multi-mode proposals of [35, 36]), allowing the observation of continuous symmetry breaking for the motional degrees of freedom of the system. Extending previous research in hot-atom pattern formation, we will focus on two feedback schemes: the single-mirror feedback geometry (Chapter 2 and Sec. 3.2) and a ring cavity geometry (similar to CARL or the Lugiato-Lefever model [6], Sec. 3.1). These systems show remarkable elegance, simplicity and tunability, offering the possibility of implementing a variety of nonlinear states, including localized patterns and solitons (Sec. 3.3). Our investigation will take a 'nonlinear dynamics' viewpoint, addressing the linear stability of semiclassical model equations, but a close connection exists with studies addressing the ground-state properties of similar systems (see e.g. the cavity-pump literature [43, 13]). We wish to clarify this concept throughout the thesis, but a clear example is given by the study of cavity-pump systems: for thermal gases self-organization is interpreted as a dynamical instability [38], while in the zero-temperature limit a description can be given in terms of a many-body hamiltonian whose ground state is degenerate at the critical point [43]. As we will deal with thermal atoms in our work, we do not investigate the quantum limit and always deal with classical transitions. However, a Dicke-like interaction is still underlying dispersive light-atom interactions, and it is therefore legitimate to ask what kind of quantum transition realizes the continuous symmetry breaking corresponding to self-structuring instabilities. Future research in this direction could aim at deepening the understanding of self-structuring transitions, using the ultimate simplicity and elegance of self-structuring in cold atoms to investigate fundamental aspects of many-body physics.

Chapter 1

Introductory concepts

In this first Chapter some introductory notions concerning the physics of cold atoms (Sec. 1.1) and the study of self-organization outside equilibrium (Sec. 1.2) are presented. These two topics are seldom found together in a single work, but the intention is to emphasize from the beginning that the aim of this thesis is to bring together these two fields. The following Chapters will clarify how the very general concepts of self-organization can be used in the realm of cold-atoms physics. In Sec. 1.3 the general scenario for self-structuring analysed in the following chapters will be presented and discussed.

1.1 Mechanical effects of light on atoms

This Section is concerned with the physics underlying cooling, trapping and manipulation of atomic gases. Far from being exhaustive on this broad subject, the concepts used in the context of this work will be presented concisely, focusing on theoretical aspects. Atoms will be systematically thought as two-level systems, a useful idealization for understanding the underlying physical mechanisms. Such a simplified theory of light-atom interaction is indeed capable of describing the relevant physical mecha-

nisms which lead to a mechanical manipulation of atoms by light, namely the scattering (radiation) force and the dipole (gradient) force.

Since Maxwell first developed the fundamental theory of electromagnetism [48], it has been clear that light can exert forces over matter, as the momentum carried by a light beam gives rise to the so-called radiation pressure. In 1933 Frisch made the first experimental studies of radiation pressure on atoms [49], following Lebedev [50] and Nichols and Hull [51] who quantitatively studied radiation pressure on macroscopic objects at the beginning of the twentieth Century. With the advent of the laser, Ashkin foresaw the potential use of intense beams to manipulate atoms: the deflection of atomic beams by laser light was demonstrated in 1970 [52]. The use of light radiation forces exerted by lasers to slow down and trap atomic gases was first proposed by Hänsch and Schawlow [53] and Wineland and Dehmelt [54]. In 1978, Ashkin proposed a trapping scheme based on a combination of radiation forces (used to slow down an atomic beam) and dipole forces (used to trap it afterwards) [55]. In the same year the first two realizations of gas cooling were obtained, by Wineland *et al* [22] with Mg ions held in a Penning trap, and Neuhauser *et al* with trapped Ba^+ ions [23]. Thirty years after these pioneering contributions, the cooling of atomic gases down to tens of μK exploiting laser light (hence the widely used term, *laser cooling*) is an everyday procedure in many laboratories worldwide. The exploding scientific interest in the field of cold-atoms physics led to the Nobel prize in 1997, awarded to Steven Chu, Claude Cohen-Tannoudji and William Phillips for their outstanding contributions in the '*development of methods to cool and trap atoms*

with laser light'.

It must be stressed at this point that the denomination 'cold atoms' may be misleading if one thinks of 'temperature' in terms of the thermodynamic, equilibrium temperature of an atomic gas. The reason why laser cooling attracted so much interest in the scientific community, in fact, is mainly that *cold* atoms are meant to be *slow*, *free* atoms. For instance, this would make measurements easier (long measurement times for atomic beams), and would drastically reduce Doppler line broadening: just to name an application, these are aspects which are crucial for the realization of an atomic clock. If the average speed of an atom at room temperature is about the speed of sound ($\sim 300\,\mathrm{m/s}$), in principle, one could reduce it by simply refrigerating the room, as the average speed scales with the square root of the temperature. However, already at 77 K a nitrogen (N_2) gas will condense, while the atoms still move at an average speed of 150 m/s. Before reaching low speed values (i.e., less than 1 m/s) by simple refrigeration, any kind of gas will reach such a low vapour pressure that essentially no atoms are in the gas phase, and thus no atoms are free. Laser cooling is concerned with the *slowing down* of the particles composing a gas via a non-equilibrium procedure, which leaves the particles moving at extremely low speed values ($\sim$ cm/s) in the gas phase.

The desire to reduce the motional degree of freedom of a gas, yet avoiding condensation, was a major motivation in the early studies of laser cooling. As the field progressed, however, the horizon of possible applications further broadened: the realization of Bose-Einstein condensates, for instance, paved the way for the study of an entirely new state of matter [24]. Optical lattices, briefly discussed in Sec. 1.1.4, form the basis of many

studies of fundamental quantum mechanics and quantum information [25, 28]. This thesis work is not concerned with laser cooling, but with one of its direct consequences: once the atoms are cooled down (i.e., are slowed down), in fact, forces exerted by light become detectable as they can compete with thermal effects. One can envisage a situation where a gas is cooled down by use of light forces, and thereafter interacts with another light beam. Because the atoms are 'frozen' at extremely low speeds, the light forces originating by this second beam will be only marginally counteracted by the thermal motion of the atoms for a long time, while these optical forces would be completely non-detectable at room temperatures.

The rest of this Chapter is organized as follows. Sec. 1.1.1 describes the mechanical action of light on atoms at rest. We will follow the line of Gordon and Ashkin [56] in introducing dipole and radiative forces, but the same concepts can be found in many reviews and textbooks [57, 58, 59]. In particular, a particularly insightful interpretation of the dipole force, due to Dalibard and Cohen-Tannoudji [60], will be presented in Sec. 1.1.4. Appendix B contains a more detailed derivation of the Maxwell-Bloch equations for two-level atoms, which complements the definitions given here.

Atoms in motion will then be discussed, and the main concepts related to Doppler cooling are presented in Sec. 1.1.2. Since the main focus of this thesis is not the laser cooling process itself, but rather to exploit low temperatures in order to make light forces dominant over thermal effects, radiative forces and optical molasses will be dealt with only briefly. However, a comprehensive description of light forces is still necessary to understand, at least

in principle, how such temperatures can be achieved experimentally.

The role of dipole forces is discussed in Sec. 1.1.4. Radiation pressure and scattering forces, in fact, are not the only players in the game: dipole forces play a fundamental role in the trapping and manipulation of cold atoms. Originally recognized by Aksar'yan [61], dipole forces can be thought of as originating from the interaction between light an the induced dipole moment of the atom. The potential use of dipole forces to trap and confine dielectric particles was shown already in 1970 by Ashkin [62], who also proposed its use to trap laser-cooled atoms [52, 55].

To conclude, in Sec. 1.1.3 the inherent limitations of laser cooling are discussed and the Doppler temperature is derived.

1.1.1 Light forces: atoms at rest

The aim of this Section is to give an introductory presentation of the main actors in laser cooling and trapping: radiative (scattering) forces and dipole forces.

To understand how light can modify the motional degree of freedom of an atom, consider a two-level system interacting with a monochromatic plane wave. Let the wave be composed by photons of frequency ω_0, wavenumber $k_0 = \omega/c$, where c is the speed of light in vacuum, and propagation axis $\hat{z}$. The two-level system is characterized by the energy of the ground state $E_1 = \hbar\omega_1$, separated from that of the excited state $E_2 = \hbar\omega_2$ by $E_{\rm at} = \hbar\omega_{\rm at}$, where $\omega_{\rm at} = \omega_2 - \omega_1$. A 2×2 density matrix is used to describe the evolution of the two-level system: $\varrho = |i\rangle\langle j|$, where $i, j = g, e$ for the ground and excited state, respectively. A fundamental quantity in the light-atom interaction is the *detuning* δ, defined as the difference between the incoming radiation frequency ω_0 and the

atomic transition (resonance) frequency $\omega_{\rm at}$:

$$\delta = \omega_0 - \omega_{\rm at} \tag{1.1}$$

At the moment of interaction between the incoming photon and the two-level system (i.e., the simplified 'atom'), two processes are possible. If the atom is in the ground state $|g\rangle$, *absorption* occurs with a given probability: the photon energy is converted into the internal energy of the atom, which operates a transition and 'jumps' on the excited state $|e\rangle$. If the atom is already in the excited state, *stimulated emission* occurs with a given probability: the internal energy of the atom is converted into a photon, which gets emitted coherently with the incoming, 'stimulating' photon. The photon emission is accompanied by an atomic transition from $|e\rangle$ to $|g\rangle$. Even in the absence of any photon, a third fundamental process is possible: *spontaneous emission* causes an atom in the excited state to decay to the ground state, converting its internal energy into a photon which gets emitted in a random direction. The corresponding process of 'spontaneous absorption', which converts fluctuations in the environment into an excitation in the internal degree of freedom of the atom, is virtually absent due to the large optical transitions involved (typically hundreds of MHz). A detailed treatment of these fundamental single atom-single photon processes can be found in [63]. As a final remark, it is common to refer to transition rates instead of transition probabilities. Hence the spontaneous emission process is associated with a lifetime τ of the excited state, and the rate of spontaneous emission is $\Gamma = \tau^{-1}$.

The Hamiltonian governing the atom-field evolution is given by

$$\mathcal{H} = H_{\rm field} + H_{\rm atom} + H_{\rm int}\,, \tag{1.2}$$

where H_{field} is the energy in the electromagnetic field, and $H_{\text{atom}} = p^2/2M + \hbar\omega_{at} |e\rangle \langle e|$ the sum of external (motional) and internal (electronic) energy of the atom. The third term is simply given by the dipole interaction: H_{int} is the energy required to align the induced dipole of the atom by applying an electric field $\vec{\mathcal{E}}$:

$$H_{\text{int}} = -\vec{\mathcal{E}} \cdot \vec{\mathcal{P}}\,, \tag{1.3}$$

where $\vec{\mathcal{P}}$ is the atomic dipole moment.
A widely used and well-verified assumption in laser physics goes under the name of Slowly Varying Envelope Approximation (SVEA) [64]. The results presented in Appendix A concerning the derivation of the Maxwell-Bloch equations, and indeed all the results presented in this thesis, also rely on this approximation. The main idea underlying the SVEA is that given the following representation of the electric field and polarization,

$$\vec{\mathcal{E}}(\mathbf{x}, t) = E(\mathbf{x}, t) e^{i(k_0 z - \omega_0 t)} \hat{\epsilon} + \text{c.c.} \tag{1.4a}$$

$$\vec{\mathcal{P}}(\mathbf{x}, t) = N_0 P(\mathbf{x}, t) e^{i(k_0 z - \omega_0 t)} \hat{\epsilon} + \text{c.c.} \tag{1.4b}$$

the spatial and temporal variations of the field envelope $E(\mathbf{x}, t)$ are much slower than the wavelength $\lambda_0 = 2\pi/k_0$ and the period $T_0 = 2\pi/\omega_0$, respectively. Here N_0 denotes the density of the medium, while the polarization direction is represented by $\hat{\epsilon}$ and assumed to lie in the x-y plane, with the wave propagating along $\hat{z}$. The dipole moment $\mathbf{P} = P\hat{\epsilon}$ describes the polarization response of the material to the incoming radiation. In the Maxwell-Bloch picture, this is connected to the raising/lowering operators of the atom (see Appendix B Eq. (13)), and can be expanded as

$$\mathbf{P} = \mu_{\text{dip}} \left[|g\rangle \langle e|\, e^{i(k_0 z - \omega_0 t)} + |e\rangle \langle g|\, e^{-i(k_0 z - \omega_0 t)} \right] \hat{\epsilon}\,, \tag{1.5}$$

where $\mu_{\rm dip}$ can be taken real without loss of generality, and the polarization vector is parallel to the electric field. Using (1.4) and (1.5), the dipole energy (1.3) reads

$$\begin{aligned} H_{\rm int} = -\vec{\mathcal{P}} \cdot \vec{\mathcal{E}} = -\mu_{\rm dip} \left|g\right\rangle \left\langle e\right| \left(E e^{2i(k_0 z - \omega_0 t)} + E^* \right) + \\ - \mu_{\rm dip} \left(E^* e^{-2i(k_0 z - \omega_0 t)} + E^* \right) \left|e\right\rangle \left\langle g\right| \simeq \\ \simeq -\mu_{\rm dip} \left\{ \left|g\right\rangle \left\langle e\right| E^* + E \left|e\right\rangle \left\langle g\right| \right\} . \end{aligned} \tag{1.6}$$

The last approximation consisted in neglecting the terms varying as $\exp[\pm 2i(k_0 z - \omega_0 t)]$, and is usually referred to as Rotating Wave Approximation (RWA). The key concept under this approximation is that performing a spatial and temporal average over characteristic time and space scales of the systems, these terms will eventually have zero mean [64].

Given the above expression for the interaction energy $H_{\rm int}$, an expression for the average force exerted on the centre-of-mass of the atom can be given. A natural (and effective) way of proceeding would be to stick with a semiclassical approach and write the force components as $f_i = -\vec{\mathcal{P}} \cdot \partial \vec{\mathcal{E}} / \partial x_i$. Alternatively, in the Heisenberg picture states are constant in time and the operators evolve according to

$$\frac{d\mathcal{O}}{dt} = -\frac{i}{\hbar} [\mathcal{O}, \mathcal{H}] \, .$$

The force $\mathbf{f}$ is thus given by the familiar expression (performing the substitution $\mathbf{p} \to -i\hbar\nabla$):

$$\mathbf{f} = \frac{d\mathbf{p}}{dt} = -\frac{i}{\hbar} [\mathbf{p}, \mathcal{H}] = -\nabla \mathcal{H} \, .$$

The only non-commuting term in the Hamiltonian is the interaction term, so that from Eq. (1.6) the force is found as

$$\mathbf{f} = \mu_{\text{dip}} \left\{ |g\rangle \langle e| \nabla E^* + \nabla E \, |e\rangle \langle g| \right\} . \tag{1.7}$$

It should be emphasized that a rigorous treatment would have taken into account the quantum field operators E and $E^\dagger$, connected to the annihilators and creators of the field Fock space. However, these can exchanged with their classical expectation values, E and E^*, by assuming the field to be in a coherent state. Hence, normal ordering of the operators needs not be respected in what follows. Also, an identical result to Eq. (1.7) can be obtained from the classical expression $\mathbf{f} = -(\vec{\mathcal{P}} \cdot \nabla)\vec{\mathcal{E}}$.
Eq. (1.7) is written in terms of the raising and lowering operators of the atom, $|e\rangle \langle g| \equiv \hat{\varrho}_{21}$ and $|g\rangle \langle e| \equiv \hat{\varrho}_{12}$. A standard derivation of the Maxwell-Bloch equations, presented in Appendix B, leads to the following equations of motion for the expectation values $\varrho_{12} = \langle \hat{\varrho}_{12} \rangle$ and $w = \langle \hat{\varrho}_{11} - \hat{\varrho}_{22} \rangle$ (see Appendix A):

$$\dot{\varrho}_{12} = -\frac{\Gamma}{2} \left(1 - i \frac{2\delta}{\Gamma} \right) \varrho_{12} + w g \tag{1.8a}$$

$$\dot{w} = -\Gamma \left(w - 1 \right) - 2 \left(\varrho_{12} g^* + \varrho_{21} g \right) \tag{1.8b}$$

Here relaxation of the population difference w with a decay rate Γ has been introduced, together with a dephasing rate $\Gamma/2$ for the coherence ϱ_{12}. Such dephasing rate is based on the assumption that collisional dephasing is negligible, which is well-verified in laser-cooled gases [58]. The detuning δ has been introduced in Eq. (1.1), while the Rabi frequency g has been defined as

$$g = \frac{i \mu_{\text{dip}}}{\hbar} E \, . \tag{1.9}$$

With this notation, the average force is found from (1.7) as

$$\mathbf{f} = -i\hbar \left[\varrho_{12}\nabla g^* - \varrho_{21}\nabla g\right] .$$

By representing $\nabla g = \left(\vec{\alpha} + i\vec{\beta}\right) g$, with $\alpha, \beta \in \mathbb{R}$, the following expression for the force is reached:

$$\mathbf{f} = -i\hbar\vec{\alpha}\left[\varrho_{21}g - \varrho_{12}g^*\right] - \hbar\vec{\beta}\left[\varrho_{21}g + \varrho_{12}g^*\right] . \tag{1.10}$$

This representation brings no loss of generality, since if $g = |g|e^{i\phi}$ with $|g|$ and ϕ real, then $\vec{\alpha} = \nabla \log|g|$ and $\vec{\beta} = \nabla\phi$.
Since motionless atoms are of interest here, the field envelope E (and hence the Rabi frequency g) can be taken to be time-independent and ϱ_{12}, w are given by the steady-state solution of the Maxwell-Bloch equations (1.8):

$$\bar{\varrho_{12}} = \frac{2g}{\Gamma(1 - i\Delta)}\frac{1}{1+s} \tag{1.11a}$$

$$\bar{w} = \frac{1}{1+s} , \tag{1.11b}$$

where the (adimensional) saturation parameter s has been defined as

$$s = \frac{8|g|^2}{\Gamma^2(1+\Delta^2)} \tag{1.12}$$

and the dimensionless detuning Δ is given by

$$\Delta = \frac{2\delta}{\Gamma} . \tag{1.13}$$

Using (1.11) and (1.10), the force can thus be rewritten again to reach its final form:

$$\mathbf{f} = -\hbar\frac{s}{1+s}\left[\delta\vec{\alpha} + \frac{\Gamma}{2}\vec{\beta}\right] . \tag{1.14}$$

The main features of the two terms appearing in the force expression (1.14) are now worth discussing: by recognizing in Eq. (1.14) the steady-state excited state population, $\Pi_2 \equiv \varrho_{22} = \frac{1}{2}s/(1+s)$, the second term on the r.h.s. can be rewritten as

$$\mathbf{f}_{\text{rad}} = -\hbar\vec{\beta}\,\Gamma\varrho_{22}\,.$$

This is the radiative (scattering) force: quanta of average momentum $\hbar\vec{\beta}$ are removed from the incoming optical field at the same rate (Γ) that the atom is undergoing spontaneous decay. This happens because a photon at average momentum $\hbar\vec{\beta}$ is absorbed and successively re-emitted in a random direction, in a scattering process. The higher the probability of having the atom in the excited state, the higher the force exerted, because an emission process is more likely.

The first term in the r.h.s. of Eq. (1.14), in contrast, describes the dipole forces originating from coherent redistribution of the field due to the stimulated emitted photons. Such forces are of conservative nature and can be derived from a potential. To show this, $\vec{\alpha}$ can be manipulated to obtain

$$\vec{\alpha} = \vec{\nabla}\log|g| = \frac{\vec{\nabla}|g|}{|g|} = \frac{1}{2|g|^2}\vec{\nabla}|g|^2 = \frac{1}{2}\frac{\vec{\nabla}s}{s}\,.$$

Plugging this result back into Eq. (1.14) one finds

$$\mathbf{f}_{\text{dip}} = -\frac{\hbar\delta}{2}\frac{\vec{\nabla}s}{1+s} = -\frac{\hbar\delta}{2}\vec{\nabla}\log(1+s) \tag{1.15}$$

which can be seen as the (conservative) force originating from the potential

$$U_{\text{dip}} = \frac{\hbar\delta}{2}\log(1+s)\,. \tag{1.16}$$

Two interesting limit cases are of particular interest: that of a purely travelling wave, and that of a standing wave (that is, two counterpropagating travelling waves). For a travelling (plane) wave of wavevector $\mathbf{k}$, the field envelope has no spatial structure, and one finds immediately that $\vec{\alpha} = 0$, $\vec{\beta} = \mathbf{k}$. Therefore dipole forces are absent in this case, as they originate from spatial gradients of the field envelope; equivalently, the potential profile (1.16) is uniform. Scattering forces from a travelling wave, on the other side, give rise to the removal of quanta with momentum $\hbar\mathbf{k}$ from the field, with a rate $\Gamma\varrho_{22}$.
Conversely, for a pure standing wave radiative forces coming from the two counterpropagating waves exactly balance each other, while interference creates a modulation in the intensity profile along the propagation axis. The effect of the corresponding potential energy modulation can be used to confine and trap atoms, as discussed in Sec. 1.1.4.

1.1.2 First-order velocity dependence: Doppler cooling

In the last Section the expressions for the dipole and scattering forces acting on atoms at rest were derived. However, to understand the main idea underlying Doppler cooling one needs to consider atoms in motion. If the atom moves with velocity $\mathbf{v}$, the time dependence of the electric field E (and thus g) must be taken into account:

$$\frac{dg(\mathbf{x},t)}{dt} = \frac{\partial g(\mathbf{x},t)}{\partial t} + \left(\mathbf{v}\cdot\vec{\nabla}\right) g(\mathbf{x},t)\,.$$

For a purely monochromatic wave the first term is still vanishing, $\partial g/\partial t = 0$, but now the second term is not since $\mathbf{v} \neq 0$. Therefore

$$\frac{dg}{dt} = \left(\mathbf{v}\cdot\vec{\nabla}\right) g = \mathbf{v}\cdot\left(\vec{\alpha} + i\vec{\beta}\right) g\,. \tag{1.17}$$

Following [56], the first-order velocity dependence of the force can be found in the following way. The steady-state solutions for motionless atoms, Eq. (1.11), is derived with respect to time using (1.17). Then the Maxwell-Bloch equations (1.8) are rewritten with these 'corrected' values of $\dot{w}$, $\dot{\varrho}_{12}$ and the new steady-state values are determined, $\varrho_{12}^{(1)}$ and $w^{(1)}$. Finally, these velocity-dependent values can be used in (1.10) to find the expression for the force.

From the definition (1.12) of s, $\dot{s} = 2s\mathbf{v}\cdot\vec{\alpha}$. Eqs. (1.11) then lead to

$$\begin{aligned}
\frac{d\varrho_{12}}{dt} &= \frac{\dot{g}}{(\Gamma/2 - i\delta)(1+s)} - \frac{g}{(\Gamma - i\delta)(1+s)^2}\dot{s} = \\
&= \frac{\mathbf{v}\cdot(\vec{\alpha} + i\vec{\beta})g}{(\Gamma/2 - i\delta)(1+s)} - \frac{g}{(\Gamma/2 - i\delta)(1+s)^2}2s\mathbf{v}\cdot\vec{\alpha} = \\
&= \frac{2g}{(\Gamma - i\Delta)(1+s)}\left[(\mathbf{v}\cdot\vec{\alpha})\frac{1-s}{1+s} + i(\mathbf{v}\cdot\vec{\beta})\right] = \\
&= \varrho_{12}\left[(\mathbf{v}\cdot\vec{\alpha})\frac{1-s}{1+s} + i(\mathbf{v}\cdot\vec{\beta})\right] \qquad (1.18)
\end{aligned}$$

and

$$\frac{dw}{dt} = -\frac{\dot{s}}{(1+s)^2} = -\frac{2s\mathbf{v}\cdot\vec{\alpha}}{1+s}w\,. \qquad (1.19)$$

The Maxwell-Bloch equations (1.8) are modified as

$$\varrho_{12}^{(1)}\left[(\mathbf{v}\cdot\vec{\alpha})\frac{1-s}{1+s} + \Gamma/2 - i(\delta - \mathbf{v}\cdot\vec{\beta})\right] = \frac{g}{1+s} \qquad (1.20a)$$

$$w^{(1)}\left[\Gamma - \frac{2s}{1+s}\mathbf{v}\cdot\vec{\alpha}\right] = \Gamma\left(1 - 2\frac{s}{1+s}\right) \qquad (1.20b)$$

Consider now the case of a plane wave with wavenumber $\mathbf{k}$. As discussed above, only scattering forces are present, as one immediately finds that $\vec{\alpha} = 0$ and $\vec{\beta} = \mathbf{k}$. Hence the only velocity modification in the previous treatment is found to be the fre-

quency Doppler shift: $\delta \to \delta - \mathbf{v}\cdot\mathbf{k}$. The corresponding value for $\varrho_{12}^{(1)}$ is given by

$$\varrho_{12}^{(1)} = \frac{g}{1+s}\left[\Gamma/2 - i(\delta - \mathbf{v}\cdot\mathbf{k})\right]^{-1} ,$$

which leads to the following expression for the force (1.10):

$$\begin{aligned}\mathbf{f}_{\rm rad} &= \hbar\mathbf{k}\left[\frac{|g|^2/(1+s)}{\Gamma/2 + i(\delta - \mathbf{v}\cdot\mathbf{k})} + \frac{|g|^2/(1+s)}{\Gamma/2 - i(\delta - \mathbf{v}\cdot\mathbf{k})}\right] = \\ &= \frac{\hbar\Gamma}{2}\frac{2|g|^2}{1+s}\frac{\mathbf{k}}{\Gamma^2/4 + (\delta - \mathbf{v}\cdot\mathbf{k})^2} .\end{aligned}$$

Expanding to first order in $\mathbf{v}$,

$$\mathbf{f}_{\rm rad} = \frac{\hbar\Gamma}{2}\frac{s}{1+s}\left(1 + 2\delta\frac{\mathbf{v}\cdot\mathbf{k}}{\Gamma^2/4 + \delta^2}\right)\mathbf{k} . \qquad (1.21)$$

This result implies that if two waves counterpropagate along $\pm\mathbf{k}$, the $\mathbf{v}$-independent contributions will cancel, and the average radiation force is linear in $\mathbf{v}$. Radiative forces thus result in a friction effect for negative detuning, $\delta < 0$ (referred to as *red detuning*), and conversely will cause heating on the blue side of the resonance, $\delta > 0$. In other words, if two red-detuned waves propagating along $\pm\mathbf{k}$ are used to illuminate the atom, the overall result will be a reduction in the translational energy of the atom, which will get 'stuck' between the two beams. In three spatial dimensions, six waves (in three orthogonal pairs) can be used to achieve cooling. Because of this friction, momentum-damping effect, such beams are usually referred to as *optical molasses*.

It is important to note that this cooling mechanism is an outside-equilibrium process: energy is taken from the translational energy $p^2/2M$ of the atom and converted into the energy of the photons emitted by spontaneous decay. Since the spontaneously emitted photons are 'lost' in the environment, energy is effectively being

taken away irreversibly from the system. As stressed in the introduction of this Chapter, this is the sort of dissipative situation needed in order to reduce kinetic energy without reaching condensation of the gas.

Beside the formal derivation presented so far, the physical interpretation of the cooling mechanism is also worth discussing. The crucial point is that when an atom absorbs a photon not only the photon energy $\hbar\omega$ needs to be converted into the internal energy of the atom, but the momentum $\hbar\mathbf{k}$ must also be conserved. Therefore at the moment of absorption the atom experiences a *recoil* $\hbar\mathbf{k}$ (i.e., gets 'kicked' by light). When the photon gets spontaneously re-emitted, a momentum $\hbar\mathbf{k}'$ is created, and again by momentum conservation the atom must experience a recoil $-\hbar\mathbf{k}'$. Although these single momentum 'jumps' are small, a sequence of many recoil events can add up to a dramatic reduction in kinetic energy.

To have a clear understanding of why this results in cooling for red-detuned beams and heating for blue-detuned beams, consider an atom moving along $-\mathbf{k}$, in the direction of a red-detuned beam of frequency $\omega < \omega_{\mathrm{at}}$, propagating along $+\mathbf{k}$. The optical frequency $\omega_{\mathbf{v}}$ observed by the atom is Doppler-shifted as $\omega_{\mathbf{v}} = \omega - \mathbf{v}\cdot\mathbf{k}$. Since $\mathbf{v} \sim -\mathbf{k}$, this results in the atom 'seeing' the field more resonant with its own transition. In turns, this makes absorption (and hence photon scattering) more likely for an atom moving away from the intersection of the molasses beams. This justifies the term *Doppler cooling* usually employed in this context; reversing the signs of the argument, it is clear that blue-detuned molasses would lead to the opposite situation in which atoms scatter less when travelling away from the inter-

section of the beams.

Otherwise stated, the spontaneous re-emission of the absorbed photon results in an elastic momentum transfer for the photon, $\mathbf{k} \to \mathbf{k}'$, with a corresponding recoil for the atom. The important point is that $\mathbf{k}'$ points in a completely random direction, while $\mathbf{k}$ always points along the beam propagation direction: after many scattering processes, on average the atom will feel a recoil along $\mathbf{k}$. If two counterpropagating beams are used (or six for a full three-dimensional cooling), this leads to the cooling of the gas. This argument also implies that the atoms composing the gas perform a random walk in momentum space. Although the recoil 'steps' have zero average because of the random nature of spontaneous emission, in fact, fluctuations about this average are unavoidable. Indeed, these fluctuations play the fundamental role of determining the final temperature of the gas, since they set the ultimate limit that can be reached by Doppler cooling: this will be discussed in Sec. 1.1.3. Methods for the so-called *sub-Doppler cooling*, based on multi-level atomic structures, are nowadays available and widely employed. Indeed, the possibility of reaching temperatures below the Doppler limit came out as an unexpected result in 1988 [65], and was explained only the following year by Dalibard and Cohen Tannoudji [66] and Ungar, Weiss, Chu and Riis [67]. However, we will limit our analysis to two level atoms in this work, and we refer to Refs. [66, 67, 58] for details on multi-level atomic cooling.

A second point worth noting about this random walk in momentum space is that it leads to diffusive motion inside the molasses. As the velocity spread grows with time as $\left\langle \Delta v^2 \right\rangle \sim t$, atoms in optical molasses are confined within the intersection region of the beams for a much longer time than they would with purely ballis-

tic motion. However, it must be stressed that optical molasses do not form a trap for the gas, as there is no restoring force: optical traps can be built based on dipole forces, discussed in Sec. 1.1.4.

1.1.3 Cooling limitation: the Doppler temperature

The aim of this Section is to briefly discuss the role of fluctuations in optical molasses, and specifically their role in determining the final temperature of a Doppler-cooled gas, usually referred to as the *Doppler temperature* T_D.
As discussed earlier, in fact, fluctuations due to spontaneous emission eventually limit the extent to which cooling can be achieved. Consider the molasses force (1.21): for two counterpropagating waves (six for 3D cooling) the average force is in the form $\mathbf{f}_{\text{mol}} = -\alpha\mathbf{v}$. Hence the average momentum $\langle\mathbf{p}\rangle$ evolves as $\langle\dot{\mathbf{p}}\rangle = -\gamma\langle\mathbf{p}\rangle$, with $\gamma = \alpha/M$, whose solution is given by

$$\langle\mathbf{p}(t)\rangle = \mathbf{p}_0 e^{-\gamma t}\,. \tag{1.22}$$

Given the evolution of the average momentum, consider the fluctuations in the Langevin equation

$$\begin{gathered}\dot{\mathbf{p}} = \mathbf{f}_{\text{mol}} + \delta\mathbf{f}(t) \\ \langle\delta\mathbf{f}\rangle = 0 \quad \langle\delta\mathbf{f}(t)\delta\mathbf{f}(t')\rangle \propto \delta(t-t')\end{gathered} \tag{1.23}$$

where the two-time correlation is obtained under the Markovian assumption. This is valid when the coherence time of the system is short compared to its evolution; in this case the system timescale is determined by the momentum damping, $t_{\text{ext}} = 1/\gamma = M/\alpha$. The coherence time is the time needed for a spontaneous decay to occur, $t_{\text{c}} = (s\Gamma)^{-1}$. Since $t_{\text{ext}} \gg t_{\text{c}}$ the Markovian assumption is valid and the autocorrelation coefficient is defined

as

$$\langle \delta\mathbf{f}(t)\delta\mathbf{f}(t')\rangle = 2D\,\delta(t-t')\,. \tag{1.24}$$

The solution of Eq. (1.23) is given by

$$\mathbf{p}(t) = \mathbf{p}_0 e^{-\gamma t} + \int_0^t dt' \delta\mathbf{f}(t') e^{-\gamma(t-t')}\,,$$

so that the temperature can be found by computing $\left\langle \mathbf{p}^2 - \langle\mathbf{p}\rangle^2 \right\rangle / 2M = 3/2 k_B T$. Hence we have

$$\begin{aligned}\left\langle \mathbf{p}^2 - \langle\mathbf{p}\rangle^2 \right\rangle &= \int_0^t dt'dt'' \,\langle \delta\mathbf{f}(t')\cdot\delta\mathbf{f}(t'')\rangle\, e^{-\gamma(t-t')} e^{-\gamma(t-t'')} = \\ &= \int_0^t dt'dt'' 2D\,\delta(t'-t'') e^{-\gamma(2t-t'-t'')} = \\ &= 2D\int_{-\infty}^{\infty} dt' e^{-2\gamma(t-t')} = \frac{D}{\gamma}\left(1-e^{-\gamma t}\right)\,,\end{aligned}$$

where the integration limits have been stretched to $\pm\infty$ in the last row since the interaction occurs on times much shorter than t. In conclusion,

$$k_B T = \frac{D}{3M\gamma}\left(1-e^{-\gamma t}\right) \tag{1.25}$$

On 'internal' atomic timescales $e^{-\gamma t} \simeq 1-\gamma t$, so that this result reduces to diffusive motion, $\left\langle \Delta\mathbf{p}^2 \right\rangle = 2Dt$. Over long times, instead, $e^{-\gamma t} \to 0$ and a lower bound for the achievable temperature is found in terms of the cooling rate α:

$$k_B T_D = \frac{D}{3\alpha}\,, \tag{1.26}$$

where T_D is the Doppler temperature.

The next step would therefore consist in evaluating D. This has been done for example in [56], where the general result for the fluctuations arising from scattering and dipole forces is derived.

Without reporting the details the result of interest is given here, concerning the case of two counterpropagating waves, each with saturation parameter p_0. The overall intensity profile $p(\mathbf{x}) = 2p_0 \cos(\mathbf{k}\cdot\mathbf{x})$ gives rise to an average dipole force: in the notation of Sec. (1.1.1) $\vec{\beta} = 0$ and $\vec{\alpha} = -\mathbf{k}\tan(\mathbf{k}\cdot\mathbf{x})$. Fluctuations of the atomic dipole lead to a correlation strength [56]

$$D = \hbar^2 |\mathbf{k}|^2 \Gamma p_0 \,. \tag{1.27}$$

For six beams, this value is multiplied by three; hence using Eq. (1.26) we find

$$k_B T = \frac{D}{3\alpha} = \frac{\hbar^2 |\mathbf{k}|^2 \Gamma p_0}{\alpha} \,.$$

The damping rate α is found from Eq. (1.21) in the limit of $p_0 \ll 1$ as

$$|\alpha| \simeq \frac{\hbar|\delta|\Gamma}{\Gamma^2/4 + \delta^2} p_0 |\mathbf{k}|^2 \,,$$

so that after some algebra

$$k_B T_D = \hbar \frac{\Gamma^2/4 + \delta^2}{|\delta|} \,.$$

The most interesting quantity is the minimum value of T_D, which also corresponds to the maximum value of the damping α. Deriving this last results with respect to $|\delta|$ the minimum values are obtained as

$$k_B T_D = \frac{\hbar\Gamma}{2} \quad \text{for} \quad \delta = -\frac{\Gamma}{2} \,. \tag{1.28}$$

As a final remark, the Doppler temperature does not depend on p_0 in the limit $p_0 \ll 1$. The maximum value of the damping rate is found, in overall, at $\delta = -\Gamma/2$ and $p_0 = 1$.

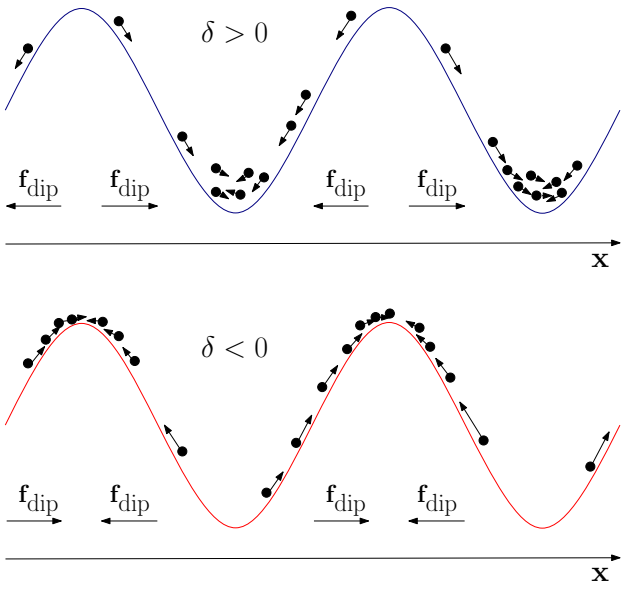

Figure 1.1: Sketch of the dipole forces acting in a modulated field: for blue detuning (upper panel) atoms accumulate in the low-intensity regions, while for red detuning (lower panel) atoms are attracted towards high-intensity regions.

1.1.4 Building an optical trap: dipole forces

The last Section focused on radiative (scattering) forces, and discussed how they can be used in order to achieve cooling of a gas of two-level atoms. The aim of this Section is to discuss in more detail dipole forces, introduced in Section 1.1.1.

We found in Eqs. (1.15) and (1.16) that the dipole force is conservative and can be derived from the potential $U_{\rm dip} = (\hbar\delta/2)\log(1+s)$. This suggests that dipole forces could be used to trap the atoms (or any kind of dielectric particles) in the regions of minimum energy: a modulated field intensity $s = s(\mathbf{x})$, in fact, will create energetically favourable spatial regions for the atoms to bunch. It is worth noting that, generally speaking, temperature fluctuations may destroy the trapping action of dipole forces, and thus should ideally kept to a minimum. To achieve this, consider again the general expression (1.14) of light forces. Assuming small light intensities, $s \ll 1$, the expansion $\log(1+s) \simeq s$ is valid and

the scaling of dipole forces is given by

$$|\mathbf{f}_{\rm dip}| \sim s|\delta| \sim |E|^2|\Delta|^{-1}\,,$$

while radiative forces scale as

$$|\mathbf{f}_{\rm rad}| \sim s \sim |E|^2|\Delta|^{-2}\,.$$

Hence large detuning values, $|\delta| \gg \Gamma$ ($|\Delta| \ll 1$), can be used to make radiative forces negligible compared to dipole forces. This is motivated by the fact that radiative forces originate from the absorptive response of the atom (proportional to $|\Delta|^{-2}$), whereas dipole forces originate from the dispersive response of the atom (proportional to $|\Delta|^{-1}$).

The sign of the detuning is important too, as it selects the sign of the potential (1.16). For blue detuning, the potential is positive and the force is attractive when going 'uphill' the potential. Since the potential is essentially given by the intensity profile, intensity minima are attractive for $\delta > 0$, while intensity maxima are repulsive. Conversely, in red-detuned traps ($\delta < 0$) the intensity maxima attract atoms, and the intensity minima repel them: Fig. (1.1) schematically represents this detuning dependence of dipole forces.

We stress that, although the attraction of the atoms towards regions of high/low intensity can be obtained directly from the form of the dipole potential, a clear physical picture of this has to be obtained through a dressed-state approach to the problem, which will be the focus of the next Section.

1.1.5 The dipole force 'revisited'

All the quantities needed for discussing opto-mechanical instabilities in cold gases were derived in the previous Sections. Before proceeding, an 'alternative' view of dipole forces is briefly presented in this Section, originally proposed by Dalibard and Cohen-Tannoudji [60]. The main reason of this is that the derivation presented earlier in the Chapter, based on the Maxwell-Bloch Equations, does not provide a physical interpretation of dipole forces - while it does for scattering forces. For instance, although the expression (1.16) for the dipole potential turns out to be correct, no explanation is given as to why atoms seek high intensity regions for red detuning, and low-intensity regions for blue detuning. A quantum treatment of the problem, based on the eigenstates of the complete Hamiltonian of the system (the *dressed states*) will provide a satisfactory physical picture, at the same time confirming the results presented earlier.

Consider again the Hamiltonian

$$\mathcal{H} = H_{\text{field}} + H_{\text{atom}} + H_{\text{int}} \,, \tag{1.29}$$

where the atomic Hamiltonian is given by $H_{\text{atom}} = p^2/2M + \hbar\omega_{\text{at}} b^\dagger b$, with the raising and lowering defined as

$$b = |g\rangle\langle e| \quad b^\dagger = |e\rangle\langle g| \,.$$

The quantum nature of the electromagnetic field is taken into account by writing the free field as

$$H_{\text{field}} = \sum_\lambda \hbar\omega_\lambda \, a_\lambda^\dagger a_\lambda \,,$$

and again expand the interaction energy by keeping only the secular terms:

$$H_{\rm int} = -\mathbf{P}\cdot\left[b^\dagger \mathbf{E}^+(\mathbf{x}) + b\mathbf{E}^-(\mathbf{x})\right] .$$

The positive and negative frequency components of the electric field may be expanded as

$$\mathbf{E}^+(\mathbf{x}) = \sum_\lambda \mathbf{E}_\lambda(\mathbf{x}) a_\lambda$$
$$\mathbf{E}^-(\mathbf{x}) = \sum_\lambda \mathbf{E}^*_\lambda(\mathbf{x}) a^\dagger_\lambda .$$

For an atom *dressed* (i.e., interacting) with monochromatic laser radiation at frequency ω , thus, the position-dependent energy is

$$H_{\rm da} = \hbar\omega_{\rm at} b^\dagger b + \hbar\omega a^\dagger_\omega a_\omega - \vec{\mu}\cdot\left[\mathbf{E}_\omega(\mathbf{x}) b^\dagger a_\omega + \mathbf{E}^*_\omega(\mathbf{x}) b a^\dagger_\omega\right] . \quad (1.30)$$

If the light-atom interaction is switched off ($\mathbf{P} = 0$), the eigenstates of (1.30) are bunched in manifolds $\mathcal{E}_n$, separated by the energy gap $\hbar\omega$. Note that in writing the eigenstates both the atom and the field systems must be considered. In the absence of coupling, these are simply given by the states $|g; n+1\rangle$ describing a ground-state atom and $n+1$ photons, and $|e; n\rangle$ describing an excited atom and n photons. The manifolds $\mathcal{E}_n$ are 'closed' with respect to absorption and stimulated emission, as the number of quanta for the atom-field system is fixed. The relative energy between $|g; n+1\rangle$ and $|e; n\rangle$ depends on whether there is more energy in a photon or in the atomic transition: if $\omega < \omega_{\rm at}$ (red detuning $\delta < 0$), the minimum energy configuration is reached with the state $|g; n+1\rangle$, and vice versa for blue detuning ($\delta > 0$) the ground state is $|e; n\rangle$.

Spontaneous emission, i.e. the coupling of the atom with the

vacuum state of the radiation field, connects manifolds at different energies: spontaneous emission events will make the system collapse from the manifold $\mathcal{E}_n$ to $\mathcal{E}_{n-1}$, until eventually the zero-quanta configuration is reached, $|g;0\rangle$. The dressed-state approach allows one to deal with spontaneous emission, for instance explaining the triplet-sideband structure of the atomic spectrum [60]. However, since dipole forces are the main focus in what follows, spontaneous emission is neglected by assuming the field to be far-detuned from resonance, $|\delta| \gg \Gamma$, and the light-matter coupling described by Eq. (1.30) is considered.
The eigenenergies of the Hamiltonian (1.30) can be found exactly as [60]:

$$E_{1n} = (n+1)\hbar\omega - \frac{\hbar\delta}{2} + \frac{\hbar\Omega(\mathbf{x})}{2}$$
$$E_{2n} = (n+1)\hbar\omega - \frac{\hbar\delta}{2} - \frac{\hbar\Omega(\mathbf{x})}{2}\,,$$

with the correspondent eigenstates (dressed states) being given by:

$$|1;n,\mathbf{x}\rangle = +e^{i\varphi(\mathbf{x})}\cos\theta(\mathbf{x})\,|e,n\rangle + e^{-i\varphi(\mathbf{x})}\sin\theta(\mathbf{x})\,|g,n+1\rangle$$
$$|2;n,\mathbf{x}\rangle = -e^{i\varphi(\mathbf{x})}\sin\theta(\mathbf{x})\,|e,n\rangle + e^{-i\varphi(\mathbf{x})}\cos\theta(\mathbf{x})\,|g,n+1\rangle\ .$$

Here *generalized Rabi frequency* was defined using the notation of Sec. 1.1.4 as

$$\Omega(\mathbf{x}) = \sqrt{4|g(\mathbf{x})|^2 + \delta^2}\,, \tag{1.31}$$

and the angle $\theta(\mathbf{x})$ by

$$\cos 2\theta(\mathbf{x}) = -\delta/\Omega(\mathbf{x}) \qquad \sin 2\theta(\mathbf{x}) = 2|g(\mathbf{x})|/\Omega(\mathbf{x})$$

With this picture in mind, the populations and coherences in the dressed state picture can be defined, given by the expectation val-

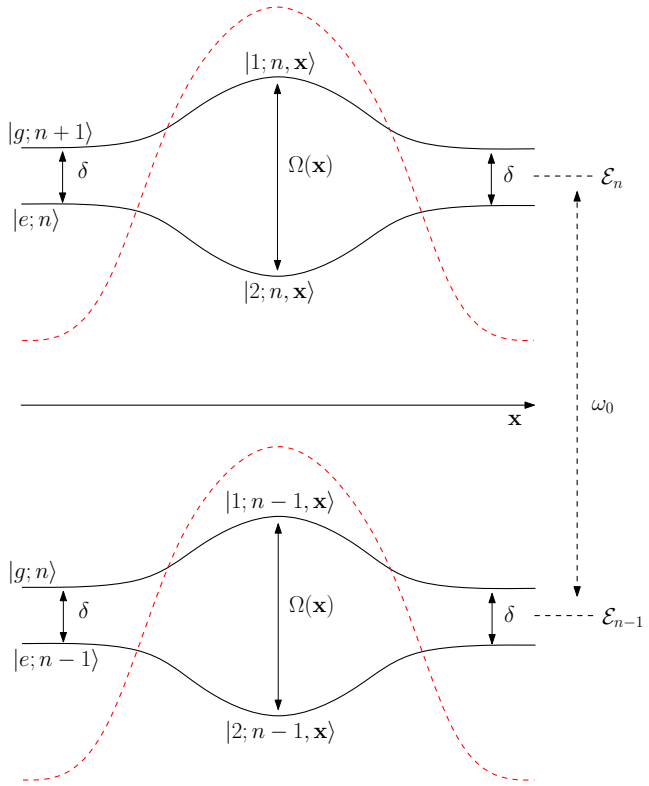

Figure 1.2: Schematic representation of the dressed-atom picture for the red-detuned case, $\delta < 0$. Outside the optical beam (red dashed line) the 'bare' eigenstates of the manifold $\mathcal{E}_n$ (upper panel) are $|g, n+1\rangle$ and $|e, n\rangle$, separated by δ. Moving inside the region illuminated by the beam, instead, the level splitting is given by the generalized Rabi frequency $\Omega(\mathbf{x})$; correspondingly, the two eigenstates are the dressed states $|1; n, \mathbf{x}\rangle$, $|2; n, \mathbf{x}\rangle$. Note that both this energy splitting and the wavefunctions are position-dependent. Different manifolds $\mathcal{E}_n$ are separated by the laser frequency ω_0 and correspond to different total excitation numbers (photons + atom internal energy).

ues of the density matrix operator $\hat{\varrho}$ over all the possible photon number values:

$$\Pi_i(\mathbf{x}) = \sum_n \langle i; n, \mathbf{x} \mid \hat{\varrho} \mid i; n, \mathbf{x} \rangle$$
$$\varrho_{ij}(\mathbf{x}) = \sum_n \langle i; n, \mathbf{x} \mid \hat{\varrho} \mid j; n, \mathbf{x} \rangle$$

In the limit of well-resolved lines, $\Omega(\mathbf{x}) \gg \Gamma$, the stationary values for the Π_i's and ϱ_{ij}'s are found to be

$$\Pi_1^{\mathrm{st}} = \frac{\sin^4\theta}{\sin^4\theta + \cos^4\theta}$$
$$\Pi_2^{\mathrm{st}} = \frac{\cos^4\theta}{\sin^4\theta + \cos^4\theta}$$
$$\varrho_{12} = \varrho_{21} = 0$$

Note that the limit of well-resolved lines is satisfied either with large intensities ($|g| \gg \Gamma$) or large detunings ($|\delta| \gg \Gamma$); as discussed above, spontaneous emission is here neglected assuming the field to be detuned far from resonance.

Physical insights related to the nature of dipole forces can be obtained by considering the work $dW = \mathbf{f}_{\mathrm{dip}} \cdot d\mathbf{r}$ needed to move a dressed atom by $d\mathbf{r}$. It turns out [60] that two contributions are relevant:

$$dW = \sum_{i=1,2} \left[\Pi_i dE_i + E_i (d\Pi_i)_{\mathrm{NA}} \right] .$$

The second contribution is related to nonadiabatic (NA) changes in the dressed state populations due to atomic motion; since the intention is to make a connection with Sec. 1.1.1, which deals with atoms at rest, this contribution will be neglected here.

The first term is instead related to the gradients of the dressed

states energy deviations from to the (position-independent) value $(E_{1n}+E_{2n})/2$, that is, is related to the gradients of the *light shifts*

$$E_1 = \frac{1}{2}\hbar\Omega(\mathbf{x}) \qquad E_2 = -\frac{1}{2}\hbar\Omega(\mathbf{x}) = -E_1$$

For atoms at rest the Π_i's can be exchanged with their stationary values, and therefore the dipole force can be written as

$$\begin{aligned} \mathbf{f}_{\text{dip}} &= \left(\Pi_2^{\text{st}} - \Pi_1^{\text{st}}\right) \nabla E_1(\mathbf{x}) \\ &= \frac{\hbar\delta}{2} \nabla \log\left(1 + \frac{2|g(\mathbf{x})|^2}{\delta^2}\right), \end{aligned} \tag{1.32}$$

which is identical to (1.15) in the limit $|\delta| \gg \Gamma$.

It should be stressed at this point that, even if the result obtained by the dressed-state approach for the expression of the dipole force is identical to (1.15), we now are provided with a clear physical picture. The force (1.32) is in fact given by the balance of two opposite tendencies, weighted by the probabilities of populating the state $|1\rangle$ and $|2\rangle$. To explain the dependence from the detuning, consider the case of blue detuning, $\delta > 0$, where the dressed state $|1\rangle$ coincide with the bare state $|g\rangle$ outside the beam. Since the occupation probability of the ground state always exceeds that of the excited state in a two-level system, it means that the state $|1\rangle$ will always be more populated than the state $|2\rangle$. As a consequence, the dipole force (1.32) will be negative, expelling the atom from high-intensity regions. Conversely, for negative detuning the state $|2\rangle$ will be more populated than $|1\rangle$, as there are fewer spontaneous decays starting from $|2\rangle$ than from $|1\rangle$. Hence $|2\rangle$ will prevail and make the force (1.32) positive, which in turns will attract the atom towards regions of high intensity.

1.2 Self-organization outside equilibrium

1.2.1 General features

In this Section some general concepts of dynamical systems and pattern formation outside equilibrium are briefly reviewed. A detailed discussion of pattern formation in non-equilibrium systems can be found in the classic review by Cross and Hohenberg [4], or in the more recent book by Cross and Greenside [68]. For a detailed presentation of the concepts used in the study of dynamical systems the reader is referred to the booktexts by Strogatz [69] or Guckenheimer and Holmes [70].

The spontaneous emergence of spatial order is a pre-eminent feature of non-equilibrium physical systems which are under constant external drive from the environment. In these systems it is in fact possible to observe macroscopic spatial structures at steady state, which can exist as long as the system is driven far from equilibrium. Note that the non-equilibrium condition is essential in order to have 'ordered', anti-entropic steady states which violate the entropy principle. The spontaneous emergence of spatial order (in short, pattern formation) received many different denominations in past research, such as *disspative structures formation* (Prigogine [2]), *synergetics* (Haken [3]), or more simply self-organization (Krinsky [71]). A pioneering study of pattern formation was carried by Turing in 1954 [1] to describe biological morphogenesis, but the applications of the concepts of self-organization are nowadays virtually endless. Ref. [4] contains an exhaustive bibliography on the subject and its many, multidisciplinary applications.
A crucial point to bear in mind when dealing with non-equilibrium

systems is that there exists no reason to assume that there is a Gibbs ensemble or some energy functional to minimize in order to obtain the steady-state behaviour. The approach therefore consists in describing the system in terms of 'microscopic equations', typically partial differential equations. The term 'microscopic' does not imply necessarily an 'atomic' scale of these equations, but only refers to the fact that these equations form the elementary blocks of the analysis. The booktext example is fluid dynamics, where the Navier-Stokes equations are taken as 'microscopic' equations (see for instance the prototypical Swift-Hohenberg model [72]). Such a 'dynamicist' approach will be taken in the following, describing the system under analysis by means of a set of partial differential equations (*pde*'s) for the system variable $E(\mathbf{x}, t)$:

$$\frac{\partial E}{\partial t} = G\left[E, \partial_{\mathbf{x}} E, \partial^2_{\mathbf{x}} E; \lambda\right] \ .$$

Note that in general E may be a vector (or a complex quantity). The functional G depends (nonlinearly) on E through its first and second-order spatial derivatives. In general G may depend also on higher order derivatives of E, but this possibility will not be considered here. The parameter λ is called the *control parameter*, and parametrizes the strength of the external driving. We remark that upon introducing the dependence from the spatial coordinate $\mathbf{x}$ the phase space of the system is made infinite-dimensional, the trajectory of the system following a curve in this space. In 'standard' dynamical systems (with no $\mathbf{x}$ dependence), instead, the phase space is typically finite-dimensional [70].

Dynamical systems can be divided in two general classes: *conservative* (or Hamiltonian) systems where the phase space volume is conserved through the evolution, and *dissipative* systems where

any subvolume will contract to zero as time progresses. The work presented in this thesis focuses on the latter case, where an energy flux is maintained through the system via driving and dissipation. In dissipative systems, the dynamics eventually brings the system in a lower-dimensional portion of phase space (with zero volume), called an *attractor*. A specific attractor needs not to be the only possible solution for the system: different attractors can have different *basins of attractions* of initial conditions. Moreover, attractors come in two species: *regular* attractors with 'simple' geometrical shape (such as fixed points, limit cycles, tori), and *chaotic* (or *strange*) attractors corresponding to chaotic dynamics and possessing unusual geometric properties [70, 69]. The difference between a conservative system and a driven-dissipative system can be summarized by the following simple example, see Fig. (1.3). A conservative oscillator is characterized by a limit cycle in phase space: if more energy is provided to the system a 'larger' limit cycle is obtained, but as long as there are no fluctuations energy is conserved and any cycle represents a marginally stable solution for the system. A driven-dissipative oscillator could have a similar limit cycle attracting the dynamics, but any small perturbation to this trajectory will be amplified or decay: the limit cycle is stable. If the injection of energy is interrupted, the dynamics is attracted toward the fixed point with zero energy (the origin of phase space).

1.2.2 Linear growth: instability types

One of the main instruments for the study of pattern formation goes under the name of linear stability analysis. The idea underlying the use of linear stability analysis to study pattern formation is that the homogeneous solution E_0 for the system (independent

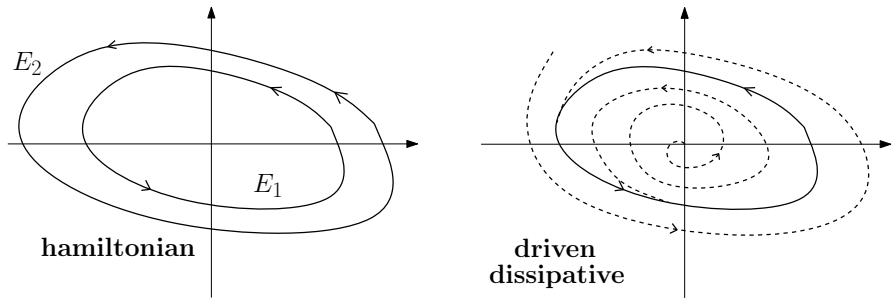

Figure 1.3: Hamiltonian versus driven-dissipative oscillators. In the hamiltonian case (left) every limit cycle is marginally stable, and perturbations can move the system from the cycle at energy E_1 to the cycle at energy $E_2 > E_1$. In the driven-dissipative case (right), the dynamics is attracted towards a stable limit cycle, and perturbations are amplified or suppressed if the system tries to leave the stable cycle.

on $\mathbf{x}$) loses stability when the control parameter exceeds a *critical*, or *threshold* value λ_c. Introducing the dimensionless quantity

$$\epsilon = \frac{\lambda - \lambda_c}{\lambda_c}\,, \tag{1.33}$$

which measures the distance from threshold, 'something interesting' is expected to happen when $\epsilon \geq 0$. This 'something interesting' is a qualitative change in the macroscopic spatial properties of the system, that is, what is commonly termed a phase transition in the realm of statistical mechanics. We remark that a connection can indeed be established between dynamical bifurcations and phase transitions [4]: for instance, in this context supercritical bifurcations are mapped into second-order transitions, while subcritical ones correspond to first-order phase transitions (see e.g. [3] for the subcritical lasing transition). In our 'nonlinear dynamics' approach the starting point is given by a system of n differential equations

$$\frac{\partial E}{\partial t} = G\left[E, \partial_{\mathbf{x}} E, \partial^2_{\mathbf{x}} E; \epsilon\right]\,,$$

where $E = E_0 = 0$ is assumed to be a solution for all values of λ. Note that given a homogeneous solution $E_0 \neq 0$, the rescaling $E \to E - E_0$ will automatically set $E_0 = 0$. The initial condition for the system is set to be $E(t = 0) = E_0 = 0$, and the evolution of modes

$$e_j(\mathbf{x}, t) = e_j(0) e^{\mathrm{i}\mathbf{q}\cdot\mathbf{x} - \mathrm{i}\omega\mathrm{t}} \tag{1.34}$$

is studied. The linearized system

$$\frac{\partial E}{\partial t} = A \cdot E \qquad A_{ij} \equiv \left.\frac{\delta G_i}{\delta e_j}\right|_{E=E_0}$$

has a set of eigenvalues $\omega_i(\mathbf{q})$, among which a specific one of them can be selected, say $\omega(\mathbf{q})$, with the property of having largest imaginary part. The critical point λ_c is defined as follows: the *growth rate* of the system is $\mathrm{Im}(\omega) < 0$ when $\lambda < \lambda_c$ ($\epsilon < 0$), and $\mathrm{Im}(\omega) = 0$ when $\lambda = \lambda_c$ ($\epsilon = 0$). The *critical wavevector* is defined as the wavevector $\mathbf{q}_c$ at which the eigenvalue crosses zero at the critical point. Because of the exponential dependence of the fluctuations $e_j \sim \exp(-\mathrm{i}\omega\mathrm{t})$, this means that fluctuations at the critical wavenumber becomes *marginally stable* at the critical point, i.e. they are not suppressed nor amplified by the dynamics. Above the critical point, $\epsilon > 0$, there is a (bounded) region in $\mathbf{q}$ space where $\mathrm{Im}(\omega(\mathbf{q})) > 0$ and the corresponding fluctuations $e_j(\mathbf{q}) \sim \exp(\mathrm{i}\mathbf{q}\cdot\mathbf{x} - \mathrm{i}\omega\mathrm{t})$ undergo exponential growth. Dynamic instabilities are usually divided in three classes [4], depending on the value of the critical wavevector. To simplify the discussion in the following the properties of the system are assumed to depend only on the wavenumber $q = |\mathbf{q}|$. If $\mathrm{Im}(\omega) = 0$ at $q_c = |\mathbf{q}_c| \neq 0$ at the critical point a class-I instability occur. Another kind of instability is possible if the growth rate is zero at $q = 0$, which typically happens in the presence of a conservation law. The

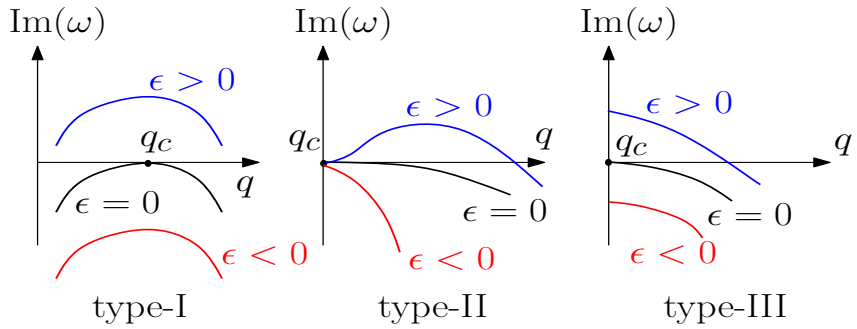

Figure 1.4: The different types of instability, see text. In addition, each instability type is classified as stationary if $\mathrm{Re}(\omega) = 0$, and oscillatory if $\mathrm{Re}(\omega) \neq 0$. ω represents the eigenvalue with largest imaginary part.

critical wavenumber is thus $q = 0$, and an unstable band $0 < q < q_+$ is obtained above threshold, $\epsilon > 0$: this is termed a type-II instability. The last option, which goes under the name of type-III instability, is realized when both the maximum growth rate and the critical wavenumber are found at $q = 0$. All these instabilities, moreover, can be of two types: *oscillatory* if $\mathrm{Re}(\omega) \neq 0$, or *stationary* if $\mathrm{Re}(\omega) = 0$ [4].

Note that type-III stationary instabilities do not involve pattern formation in a fundamental way, since the instability is at $q = 0$. In the nonlinear-optical framework of this thesis we will deal with type-I stationary instabilities.

1.2.3 Nonlinear saturation: ideal patterns

The role of the nonlinearity is to saturate the linear growth of perturbations. Since the superposition principle does not hold, the system is free to select between different symmetry-related states which grow equally fast in the linear regime. In particular, for rotationally symmetric systems in which the stability properties depend only on the wavenumber $|\mathbf{q}|$ any roll pattern at the critical wavenumber in the form $\exp(i\mathbf{q}_c \cdot \mathbf{x})$ is linearly unstable. Superpositions of rolls at different angles give rise to different pat-

terns, such as squares (created by a $\pi/2$ angle between rolls) or hexagons ($\pm\pi/3$ angle). In a variety of systems without inversion symmetry $E \to -E$, however, hexagons are often favoured close to the critical point [4].

The main point of these nonlinear states, obviously, is that they all break the translation symmetry which is instead preserved below the critical point. Hence a spontaneous breaking of a continuous $U(1)$ symmetry is observed in one dimension, and additional groups are broken in higher dimensions. For the two-dimensional situations analyzed in Chap. 3, for example, we also obtain a breaking of the rotational symmetry. For the simple case of a roll pattern, the self-selection of a critical wavenumber $q_c \neq 0$ breaks the translational symmetry, while the choice of the roll rotation breaks the rotational symmetry. Looking at this in the Fourier $(q_x - q_y)$ plane, in particular, this means the the Fourier peaks are obtained at a self-selected distance from the origin $|\mathbf{q}| = 0$, with a self-selected orientation. Other symmetries, however, may be preserved by the transition. In particular, discrete translational symmetries are not broken in the case of ideal patterns. These are in fact defined as periodic solutions $E(x) = E(q_c x)$, so that given the phase $\varphi = q_c x$ the system is invariant under the transformation $\varphi \to \varphi + 2\pi$. In general, ideal patterns are invariant under some subgroup of the original symmetry group, as was also found in the Landau theory of phase transitions [4, 73]. While determining the overall stability of a system is a relatively easy task, the same cannot be said for the determination of which nonlinear state will arise above threshold. Far from the threshold point $\epsilon = 0$, one typically relies on numerical simulations of the model equations. Close to the critical point, instead, linearization of the non-homogeneous solution can determine whether rolls are stable

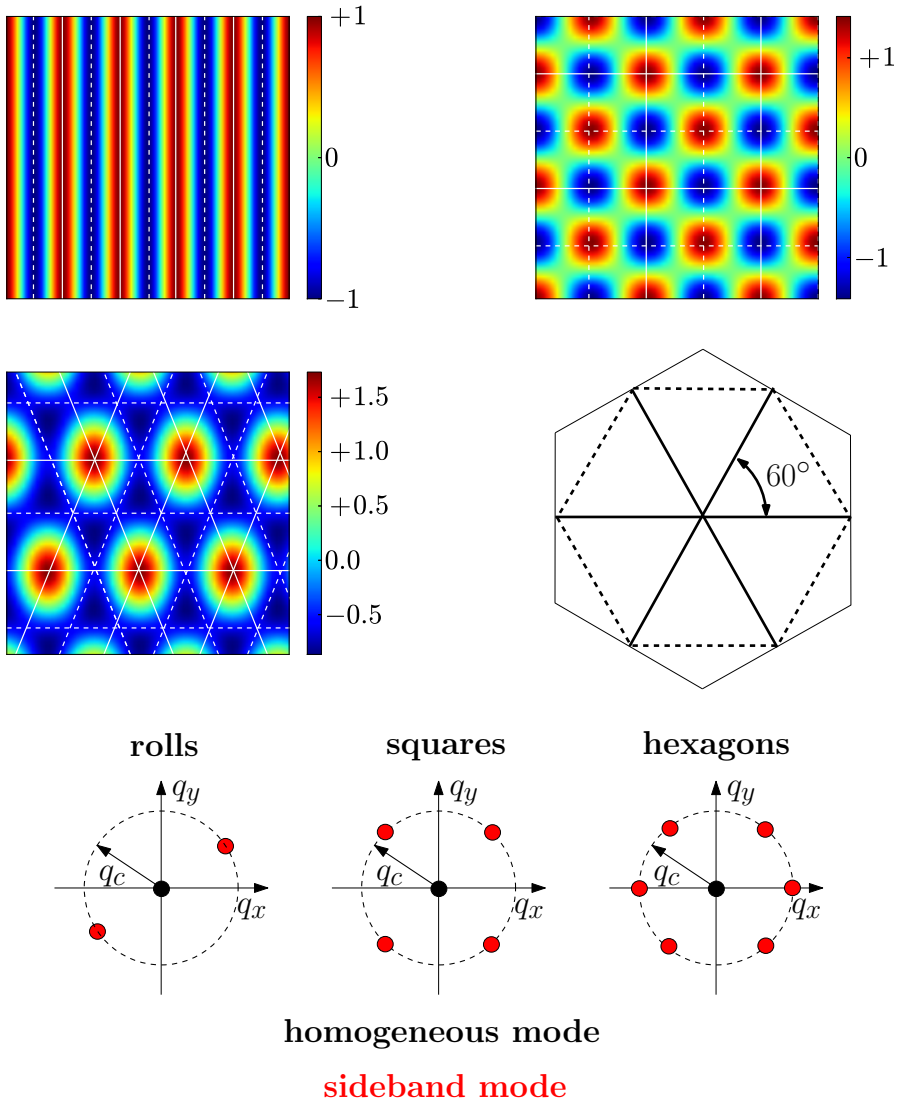

Figure 1.5: Ideal patterns in two dimensional systems: rolls (top left), squares (top right), hexagons (middle left). Full white lines indicate the maxima of the corresponding roll state, dashed white lines its minima. The middle right panel shows in detail the configuration for the hexagonal state, where three rolls intersect at an angle of $2\pi/3$ (120°). In the bottom row we show the far-field corresponding to each state.

against hexagons, or squares, etc. Some insightful results related to this problem, at least for system with cubic nonlinearities, are presented below.

Addressing the stability of ideal patterns: the amplitude equation

Consider first a single unstable roll mode: the quantity $E(\mathbf{x}, t)$ is expanded as

$$E(\mathbf{x}, t) = E_0 \exp(\mathrm{i}\mathbf{q}_\mathrm{c} \cdot \mathbf{x} - \mathrm{i}\omega \mathrm{t})$$

and close to threshold, $0 < \epsilon \ll 1$, it can be approximated as (assuming the roll state to be periodic in x)

$$E(\mathbf{x}, t) = [E_0 A(x, y, t) \exp(\mathrm{i}q_\mathrm{c}\mathrm{x}) + c.c.] + \mathcal{O}(\epsilon)$$

Note that, since a phase change results in a spatial shift of the pattern, a complex amplitude A is chosen. For isotropic systems the complex amplitude A obeys an amplitude equation of the form [4]

$$\tau_0 \frac{\partial A}{\partial t} = \epsilon A + \xi_0^2 \left[\frac{\partial}{\partial x} - \frac{\mathrm{i}}{2q_c} \frac{\partial^2}{\partial y^2} \right]^2 A - g_0 |A|^2 A \tag{1.35}$$

A particularly insightful derivation of Eq. (1.35) can be found in [3], emphasizing the idea that the critical mode slaves all the other modes close to threshold (since it has largest growth rate). The form of this equation reflects the symmetries of type-I stationary instabilities, with the scaling determined by the linear

properties of the system:

$$\tau_0^{-1} = \left.\frac{\partial \mathrm{Im}(\omega)}{\partial \epsilon}\right|_{q=q_c,\epsilon=0}$$
$$\tau_0^{-1}\xi_0^2 = -\left.\frac{1}{2}\frac{\partial^2 \mathrm{Im}(\omega)}{\partial q^2}\right|_{q=q_c,\epsilon=0}$$

The parameter $g_0 > 0$ sets the scale of the amplitude variation: upon rescaling

$$X = |\epsilon|^{1/2} x/\xi_0$$
$$Y = |\epsilon|^{1/4} y\,(q_c/\xi_0)^{1/2}$$
$$T = |\epsilon| t/\tau_0$$
$$\mathcal{A} = (g_0/\epsilon)^{1/2}\, A\,,$$

Eq. (1.35) can be written in the universal form

$$\frac{\partial \mathcal{A}}{\partial T} = \pm\mathcal{A} + \left[\frac{\partial}{\partial X} - \frac{\mathrm{i}}{2}\frac{\partial^2}{\partial Y^2}\right]^2 \mathcal{A} - |\mathcal{A}|^2\mathcal{A}\,. \qquad (1.36)$$

The amplitude equation (1.35) forms the basis of many general considerations about pattern formation processes, including the study of ideal pattern stability. Consider in fact the linear superposition of roll states

$$E = E_0\left[\sum_{i=-1}^{n} A_i(\mathbf{x},t)\exp\left(\mathrm{i}\mathbf{q}_\mathrm{i}\cdot\mathbf{x}\right) + c.c.\right] + \mathcal{O}(\epsilon)$$

where all the $\mathbf{q}_i$'s lie on the critical circle, $|\mathbf{q}_i| = q_c$. Here we denote by $\mathbf{x} = (x, y)$ the transverse coordinates. Rescaling $\mathbf{x} \to \mathbf{x}/\xi_0$, $q_c \to q_c\xi_0$, $t \to t/\tau_0$, and $A \to g_0^{1/2}A$ the amplitude equation (1.35) for each mode reads

$$\partial_t A_i = \epsilon A_i - \sum_{j=1}^{n} g_{ij}|A_j|^2 A_i$$

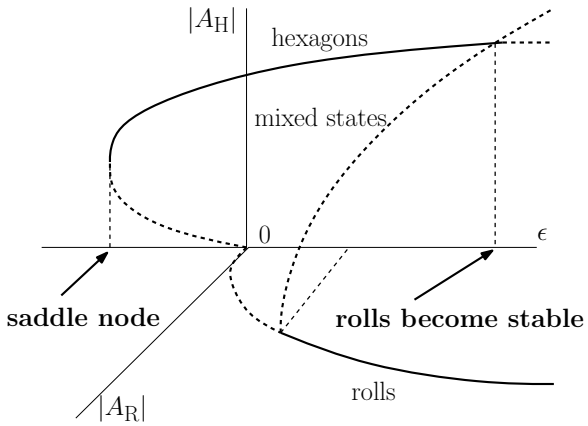

Figure 1.6: Hexagons become unstable via a saddle-node bifurcation at $\epsilon = \epsilon_{\rm SN} < 0$. Further increasing ϵ far from threshold, rolls become stable at $\epsilon = \epsilon_{\rm R}$. Here A_H: hexagons amplitude, A_R: rolls amplitude. Adapted from Ref. [74].

where g_{ij} depends on the angles $\mathbf{q}_i \cdot \mathbf{q}_j = \cos(\theta_{ij})$ via a function $g_{ij} = \mathcal{G}(\theta_{ij})$. Suppose that one wishes to study the stability of hexagons, formed by three wavevectors at $2\pi/3$ angle, satisfying $\mathbf{q}_1 + \mathbf{q}_2 + \mathbf{q}_3 = 0$. This condition brings an additional quadratic nonlinearity, and the amplitude equation for the mode amplitude A_1 reads [74] (similar equations holds for $A_{2,3}$):

$$\partial_t A_1 = \epsilon A_1 - \gamma A_2^* A_3^* - \left[|A_1|^2 + g_1\left(|A_2|^2 + |A_3|^2\right)\right] A_1\,, \quad (1.37)$$

where $g_1 = \mathcal{G}(2\pi/3)$. If $\gamma \neq 0$ the quadratic nonlinearity $\sim A_2^* A_3^*$ dominates at threshold, and this is the generic case when inversion symmetry $E \to -E$ is absent. In particular, for $\gamma \ll 1$ it can be shown that hexagons dominate the dynamics close to the critical point via a saddle-node bifurcation, but are unstable against rolls far from threshold (see Fig. (1.6)). The critical values of ϵ can be obtained from the amplitude equation as [74]:

$$\epsilon_{\rm SN} = -\frac{\gamma^2}{4(1+2g_1)} < 0 \qquad \text{saddle-node: hexagons become stable}$$

$$\epsilon_{\rm R} = \frac{\gamma^2}{(g_1-1)^2} \qquad \text{rolls become stable}$$

This argument shows that hexagons are expected close to threshold for systems following the amplitude equation (1.37). This prediction will be confirmed in the numerical simulations of Sec. 3.1.4 and Sec. 3.2.2.

1.3 The self-structuring scenario

In this Section the general setup analysed in the rest of the thesis is presented, in order to clarify the basic ideas of self-structuring in cold atoms.

The term *self-structuring instability* refers to the spontaneous formation of spatial structures in the density of a cold atomic gas, in the plane transverse to the propagation of a single pump beam. Corresponding structures are then encoded in the transverse profile of the optical beams, which drive the instability and transport the information to and from the atomic medium. Alternatively, this process can be thought in terms of a spontaneous bunching of the atoms, which scatter light in off-axis sidebands. Such sideband emission further supports the bunching, which creates the runaway process leading to a macroscopic bunching starting from infinitesimal fluctuations. As the spatial scale and orientation of the emerging structures is self-selected, self-structuring instabilities break the rotational and translational symmetries[1].
A key point worth emphasizing is that self-structuring instabilities are *diffractive* in nature, as diffraction of the optical beams provides spatial coupling between neighbouring points. With this respect, self-structuring in cold atoms realizes a Turing instability [1, 75], where

[1] In two transverse dimensions; only the translational symmetry is broken in one transverse dimension.

- the nonlinearity is provided by dipole forces;
- the spatial coupling is provided by diffraction;
- the driving is provided by continuously injecting energy through the pump beam.

To fully understand the role of diffraction in nonlinear optical systems, consider for the moment the general situation of a medium with an intensity-dependent refractive index, $n = n(I)$ (I being the optical intensity). As the pump beam propagates through the sample, any refractive index modulation (in the plane transverse to the propagation axis z) results in a phase modulation of the transmitted beam. This phase modulation is converted into an amplitude modulation by diffraction after $\frac{1}{4}z_T$, where z_T is the Talbot distance at which the phase structure of the input field is rebuilt (see also Sec. 2.3.3 for a discussion of the Talbot effect). Using an optical mirror the intensity-modulated optical beam can be resent back onto the medium, and since the refractive index is intensity-dependent an effective 'self-interaction' is created for the medium (with a delay time determined by the round-trip to the mirror and back). If the round-trip time is much shorter than the typical timescale for the refractive index dynamics, this interaction is effectively instantaneous and long-range.
The general mechanism outlined above lies at the heart of transverse pattern formation in any kind of nonlinear optical media (see e.g. [8]); what is new in cold atoms is the source of the intensity dependence in the refractive index. This comes in cold media from optical forces, and specifically from dipole forces in the work presented in this thesis. Otherwise stated, the density distribution of the gas determines the refractive index profile of the could (more atoms $\rightarrow$ stronger response, as the polarization is propor-

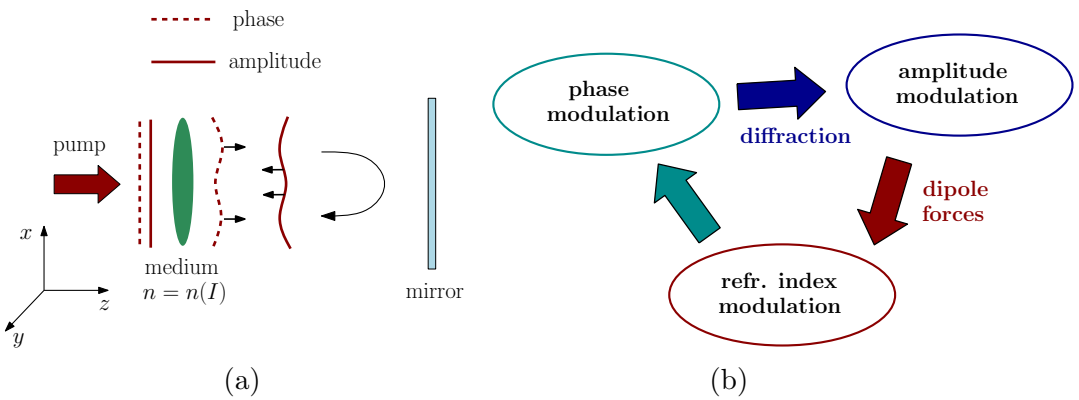

Figure 1.7: The basic scheme of the self-structuring feedback loop. A plane wave (with transversally flat phase and amplitude profiles) illuminates the medium, which imposes a phase modulation on the transmitted beam. Diffraction converts phase modulations into amplitude modulations, which consequently affect the refractive index of the medium via dipole forces.

tional to the density), this density distribution being shaped by the dipole forces arising from the intensity modulations which result from diffraction. The feedback loop is therefore built as follows:

- A plane wave (no transverse structure in phase nor amplitude) illuminates the gas
- Fluctuations in the atomic density profile (i.e. in the refractive index) impose fluctuations in the phase profile of the beam (equivalently, infinitesimal off-axis sidebands are emitted in the far-field)
- Diffraction in the round-trip to the mirror and back converts phase fluctuations into amplitude fluctuations. The mirror distance sets the preferred transverse spatial scale as the one that fulfils the Talbot requirement, see Sec. 2.3.3
- Amplitude fluctuations result in dipole forces, which move the atoms towards the minima of the optical potential
- Atomic motion enhances the initial refractive index fluctua-

tion

The scenario depicted above indicates that opto-mechanical self-structuring due to dipole forces should occur every time a feedback loop is created for an atomic sample which is sufficiently cold and dense. It is the aim of the next Chapters to investigate in more detail this scenario, and provide answers to questions such as: what is the required temperature to observe the formation of a pattern? What is the minimum pump intensity? What is the role of the velocity distribution? What is the role of the atomic internal state?

Chapter 2

Self-structuring instabilities: viscosity-free systems

This Chapter presents the theoretical and numerical analysis of symmetry-breaking instabilities in cold atoms, occurring in viscosity-free arrangements. By 'viscosity-free' (or 'damping-free' in the following) it is meant that no optical molasses are assumed to act on the atomic cloud during the pattern formation process, so that no velocity damping is present. The basic functioning of optical molasses in cooling and velocity damping is illustrated in Sec. 1.1.2. The 'viscous' situation where cold-atoms pattern forming instabilities take place in the presence of velocity damping is discussed in Chap. 3. The main consequence of the absence of optical molasses is that the atomic velocities are left free to evolve, so that their dynamics must be taken into account. The dynamics of the atomic cloud will be captured by a phase-space distribution $f(\mathbf{x}, \mathbf{v}, t)$, while a simplified description in terms of a spatial density distribution $n(\mathbf{x}, t)$ suffices in the 'viscous' regime. The resulting theory is strongly reminiscent of plasma stability theory [76]. This is not surprising, since the results discussed below are obtaining starting from the same premises, namely a collisionless Boltzmann equation for the gas (also known as the

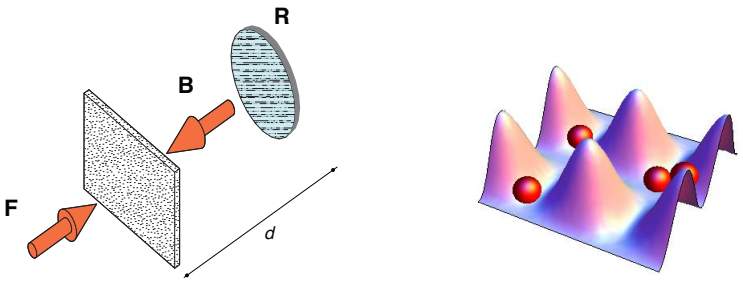

Figure 2.1: On the left, a sketch of the single-mirror-feedback scheme. The 'forward' plane wave F illuminates a diffractively thin layer of cold atoms and is retroreflected as the 'backward' beam B by a mirror of reflectivity R placed at a distance d from the medium. If a transverse modulation for the optical intensity is obtained, the atoms will seek the minima of the resulting dipole potential (right).

Vlasov equation). A Vlasov-based method for the study of cold-atoms dynamics in optical resonators already proved to be effective in previous research [77], and the analysis is extended here to single-mirror configurations. The damping-free dynamics investigated in this Chapter realizes an effective long range interaction between the atoms, and the resulting collective behaviour can give rise to a synchronization process analogous to the one studied in Refs. [78, 79, 80] (Sec. 2.6).

Our study will be focused on the so-called single-mirror-feedback geometry [5, 81, 82]. This can be seen as a 'half-cavity', where the cloud is illuminated from one side, and the transmitted beam is then retro-reflected by a mirror placed at a distance d, see Fig. (2.1). The single-mirror setup is particularly attractive from a theoretical/computational standpoint because the light-matter interaction can be separated from the propagation, at least in the simple case of a medium which is diffractively thin. All the work presented in this thesis will rely on the thin medium assumption, discussed below, and effects of propagation within the medium will be neglected. However, it should be stressed that the theory developed here is in good agreement with experimental results

from a setup where the medium thickness is non-negligible. This indicates that the main physics of self-structuring instabilities (see e.g. the experimental results of [83]) is captured by a thin-medium model. Ref. [83] also presents some results obtained taking into account the thickness of the medium, which somewhat 'corrects at higher orders' the results presented in the following Sections, particularly with respect to the spatial size of the structures observed experimentally (see Chap. 4).

2.1 Model equations

The coupled light-atoms dynamics is investigated starting from the description of the medium. The atomic sample is assumed to be cooled at a temperature $T \sim 100\,\mu$K, and subsequently is left free to interact with the pump beam (with the molasses beams turned off). The analysis presented in this thesis focuses on the dynamics in the plane of coordinates $\mathbf{x} = (x, y)$ transverse to the pump propagation axis $\hat{z}$; the atomic properties are homogeneous along the $\hat{z}$ direction. Alternatively, one could consider a pancake-shaped cloud which is extended along the $x - y$ directions. At the temperatures under consideration collisions are rare, and are neglected in what follows. Low temperatures thus result in a strong simplification, since the collision integral can be set to zero in the Boltzmann equation for the gas [84], and the dynamics is governed by (see also [77]):

$$\frac{\partial f}{\partial t} + \mathbf{v} \cdot \frac{\partial f}{\partial \mathbf{x}} + \frac{\mathbf{f}_{\mathrm{dip}}}{M} \cdot \frac{\partial f}{\partial \mathbf{v}} = 0\,. \tag{2.1}$$

Eq. (2.1) can be rigorously derived starting from the microscopic equations for the system: such derivation is discussed in the Appendix A and can be found in more detail in [77]. Here M denotes

the atom mass, $\mathbf{v} = (v_x, v_y)$ the transverse velocity coordinate, and $\mathbf{f}_{\rm dip}$ the dipole force given by Eq. (1.15):

$$\mathbf{f}_{\rm dip} = -\frac{\hbar\delta}{2}\nabla \log(1 + s(\mathbf{x}, t)) \,, \tag{2.2}$$

with $\delta = \omega_0 - \omega_{\rm at}$ the light-atom detuning and s the saturation parameter associated to the total intensity illuminating the cloud. Without loss of generality the phase-space distribution function can be be normalized to the system transverse size $A_\perp$:

$$\int_{A_\perp} d\mathbf{x} \int_{\mathbb{R}^2} d\mathbf{v}\, f(\mathbf{x}, \mathbf{v}, t) = A_\perp \,. \tag{2.3}$$

The total intensity $s(\mathbf{x}, t)$ entering the force expression (2.2) is obtained by summing up incoherently the forward and backward beam intensities, $s(\mathbf{x}, t) = |F|^2 + |B(\mathbf{x}, t)|^2$. This is consistent with the assumption of a diffractively thin medium; similar assumptions also proved to be effective in describing internal-state, 'hot-atom' instabilities [11]. As also discussed in the following, accounting for propagation inside the medium is not crucial to describe the main physics of self-structuring instabilities.

To describe the coupling between light and the atoms one needs to express the force (2.2), and thus the backward field $B(\mathbf{x}, t)$. This is obtained by propagating the forward pump field through the cloud, and successively calculating its evolution in the free-space propagation to the mirror and back. Assuming the atoms to be two-level systems as in Sec. 1.1, the forward field is simply absorbed and phase-shifted by the cloud as

$$\frac{\partial F(\mathbf{x}, z, t)}{\partial z} = -\alpha_0(1 - i\Delta) n(\mathbf{x}, t) w(\mathbf{x}, t) F \,, \tag{2.4}$$

where $\Delta = 2\delta/\Gamma$ as already defined in sec. 1.1, $n(\mathbf{x}, t)$ is the transverse atomic density, and $w(\mathbf{x}, t)$ the population difference

between the ground level and the excited level of the atoms. For two-level atoms the cloud susceptibility is parametrized by (see Appendix A)

$$\alpha_0 = \frac{b_0}{2L(1+\Delta^2)}\,, \tag{2.5}$$

where b_0 is the optical density in line center and L the medium thickness. Eq. (2.4) is obtained from the full wave equation in the slowly-varying, paraxial and rotating wave approximations by neglecting diffraction within the medium (which is exactly the thin medium assumption). As a consequence, the thickness L will turn out to be an unessential parameter in the theory, as everything will depend only on the product $\alpha_0 L$ and the dependence from L will cancel out. Diffraction takes place only in the free-space propagation to the mirror and back:

$$\frac{\partial F}{\partial z} = -\frac{i}{2k_0}\nabla^2 F\,, \tag{2.6}$$

where k_0 is the radiation wavenumber.

As in Sec. 1.1.1, where dipole forces on atoms at rest were discussed, using the steady-state solution of the Maxwell-Bloch equations the population difference is given by

$$w(\mathbf{x},t) = \frac{1}{1+s(\mathbf{x},t)}\,. \tag{2.7}$$

This is justified by the fact that the 'external' timescale for atomic motion is much slower (typically, $\tau_{\rm ext} = 10\,\mu$s to move $1\,\mu$m at a temperature of $100\,\mu$K) than the 'internal' timescale for relaxation of the populations and coherences ($\Gamma^{-1} \sim 10 - 100\,$ns). Essentially, the assumption taken here is that the internal degrees of freedom of the system to evolve infinitely fast, $\Gamma \to \infty$, which will have important consequences in Sec. 2.4.1.

Once a solution $f(\mathbf{x},\mathbf{v},t)$ is found for the Boltzmann equation (2.1),

the spatial density $n(\mathbf{x}, t)$ to be plugged into Eq. (2.4) is obtained by integrating over the velocities:

$$n(\mathbf{x}, t) = \int d\mathbf{v}\, f(\mathbf{x}, \mathbf{v}, t)\,. \tag{2.8}$$

Note that the backward field B, and thus the total intensity s, depend on f only through the spatial density $n = n(\mathbf{x}, t)$, so that $s = s(\mathbf{x}, t)$ depends on $\mathbf{x}$ but not on $\mathbf{v}$.

2.2 Linear stability analysis

2.2.1 Stationary homogeneous solution

The first step in the linear analysis consists in determining the stationary and spatially homogeneous solution of the coupled system (2.1-2.4). If the optical field is spatially homogeneous, there are no dipole forces active on the system, $\mathbf{f}_{\text{dip}} = 0$. Therefore the Boltzmann equation is solved by any spatially homogeneous velocity distribution $f_0(\mathbf{v})$. Taking $f_0(\mathbf{v})$ to be normalized to unity without loss of generality, and given the normalization condition (2.3), the corresponding homogeneous density is simply $n_0 = 1$. To obtain the spatially homogeneous solution for the field, consider first the propagation of a pump beam of amplitude $F_0 = \sqrt{p_0}$ through a cloud with homogeneous $n = n_0$ and $s = s_0$: from Eq. (2.4) the transmitted field is

$$F(z = L) = F_0 \exp\left\{-\frac{\alpha_0 L(1 - i\Delta)}{1 + s_0}\right\}.$$

It is important to realize that this contribution represents the zero-frequency component of the field spectrum, and as such it does not undergo diffraction in the free-space propagation, see Eq. (2.6). This can be seen moving to Fourier space for the trans-

verse coordinate $\mathbf{x}$:

$$F(\mathbf{x}) \longrightarrow F(\mathbf{q}) = \int d\mathbf{x} F(\mathbf{x}) e^{i\mathbf{q}\cdot\mathbf{x}} ,$$

so that $\nabla^2 \to -|\mathbf{q}|^2$ and the field after a propagation distance l_{pr} is obtained by solving Eq. (2.6) as

$$F(z = l_{\mathrm{pr}}, \mathbf{q}) = F(z = 0, \mathbf{q}) \exp\left(\frac{i l_{\mathrm{pr}}}{2k_0}|\mathbf{q}|^2\right) . \tag{2.9}$$

As a consequence the homogeneous mode $F(\mathbf{q} = 0)$ is unaffected by the propagation, and the homogeneous component of the backward field amplitude $|B|$ is simply the transmitted part of the homogeneous forward beam, further reduced by a factor $\sqrt{R}$ due to the mirror reflectivity R. The total homogeneous intensity then reads

$$s_0 = |F|^2 + |B|^2 = p_0 + R p_0 \exp\left(-\frac{2\alpha_0 L}{1 + s_0}\right) = (1 + R\gamma_0) p_0 , \tag{2.10}$$

where the absorption factor has been defined as

$$\gamma_0 = \exp\left(-\frac{2\alpha_0 L}{1 + s_0}\right) . \tag{2.11}$$

The presence of this term makes Eq. (2.10) implicit in s_0, so that a numerical zero-finding method is needed in practice to evaluate s_0. In this thesis the Newton-Raphson method [85] implemented within the `FindRoot` function of Mathematica [86] will be used.

2.2.2 Perturbation analysis

Now that the stationary, homogeneous solution for the system has been established, linear analysis is performed by considering

small perturbations to such solution,

$$f(\mathbf{x}, \mathbf{v}, t) = f_0(\mathbf{v}) + f_1(\mathbf{x}, \mathbf{v}, t) \tag{2.12a}$$

$$s(\mathbf{x}, t) = s_0 + s_1(\mathbf{x}, t)\,, \tag{2.12b}$$

and studying the dynamics of these perturbations to first order in f_1, s_1. The forward field is found at the exit of the medium ($z = L$) as

$$\begin{aligned} F(z = L, \mathbf{x}, t) &= F_0 \exp\left\{-\alpha_0 L(1 - i\Delta)\frac{n(\mathbf{x}, t)}{1 + s(\mathbf{x}, t)}\right\} \simeq \\ &\simeq F_0 \exp\left\{-\frac{\alpha_0 L(1 - i\Delta)}{1 + s_0}\left[1 + n_1(\mathbf{x}, t)\right]\left[1 - \frac{s_1(\mathbf{x}, t)}{1 + s_0}\right]\right\} \simeq \\ &\simeq F_0 \exp\left\{-\frac{\alpha_0 L(1 - i\Delta)}{1 + s_0}\right\}\left[1 - \frac{\alpha_0 L(1 - i\Delta)}{1 + s_0}\left(n_1(\mathbf{x}, t) - \frac{s_1(\mathbf{x}, t)}{1 + s_0}\right)\right]\,. \end{aligned}$$

The backward field is obtained propagating F to the mirror and back for a distance $l_{\mathrm{pr}} = 2d$ (d being the mirror distance). This is done moving to Fourier space for the coordinate $\mathbf{x}$ and using Eq. (2.9):

$$B(\mathbf{q}, t) = \sqrt{R}\left\{\int F(z = L, \mathbf{x}, t) \exp\left(i\mathbf{q} \cdot \mathbf{x}\right) d\mathbf{x}\right\} \exp\left(i\frac{d|\mathbf{q}|^2}{k_0}\right)$$

where the factor $\sqrt{R}$ again captures the losses due to a finite transmittivity of the mirror. Note that no special symbol is used to denote spatially Fourier-transformed functions (or temporally Laplace-transformed one, see below): these will be distinguished by means of their arguments, or otherwise the distinction will be clear from the context.

Combining the last two equations, the backward field in Fourier

space is found as

$$B(\mathbf{q},t) = \sqrt{R}\exp\left(-\frac{\alpha_0 L(1-i\Delta)}{1+s_0}\right)\times \\ \times\left[\delta(\mathbf{q}) - \frac{\alpha_0 L(1-i\Delta)}{1+s_0}\left(n_1(\mathbf{q},t) - \frac{s_1(\mathbf{q},t)}{1+s_0}\right)\right]e^{i\Theta}\,, \tag{2.13}$$

where the diffractive phase shift Θ has been defined as:

$$\Theta = \frac{d|\mathbf{q}|^2}{k_0}\,. \tag{2.14}$$

The expansion $s(\mathbf{x},t) = s_0 + s_1(\mathbf{x},t)$ corresponds to setting $B(\mathbf{q},t) = B_0[\delta(\mathbf{q}) + b_1(\mathbf{q},t)]$ in Fourier space, and correspondingly $s(\mathbf{q},t) = s_0\delta(\mathbf{q}) + |B_0|^2[b_1(\mathbf{q},t) + b_1^*(\mathbf{q},t)]$. The homogeneous contribution $|B_0|^2 = R\gamma_0 p_0$ was found in the previous Section, while the inhomogeneous perturbation in Eq. (2.13) can be recognized as

$$b_1(\mathbf{q},t) = -\frac{\alpha_0 L(1-i\Delta)}{1+s_0}\left(n_1(\mathbf{q},t) - \frac{s_1(\mathbf{q},t)}{1+s_0}\right)e^{i\Theta}\,. \tag{2.15}$$

The corresponding intensity perturbation is

$$\begin{aligned} s_1(\mathbf{q},t) &= R\gamma_0 p_0\left[b_1(\mathbf{q},t) + b_1^*(\mathbf{q},t)\right] = \\ &= R\gamma_0 p_0\left[-\frac{\alpha_0 L(1-i\Delta)}{1+s_0}\left(n_1(\mathbf{q},t) - \frac{s_1(\mathbf{q},t)}{1+s_0}\right)e^{i\Theta} + \text{c.c.}\right] = \\ &= -R\gamma_0 p_0 \frac{2\alpha_0 L}{1+s_0}\left(n_1(\mathbf{q},t) - \frac{s_1(\mathbf{q},t)}{1+s_0}\right)\left[\cos\Theta + \Delta\sin\Theta\right]\,. \end{aligned}$$

Isolating $s_1(\mathbf{q},t)$ the following expression is obtained:

$$s_1(\mathbf{q},t) = -\frac{\frac{2R\gamma_0 p_0}{1+s_0}\left[\cos\Theta + \Delta\sin\Theta\right]}{1 - \frac{2R\gamma_0 p_0 \alpha_0 L}{(1+s_0)^2}\left[\cos\Theta + \Delta\sin\Theta\right]}\int f_1(\mathbf{q},\mathbf{v},t)d\mathbf{v}\,, \tag{2.16}$$

where the density perturbation $n_1(\mathbf{q},t)$ was explicitly expressed as the velocity integral of the distribution function perturbation

$f_1(\mathbf{q}, \mathbf{v}, t)$:

$$n_1(\mathbf{q}, t) \equiv \int d\mathbf{v}\, f_1(\mathbf{q}, \mathbf{v}, t)\,.$$

The term $[\cos\Theta + \Delta \sin\Theta]$ is found in complete analogy with previous research on single-mirror-feedback instabilities. The two contributions derive respectively from the medium absorptive response (the $\cos\Theta$ term) and the dispersive response (the $\Delta \sin\Theta$ term), independently on the physical mechanism underlying the nonlinearity. In the large detuning limit analyzed in the following Sections one retrieve the simpler $\Delta \sin\Theta$ dependence of pure dispersive media, see e.g. the original treatment of [5].

In order to obtain a closed expression for $s_1(\mathbf{q}, t)$ an expression for $f_1(\mathbf{q}, \mathbf{v}, t)$ has to be obtained from the linearization of the Boltzmann equation (2.1), which is rewritten here for convenience:

$$\frac{\partial f}{\partial t} + \mathbf{v} \cdot \frac{\partial f}{\partial \mathbf{x}} + \frac{\mathbf{f}_{\text{dip}}}{M} \cdot \frac{\partial f}{\partial \mathbf{v}} = 0\,. \tag{2.17}$$

The dipole force $\mathbf{f}_{\text{dip}}$ derives from spatial gradients of the optical intensity, and is therefore already a first-order quantity (the zero-order contribution s_0 only shifts the potential energy of the system). In Fourier space the last, nonlinear term of the Boltzmann equation becomes a convolution integral, but since the force is a first-order quantity only the zero-order term $\partial f_0/\partial \mathbf{v}$ will survive linearization. Given the intensity perturbation $s_1(\mathbf{q}, t)$, the force (2.2) is found in Fourier space as ($\nabla \to i\mathbf{q}$)

$$\mathbf{f}_{\text{dip}}(\mathbf{q}, t) = -\frac{\hbar\delta}{2} \frac{i\mathbf{q}}{1 + s_0} s_1(\mathbf{q}, t)\,. \tag{2.18}$$

The last step needed to obtain $f_1(\mathbf{q}, \mathbf{v}, t)$ involves a Laplace transform in the temporal variable:

$$h(\lambda) = \int_0^\infty h(t) \exp(-\lambda t) dt \tag{2.19a}$$

$$h(t) = \int_{a-i\infty}^{a+i\infty} h(\lambda) \exp(\lambda t) \frac{d\lambda}{2\pi i} \tag{2.19b}$$

where a lies to the right of all the singularities of $h(\lambda)$ in the complex λ-plane. For future convenience the λ-plane can be rotated by $\pi/2$ defining $\omega = -i\lambda$, so that temporal derivatives are Laplace-transformed as $\partial_t h(t) \to -i\omega h(\omega) - h(t = 0)$. Using Eq. (2.16) and (2.18) the Boltzmann equation (2.17) is thus linearized as

$$f_1(\mathbf{q}, \mathbf{v}, \omega) = \left[f_1(0) + \frac{\hbar\delta}{2M} \frac{s_1(\mathbf{q}, \omega)}{1 + s_0} i\mathbf{q} \cdot \frac{\partial f_0(\mathbf{v})}{\partial \mathbf{v}} \right] \times \left[i\mathbf{q} \cdot \mathbf{v} - i\omega \right]^{-1} , \tag{2.20}$$

where $f_1(0) = f_1(\mathbf{q}, \mathbf{v}, t = 0)$ denotes the initial disturbance to the atomic distribution.

With the expression of $f_1(\mathbf{q}, \mathbf{v}, \omega)$ at disposal the main result concerning the stability of the system can be derived. Plugging Eq. (2.20) into the Laplace-transformed Eq. (2.16), and again isolating all the contributions in s_1 one finds:

$$s_1(\mathbf{q}, \omega) = -\frac{\frac{2R\gamma_0 p_0}{1+s_0} \left[\cos\Theta + \Delta \sin\Theta\right]}{1 - \frac{2R\gamma_0 p_0 \alpha_0 L}{(1+s_0)^2} \left[\cos\Theta + \Delta \sin\Theta\right]} \int f_1(\mathbf{q}, \mathbf{v}, \omega) d\mathbf{v} =$$

$$= -\left[\frac{(1 + s_0)K}{1 - K} \int \frac{f_1(0)}{i\mathbf{q} \cdot \mathbf{v} - i\omega} \right] \times$$

$$\times \left[1 - \frac{\hbar\delta}{2M} \frac{K}{1 - K} \int \frac{\hat{e}_\mathbf{q} \cdot \frac{\partial f_0(\mathbf{v})}{\partial \mathbf{v}}}{\omega/|\mathbf{q}| - \hat{e}_\mathbf{q} \cdot \mathbf{v}} d\mathbf{v} \right]^{-1} , \tag{2.21}$$

where $\hat{e}_{\mathbf{q}} \equiv \mathbf{q}/|\mathbf{q}|$, and the quantity K has been defined as

$$K = \frac{2R\gamma_0 p_0 \alpha_0 L}{(1+s_0)^2} \left[\cos\Theta + \Delta \sin\Theta\right] . \tag{2.22}$$

2.2.3 Dispersion relation

Before proceeding, a brief summary of the results obtained in the previous Sections is presented. The coupled dynamics of light and cold atoms was modelled in terms of a wave equation for the light fields and a collisionless Boltzmann equation for the atoms. Propagation inside the cloud by assuming the medium to be diffractively thin, the atomic dynamics was considered in the plane transverse to the pump beam propagation. A spatially homogeneous solution for the system was identified, corresponding to a flat density profile ($n_0 = 1$) and plane-wave profiles for the forward and backward beams. So far the form of the initial velocity distribution was specified, as any normalized function $f_0(\mathbf{v})$ of the velocity only will produce a valid stationary homogeneous solution.

Assuming infinitesimal fluctuations around this homogeneous solution the dynamical equations for the light and the atoms has been linearized Fourier-transforming the spatial variables ($\mathbf{x} \to \mathbf{q}$) and Laplace-transforming the temporal variable ($t \to \omega$). Considering the linearized equations for the perturbations modes $f_1(\mathbf{q}, \mathbf{v}, \omega)$, $s_1(\mathbf{q}, \omega)$, these solutions for these modes evolve as

$$f_1, s_1 \sim \exp\left(-i\omega t + i\mathbf{q}\cdot\mathbf{x}\right)$$

Of course it would be non-physical to have exponentially exploding modes: as soon as f_1, s_1 grow to macroscopic values, the nonlinearity will saturate their growth. The reader is referred to Sec. 1.2 and Refs. [68, 4] for a deeper analysis of the concepts

of linear stability analysis, but for the moment it suffices to note that

$$\begin{aligned} &\text{if } \ \mathrm{Im}(\omega) > 0 \qquad \text{infinitesimal fluctuations will grow} \\ &\text{if } \ \mathrm{Im}(\omega) < 0 \qquad \text{infinitesimal fluctuations will decay} \end{aligned}$$

In the first case the system is said to be *unstable* to fluctuations, in the second case it is said to be *stable*. In the critical limit $\mathrm{Im}(\omega) = 0$ the system is *marginally* (or *neutrally*) stable. Given that $\omega = -i\lambda$ in the definitions (2.19), we will refer to $\mathrm{Im}(\omega) = \mathrm{Re}(\lambda)$ as the *growth rate* of the system. The real part of the eigenvalues $\mathrm{Re}(\omega) = -\mathrm{Im}(\lambda)$ captures the fact that when $\mathrm{Im}(\omega) > 0$ the resulting instability can be *oscillatory* ($\mathrm{Re}(\omega) \neq 0$, the perturbation grows and oscillates in time) or *stationary* ($\mathrm{Re}(\omega) = 0$, the perturbation grows without oscillations). From the above general expression of the perturbation modes we see that when $\mathrm{Im}(\omega) > 0$ the growing perturbations are sinusoidal waves of wavevector $\mathbf{q}$ (rolls states in the language of Sec. 1.2). Of course it could be the case that $\mathrm{Im}(\omega) > 0$ for many different modes, so that a complex periodicity is eventually observed in real space. As will be demonstrated in the following, however, there is a *critical mode* $\mathbf{q}_\mathrm{c} \neq 0$ which grows faster than all the other modes and suppresses them, at least close to the critical point for the instability. In the language of Sec. 1.2, it will be found that the system undergoes a type-I stationary instability.

The next step in the analysis requires us to find relation which links the eigenvalue ω to the wavevector $\mathbf{q}$, i.e. the so-called *dispersion relation* $\omega = \omega(\mathbf{q})$. To do so, consider again the expression (2.21) for the intensity perturbation modes $s_1(\mathbf{q}, \omega)$. The dynamics of the system is in principle fully captured by anti-

Laplace-transforming this expression in ω, but this presents itself as a task of formidable difficulty. The dispersion relation can be found, however, relying on the definition (2.19) for the anti-transform, and specifically on the fact that contributions to the integral (to be carried in the complex ω-plane) will come only from the poles of $s_1(\mathbf{q}, \omega)$. In particular, the pole with largest imaginary part $\mathrm{Im}(\omega)$ will dominate the dynamics, as it corresponds to the mode with largest growth rate.
From inspection of Eq. (2.21) it can be seen that a pole can be found in two relevant cases:

- when $K = 1$. The divergences arising when $K = 1$ have an important physical interpretation, which will be discussed in detail later. They identify the condition for an electronic instability to occur, i.e. a pattern-forming instability triggered by the internal-state nonlinearity. Unless otherwise stated, the emphasis will always be on the case $K < 1$, as this captures the main novelty of the work presented in this thesis, namely opto-mechanical self-structuring instabilities.

- when the denominator (i.e. the second square bracket term) of Eq. (2.21) vanishes. Since this can happen also for $K < 1$, this condition triggers opto-mechanical self-structuring instabilities.

Discarding the first point as a possible origin of poles in the anti-transform of (2.21) (this point will be considered in Sec. 2.4.1), a non-zero contribution to the anti-transform of $s_1(\mathbf{q}, \omega)$ must arise from the condition

$$D(\mathbf{q}, \omega) = 1 - \frac{\hbar\delta}{2M} \frac{K}{1-K} \int \frac{\hat{e}_{\mathbf{q}} \cdot \partial f_0 / \partial \mathbf{v}}{\omega/|\mathbf{q}| - \hat{e}_{\mathbf{q}} \cdot \mathbf{v}} d\mathbf{v} = 0 \,. \qquad (2.23)$$

As a consequence, the condition $D(\mathbf{q}, \omega) = 0$ implicitly identifies the dispersion relation $\omega = \omega(\mathbf{q})$ for our system.

2.2.4 Growth rate

Solving Eq. (2.23) for ω provides the eigenvalues for the system. If $\mathrm{Im}(\omega) > 0$ for some $\mathbf{q}$ a periodic structure will appear with periodicity $\Lambda = 2\pi/|\mathbf{q}|$. Naturally one has to provide an initial condition for the system, i.e. specify the initial velocity distribution $f_0(\mathbf{v})$. In this thesis a Maxwell-Boltzmann initial distribution will be used, which represents the equilibrium distribution for the gas before interacting with the pump beam and is given by:

$$f_0(\mathbf{v}) = \frac{1}{2\pi v_{\mathrm{th}}^2} e^{-|\mathbf{v}|^2/2v_{\mathrm{th}}^2}\,, \tag{2.24}$$

where the thermal velocity of the gas is connected to the initial temperature T as

$$v_{\mathrm{th}} = \sqrt{\frac{k_B T}{M}}\,. \tag{2.25}$$

Before facing the task of solving the dispersion relation (2.23), however, a remark should be made regarding the dependence on the system dimensionality of the dispersion relation. In other words, the question is whether the stability properties of the system differ in one and two transverse dimensions. A dependence on the number of dimensions can arise only from the dispersion integral

$$\int \frac{\hat{e}_{\mathbf{q}} \cdot \partial f_0/\partial \mathbf{v}}{\omega/|\mathbf{q}| - \hat{e}_{\mathbf{q}} \cdot \mathbf{v}} d\mathbf{v}\,,$$

which involves scalar products of $\mathbf{q}$ and $\mathbf{v}$. Since the analysis will be limited in this thesis to initial velocity distributions which depend only on the modulus of the velocity, $f_0(|\mathbf{v}|)$, one has that

$\partial f_0/\partial \mathbf{v} = (\mathbf{v}/|\mathbf{v}|)\,(\partial f_0/\partial|\mathbf{v}|)$ is parallel to $\mathbf{v}$. Then for a given $\mathbf{q}$ the dispersion integral can be evaluated rotating the $\mathbf{v}$-plane until v_x is parallel to $\mathbf{q}$, so that for the Maxwell-Boltzmann distribution (2.24)

$$\int \frac{\hat{e}_{\mathbf{q}} \cdot \partial f_0/\partial \mathbf{v}}{\omega/|\mathbf{q}| - \hat{e}_{\mathbf{q}} \cdot \mathbf{v}} d\mathbf{v} = \int_{-\infty}^{\infty} \frac{(v_x/|\mathbf{v}|)\partial f_0/\partial|\mathbf{v}|}{\omega/|\mathbf{q}| - v_x} dv_x dv_y = \\ = -\frac{1}{v_{\mathrm{th}}^2} \int_{-\infty}^{\infty} \frac{v_x f_0(v_x, v_y)}{\omega/|\mathbf{q}| - v_x} dv_x dv_y \,,$$

where the fact that

$$\frac{\partial f_0}{\partial|\mathbf{v}|} = -\frac{|\mathbf{v}|}{v_{\mathrm{th}}^2} f_0 \,.$$

was used. Another property of the two-dimensional Maxwell-Boltzmann distribution is that it is simply obtained as the product of two one-dimensional Maxwell-Boltzmann distributions:

$$\frac{1}{2\pi v_{\mathrm{th}}^2} e^{-|\mathbf{v}|^2/2v_{\mathrm{th}}^2} = \left(\frac{1}{\sqrt{2\pi v_{\mathrm{th}}^2}} e^{-v_x^2/2v_{\mathrm{th}}^2} \right) \times \left(\frac{1}{\sqrt{2\pi v_{\mathrm{th}}^2}} e^{-v_y^2/2v_{\mathrm{th}}^2} \right) .$$

Hence the v_y integral can be evaluated independently and gives unity due to the normalization of the v_y-distribution. The dispersion integral can thus be rewritten as

$$\int \frac{\hat{e}_{\mathbf{q}} \cdot \partial f_0/\partial \mathbf{v}}{\omega/|\mathbf{q}| - \hat{e}_{\mathbf{q}} \cdot \mathbf{v}} d\mathbf{v} = -\frac{1}{v_{\mathrm{th}}^2} \int_{-\infty}^{\infty} \frac{v_x f_0(v_x)}{\omega/|\mathbf{q}| - v_x} dv_x \,, \qquad (2.26)$$

where $f_0(v_x)$ is a one-dimensional distribution. The dispersion integral (2.26), in its one-dimensional form, finds a one-to-one correspondence in the study of Langmuir wave instabilities in one-species electron plasmas [76].

Interlude: the Lorenz distribution

A natural next step would be to look for a solution to the dispersion integral (2.26) with $f_0(v_x)$ given by a one-dimensional Maxwell-Boltzmann distribution. However, such a solution does not exist, i.e. no analytic result can be found for the Maxwell-Boltzmann case. Since the eigenvalues of the system are identical in one and two transverse dimensions, however, one can turn the attention to different one-dimensional initial distributions $f_0(v)$ which admit an exact solution. Hopefully the study of analytically solvable cases can shine some light on the solution of the Maxwell-Boltzmann case, and this indeed will be the case.
It is known for the study of plasma systems [76] that the one-dimensional Lorenz velocity distribution

$$f_0(v) = \frac{v_{\mathrm{th}}}{\pi} \frac{1}{v^2 + v_{\mathrm{th}}^2} \tag{2.27}$$

gives rise to an exact solution of the dispersion integral, namely

$$\int_{-\infty}^{+\infty} \frac{\partial f_0/\partial v}{\omega/|q| - v} dv = \frac{|q|^2}{(|q| v_{\mathrm{th}} - i\omega)^2} \qquad \text{if} \quad \mathrm{Im}(\omega) > 0\,. \tag{2.28}$$

Here v_{th} denotes the half width at half maximum (HWHM) of the distribution. The solution (2.28) holds for $\mathrm{Im}(\omega) > 0$, that is, as long as the poles along the real axis are left above the path of integration. The study of the correct solution to the dispersion integral dates back to the works by Landau [87], who corrected earlier results by Vlasov containing contributions from both paths circumnavigating the poles from above and from below. This can be shown to be a subtle mistake with tragic consequences, as causality is violated if the path circumnavigating the pole from above is considered [88].
Inserting the result (2.28) into the dispersion relation (2.23) the

dispersion relation becomes (in one dimension)

$$D(q,\omega) = 1 - \frac{\hbar\delta}{2M}\frac{K}{1-K}\frac{|q|^2}{(|q|v_{\rm th} - i\omega)^2} = 0\,,$$

which can be easily solved for ω as

$$\omega_{\pm}(q) = i|q|\left\{-v_{\rm th} \pm \sqrt{\frac{\hbar\delta}{2M}\frac{K}{1-K}}\right\}\,. \tag{2.29}$$

It can be seen from inspection of thus result that the two eigenvalues are complex conjugates of each other, but the condition $\mathrm{Im}(\omega) > 0$ requires

$$J \equiv \frac{\hbar\delta}{2M}\frac{K}{1-K} > 0\,,$$

as this ensures that the square-root term in Eq. (2.28) is real. Moreover, the solution ω_- is to be discarded since $\mathrm{Im}(\omega_-) < 0$; in the following we will refer simply to $\omega = \omega_+$ as the eigenvalue of the system. The definition of J will be useful in discussing the relative roles of opto-mechanical and internal-state nonlinearities, see Sec. 2.4.1.
Moreover $\mathrm{Re}(\omega) = 0$, so that the instability is of stationary type.

The Maxwell-Boltzmann distribution

The aim is to make use of result (2.29) for the Lorenz growth rate in the Maxwell-Boltzmann case. In this case no analytic solution is possible, but the following technique can be used

- given a set of parameters δ, T, b_0, p_0, numerically evaluate the dispersion integral
- select a value of the wavevector q

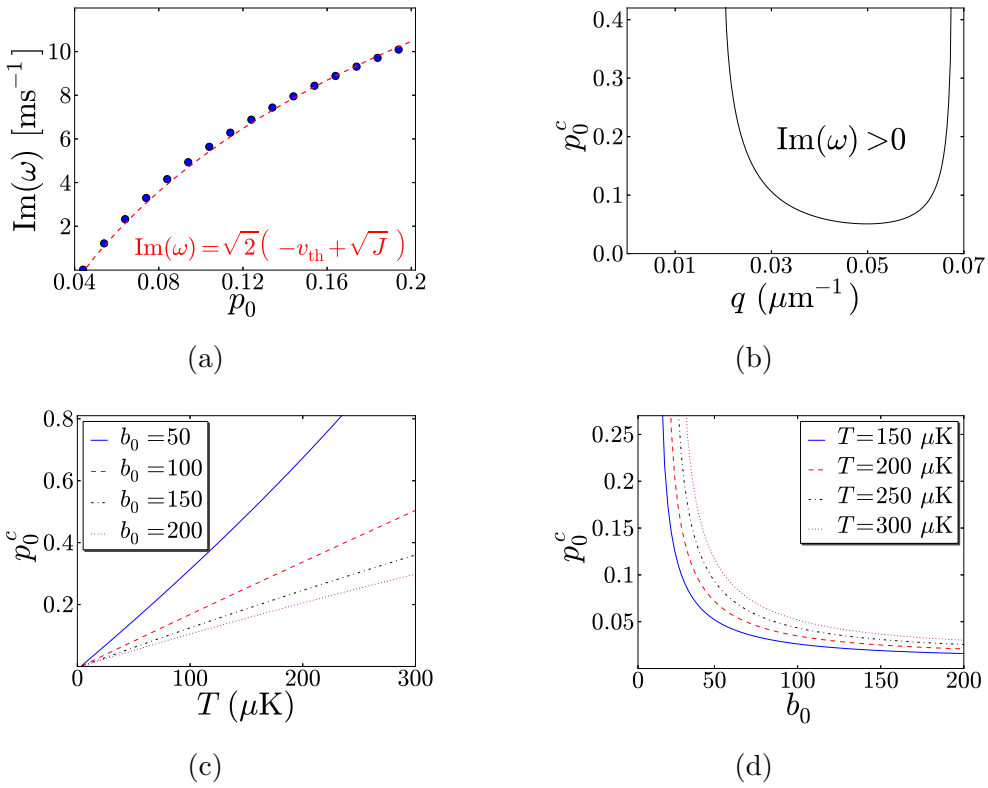

Figure 2.2: Linear stability analysis results for the Maxwell-Boltzmann case: growth rate versus injected power (top left), power threshold versus q (top right), power threshold versus temperature (bottom left), and power threshold versus optical density. Common parameters in all the plots are: $\delta = 10\Gamma$ ($\Delta = 20$), $d = 5\,\mathrm{mm}$, $R = 1$. Fig. a and b are obtained at $T = 300\,\mu\mathrm{K}$, $b_0 = 100$.

- use a Newton-Raphson routine to numerically determine the zero of the dispersion relation (2.23)
- the value of ω at which the zero occurs is the desired eigenvalue of the system

In particular, this routine is followed to evaluate the growth rate ω as a function of the injected pump p_0. The growth rate ω is found to be well-fitted by an expression which is identical (up to a numerical prefactor $\sqrt{2}$) to the one obtained for the Lorenz case (see Eq. (2.28)):

$$\omega(q) = i\sqrt{2}|q| \left\{ -v_{\mathrm{th}} + \sqrt{\frac{\hbar\delta}{2M}\frac{K}{1-K}} \right\} . \tag{2.30}$$

Note that the numerical evaluation of the dispersion integral is performed in one dimension, as the result is known to be identical in two dimensions, see Eq. (2.26). The `FindRoot` built-in function of Mathematica [86] was used. As in the Lorenz case, opto-mechanical self-structuring requires the square-root term to be real:

$$J \equiv \frac{\hbar\delta}{2M}\frac{K}{1-K} > 0 .$$

Numerical evaluations of the growth rate from the dispersion relation, together with the theoretical predicition (2.30), are plotted in Fig. (2.2a).

2.2.5 Threshold condition

The threshold condition for the instability can now be determined by setting $\mathrm{Im}(\omega) = 0$ in Eq. (2.30). Since the analysis is restricted here to the case where the square root term in (2.30) is real we

have

$$\mathrm{Im}(\omega) = 0 \Longleftrightarrow v_{\mathrm{th}}^2 - \frac{\hbar\delta}{2M}\frac{K}{1-K} = 0\,.$$

By defining the dimensionless quantity

$$\sigma = \frac{\hbar\delta}{2k_B T} \tag{2.31}$$

the threshold condition can be written as

$$1 - \sigma\frac{K}{1-K} = 0\,. \tag{2.32}$$

From this expression all the threshold values for the quantities of interest can be (numerically) evaluated, such as injected power, optical density, and temperature. Sec. 2.3.3 contains a more detailed discussion related to the critical wavenumber q_c. Note that the threshold condition (2.32) can also be found by simply setting $\omega = 0$ in the dispersion relation (2.23), as the eigenvalue (2.30) is purely imaginary: $\omega = i\,\mathrm{Im}(\omega)$.

2.3 Low saturation limit

The results presented in the previous Sections involve two nonlinear mechanisms in the cloud polarization $P = \chi E$ (see Eq. (2.4)):

- the *internal-state* nonlinearity stemming from the saturation of the atoms two-level transition, $\chi \sim w = 1/(1 + s(\mathbf{x}, t))$
- the *opto-mechanical* nonlinearity arising from density redistributions, $\chi \sim n(\mathbf{x}, t) = \int f(\mathbf{x}, \mathbf{v}, t) d\mathbf{v}$

The second point represents the main novelty of this work, and it is worth asking the following question: is an instability possible arising only from the density-redistribution nonlinearity?

Answer this question requires to move into a regime where the 'electronic' polarization is linear, i.e. in a regime of low saturation $s \ll 1$ where the polarization response to the field E (of associated saturation parameter s) can be approximated as

$$P_{\mathrm{el}} = -\frac{\alpha_0(1-i\Delta)}{2(1+\Delta^2)}\frac{E}{1+s} \simeq -\frac{\alpha_0(1-i\Delta)}{2(1+\Delta^2)}E\,.$$

Reducing the saturation of the transition will naturally make it necessary to work at large detuning, $|\Delta| \gg 1$ (as well as small intensities). Hence we simplify our model by neglecting absorption:

$$P_{\mathrm{el}} \simeq i\frac{\alpha_0\Delta}{2(1+\Delta^2)}E\,.$$

As a last approximation, in the limit $s \ll 1$ the dipole potential can be approximated as

$$U_{\mathrm{dip}} = \frac{\hbar\delta}{2}\log(1+s) \simeq \frac{\hbar\delta}{2}s\,.$$

Note that the elimination of absorption from the problem automatically sets $\gamma_0 = 1$ in Eq. (2.11). This results in a strong simplification, as the homogeneous solution (2.10) reduces to

$$s_0' = (1+R)p_0\,, \tag{2.33}$$

and does not need a zero-finding routine to be evaluated. In general, a remarkable advantage of the low-saturation treatment described in this Section is that it allows for exact solutions. As a matter of convention, all the primed quantities (such as s_0') denote 'pure opto-mechanical' quantities obtained in the low-saturation limit. The only exception to this rule is made for the critical wavenumber q_c, see Sec. 2.3.3.

All the analysis presented in the previous Sections could now be repeated for the low-saturation case, but it is much more convenient to jump to the final solution simply by keeping only first-order contributions in p_0 from the dispersion relation. In particular, this involves the following approximations:

- from Eq. (2.22), $K \simeq K' = 2Rp_0\alpha_0\Delta L \sin\Theta$, where the absorptive term $\cos\Theta$ is neglected over the dispersive term $\Delta \sin\Theta$
- $K' \ll 1$ and $K'/(1-K') \simeq K'$

The dispersion relation (2.23) reads in the low-saturation limit:

$$D'(\mathbf{q},\omega') = 1 - J' \int \frac{\hat{e}_{\mathbf{q}} \cdot \partial f_0/\partial \mathbf{v}}{\omega'/|\mathbf{q}| - \hat{e}_{\mathbf{q}} \cdot \mathbf{v}} d\mathbf{v} = 0\,, \tag{2.34}$$

where

$$J' = \frac{\hbar\delta}{2M} K'\,. \tag{2.35}$$

The additional quantity J' was introduced to clarify the following point. In the 'full' theory presented in the previous Section the quantity $J = (\hbar\delta/2M)K/(1-K)$ was assumed to be positive in describing density-driven self-structuring instabilities. When this condition is not fulfilled the role of the internal-state nonlinearity is crucial in triggering the instability, see Sec. 2.4.1. Since $K' \sim \delta$, it now appears clear that $J' \sim \delta^2 > 0$ always. This emphasizes the fundamental point of the low-saturation limit: if an instability occurs, it must be of opto-mechanical nature since, as a matter of fact, there is no internal-state nonlinearity to make an electronic instability possible. This is also confirmed by the fact that $K' \ll 1$, since the condition $K \geq 1$ parametrizes the regions of electronic-only self-organization, see Sec. 2.4.1.

2.3.1 Threshold condition

The relevant quantities related to the stability of the system can now be determined analytically, at least in the low-saturation limit. The growth rate is found from Eq. (2.30) as (recall that (2.30) is identical in one and two dimensions)

$$\omega'(\mathbf{q}) = i\sqrt{2}|\mathbf{q}| \left\{ -v_{\mathrm{th}} + \sqrt{J'} \right\} , \tag{2.36}$$

while the threshold condition is obtained from Eq. (2.32) as

$$1 - \sigma K' = 0 \, .$$

From the last expression the threshold value for the injected intensity p_0^c can be expressed as a function of all the other parameters:

$$p_0'^c = \frac{1}{2\sigma R \alpha_0 \Delta L \sin\Theta} \quad \text{with} \quad \sigma = \frac{\hbar\delta}{2k_B T} \, . \tag{2.37}$$

Obviously this relation can be used to express other 'critical' quantities, notably the optical density b_0 as a function of the injected power. However, in the low-saturation limit there is no absolute threshold for the optical density: for a given b_0 it is always possible to increase the injected power and reach the instability threshold. This no longer holds for the 'full' model discussed in Sec. 2.2, see also Fig. (2.2d).

However, the absolute threshold for b_0 is not a consequence of the internal-state nonlinearity, as it is retrieved if the approximation $\log(1+s) \simeq s$ for the dipole potential is not made. For linear scatterers (with no internal-state nonlinearity, i.e. population difference $w = 1$) under the action of a dipole potential $U_{\mathrm{dip}} = (\hbar\delta/2)\log(1+s(\mathbf{x}))$, the threshold (2.37) is corrected as

$$p_0'^c = \frac{1}{2\sigma R \alpha_0 \Delta L \sin\Theta - (1+R)/2} \, , \tag{2.38}$$

which displays an absolute threshold for α_0 (and thus b_0), namely

$$\alpha_0^c = \frac{1+R}{4\sigma\Delta RL\sin\Theta} \qquad \alpha_0^c = \frac{b_0^c}{2L(1+\Delta^2)}\,. \tag{2.39}$$

This result will not be used in the following, and Eq. (2.37) will be referred to as the low-saturation threshold for the system. However, it is important to bear in mind that the theoretical model presented here in general displays an absolute threshold for the optical density if the approximation $\log(1+s) \simeq s$ is not taken. An analogous argument holds for 'hot-atoms' internal-state instabilities: a pure Kerr medium does not display an absolute threshold for the optical thickness, while a saturable Kerr medium does.

2.3.2 The detuning dependence

The dependence of the low-saturation threshold (2.37) from the detuning is of particular interest, and deserves a separate discussion.

The whole point of the low-saturation limit is to reduce the internal-state response up to the point where density redistribution effects become dominant, so that they can be studied independently from internal-state ones. A natural way to obtain this is to increase the detuning $|\Delta|$ (either on the blue or the red side of the resonance), weakening the dipole moment of the atom by a factor $|\Delta|^{-1}$ (absorption drops even faster as $|\Delta|^{-2}$). For this to work, however, one must ensure that the power required to observe the instability, i.e. the power threshold, does not grow too fast with the detuning. If the threshold for the saturation parameter cannot be considered in the 'low-saturation' range $s \ll 1$, in fact, there is no point in studying opto-mechanical-only self-structuring, since internal-state effects cannot be neglected. The same problem, for

examples, makes it difficult to reach the purely dispersive Kerr limit in 'hot' two-level atoms. In this case the threshold grows in fact as $p_0^{\rm Kerr} \sim \Delta$, so that one needs large optical densities to lower the threshold into the low-saturation regime. This is achievable in warm gases, but much harder to obtain in cold samples.

Inspection of the threshold expression (2.37), however, reveals a remarkable property of the opto-mechanical nonlinear mechanism. As one tunes the optical field far from resonance, in fact, the threshold p_0^c varies as (using $\Delta = 2\delta/\Gamma$)

$$p_0^c = \frac{4k_B T(1+\Delta^2)}{\hbar\Gamma R\Delta^2} \sim \frac{1+\Delta^2}{\Delta^2} \sim \text{constant for large } |\Delta|$$

As a consequence, one can increase the detuning at will, weakening the internal-state response, but the saturation parameter required for the instability stays the same. As the detuning is increased while keeping the pump fixed, electronic-only instabilities become out of reach and one approaches a regime where only density redistribution effects are relevant for the self-organizing dynamics. The physical origin of this peculiar behaviour, which makes the opto-mechanical self-structuring instability different with respect to usual internal-state instabilities, is the dipole energy dependence from the detuning: $U_{\rm dip} \simeq (\hbar\delta/2)s$. This detuning dependence enters the parameter $\sigma \sim \delta$ defined in Eq. (2.37), and balance the $1/\delta$ dependence of the atomic dipole moment. The 'extra' detuning dependence coming in via the dipole potential also explains why one formally obtains a self-focusing nonlinearity on both sides of the resonance, see Sec. 2.3.5.

To show that the 'pure opto-mechanical', low-saturation limit studied in this Section is indeed relevant and experimentally reachable, Fig. (2.3b) shows the power threshold of the 'full' model (see Sec. 2.32) as a function of Δ, together with the 'pure opto-

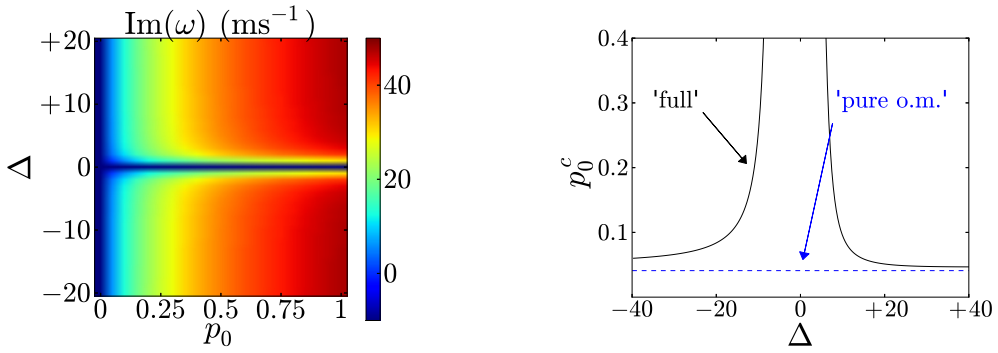

(a) (b)

Figure 2.3: On the left, the growth rate (at the critical wavenumber) for the low-saturation case. Note that the 'pure opto-mechanical' system is symmetric for blue/red detuning, and that the instability is suppressed on resonance. On the right, the power threshold as a function of the detuning: the 'full' system is asymmetric for red/blue detuning, and the low-saturation limit is reached at large $|\Delta|$. Parameters are: $b_0 = 100$, $T = 300\,\mu$K, $d = 5\,$mm, $R = 1$.

mechanical' prediction (2.37). Already at $|\Delta| = 20$ the required saturation parameter for the instability is only $p_0^c < 0.1$, and the simple low-saturation theory is quite reliable for $|\Delta| \geq 20$.
A close inspection of Fig. (2.3b) also reveals that the behaviour of the 'full-model' threshold is not perfectly symmetric for blue/red detuning. On the other hand, the linear properties of the low-saturation model are completely symmetric on the blue and red side of the resonance, as shown in Fig. (2.3a): this point will be addressed in more detail in Sec. 2.4.2.

2.3.3 Critical wavenumber

A particularly important quantity that can be analytically derived in the low-saturation limit is the critical wavenumber q_c, i.e. the value of $q = |\mathbf{q}|$ at which the growth rate $\mathrm{Im}(\omega)$ crosses zero when hitting the instability threshold. The critical wavenumber sets in fact the spatial scale Λ_c of the structure emerging from the instability, as close to theshold the critical mode dominates the

dynamics:

$$\Lambda_c = \frac{2\pi}{q_c}\,. \tag{2.40}$$

Assuming that all the parameters fixed but the injected intensity p_0, the critical wavenumber can be found by minimizing the expression for the power threshold $p_0^c = p_0^c(q)$. From the low-saturation threshold (2.37) (or analogously from (2.38)) the critical wavenumber is obtained by simply setting $\sin\Theta_c = 1$, which yields

$$\Theta_c \equiv dq_c^2/k_0 = \pi/2 \Longrightarrow q_c = \sqrt{\frac{\pi k_0}{2d}}\,. \tag{2.41}$$

Some points are worth remarking about this result. First, since the threshold depends only on the wavenumber $|\mathbf{q}|$ any transverse wavevector $\mathbf{q}$ on the 'critical circle' of radius q_c will satisfy Eq. (2.41). This means that at threshold the system can emit any 'sideband' (off-axis) beam at the angle determined by q_c, and the fact that only some of these off-axis beams are eventually selected is a signature that a symmetry-breaking process is occurring. As different experimental runs are performed, in fact, it is expected to observe the same structure (e.g. hexagons) with the same spatial scale $\Lambda = 2\pi/q_c$ but different orientations. Different near-field structures in turn correspond to different numbers of peaks in the far-field profile: for instance two sidebands give rolls, six sidebands give hexagons (see Sec. 1.2 for a discussion of ideal two-dimensional patterns).

The second point is related to the 'full' theory discussed earlier, involving both internal-state and opto-mechanical nonlinearities. In this case the threshold expression cannot be found analytically, but the driving term K depends on the diffractive phase shift Θ as $K \sim \cos\Theta + \Delta\sin\Theta$ (and not just $\Delta\sin\Theta$ as in the low-saturation limit). As a consequence, the critical wavenumber is no

longer given by the simple condition $\sin\Theta = 1$. However, all the results presented in this work assume a large detuning (typically $|\Delta| \geq 20$) as we are interested in dispersive dipole forces, while we neglect scattering forces (which are stronger close to resonance). Hence the dispersive term $\Delta \sin\Theta$ dominates over the absorptive contribution $\cos\Theta$ (independently of the value of the saturation parameter), and the critical wavenumber is always found to be very close to the low-saturation result (2.41). Fig. (2.4d) shows the numerically determined critical wavenumber from the 'full' model (circles) versus the detuning. For $|\delta| \geq 10\Gamma$ the relative discrepancy between this 'exact' critical wavenumber (corresponding to the lowest threshold) and the low-saturation result (2.41) is $\leq 2 \times 10^{-2}$. In general, this distinction will not be made again in the following and Eq. (2.41) will be referred to as the critical wavenumber of the system. This is why the low-saturation critical wavenumber as is denoted as q_c and is not 'primed' as q_c' (which would be consistent with all the other definitions of the low-saturation limit): the low-saturation critical wavenumber fulfils its role sufficiently well also outside the low-saturation limit. It should also be noted that the instability is of dispersive kind, i.e. as $\delta \to 0$ one finds that even if the $\cos\Theta$ term is dominant, the growth rate is negative because

$$\omega = i\sqrt{2}|q| \left\{ -v_{\mathrm{th}} + \sqrt{\frac{\hbar\delta}{M} J} \right\} \longrightarrow -i\sqrt{2}|q| v_{\mathrm{th}}$$

independently on J.

2.3.4 Periodicity in $|\mathbf{q}^2|$ and the Talbot effect

The last point worth noting about the result (2.41) is that the condition $\sin\Theta = 1$ is satisfied by any multiple $\Theta_n = (4n+1)\Theta_c$,

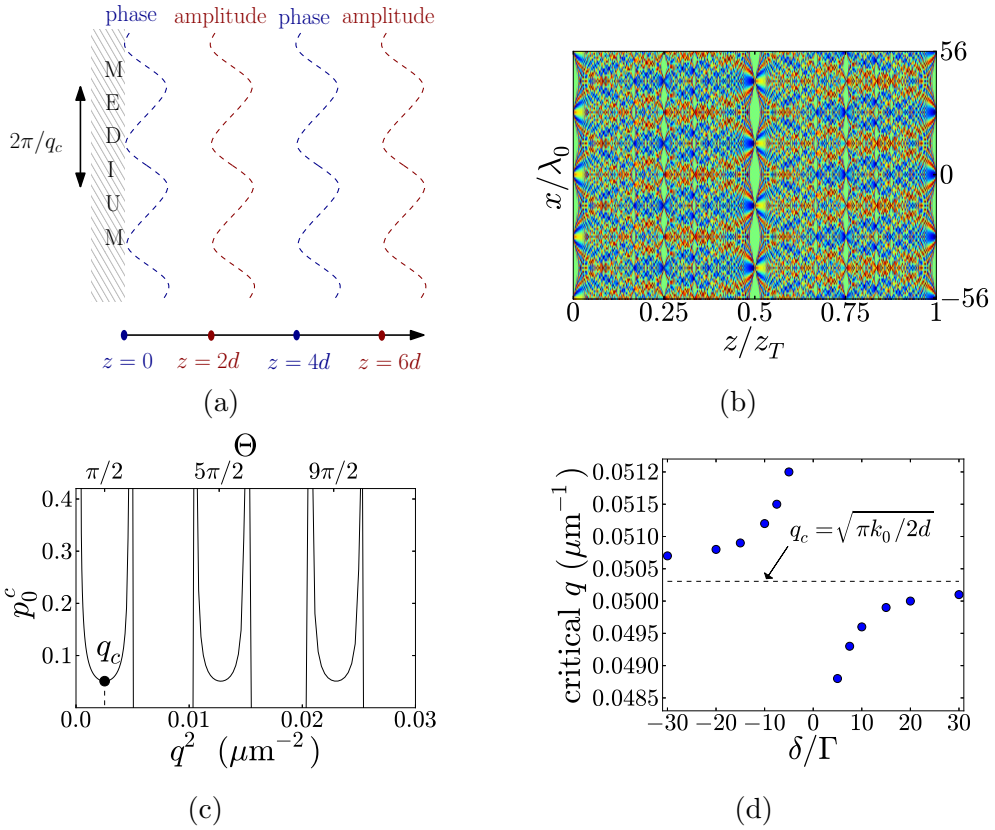

Figure 2.4: In Fig. (a) a sketch of the instability mechanism is depicted: phase perturbations at the critical wavenumber are fully converted into amplitude perturbations by the free-space propagation. In Fig. (b) a Talbot carpet is shown, see text. In Fig. (c) the threshold 'balloons' as a function of the wavenumber are shown, while Fig. (d) displays the difference between the (smallest) low-saturation critical wavenumber and the numerically exact one for the 'full' theory. Parameters are as in Fig. (2.3).

$n = 0, 1, 2, \ldots$, of the 'fundamental' phase shift $\Theta_c = \pi/2$. This is indeed a quintessential property of the single-mirror feedback scheme (for any kind of nonlinear medium), and relies on the Talbot effect [89]. The key point of the single-mirror scheme, in fact, consists of the conversion of phase fluctuations into amplitude modulations operated by the free-space diffraction. The mirror distance selects the self-amplifying perturbations at the critical wavenumber q_c as those which are fully converted from phase to amplitude in the distance $2d$, gaining a factor $\exp\{i(4n+1)\pi/2\} = +i$ through the free-space propagation (see Fig. (2.4a)). If the mirror distance is now doubled, these same phase fluctuations at $|\mathbf{q}| = q_c$ will re-appear as phase-only modulations at the re-entrance of the medium, as amplitude modulations at distance $2d$ will be re-converted into phase modulations at distance $4d$. If an additional free-space propagation of $2d$ is added, the situation is identical to the original one: phase perturbations are fully converted into amplitude perturbations at $2d$, into phase fluctuations at $4d$, and again into amplitude modulations at $6d$. The periodic recurrence of these diffractive structures is termed a Talbot carpet, and explains why a periodic behaviour is found in the perturbation wavenumber for single-mirror-based transverse instabilities. Phase modulations emerging from a grating of step $a = 2\pi/q_c$ are in fact converted to amplitude modulations after a propagation of $\frac{1}{4}z_T = a^2/2\lambda_0$. Setting $2d = \frac{1}{4}z_T$ we retrieve $q_c = \sqrt{\pi k_0/2d}$ as in Eq. (2.41). Fig. (2.4b) depicts the Talbot carpet for a monochromatic beam, showing the periodic recurrence of diffractive structures.

As a final remark, the condition $\sin\Theta = -1$ also leads to a critical condition for self-defocusing media [5]. However, these modes will not be considered in the following since opto-mechanical non-

linearities are always of the self-focusing kind, as discussed in the next paragraph.

2.3.5 The self-focusing nature of the nonlinearity

The fact that in the low-saturation limit $J' > 0$ always, independent of the sign of the detuning, might seem surprising at first. After all, in typical nonlinear optical experiments changing the sign of the light-atom detuning changes the nonlinearity from self-focusing (for $\delta > 0$) to self-defocusing (for $\delta < 0$). The nonlinearity emerging from density redistribution effects, on the other hand, appears to be always of the self-focusing kind.
This was indeed already pointed out in early works on dielectric particles, and can be explained as follows [90, 91]. Consider a single atom, and compare its refractive index (n_{at}) with respect to the background value (n_{bg}). Changing the sign of the detuning results in swapping the relative roles of the atom and the background, with the blue detuning corresponding to a particle having a refractive index lower than the background and viceversa for red detuning. As particles are attracted towards the minima (maxima) of the optical intensity for blue (red) detuning, however, regions of relatively high optical intensity always have a refractive index higher than the background, and thus attract light. Hence for both signs of the detuning one finds that light attracts light, yielding a self-focusing behaviour.

2.4 Internal and external degrees of freedom

The previous Sections were devoted to the study of the system stability under both internal-state and density redistribution nonlinearities. The focus was on identifying the conditions under which

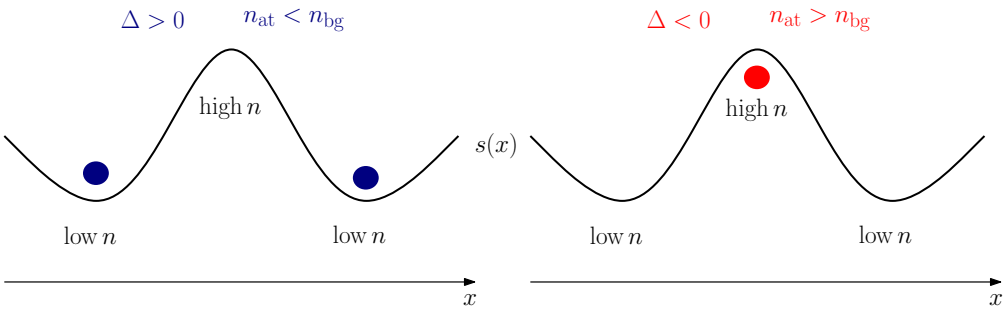

Figure 2.5: Dipole forces always lead to a self-focusing nonlinearity in which regions of higher optical intensity $s(x)$ correspond to higher refractive index $n(x)$, and thus attract light. Here $n_{\rm at}$: refractive index of the atom, $n_{\rm bg}$: refractive index of the background.

fluctuations in the transverse profile of the atomic cloud and/or the injected optical beam result in a runaway *self-structuring* instability, leading to the spontaneous emergence of macroscopic coupled light-density structures. An important point to stress is the following: whenever transverse spatial structures emerge for the optical fields, they do not result only in optical forces on the atoms center of mass. Transverse modulations in the optical intensity also affect the atomic internal-state polarization response, stemming from populations and coherences of the two-level internal structure. These internal-state modulations also provide feedback to the system, as they contribute to the overall refractive index of the atomic gas.

Although self-structuring instabilities involving the external, center-of-mass degrees of freedom of the atomic cloud are the main focus and novelty of this work, thus, the two-level internal state was included in the theoretical analysis, see Sec. 2.1. Sec. 2.3 focused on the low-saturation limit and dropped the internal-state nonlinear response from the atoms, but for generic choices of the injected intensity these effects cannot be neglected. After all, 'standard' optical self-organization typically relies exactly on these internal-state nonlinearities. This Section is thus devoted

to the study of the relative roles of the 'internal-state' and 'opto-mechanical' nonlinear mechanisms.

2.4.1 Growth rate divergence

It has been stressed in Sec. 2.2.4 that a positive growth rate $\mathrm{Im}(\omega) > 0$ (that is, an instability) is obtained under the constraint

$$J = \frac{\hbar\delta}{2M}\frac{K}{1-K} > 0\,.$$

All the results derived earlier on the self-structuring threshold, the growth rate, etc., rely on this condition. The quantity J, however, seems to be quite prone to misbehaviour as it diverges when $K = 1$. Moreover, it is not known if something 'interesting' happens in the regions $J < 0$, as in this case $\mathrm{Im}(\omega) < 0$ and the solution to the dispersion integral (2.28) breaks down. For typical parameters the condition $J \leq 0$ is obtained when $1 - K \leq 0$, since the quantity $(\hbar\delta/2M)K$ is always positive. This holds for the large detunings assumed throughout this work because $K \sim \cos\Theta + \Delta\sin\Theta \simeq \Delta\sin\Theta$, so that $\delta K \sim \Delta^2 > 0$ (essentially as in the low-saturation limit, see Sec. 2.3). The bottom line of all this is that to understand what happens in the regions where $J \leq 0$ it is sufficient to focus on the regions where $1 - K \leq 0$, i.e. $K \geq 1$.

To fully appreciate the importance of the 'critical' condition $K = 1$ the expression (2.21) for the intensity perturbation $s_1(\mathbf{q}, \omega)$ may

be retrieved:

$$s_1(\mathbf{q},\omega) = -\frac{\frac{2R\gamma_0 p_0}{1+s_0}\left[\cos\Theta + \Delta\sin\Theta\right]}{1-\frac{2R\gamma_0 p_0\alpha_0 L}{(1+s_0)^2}\left[\cos\Theta+\Delta\sin\Theta\right]}\int f_1(\mathbf{q},\mathbf{v},\omega)d\mathbf{v} =$$

$$= -\left[\frac{(1+s_0)K}{1-K}\int\frac{f_1(0)}{i\mathbf{q}\cdot\mathbf{v}-i\omega}\right]\times$$

$$\times\left[1-\frac{\hbar\delta}{2M}\frac{K}{1-K}\int\frac{\hat{e}_{\mathbf{q}}\cdot\frac{\partial f_0(\mathbf{v})}{\partial\mathbf{v}}}{\omega/|\mathbf{q}|-\hat{e}_{\mathbf{q}}\cdot\mathbf{v}}d\mathbf{v}\right]^{-1}.$$

In the discussion following Eq. (2.21) poles arising from the numerator were discarded and the focus was on the denominator, which led to the dispersion relation (2.23). When $K = 1$, however, a pole arises from the numerator term, which in turns will contribute to the anti-Laplace transform of $s_1(\mathbf{q},\omega)$. Hence a non-trivial behaviour should indeed be expected when $K = 1$ and $J \to \infty$, which will be demonstrate shortly to be an internal-state-only transverse instability. The condition $K = 1$, in fact, parametrizes the marginality condition for a system of 'hot' two-level systems in which density redistribution effects are absent, $n(\mathbf{x},t) = 1\,\forall t$.

Fig. (2.6a) shows the growth rate $\mathrm{Im}(\omega)$ as a function of injected power and detuning. Note that it is not needed to study here the linear stability of this system, as the threshold condition can simply be obtained from Eq. (2.32) by setting $\sigma = 1$ [92]. It can seen from Fig. (2.6a) that there is a region in parameter space where the growth rate diverges (highly saturated region in Fig. (2.6a)), triggering internal-state instabilities. This is confirmed by Fig. (2.6c), where the threshold curve for a 'hot' system of two-level atoms is plotted (red dashed line). The black solid line depicts the self-structuring threshold curve from the 'full'

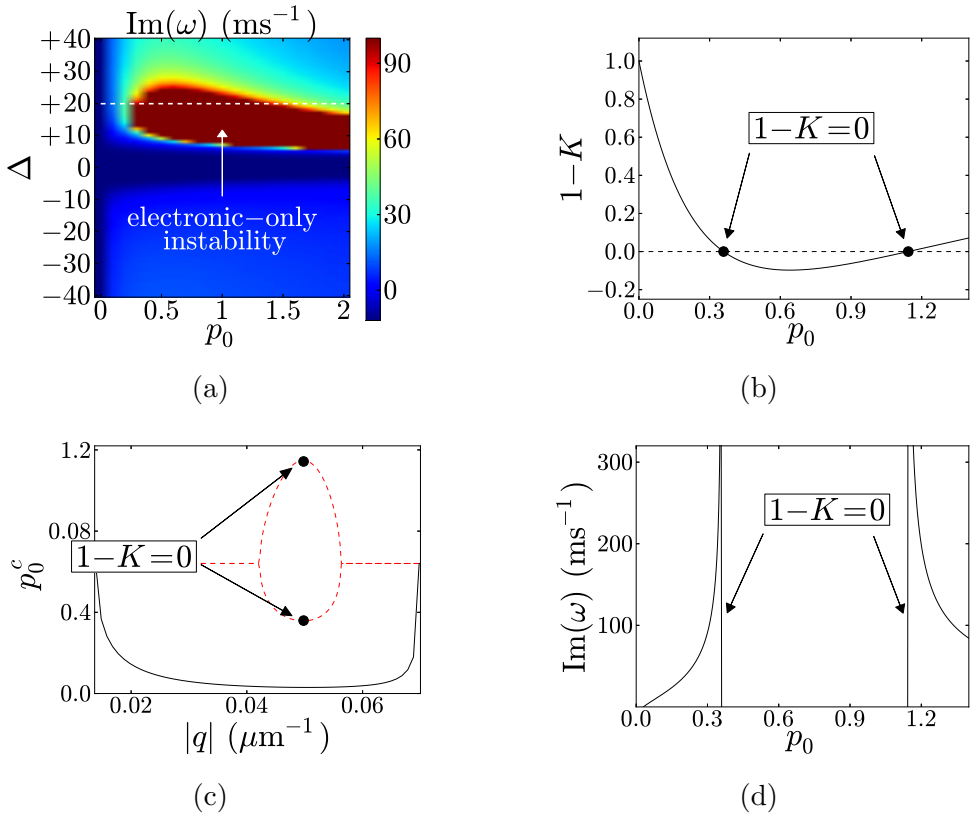

Figure 2.6: The regions parametrized by $1-K \leq 0$ identify electronic-only instabilities, see Fig. (b). The marginality condition $1-K=0$ identifies the threshold for electronic-only instabilities (red curve in Fig. (c)). In correspondence with this condition the growth rate diverges, see Fig. (a) and (d). The curves in Fig. (a), (b) and (d) are obtained at the critical wavenumber $q_c = \sqrt{\pi k_0/2d}$, see Sec. 2.2.5. Other parameters are: $T = 300\,\mu$K, $\delta = 10\Gamma$, $b_0 = 200$, $d = 5\,$mm, $R = 1$.

model for a temperature of $T = 300\,\mu$K (which gives $\sigma \simeq 4.895$). The points where $1-K=0$ are identified in the figure, and clearly mark the points where the system 'enters' and 'leaves' the internal-state instability region[1]. Within these two points the condition $1-K \leq 0$ is verified (see Fig.(2.6b)), parametrizing the regions of electronic-only instabilities.

An important feature of electronic-only instabilities is that they are expected to occur on a much faster timescale than density-

[1]The electronic-only stability balloon is expected to close at high p_0 due the nonlinearity saturation.

driven ones. The timescale for the development of an internal-state structure is in fact determined by the lifetime of the transition ($\Gamma^{-1} \sim 10 - 100\,\mathrm{ns}$ for alkali gases), since it is sufficient to excite an atom at the position $\mathbf{x}_1$ and de-excite an atom at the position $\mathbf{x}_2$ to create a structure of size $|\mathbf{x}_1 - \mathbf{x}_2|$, independently on the structure size. We remark that for typical parameters the (self-selected) pattern size turns out to be rather large, in the order of hundreds of micrometers. Therefore it will take a much longer time to move atoms from $\mathbf{x}_1$ to $\mathbf{x}_2$ and form a density pattern: for a typical temperature of $\sim 100\,\mu\mathrm{K}$ this time is about $10\,\mu\mathrm{s}$. The same argument was used in Sec. 2.1 to adiabatically eliminate the internal-state dynamics of the atoms. Indeed, this timescale difference between the two nonlinear mechanisms is the crucial feature which allows to distinguish between them, and is naturally accounted for in our theoretical model. Consider in fact Fig. (2.6d), where a section at $\Delta = 20$ of Fig. (2.6a) is shown. The growth rate $\mathrm{Im}(\omega)$ of the system is found to diverge between the two vertical lines at $1 - K = 0$, which is the reason why we refer to this phenomenon as 'growth rate divergence'. This means that in this region a transverse internal-state instability occurs on a much faster timescale than density-driven self-structuring. It is worth pointing out that the spatial scale obtained from internal-state and opto-mechanical instabilities is the same, see Fig. (2.6c), and therefore it cannot be used to discern which one of the two nonlinear mechanisms is driving the instability. This is due to the fact that in the single-mirror scheme the scale selection is operated by the free-space propagation, and not by the nonlinear interaction.

The fact that the growth rate diverges to infinitely large values is explained by the adiabatic elimination of the internal state dy-

namics, which essentially sets the atomic inverse lifetime to infinity, $\Gamma = \infty$. This was justified in Sec. 2.1 by the fact that the internal state evolves much faster that the center-of-mass of the atoms, but now that the relevant dynamics is the internal-state one we are formally left with an infinitely fast timescale. Physically, the instability will occur on a timescale which is dictated by the atomic lifetime of the two-level transition. Outside the electronic-only instability domain (i.e. where $1 - K > 0$ in Fig. (2.6b)) the growth rate takes finite values which are compatible with atomic motion at the considered temperature, $\mathrm{Im}(\omega)^{-1} \sim 10\,\mu\mathrm{s} - 1\,\mathrm{ms}$.

As a final remark for this Section, even if internal-state instabilities are expected in 'hot' as well as cold atoms, the outcome of the instability is still very different in the two cases. For cold atoms, in fact, modulations of the optical profile arising from internal-state pattern formation will lead to trapping of the atoms, which in turns will provide further feedback to the instability. Hence at high saturation we expect a 'fast' pattern formation involving internal degrees of freedom, followed by a 'slow' bunching of the atoms in the minima of the resulting potential. The reverse is also true: pattern formation triggered by atomic motion at low saturation levels will also call for modulation in the internal state properties. This in turns will affect the overall refractive index and provide feedback for the instability. In general, the first situation will be referred to as an *internal-state driven* (or *electronically driven*) instability, while the second as a *density driven* (or *opto-mechanically driven*) instability.

2.4.2 Cooperation and competition between internal and external degrees of freedom

This Section deals with an issue which was already raised in discussing Fig. (2.3b), namely the fact that the power threshold is higher for a red-detuned pump than for a blue-detuned one. The dependence of the linear properties (i.e. the growth rate and the threshold) of the system from the detuning, in fact, is not 'symmetric' when crossing the pump frequency across the resonance. This is true despite the fact that the properties of the system in the low-saturation limit are symmetric under the change $\Delta \rightarrow -\Delta$, see Fig. (2.3a). The natural conclusion is that the reason for this asymmetry is to be found in the internal-state response of the system. An even more dramatic asymmetry can be seen in Fig. (2.6a), where a divergence of the growth rate is found only for a blue-detuned pump.

At this point it is important to bear in mind that the opto-mechanical nonlinearity is always of self-focusing nature, both on the red and the blue sides of the resonance, see Sec. 2.3. On the other hand, changing the sign of the detuning will change the internal-state nonlinearity from self-focusing to self-defocusing. In the single-mirror feedback scheme both focusing and defocusing nonlinearities lead to transverse instabilities, but on different regions of the $q-$domain [5]. As shown in Fig. (2.7a), for blue detuning both mechanisms are self-focusing and lead to an instability in the same wavenumber regions (marked as 1, 3, 5 and 7). Otherwise stated, they 'cooperate' to create a spatial pattern on the same length scale. For red detuning, instead, the two mechanisms 'compete' for the unstable regions, as the internal-state nonlinearity lead to instabilities in the regions marked as 2, 4, 6 in Fig. (2.7b). For the parameters of interest, the opto-

mechanical mechanism dominates over the internal-state effects and the pattern-forming process eventually results in the same spatial scale for both signs of the detuning. However, a sign of the influence of internal-state effects is still evident in the detuning dependence of the power threshold, which is higher on the red-detuned side. The turning point where opto-mechanical and internal-state effects are of the same strength is parametrized by $\sigma = 1$, since for this case the 'pure' opto-mechanical threshold (2.37) is identical to that of a Kerr medium [5].

An early discussion of the relative roles of opto-mechanical and internal-state nonlinearities in determining the threshold for pattern formation was already presented by Saffman and collaborators [92, 93]. However, these works focused mainly on the threshold for the instability (for a counterpropagating geometry). Here the emphasis is put on the timescale of the two nonlinearities, i.e. on the growth rate associated with internal-state and motional processes. This in fact leads to the possibility of internal-state driven instabilities (as discussed in Sec. 2.4.1). Moreover, the main instrument to experimentally discern between the two mechanisms is the different timescale associated with the two mechanisms, and not their relative contributions to the threshold (see Chap. 4).

2.5 Numerical simulations

This Section presents the results from numerical simulations of the dynamics given by Eqs. (2.1-2.4), which are rewritten here

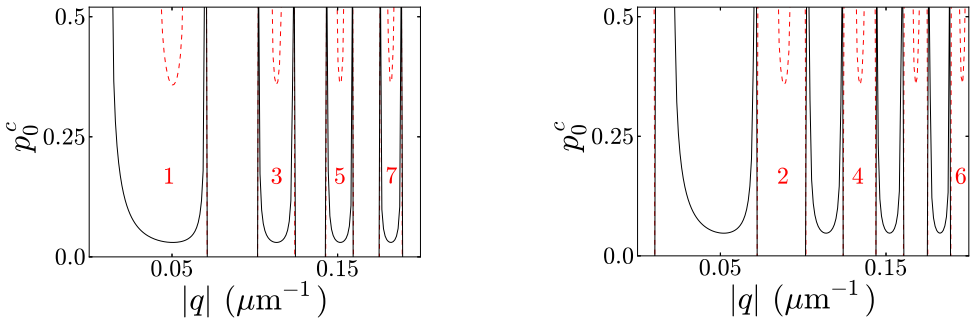

(a) (b)

Figure 2.7: Threshold curves for the 'full' system (black full lines) and for a system of 'hot' two level atoms (red dashed lines). The left panel corresponds to $\Delta = 20$, the right panel to $\Delta = -20$: the opto-mechanical and internal-state nonlinear mechanisms cooperate for blue red detuning, but compete for red-detuning. This explains the blue/red asymmetry observed in Fig. (2.3b). Parameters are: $b_0 = 200$, $\Delta = \pm 20$, $R = 1$, $d = 5\,\mathrm{mm}$, $T = 300\,\mu\mathrm{K}$ (yielding $|\sigma| \simeq 5$).

for clarity:

$$\frac{\partial f}{\partial t} + v\frac{\partial f}{\partial x} + \frac{f_{\mathrm{dip}}}{M}\frac{\partial f}{\partial v} = 0 \tag{2.42a}$$

$$\frac{\partial F}{\partial z} = -\alpha_0(1 - i\Delta)\frac{n}{1+s}F\,. \tag{2.42b}$$

All the numerical results presented below are obtained from simulations in one transverse dimension, and the equations are adapted accordingly. Limiting to one-dimensional (1D) simulations has the obvious advantage of reducing computational costs with respect to two-dimensional simulations (which require four variables+time). However, limiting to the 1D case one does not lose too much information about the system, since all the linear properties depend on the modulus of the wavevector, but not its orientation in the plane (q_x, q_y). The main aim of our numerical work is in fact that of confirming the stability analysis presented in the previous Section. We will not address here topics that would necessarily require two-dimensional simulations, such as whether hexagons are formed at threshold or competition effects

between different patterns (e.g. rolls and hexagons). Insights on these nonlinear effects can be obtained either from experimental results [83], or from the simplified model presented in Chap. 3, where velocity damping is assumed and the dimensionality of the problem is reduced.

Eqs. (2.42) form a self-consistent set of equations given that $s = |F|^2 + |B|^2$, B being the retro-reflected field, $n(x,t)$ is the velocity integral of $f(x,v,t)$, and $f_{\rm dip}$ is the dipole force arising from the gradients of s. Before proceeding, it is convenient to rewrite the model equations in dimensionless form. First, given an initial Maxwell-Boltzmann distribution for the gas

$$f_0(v) = \frac{1}{\sqrt{2\pi v_{\rm th}^2}} e^{-v^2/2v_{\rm th}^2} \qquad v_{\rm th} = \sqrt{\frac{k_B T}{M}}\,,$$

the velocity variable v is rescaled to the thermal velocity $v_{\rm th}$, $v' = v/v_{\rm th}$. Space is subsequently rescaled to the critical length $\Lambda_c = 2\pi q_c^{-1}$ by defining $x' = x/\Lambda_c$. A characteristic time scale is defined as the time it takes a thermal atom to travel a critical length, $\tau = \Lambda_c/v_{\rm th} = 2\pi/(q_c v_{\rm th})$. The temporal variable is thus rescaled as $t' = t/\tau$. Using these definitions Eqs. (2.42) read

$$\frac{\partial f}{\partial t'} + v' \frac{\partial f}{\partial x'} - \sigma \frac{\partial s/\partial x'}{1+s} \frac{\partial f}{\partial v'} = 0 \tag{2.43a}$$

$$\frac{\partial F}{\partial z} = -\alpha_0 (1 - i\Delta) \frac{n}{1+s} F\,, \tag{2.43b}$$

where the parameter $\sigma = \hbar\delta/2k_B T$ parametrizes the strength of density-driven nonlinear effects. Note that the choice of the timescale τ in Eq. (2.43a) is arbitrary, and can be reset as $\tau \to \tau\bar{T}$ for any (dimensionless) $\bar{T}$. This can be used to 'speed up' or 'slow down' the dynamics in the simulations: in the following the scal-

ing $\bar{T} = 10^{-2}$ will be used.

The remaining part of this Section is organized as follows: first, numerical evidence of transverse self-organization due to opto-mechanical effects only will be presented, see Sec. 2.3. The 'pure' opto-mechanical regime is of particular interest as it shows that density redistribution effects alone can drive the instability, and will be discussed in the next Section. Subsequently, numerical results showing transverse instabilities which involve both internal-state and motional effects are discussed. In particular, the scenario of internal-state driven instabilities (see Sec. 2.4.1) will be numerically investigated.

2.5.1 Low-saturation limit: linear scatterers

As in Sec. 2.3, the analysis is restricted here to the low-saturation limit where $s \ll 1$ and the internal-state dynamics can be neglected. This leads to a model where the atoms essentially act as linear Rayleigh scatterers under the action of dipole forces. In Sec. 2.3 it was predicted that density redistribution effects due to dipole forces can sustain the instability without the need of the internal-state nonlinearity, similarly to e.g. CARL systems [30, 31, 32]. Neglecting nonlinear dispersion, absorption and to first order in s the system (2.43) reduces to

$$\frac{\partial f}{\partial t'} + v' \frac{\partial f}{\partial x'} - \sigma \frac{\partial s}{\partial x'} \frac{\partial f}{\partial v'} = 0 \tag{2.44a}$$

$$\frac{\partial F}{\partial z} = +i\alpha_0 \Delta n F \,. \tag{2.44b}$$

Figures (2.8) and (2.9) show the dynamics of the phase space distribution $f(x, v)$ up to 2.5 ms, obtained from numerical simulations on both sides of the resonance ($\Delta = \pm 40$). Details on the

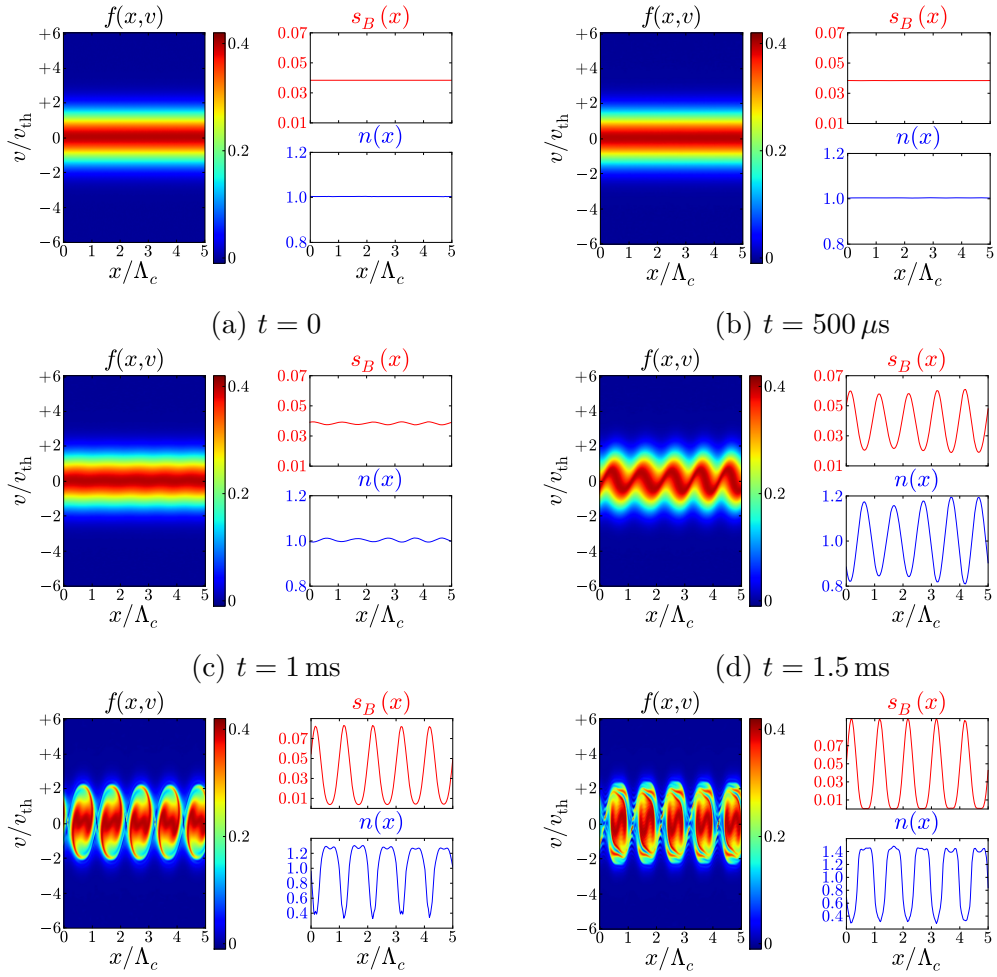

(a) $t = 0$ (b) $t = 500\,\mu$s

(c) $t = 1\,$ms (d) $t = 1.5\,$ms

(e) $t = 2\,$ms (f) $t = 2.5\,$ms

Figure 2.8: 'Pure optomechanical' instability (low saturation limit) for $\Delta = 40$, $T = 300\,\mu$K, $d = 5\,$mm, $R = 1$, $b_0 = 120$, $dt = 0.17\,\mu$s. Noise of amplitude 10^{-3} is added to the initial atomic distribution, the injected power is 5% above threshold. $s_B = |B|^2$ denotes the intensity of the backward beam.

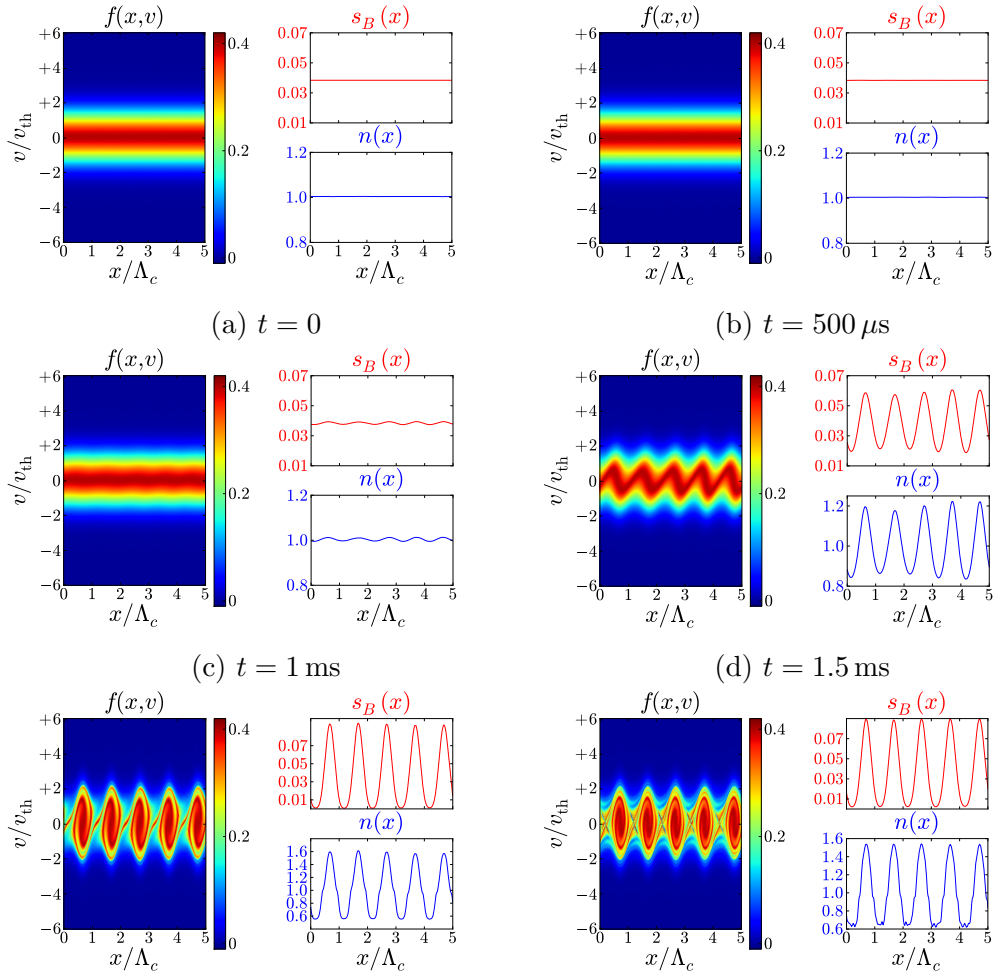

(a) $t = 0$ (b) $t = 500\,\mu$s

(c) $t = 1\,$ms (d) $t = 1.5\,$ms

(e) $t = 2\,$ms (f) $t = 2.5\,$ms

Figure 2.9: 'Pure optomechanical' instability (low saturation limit) for $\Delta = -40$, $T = 300\,\mu$K, $d = 5\,$mm, $R = 1$, $b_0 = 120$, $dt = 0.17\,\mu$s. Noise of amplitude 10^{-3} is added to the initial atomic distribution, the injected power is 5% above threshold. $s_B = |B|^2$ denotes the intensity of the backward beam.

numerical methods are discussed in Appendix B. The panels on the right of each figure show the backward beam intensity profile $s_B(x) \equiv |B(x)|^2$ (red) and the density distribution $n(x)$ (blue). The injected pump is set to $p_0 = 3.58 \times 10^{-2}$, which is 5% above the threshold value $p_0^c = 3.41 \times 10^{-2}$ for the parameters under consideration. The spatial domain is set to accommodate 5 critical lengths Λ_c and discretized using 256 grid points, implementing periodic boundary conditions. The velocity space is limited to the range $-6v_{\rm th} < v < 6v_{\rm th}$ and discretized using 256 points. In dimensionless units this translates as $x' \in (0, 5)$ and $v' \in (-6, 6)$. Time is discretized using 1.5×10^4 time steps, which gives a time step of $dt = 0.17\,\mu$s. It was checked that different choices of the velocity domain size, or of the grid steps (for space, velocity and time) lead to analogous results.

The dynamics are started with a spatially homogeneous Maxwell-Boltzmann distribution for the gas, which spontaneously evolves into the phase portrait of an anharmonic oscillator. White noise of amplitude 10^{-3} is added to the initial distribution $f_0(v)$. The fact that 5 'potential wells' are observed as a result of the instability confirms that the system self-selects (at least close to threshold) the critical wavenumber. A continuous symmetry breaking is obtained as the resulting structure can be shifted in space as $q_c x \to q_c x - \psi$: the phase $\psi \in [0, 2\pi)$ is in fact selected by the initial fluctuation. The emerging structure for the phase space distribution shows that a considerable fraction of the atoms is trapped into the potential determined by the optical profile. The velocity integral of f gives the atomic density profile, which shows a considerable modulation around the homogeneous value $n = 1$. It is observed that in the blue (red) detuned regime the atoms

bunch in the minima (maxima) of the optical intensity profile, as expected.

The timescale for the development of the pattern is consistent with the timescale of atomic motion, as it takes a few milliseconds to develop a 'high contrast' pattern. To quantitatively address this, the *field bunching factor*

$$\mathcal{B} = \frac{\int B(x) e^{-iq_c x}\, dx}{\int B(x)\, dx} \equiv \frac{B(q_c)}{B(0)}\,, \tag{2.45}$$

is calculated. $\mathcal{B}$ represents the amplitude of the backward field sideband at the critical wavenumber rescaled to the homogeneous mode, and is used to monitor the emission of an off-axis sideband at the critical wavenumber. The field spectral properties are monitored because they are easily accessible experimentally, but analogous results are obtained looking at the spectral distribution of n. Viewing q as the transverse momentum of the pattern, then, $|\mathcal{B}|$ can be seen as the relative population of a high momentum state ($q = 0$ being the lower state). In any case, $\mathcal{B}$ acts as a complex order parameter for the instability, with the property of having a self-selected phase.

Fig. (2.11) shows the evolution of the bunching factor for the dynamics of Fig. (2.8). As expected, initial fluctuations grow exponentially in time, with a least squares estimation of a timescale of $\omega_{\rm fit}^{-1} \simeq 97\,\mu$s.

It is also expected to observe oscillations of the atoms in the self-organizaed optical potential. The typical timescale for this process will be dictated by $(q_c v_{\rm th})^{-1} \simeq 736\,\mu$s for the parameters of Figs. 2.8 and 2.9. This is indeed confirmed by the numerical simulations, see the (damped) oscillations in the field bunching factor shown in Fig. 2.10. The 'sloshing' time is found to be of about $600\,\mu$s, which is good agreement with the expected value

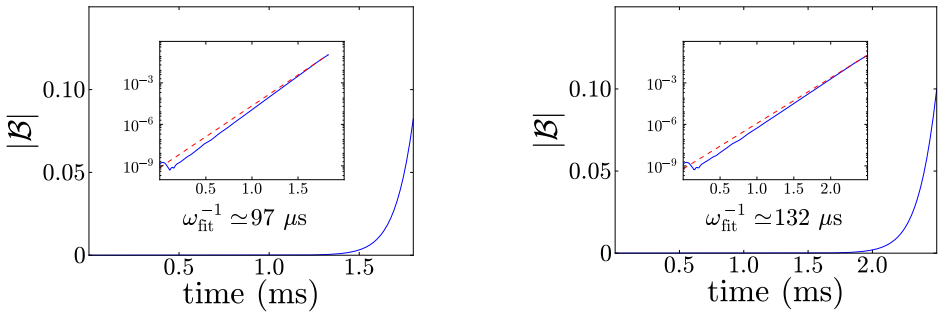

Figure 2.10: Bunching factor evolution for same parameters as Fig. (2.8) (left) and Fig. (2.9) (right). The red dashed line in the log-scale plot shows a least-squares fit.

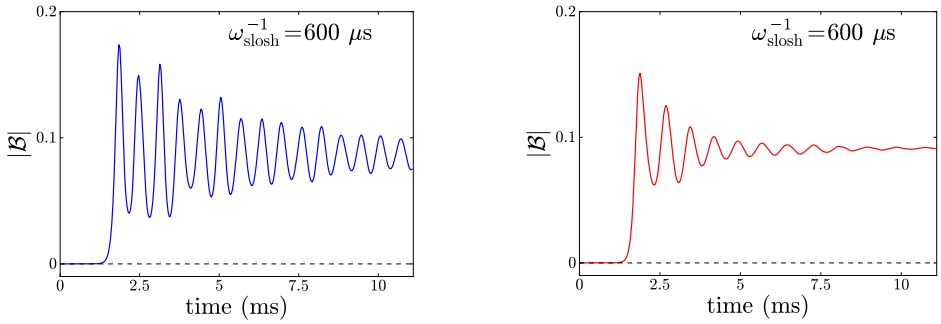

Figure 2.11: Bunching factor evolution for same parameters as Fig. (2.8) (left) and Fig. (2.9) (right). The conservative atomic motion in the self-organized optical potential lead to oscillations in the field bunching factor.

at the temperature under consideration. It is important to note that $\mathcal{B}$ measures only the transfer of energy to the mode at q_c: as other wavenumbers $q \neq q_c$ are introduced the bunching factor decreases.

2.5.2 Internal-state driven instabilities

The next step in the numerical analysis consists in including internal-state effects. Parameters are set as in Fig. (2.6a), so that an internal-state driven instability is possible: at $\delta = 10\Gamma$, the threshold for this process is $p_0 \simeq 0.36$ (as this satisfies the condition $1 - K = 0$). We choose to operate in two regimes:

- for $p_0 = 0.6$ an internal-state pattern formation process is

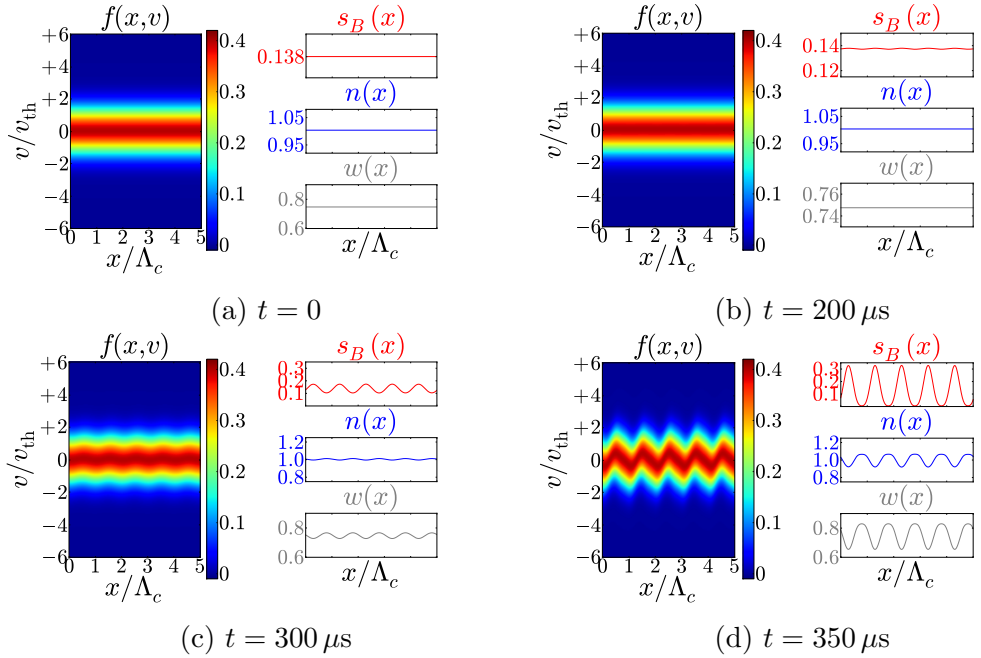

Figure 2.12: Density driven instability for $\Delta = 20$, $T = 300\,\mu$K, $d = 5\,$mm, $R = 1$, $b_0 = 200$, $dt = 0.17\,\mu$s, $p_0 = 0.2$. Noise of amplitude 10^{-3} is added to the initial atomic distribution. $s_B = |B|^2$ denotes the intensity of the backward beam.

expected, with subsequent bunching of the atoms.

- for $p_0 = 0.2$ a density driven instability is expected, essentially similar to the one of Fig. (2.8) but further sustained by a modulation of the internal-state population.

It is worth emphasized again that the internal-state process is made artificially fast by the adiabatic elimination of the internal-state dynamics, $\Gamma \to \infty$. Any consideration on the timescale of the internal-state dynamics is therefore not obtainable from the simulations: internal-state effects will occur on the scale of a single time step, independently on its value.

Fig. (2.12) shows our numerical results for the regime of relatively low saturation, $p_0 = 0.2$. In dimensional units, the pattern period is $\Lambda_c \simeq 125\,\mu$m. The growth time of the structure is in the hundreds of microseconds range, which is therefore consistent

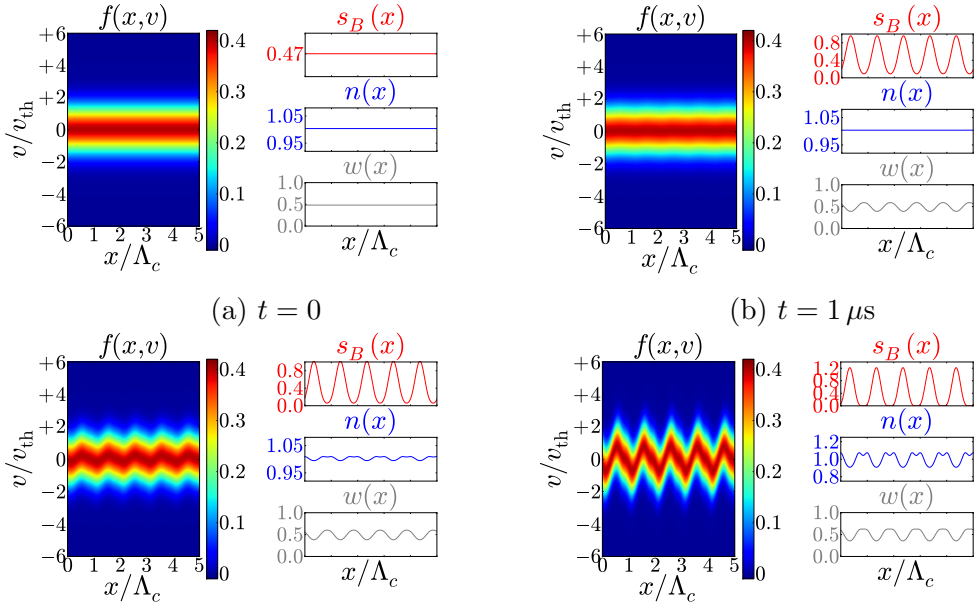

Figure 2.13: Internal-state driven instability for $\Delta = 20$, $T = 300\,\mu$K, $d = 5\,$mm, $R = 1$, $b_0 = 200$, $dt = 1\,$ns, $p_0 = 0.6$. $s_B = |B|^2$ denotes the intensity of the backward beam. Noise of amplitude 10^{-3} is added to the initial atomic distribution.

with the time for atomic motion (an atom at $T = 300\,\mu$K travels $10\,\mu$m in $10\,\mu$s). The 'long' timescale is a signature of the fact that the instability mainly relies, at least at its onset, on density redistribution effects. However, the internal state provides further feedback to the instability. The internal-state dynamics is monitored through the steady-state population difference

$$w(x) = \frac{1}{1 + s(x)} \qquad s(x) = p_0 + s_B(x)\,, \tag{2.46}$$

depicted in the bottom-right panel of each picture (gray line). As in Fig. (2.8), the red line shows the backward field intensity, and the blue line the atomic density. Fig. (2.14a) shows the evolution of the field bunching factor $|\mathcal{B}|$. As expected, the bunching factor starts from zero and increases exponentially in time.

Increasing the injected power to a relatively high value, $p_0 = 0.6$, the system enters the region of internal-state instability, see

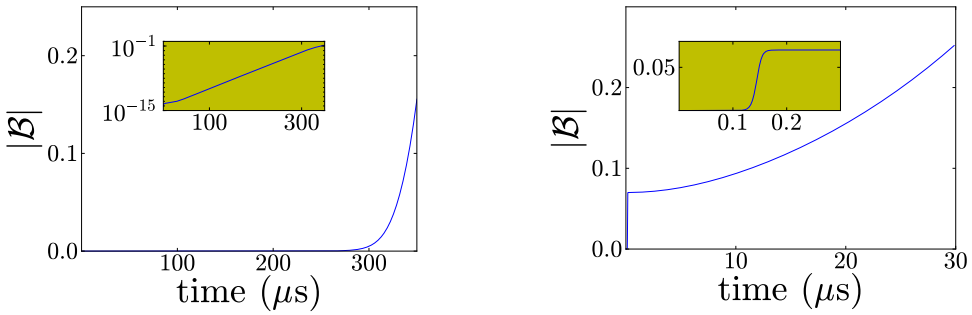

(a) (b)

Figure 2.14: Evolution of the field bunching factor $\mathcal{B}$ as a function of time, for the same parameters as Fig. (2.12) (left) and Fig. (2.13) (right).

Fig. (2.13). Now a fast (on the microsecond timescale) pattern-forming process occurs for the optical field, with spatial structures encoded in the population difference $w(x)$. In such a short time, the atomic phase-space profile is unaltered. On the tens of microseconds timescale the optical modulation starts to bunch the atoms in the potential minima, which provides further feedback for the instability. Fig. (2.14b) shows the field bunching factor corresponding to this dynamics: as evidenced in the inset, a sharp transition to a high-contrast pattern is obtained for the reentrant field almost instantaneously (depending on the time step and the numerical noise). Starting from this non-zero value, the bunching factor increases exponentially.

2.6 A sync perspective: Kuramoto model without damping

The Kuramoto model [94] is a prototypical framework for the study of *temporal* synchronization processes, so it might seem surprising to find it in a study of *spatial* instabilities. However, as also pointed out by Steven Strogatz in its widely known book *Sync* [95], spatial self-organization can always be seen as tempo-

ral synchronization. Suppose in fact to have a periodic structure emerging from a spatial instability, characterized by the spatial wavenumber q. All the physical properties of the system (for ideal patterns, at least) are periodic with period $\Lambda = 2\pi/q$, so that the physically relevant quantity phase $\theta = qx$. Atomic self-bunching in the minima of a periodic potential, thus, corresponds to a synchronization transition where all the 'oscillators' with phase θ_j bunch around the same value of the phase ψ. This can be intuitively visualized by 'wrapping up' the periodic structure on a circle parametrized by $\theta \in [0, 2\pi)$, see Fig. (2.15). It thus ap-

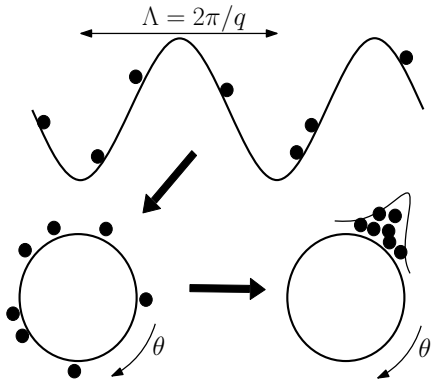

Figure 2.15: Spatial pattern formation as a synchronization process

pears natural to ask which model describes the synchronization transition for the self-structuring instabilities analyzed in the previous Sections. Indeed, this line of research has already been successfully investigated in the context of CARL [96], where it was found that a Kuramoto model with phase noise describes the self-organizing transition in viscous CARL systems. The analysis will be extended here to single mirror geometries, and find an identical model for our 'viscous' single-mirror self-structuring, see Sec. 3.4. In the 'viscous' regime stochastic noise originates from the action of optical molasses, but it is possible to describe also damping-free self-structuring instabilities in term of the Kuramoto model. As found in the low-saturation damping-free model (Sec. 2.3), in

this case a threshold for the self-organization process is set by the spread of the atomic velocities (i.e. the gas temperature), which is reinterpreted here as a spread in the distribution of the oscillators 'natural frequencies'.

The Kuramoto model describes the dynamics of N oscillators with natural frequencies ω_j subjected to an all-to-all coupling in the form $r\sin(\psi-\theta_j)$. The dynamical equations for each oscillator is given by

$$\dot{\theta}_j = \omega_j + Kr\sin(\psi - \theta_j) + \xi_j(t)\,. \tag{2.47}$$

Here $\xi_j(t)$ represents white noise with zero mean and autocorrelation $2D$, and K represents the externally-imposed coupling strength. In our pattern-formation analogy, K represents the injected energy. The coupling enters through the complex order parameter $\mathcal{B} = r\exp(i\psi)$, defined by

$$r = \frac{1}{N}\sum_{j=1}^{N} e^{i(\theta_j-\psi)}\,. \tag{2.48}$$

Note that in this framework he atomic positions determine the phases, and the velocities determine the frequencies:

$$\theta_j = qx_j \qquad \omega_j = qv_j \qquad q \text{ critical wavenumber}\,. \tag{2.49}$$

In the following the system is assumed to be driven close to the critical point, so that q is the only spatial mode excited in the system.

From the definition (2.48) it can be seen that when all the oscillators are locked on the common phase ψ, then $r = 1$ and the coupling Kr is strongest. If the oscillators are uniformly spread on the limit cycle, the coupling strength vanishes. The

synchronization transition exactly corresponds to the transition from $r = 0$ to a value $r \neq 0$. In the pattern-formation analogy, the order parameter $\mathcal{B}$ corresponds to what was termed *bunching factor* above (also in line with CARL literature), and the self-structuring transition to the emergence of a non-zero $|\mathcal{B}| = r$ at some critical point K_c.

In the viscousless case analyzed here there is no source of stochastic noise, so that the noise strength can be set as $D = 0$. In order to establish a connection between Eq. (2.47) and single-mirror self-structuring instabilities, the starting point is the wave equation (2.44b) in the low-saturation limit,

$$\frac{\partial F}{\partial z} = i\alpha_0 \Delta n F$$

describing the phase shift induced by the cloud on the forward field F. Close to the critical point, the density modulation can be expanded as

$$n(x) = 1 + r\cos(qx - \psi) \qquad r \ll 1\,,$$

where $r\exp(i\psi)$ represents the amplitude of the q-sideband (the bunching factor). Since $n(x)$ is real, the Fourier mode at wavevector $-q$ is simply given by $r\exp(-i\psi)$. A remarkable difference with the original Kuramoto model is that the locking phase ψ is now self-selected by the system, arising from a symmetry-breaking process [96]. The forward field after the interaction with the cloud (of thickness L) is then

$$F(z = L) = F(0)e^{i\chi_0}\left[1 + i\chi_0 r\cos(qx - \psi)\right]\,,$$

where $\chi_0 = \alpha_0 L\Delta$. The backward field is obtained after a propagation of $z = 2d$, and reads in Fourier space:

$$B(q, z = L + 2d) = \sqrt{R}F(0)e^{i\chi_0}\left[\delta(q) + i\chi_0\tfrac{r}{2}\left(e^{i(qx-\psi)} + e^{-i(qx-\psi)}\right)\right]e^{i\Theta}\,,$$

where $\Theta = dq^2/k_0$ is the diffractive phase shift of the q-mode. The crucial point is now that q is not a generic wavenumber, but the critical wavenumber for the system. This means that phase modulations are fully converted into amplitude modulations within the distance $z = 2d$. This is encoded in the requirement that the critical wavenumber satisfies (see Eq. (2.41))

$$\sin\Theta = 1 \quad \Longrightarrow \quad e^{i\Theta} = i$$

Hence the real-space backward field intensity is obtained as

$$\begin{aligned} |B(x)|^2 &= R|F(0)|^2\left[1 - \chi_0 rq\cos(qx - \psi)\right]^2 \\ &\simeq R|F(0)|^2\left[1 - 2\chi_0 rq\cos(qx - \psi)\right]\,, \end{aligned}$$

where terms in r^2 were neglected using the fact that at threshold the sideband amplitude is small, $r \ll 1$. Defining as in previous Sections the injected pump as $|F(0)|^2 = p_0$, the dipole force reads

$$f_{\rm dip} = -\frac{\hbar\delta}{2}\frac{\partial s(x)}{\partial x} = -\frac{\hbar\delta}{2}\frac{\partial|B(x)|^2}{\partial x} = \frac{\hbar\delta}{2}2Rp_0\chi_0 rq\sin(\psi - qx) \tag{2.50}$$

The dynamics of the N atoms is simply given by the Newton equations

$$\dot{x}_j = v_j \tag{2.51a}$$

$$\dot{v}_j = f_{\rm dip}(x_j)/M\,. \tag{2.51b}$$

In order to integrate these equations, the crucial idea is that at the critical point the emergence of a macroscopic pattern (i.e. the transition to a non-zero value $r \neq 0$) is subject to *critical slowing down*. Since the growth rate $\mathrm{Im}\,(\omega(q_c))$ vanishes at threshold ($p_0 = p_0^c$), in fact, fluctuations at the critical wavenumber have infinite lifetime. As a consequence, one can assume there exists a time t^* at which atomic motion occurred in such a way that the corresponding dipole f_{dip} stays unaffected. The characteristic time is given by the time it takes an atom at the thermal speed (v_{th}) to travel a pattern wavelength ($\Lambda_c = 2\pi/q_c$):

$$t^* = \frac{1}{q_c v_{\mathrm{th}}} \tag{2.52}$$

Assuming the dipole force f_{dip} to be unchanged for $t \leq t^*$, Eq. (2.51b) can be integrated as

$$v_j(t^*) \simeq v_j(0) + \frac{1}{M} f_{\mathrm{dip}}(x_j) t^*$$

so that Eq. (2.51a) reads

$$\dot{x}_j = v_j(0) + \frac{1}{M} f_{\mathrm{dip}}(x_j) t^*$$

Multiplying this equation by q and using the definitions (2.49) and the force expression (2.50), an equation for the phases is reached:

$$\dot{\theta}_j = \omega_j + Kr \sin(\psi - \theta)\,, \tag{2.53}$$

where the coupling strength has been defined as

$$K = \frac{\hbar \delta}{M} R p_0 \chi_0 q^2\,.$$

The 'natural frequencies' ω_j of the oscillators are determined by the initial velocities of the atoms as $\omega_j = q v_j(0)$. In order

to characterize the synchronization transition of the Kuramoto model (2.53) one needs to specify an initial frequency distribution $g(\omega)$, which in the notation of Sec. 2.2 is the initial velocity distribution of the gas, $f_0(v)$. Unsurprisingly, the Kuramoto model is analytically solvable for a Lorentzian $g(\omega)$, as was the case in the single-mirror self-structuring theory: the two models share many formal properties in the linear regime. This is ultimately due to the fact that the linear properties of these systems are determined by a dispersion integral in the form

$$\int_{-\infty}^{+\infty} \frac{\partial g/\partial \omega}{\omega - i\lambda} d\omega \tag{2.54}$$

where λ represents here the eigenvalue of the system.
Taking $g(\omega)$ to be a Lorentzian distribution with half-width at half-maximum $\omega_{\rm th} = q v_{\rm th}$, the critical point is given by [94]

$$K_c = 2\omega_{\rm th}^2 \, .$$

Using the definition of thermal speed, $v_{\rm th}^2 = k_B T/M$, in terms of injected power we thus find again the threshold value of Eq. (2.37):

$$p_0^c = \frac{1}{R\sigma\chi_0} \, . \tag{2.55}$$

This argument shows that the spontaneous emergence of spatial structures in damping-free single-mirror systems (with no internal-state effects) can be interpreted as a synchronization transition described by the Kuramoto model. The argument, however, can be rephrased in a slightly more general way, as the damping-free dynamics is captured by a collisionless Boltzmann equation which occur in many other physical systems (e.g. plasma physics), and the light-atom coupling can be seen as an effective atom-atom long range interaction. General studies of

synchronization transitions in viscousless Vlasov[2] systems with long-range interactions can be found in Refs. [78, 79, 80]. We showed above that cold atoms in a single-mirror arrangement are a versatile and powerful tool for the study of these systems, as they essentially realize a Vlasov dynamics with all-to-all coupling.

The results presented above are supported by numerical simulations, as the emergence of periodic structures for the atomic density $n(x)$ corresponds to a maximum of the phase probability distribution $n(\theta)$ describing the distribution of the θ_j's. Fig. (2.16) shows snapshots of the dynamics obtained for $T = 300\,\mu$K, $\Delta = 30$ ($\delta = 15\Gamma$), $b_0 = 100$, $R = 1$ and $p_0 = 0.043$ (5% above threshold). These results are similar to the ones shown in Sec. 2.5, but now the density distribution is sampled with $N = 10^5$ 'particles' to build a discrete histogram of the $n(\theta)$ (depicted in the bottom right panel of each figure). The phase θ is obtained from the spatial coordinate x as $\theta = \mathrm{mod}(q_c x, 2\pi) - \pi$, and the phase distribution is approximated by a continuous spline curve (red dashed line) whose values are represented in polar form in the top-right panels of each figure. The self-structuring transition leading to a modulated $n(x)$ corresponds to a a self-synchronisation of the phases around a value $\psi \simeq \pi/2$.

[2]The collisionless Boltzmann equation if often referred to as the Vlasov equation, particularly in the plasma community.

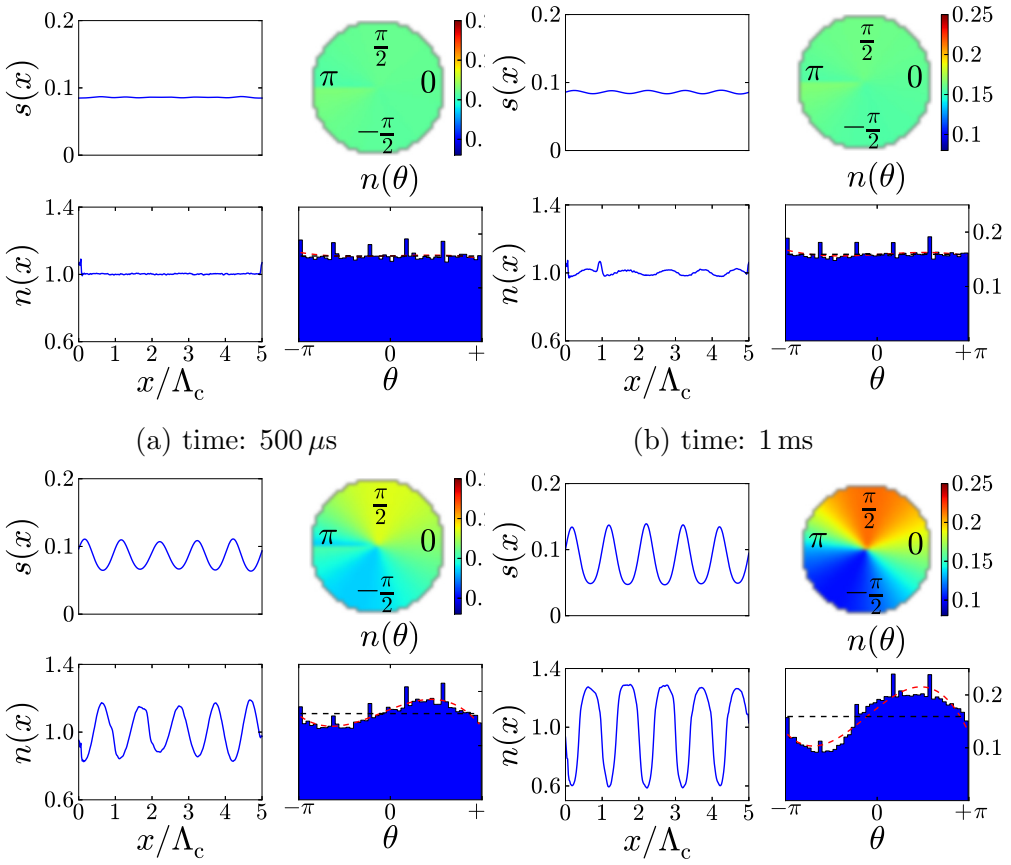

(a) time: 500 μs (b) time: 1 ms

(c) time: 1.5 ms (d) time: 2 ms

Figure 2.16: Snapshots of the synchronization dynamics taken after 500 μs (a), 1 ms (b), 1.5 ms (c) and 2 ms (d) for $T = 300\,\mu$K, $\Delta = 30$ ($\delta = 15\Gamma$), $b_0 = 100$, $R = 1$ and $p_0 = 0.043$ (5% above threshold). Each panel shows the intensity profile $s(x)$ (top left), the density profile $n(x)$ (bottom left), and the discrete sampling ($N = 10^5$ particles) of the phase probability distribution as a function of $\theta = \mathrm{mod}(q_c x, 2\pi) - \pi$ in both a linear (bottom right) and polar (top right) plot. In the bottom right panel, the black dashed line indicates the uniform probability value $(2\pi)^{-1}$, the red dashed line continuously approximates the data.

Chapter 3

Self-structuring instabilities: viscous systems

This Chapter presents theoretical and numerical results for the 'viscous' situation in which strong velocity damping is imposed by the action of optical molasses. A similar description proved to be successful in the context of CARL [31, 32], and also in more recent studies of counterpropagating instabilities [92, 93]. Its main advantage consists in a reduction of the dimensionality of the problem, as the atomic velocities can be eliminated and one is left with a theory involving only the atomic positions.

In Sec. 3.1 the viscous theory is specified in a ring cavity: the resulting model is strongly reminiscent of the original Lugiato-Lefever model for pattern formation in Kerr media [6], and indeed many features of Kerr systems are retrieved. One of these features is the possibility of implementing opto-mechanical cavity solitons (Sec. 3.3), where bistable localized states are encoded 'at will' in the density distribution of the medium (and not its excitation).

In Sec. 3.2 the single-mirror configuration of Chap. 2 is revisited, but in the viscous regime. It will be found that many of the features of the damping-free regime are recovered (e.g. the threshold

properties), but numerical simulations are made much less expensive in this case, and the numerical analysis is extended to two transverse dimensions. This will show that hexagons are selected close to threshold (as in Kerr media, for instance), but as in other cubic nonlinear systems hexagons-to-rolls transition far from the critical point are also possible.
As in the previous Chapter, a simple argument is presented to show that 'viscous' spatial self-structuring can be interpreted (at least at threshold) as a Kuramoto model for temporal synchronization. In contrast to Sec. 2.6, the threshold for the synchronization process will be set here by stochastic fluctuations. A similar theory was already developed for viscous CARL, see Ref. [96].

The viscous theory for self-organization in cold atoms might appear over-simplified, as the role of optical molasses is modelled simply in terms of damping and stochastic noise (with a scalar coefficient). However, this simple model is prototypical for soft matter systems, where linearly polarizable particles are subject to a strong viscous force and follow a Fokker-Planck dynamics. Opto-mechanical nonlinear effects were predicted and demonstrated by Ashkin and collaborators in what was termed 'artificial Kerr media', leading to self-focusing and wave mixing [97, 98]. Pattern formation was recently demonstrated in [99], and it is perhaps unsurprising that in the presence of feedback transverse self-structuring can be obtained (without the need of an internal structure, i.e. for linear particles). The viscous cold-atom dynamics thus presents itself as a good candidate for the realization of soft-matter complex dynamics [100, 101, 90, 91, 102] via the implementation of tunable opto-mechanical, 'artificial Kerr' nonlinearities.

3.1 Ring cavity

3.1.1 Model equations

This Section presents theoretical and numerical results for the 'viscous' situation where molasses beams act on the cloud, focusing on a ring cavity configuration. The presence of momentum dissipation and stochastic fluctuations qualitatively changes the physics of the instability with respect to the 'damping-free' situation of Chapter 2. Moreover, the cavity configuration opens up new opportunities for the control of the coupled light-matter dynamics, which are absent in the single-mirror configuration: in Sec. 3.3 the possibility of engineering bistable, nonlinearity-sustained cavity solitons which arise from the opto-mechanical coupling of light and cold atoms is discussed.

As in the previous Chapter, the starting point of the theoretical treatment is the discussion of the medium dynamics. Consider a sample of N identical, non-interacting atoms of mass M interacting with an intracavity field $E(\mathbf{x}, t)$. Let $\mathbf{x}_j$ and $\mathbf{v}_j$ denote the positions and velocities of the atoms in the plane transverse to the cavity axis $\hat{z}$. Optical molasses are assumed to act on the gas during the interaction, which yields momentum damping with a rate γ/M and stochastic fluctuations with autocorrelation strength $2D$ (see Sec. 1.1.2 for a brief discussion of the role of optical molasses). The dynamics of the atoms is thus governed by

$$\dot{\mathbf{x}}_j = \mathbf{v}_j \tag{3.1a}$$

$$\dot{\mathbf{v}}_j = \frac{1}{M}\left\{\mathbf{f}_{\text{dip}} - \gamma \mathbf{v}_j + M\eta_j(t)\right\} \tag{3.1b}$$

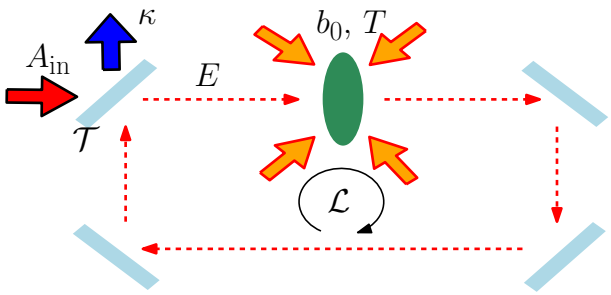

Figure 3.1: Sketch of the viscous cavity setup. A plane wave of amplitude $A_{\rm in}$ drives a single-longitudinal-mode cavity characterized by a length $\mathcal{L}$, mirror transmittivity $\mathcal{T}$, and lifetime κ^{-1}. The intracavity field E interacts with a cloud of optical density b_0 and temperature T. Optical molasses are assumed to act on the cloud during such interaction, so that T is kept constant.

where the dot denotes a temporal derivative and the η_j's represent stochastic force fluctuations due to absorption-emission 'kicks'. The main assumption made on the system is the following: the damping effect of the molasses is so strong that the velocity dynamics can be eliminated by setting $\dot{\mathbf{v}}_j = 0$. Essentially this requires the damping rate γ to be much larger than all the other terms in the equation for $\mathbf{v}_j$. The system (3.1) then becomes a first-order system for the $\mathbf{x}_j$'s:

$$\dot{\mathbf{x}}_j = \mathbf{f}_{\rm dip}/\gamma + \xi_j(t)\,, \tag{3.2}$$

where $\xi_j = M\eta_j/\gamma$ represents white gaussian noise:

$$\text{mean} \quad \langle \xi_j(t) \rangle = 0 \tag{3.3a}$$

$$\text{correlation} \quad \langle \xi_i(t)\xi_j(t') \rangle = 2D\delta_{ij}\delta(t-t') \tag{3.3b}$$

The theoretical analysis presented here deals with a 'fluid-dynamical' description in terms of a continuous density $n(\mathbf{x}, t)$, rather than individual particles. This is justified by the large density of the sample ($N_0 = N/V \sim 10^{11}\text{at/cm}^3$), and by the fact that the spatial scales under consideration are much larger than the interatomic distance $N_0^{-1/3} \sim 1 - 10\,\mu\text{m}$. Following standard pro-

cedures [103, 104], Eq. (3.2) is transformed into a Fokker-Planck equation for the probability density $n(\mathbf{x}, t)$ (see also Appendix A):

$$\frac{\partial n(\mathbf{x}, t)}{\partial t} = -\frac{1}{\gamma}\nabla \cdot [n(\mathbf{x}, t)\mathbf{f}_{\rm dip}(\mathbf{x}, t)] + D\nabla^2 n(\mathbf{x}, t)\,, \qquad (3.4)$$

where $\nabla = \partial/\partial\mathbf{x}$. Note that the Fokker-Planck equation can be seen as the conservation law for the probability density $n(\mathbf{x}, t)$:

$$\frac{\partial n(\mathbf{x}, t)}{\partial t} + \nabla \cdot \mathbf{j} = 0 \qquad\qquad \mathbf{j} = \frac{1}{\gamma} n\mathbf{f}_{\rm dip} - D\nabla n\,,$$

where $\mathbf{j}$ represents the probability current.
Recovering the expression (1.15) for the dipole force in terms of the intracavity intensity $s = |E|^2$,

$$U_{\rm dip} = \frac{\hbar\delta}{2}\log(1 + s) \qquad \mathbf{f}_{\rm dip} = -\nabla U_{\rm dip}\,,$$

the Fokker-Planck equation (3.4) becomes

$$\frac{\partial n(\mathbf{x}, t)}{\partial t} = \frac{\hbar\delta}{2\gamma}\nabla \cdot \left[n(\mathbf{x}, t)\frac{\nabla s(\mathbf{x}, t)}{1 + s(\mathbf{x}, t)}\right] + D\nabla^2 n(\mathbf{x}, t)\,. \qquad (3.5)$$

To write the Fokker-Planck equation in its final form the fluctuation-dissipation relation can be invoked:

$$D\gamma = k_B T\,. \qquad (3.6)$$

This relation accounts for the fact that when the molasses beams illuminate the gas, the damping effect tries to 'freeze' the gas at $T = 0$, but this cooling effect is limited by stochastic spontaneous emission processes. Hence the gas reaches a non-equilibrium temperature (the Doppler temperature) which is obtained when the two effects balance. For alkali gases this temperature is typically around $100\,\mu$K.

Plugging (3.6) into (3.5) the Fokker-Planck equation for $n(\mathbf{x},t)$ reaches its final form (also known as the Smoluchowski equation, see Appendix A and Ref. [105, 106])

$$\frac{\partial n(\mathbf{x},t)}{\partial t} = \frac{\hbar\delta}{2k_BT} D\nabla\cdot\left[n(\mathbf{x},t)\frac{\nabla s(\mathbf{x},t)}{1+s(\mathbf{x},t)}\right] + D\nabla^2 n(\mathbf{x},t)\,, \quad (3.7)$$

where the dimensionless parameter

$$\sigma = \frac{\hbar\delta}{2k_BT} \quad (3.8)$$

represents the strength of the nonlinear opto-mechanical coupling. This coefficient was already encountered in the damping-free theory (see Eq. (2.31)), and will again play a fundamental role in determining the linear properties of the system.
Moreover, Eq. (3.7) is linear in $n(\mathbf{x},t)$, and can thus be rescaled by any constant factor. As everywhere in this thesis, $n(x)$ is defined to describe modulations around the homogeneous density N_0. As a consequence, $n(\mathbf{x},t)$ is dimensionless and must have unity mean, so that the conservation of the number of atoms translates as a normalization condition in the form

$$\int_A d\mathbf{x}\, n(\mathbf{x},t) = A \quad \text{transverse size of the cloud} \quad (3.9)$$

The dynamics of the intracavity field $E(\mathbf{x},t)$ is described under a set of assumptions which can be considered 'standard' in the field of cavity optical pattern formation. Essentially the same field dynamics was in fact considered in the original treatment of Lugiato and Lefever [6] for pattern formation in Kerr media. A more detailed presentation dealing with two-level 'internal-state' instabilities can be found in [107]. Essentially, the work presented

here extends those works to the dynamics of the atoms center of mass.

First, consider a cavity supporting only one longitudinal mode (the fundamental one); this assumption commonly goes under the name of *mean field limit*. Since this mode has no dependence on the longitudinal coordinate z all the derivatives with respect to z can be eliminated from the wave equation. The mirrors are assumed to have an overall reflectivity $\mathcal{R}$ (transmittivity $\mathcal{T} = 1 - \mathcal{R}$), the medium to have a thickness L and the cavity length to be $\mathcal{L}$. Under the rotating wave, paraxial and slowly varying envelope approximations, the dynamics of the slowly-varying complex amplitude E of the electric field is described by [107]

$$\frac{\partial E}{\partial t} = -\kappa(1 + i\theta)E + A_{\text{in}} + \mathcal{P}E + i\kappa\frac{\mathcal{L}}{2k_0\mathcal{T}}\nabla^2 E, \tag{3.10}$$

where

- $\kappa = c\mathcal{T}/\mathcal{L}$ is the cavity linewidth (equal for each transverse mode)
- The $-\kappa E$ terms describe mirror losses. The $-i\theta E$ term describes the phase shift imposed by an empty cavity, $\theta = (\omega_0 - \omega_{\text{c}})/\kappa$ being the dimensionless detuning between the field frequency ω_0 and the cavity frequency ω_{c} of the closest supported mode
- A_{in} is the pump rate associated with the injected plane wave. A_{in} can be set real without loss of generality
- the last term describes field diffraction through the propagation, with a diffraction coefficient $a = \mathcal{L}/2k_0\mathcal{T}$.

The last term left to discuss is the nonlinear coupling $\mathcal{P}E$, where

$\mathcal{P}$ parametrizes the gas polarizability. As in Chapter 2, there are two sources of nonlinearity in the response $\mathcal{P}$ of the system. The first arises from the internal-state structure of the two-level system, and is the one involved in 'hot-atom' pattern formation [107]. The second arises from the coupling with the center-of-mass motion, whose dynamics is described by Eq. (3.7). For a single pass of the field through the cloud the field dynamics is governed by (neglecting propagation inside the medium):

$$\frac{\partial E}{\partial t} = -\alpha_0 c(1+i\Delta)\frac{n\,E}{1+|E|^2} = -\kappa\frac{\alpha_0 L}{\mathcal{T}}(1+i\Delta)\frac{n\,E}{1+s} \qquad (3.11)$$

where as usual $\Delta = 2\delta/\Gamma$ is the half-linewidth detuning, and $s = |E|^2$ the saturation parameter associated to the intracavity intensity. The dimensionless *cooperativity parameter* can be defined as $C = \alpha_0 L/\mathcal{T}$, which is connected to the on-resonance optical thickness b_0 of the cloud as

$$\alpha_0 = \frac{b_0}{2L(1+\Delta^2)} \qquad\qquad C = \frac{b_0}{2\mathcal{T}(1+\Delta^2)} \qquad (3.12)$$

Eq. (3.10) can then be rewritten as

$$\frac{\partial E}{\partial t} = \kappa\left\{-(1+i\theta)E + A_{\rm in} - C(1+i\Delta)\frac{n\,E}{1+s} + ia\nabla^2 E\right\}, \qquad (3.13)$$

where the pump has been rescaled as $A_{\rm in} \to A_{\rm in}/\kappa$.

3.1.2 Linear analysis

As a first step in the stability analysis the stationary homogeneous solution for the system is identified: a transversally 'flat' intracavity field E_0 generates no forces, and hence $n_0 = 1$ solves

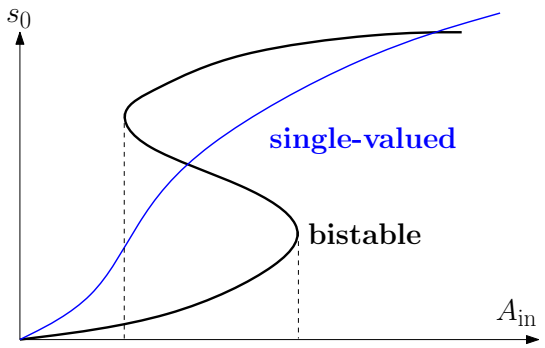

Figure 3.2: Qualitative representation of the input-ouput cavity characteristic: varying θ (at given C and Δ) it is possible to switch from a regime where the plane-wave steady-state intracavity intensity s_0 is a multi-valued curve of $A_{\rm in}$ to a regime where it is single-valued. For the multi-valued case, the system displays histeretic behaviour, see Refs. [108, 109]. The dashed lines indicate the bistability domain.

Eq. (3.7) identically. From Eq. (3.10), thus, E_0 must satisfy

$$\left[\left(1+\frac{C}{1+|E_0|^2}\right)+i\left(\theta+\frac{C\Delta}{1+|E_0|^2}\right)\right]E_0 = A_{\rm in}\,. \qquad (3.14)$$

Solving this equation for $s_0 \equiv |E_0|^2$ gives the steady-state input-output relationship for the cavity. Since the homogeneous state is obtained for $n = 1$, this result is identical to the one obtained for hot vapours. In particular, the internal-state nonlinearity is well-known to lead to the phenomenon of plane-wave optical bistability [108, 109], see Fig. (3.2). This effect will not be considered here, always operating in a region of parameter space where plane-wave bistability is suppressed. This practically means that the regimes of operations are such that the relationship $s_0 = s_0(A_{\rm in})$ is single-valued, and the intracavity homogeneous intensity s_0 can be conveniently used as a control parameter instead of $A_{\rm in}$.

Consider now small perturbations around the homogeneous val-

ues,

$$
\begin{aligned}
n(\mathbf{x},t) &= 1 + n_1(\mathbf{x},t) \\
E(\mathbf{x},t) &= E_0 + E_1(\mathbf{x},t) \\
s(\mathbf{x},t) &= s_0 + E_0^* E_1(\mathbf{x},t) + E_0 E_1^*(\mathbf{x},t)
\end{aligned}
$$

with the perturbations in the Fourier form

$$
n_1, E_1 \sim \exp(i\mathbf{q}\cdot\mathbf{x})\exp(-i\omega t)\,.
$$

As usual, the underlying idea is that if $\mathrm{Im}(\omega) > 0$ for a perturbation at wavevector $\mathbf{q}$, this perturbation will undergo exponential growth and will give rise to a macroscopic pattern of spatial scale $\Lambda = 2\pi/|\mathbf{q}|$, see Sec. 1.2. To study the stability of the perturbations, Eqs. (3.7) and (3.13) are linearized as

$$
\begin{aligned}
\kappa^{-1}\dot{n}_1(\mathbf{q},t) = &-\frac{D}{\kappa a}\sigma|\sqrt{a}\mathbf{q}|^2\frac{E_0^* E_1(\mathbf{q},t) + E_0 E_1^*(\mathbf{q},t)}{1+s_0} + \\
&- \frac{D}{\kappa a}|\sqrt{a}\mathbf{q}|^2 n_1(\mathbf{q},t) \qquad (3.15a) \\
\kappa^{-1}\dot{E}_1(\mathbf{q},t) = &-(1+i\theta)E_1(\mathbf{q},t) - \frac{C(1+i\Delta)E_0}{1+s_0}n_1(\mathbf{q},t) + \\
&- \frac{C(1+i\Delta)}{1+s_0}E_1(\mathbf{q},t) + \\
&+ \frac{C(1+i\Delta)E_0}{(1+s_0)^2}\left[E_0^* E_1(\mathbf{q},t) + E_0 E_1^*(\mathbf{q},t)\right] + \\
&- i|\sqrt{a}\mathbf{q}|^2 E_1(\mathbf{q},t) \qquad (3.15b)
\end{aligned}
$$

Moving to dimensionless units by rescaling time to the cavity lifetime and space to the diffracion length:

$$
t' = \kappa t \quad \mathbf{x}' = \mathbf{x}/\sqrt{a} \quad \mathbf{q}' = \sqrt{a}\,\mathbf{q} \quad \bar{D} = D/(\kappa a)\,,
$$

the stability of the perturbations is determined by the eigenvalues

of the linearized system

$$\frac{\partial}{\partial t'}\begin{pmatrix} E_1(\mathbf{q}',t') \\ E_1^*(\mathbf{q}',t') \\ n_1(\mathbf{q}',t') \end{pmatrix} = \begin{bmatrix} A_{11} & A_{12} & A_{13} \\ A_{12}^* & A_{11}^* & A_{13}^* \\ A_{31} & A_{32} & A_{33} \end{bmatrix} \begin{pmatrix} E_1(\mathbf{q}',t') \\ E_1^*(\mathbf{q}',t') \\ n_1(\mathbf{q}',t') \end{pmatrix} ,$$

where

$$\begin{aligned} A_{11} &= -(1+i\theta) - \frac{C(1+i\Delta)}{1+s_0}\left[1 - \frac{s_0}{1+s_0}\right] - i|\mathbf{q}'|^2 \\ A_{12} &= \frac{C(1+i\Delta)}{(1+s_0)^2}E_0^2 \\ A_{13} &= -\frac{C(1+i\Delta)E_0}{1+s_0} \\ A_{31} &= -\bar{D}\sigma|\mathbf{q}'|^2\frac{E_0^*}{1+s_0} \\ A_{32} &= -\bar{D}\sigma|\mathbf{q}'|^2\frac{E_0}{1+s_0} \\ A_{33} &= -\bar{D}|\mathbf{q}'|^2 . \end{aligned}$$

To obtain the critical properties of the system (such as threshold and critical wavenumber) the eigenvalue is set to zero, $\lambda = -i\omega = 0$. This will be justified in the following, as it will be shown that the instability is stationary, $\mathrm{Im}(\lambda) = 0$. This gives the density perturbation n_1 as

$$n_1(\mathbf{q}') = -\frac{\sigma}{1+s_0}\left(E_0 E_1^*(\mathbf{q}') + E_0^* E_1(\mathbf{q}')\right) ,$$

so that the equation for the field can be seen as a two-dimensional system

$$0 = \begin{bmatrix} B_{11} & B_{12} \\ B_{12}^* & B_{11}^* \end{bmatrix} \begin{pmatrix} E_1(\mathbf{q}',t') \\ E_1^*(\mathbf{q}',t') \end{pmatrix} ,$$

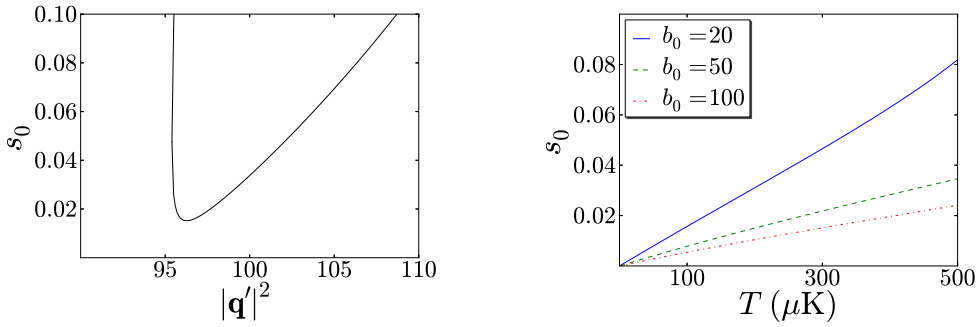

(a) (b)

Figure 3.3: On the left, the stability domain in q-space: note that in contrast to the single-mirror system, no periodicity is observed in q (there is a single threshold minimum). On the right, the dependence of the power threshold from the temperature: as expected, lower temperatures enhance the opto-mechanical coupling and lower the threshold for the instability. Other parameters are: $b_0 = 20$, $\Delta = 20$, $\theta = -100$, $\mathcal{T} = 0.1$, $T = 100\,\mu$K. The corresponding cooperativity is $C \simeq 0.25$, which yields a single-valued input-output characteristic at $\theta = -100$. The pattern size corresponding to the critical wavenumber (the minimum in Fig. (a)) is in the tens of microns range, see discussion below.

with

$$B_{11} = -(1+i\theta) - \frac{C(1+i\Delta)}{1+s_0}\left[1 - \frac{s_0(1+\sigma)}{1+s_0}\right] - i|\mathbf{q}'|^2$$
$$B_{12} = \frac{C(1+i\Delta)}{(1+s_0)^2}E_0^2(1+\sigma)\,.$$

The eigenvalues μ of this system are determined by (note that we are interested only in $\mu = 0$):

$$\mu^2 - \mathrm{Tr}(B)\mu + \det(B) = 0 \Longrightarrow \det(B) = 0\,.$$

The threshold condition is thus given by:

$$\begin{aligned}\det(B) =&|B_{11}|^2 - |B_{12}|^2 = 1 + \frac{C^2}{(1+s_0)^2}\left[1 - \frac{s_0(1+\sigma)}{1+s_0}\right]^2 + \\ &+ \frac{2C}{1+s_0}\left[1 - \frac{s_0(1+\sigma)}{1+s_0}\right] + (\hat{\theta} + |\mathbf{q}'|^2)^2 + \\ &- 2(1+\sigma)(\hat{\theta} + |\mathbf{q}'|^2)\frac{C\Delta}{(1+s_0)^2} - \frac{C^2}{(1+s_0)^4}s_0^2(1+\sigma)^2 = 0\,,\end{aligned}$$

where the total linear phase shift due to the cavity and the medium has been defined as

$$\hat{\theta} = \theta + \frac{C\Delta}{1+s_0}\,. \tag{3.16}$$

Fig. (3.3) shows the threshold curve $s_0 = s_0(|\mathbf{q}'|^2)$ for the system, together with the temperature dependence of the threshold. As in the 'viscousless' case of Chap. 2, the threshold is lowered by lowering the temperature. The dependence on the optical density is somewhat more complicated, as it enters the cooperativity parameter which determines the critical wavenumber through $\hat{\theta}$. Studying the limit of linear single-atom response (low-saturation limit) will give insight into these effects. However, it can already be appreciate here one of the main advantages of the cavity arrangement: already at $b_0 = 20$ and $\delta = 10\Gamma$, the required saturation level is of the order of $s_0 \sim 0.01$. In contrast, single-mirror experiments would require higher optical densities, around $b_0 \sim 100$ or more to achieve the same threshold. The advantage of the cavity is that light is recirculated many times, effectively increasing the interaction strength. The 'effective' optical density (which enters the cooperativity factor C) is in fact increased by a factor $1/\mathcal{T}$, which is large in the limit considered here.

The next step consists in studying the growth rate for the system. Beside yielding useful information on the timescale of the

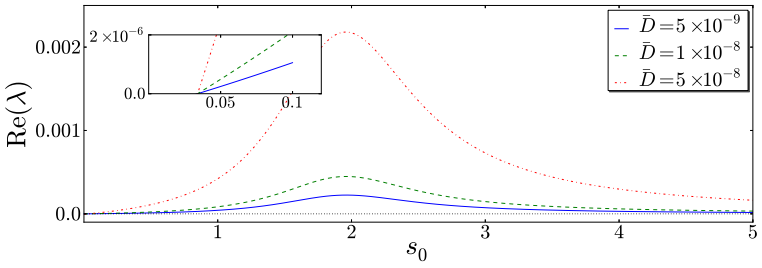

(a)

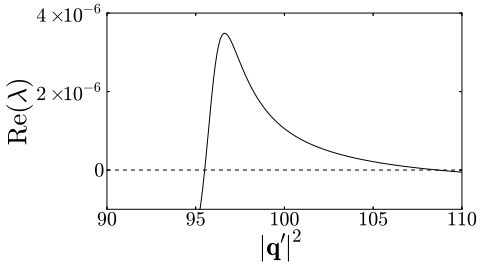

(b)

Figure 3.4: The top panel shows the growth rate for the viscous cavity system, including internal-state effects. Parameters are as in Fig. (3.3a) with $|\mathbf{q}'|^2 = 100$, varying the diffusion coefficient $\bar{D}$. Note that varying $\bar{D}$ leads to different growth rates for the system, but does not affect the threshold condition $\mathrm{Re}(\lambda) = 0$. The flat dashed black line depicts the imaginary part $\mathrm{Im}(\lambda) = 0$ of eigenvalue: the instability is stationary (for any $\bar{D}$). The bottom panel displays the growth rate as a function of $|\mathbf{q}'|^2$ for the same parameters, setting $\bar{D} = 5 \times 10^{-9}$ and $s_0 = 0.1$.

process, the growth rate also gives information about the role of the diffusion coefficient $\bar{D}$, which does not enter the threshold expression (3.20). We remark in fact that $\bar{D}$ appears in both terms of the density equation (3.7), so that imposing the marginality condition the dependence from $\bar{D}$ is lost. The role of the diffusion coefficient is that of 'speeding up' or 'slowing down' the instability, but $\bar{D}$ does not determine the threshold conditions for the instability (see the inset of Fig. (3.4a)). Moreover, the instability is found to be stationary, $\mathrm{Im}(\lambda) = 0$ for any value of $\bar{D}$ (black dashed line in Fig. (3.4a)). This fact was used in determining the threshold condition above, as imposing $\mathrm{Re}(\lambda) = 0$ automatically gives $\lambda = 0$. The values of $\bar{D}$ considered corresponds to a cavity of length $\mathcal{L} = 10\,\mathrm{cm}$ and 10% mirror transmittivity, and a diffusion coefficient in the range $10^{-7} - 10^{-8}\,\mathrm{m}^2/\mathrm{s}$. The exact value of the diffusion coefficient is dependent of the details of the optical molasses (detuning and saturation intensity), but as demonstrated in [110] these numbers are obtainable in Rb molasses. The value of $\bar{D}$, however, does not change the main physics of the instability, only the expected growth rate. For the values used here the corresponding growth rates are of the order of $1 - 10\,(\mu\mathrm{s})^{-1}$.

3.1.3 Low saturation limit

In this Section the 'viscous' equivalent of the damping-free situation analyzed in Sec. 2.3 is studied, assuming low saturation and neglecting internal-state effects. This means that the susceptibility is a c-number independent on the intensity, so that the polarisation is proportional to the field, $\mathcal{P} \sim E$. Neglecting absorption and keeping only first-order terms, Eqs. (3.7) and (3.13)

reduce to (in dimensionless units):

$$\frac{\partial E}{\partial t'} = -(1+\theta)E + A_{\text{in}} - iC\Delta nE + i\nabla'^2 E \tag{3.17a}$$

$$\frac{\partial n}{\partial t'} = \sigma\bar{D}\nabla' \cdot \left[n\nabla'|E|^2\right] + \bar{D}\nabla'^2 n\,, \tag{3.17b}$$

where $\nabla' = \partial/\partial\mathbf{x}'$. Repeating the procedure described above these equations are linearized, and imposing $\dot{n}_1 = 0$ gives

$$n_1(\mathbf{q}') = -\sigma\left[E_0 E_1^*(\mathbf{q}') + E_0^* E_1(\mathbf{q}')\right]$$

Plugging this into the equation for $E_1(\mathbf{q}')$ the following system is obtained:

$$0 = \begin{bmatrix} B_{11} & B_{12} \\ B_{12}^* & B_{11}^* \end{bmatrix} \begin{pmatrix} E_1(\mathbf{q}', t') \\ E_1^*(\mathbf{q}', t') \end{pmatrix}$$

with the matrix elements defined by

$$B_{11} = -(1 + i\hat{\theta}) + iC\Delta\sigma s_0 - i|\mathbf{q}'|^2$$
$$B_{12} = iC\Delta\sigma E_0^2$$

and the linear cavity shift defined by $\hat{\theta} = \theta + C\Delta$.
In the low saturation limit the threshold condition $\det(B) = 0$ is linear in s_0, and can therefore be easily solved to give the threshold value

$$s_0(|\mathbf{q}'|^2) = \frac{1 + (\hat{\theta} + |\mathbf{q}'|^2)^2}{2C\sigma\Delta(\hat{\theta} + |\mathbf{q}'|^2)}\,. \tag{3.18}$$

Two features of this threshold expression are worth remarking: first, the threshold depends only on $\sigma\Delta \sim \Delta^2$, and therefore a symmetric behaviour is found for blue/red detuning. This result replicates the one found in Sec. 2.3 for damping-free single-mirror systems. Secondly, by setting $\partial s_0^c/\partial|\mathbf{q}'|^2 = 0$ the critical

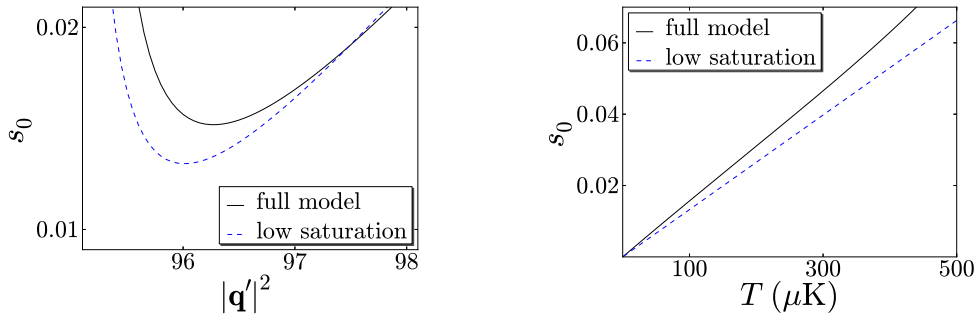

(a) (b)

Figure 3.5: Comparison between the 'full' threshold and the 'low-saturation' one, Eq. (3.18), for the same parameters as Fig. (3.3a) (left panel). On the right panel, the temperature dependence is qualitatively similar for the 'full' and 'low-saturation' model. Here we used the same parameters as in the left panel, and set $|\mathbf{q}'|^2 = 96$ (blue curve) and $|\mathbf{q}'|^2 = 96.2$ (black curve).

wavenumber $q'_c = |\mathbf{q}'_c|$ can be analytically obtained as:

$$q'_c = 1 - \hat{\theta} = 1 - (\theta + C\Delta) \tag{3.19}$$

so that the critical saturation value is found as

$$s_0^c = \frac{1}{C\sigma\Delta}\,. \tag{3.20}$$

From this expression it can be seen that the threshold scales as T/b_0 (as in the viscousless case, see Chap. 2). The threshold is also flat with respect to the detuning, since $C \sim \Delta^{-2}$ and $\sigma\Delta \sim \Delta^2$. Moreover, varying the optical density b_0 and/or the detuning will result in a shift of the critical wavenumber (3.19). However, $\hat{\theta}$ (and hence q_c) can be freely tuned by varying the cavity detuning θ. Taking the D_2 line of ^{87}Rb as reference ($\lambda_0 = 780\,\mathrm{nm}$), the diffraction length associated to a 10 cm long cavity with mirror transmittitvity $\mathcal{T} = 0.1$ is $\sqrt{a} = [\lambda_0 \mathcal{L}/4\pi\mathcal{T}]^{1/2} \simeq 2.5 \times 10^{-4}$. The typical value (see e.g. Fig. (3.3)) of the critical wavenumber is

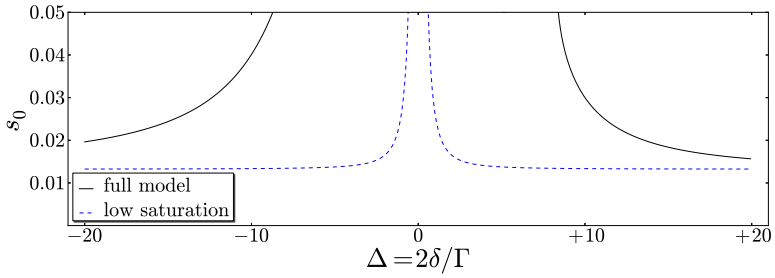

Figure 3.6: Detuning dependence of the power threshold in the 'full' and 'low saturation' models for the same parameters as Fig. (3.5a) and $|\mathbf{q}'|^2 = 1-\hat{\theta}$. The instability is suppressed on resonance, and the behaviour is non symmetrical for blue/red detuning in the full model, due to the presence of internal-state effects.

$q_c' \sim 100$, which gives

$$\Lambda_c = \frac{2\pi\sqrt{a}}{q_c'} \sim \frac{2\pi\sqrt{a}}{100} \sim 15\,\mu\mathrm{m}\,.$$

The tunability of q_c' and $\sqrt{a}$ (e.g. via the cavity length) offers substantial tunability of the pattern size in the tens to hundreds of micrometers range.

As a conclusive remark for this Section, for the choice of parameters used here the behaviour of the system is nearly identical in the 'full' model (including internal-state effects) and in the simpler 'low-saturation' model. This holds already for an intermediate choice of detuning, $\delta = 10\Gamma$ ($\Delta = 20$) in this Section. However, the sign of the detuning is important: for the values of cavity detuning used here, in fact, no internal-state-only instability is possible. Otherwise stated, no 'hot-atom' pattern formation [107] can occur for a self-defocusing medium. On the other hand, as already discussed in the context of damping-free single-mirror setups (see Sec. 2.3.5), density redistribution effects always lead to a self-focusing nonlinearity. This is reflected by the fact that the low-saturation model is completely symmetric

for blue/red detuning, while the 'full' model is not, see Fig. (3.6).

3.1.4 Numerical results

This Section presents results from the numerical simulations of the system in the 'low-saturation' regime (no internal-state effects). The role of internal-state nonlinearities will be investigated in the single-mirror configuration, see Sec. (3.2).

We rewrite for clarity the model equations for the 'viscous' cavity system in dimensionless units:

$$\frac{\partial E}{\partial t'} = -(1+i\theta)E + A_{\text{in}} - iC\Delta n E + i\nabla'^2 E \tag{3.21a}$$

$$\frac{\partial n}{\partial t'} = \sigma\bar{D}\nabla' \cdot \left[n\nabla'|E|^2\right] + \bar{D}\nabla'^2 E \tag{3.21b}$$

Since the aim of the numerical analysis is to determine the stationary state of the system, the task of solving Eqs. (3.21) can be simplified as follows. The stationary state of the Fokker-Planck equation is determined by the Gibbs state

$$n_{\text{eq}}(\mathbf{x}) = \frac{\exp\left\{U_{\text{dip}}(\mathbf{x})/k_B T\right\}}{\int \exp\left\{-U_{\text{dip}}/k_B T\right\} d\mathbf{x}} = \frac{\exp\left\{-\sigma s(\mathbf{x})\right\}}{\int \exp\left\{-\sigma s(\mathbf{x})\right\} d\mathbf{x}}\,, \tag{3.22}$$

where the definitions $U_{\text{dip}}(\mathbf{x}) = (\hbar\delta/2)s(\mathbf{x})$ and $\sigma = \hbar\delta/2k_B T$ have been used. Looking for the stationary state which satisfies $\partial E/\partial t' = \partial n/\partial t' = 0$, the Gibbs state n_{eq} can be plugged into the field equation, solving the latter until a stationary value for E is reached. Since n_{eq} depends from E through the dipole potential $\sim |E|^2$, this effectively introduces a nonlinearity in the field dynamics. It should be emphasized that this technique, already introduced in [92], is effective in determining the stationary state, but it is not able to resolve the dynamics for the system. Its major

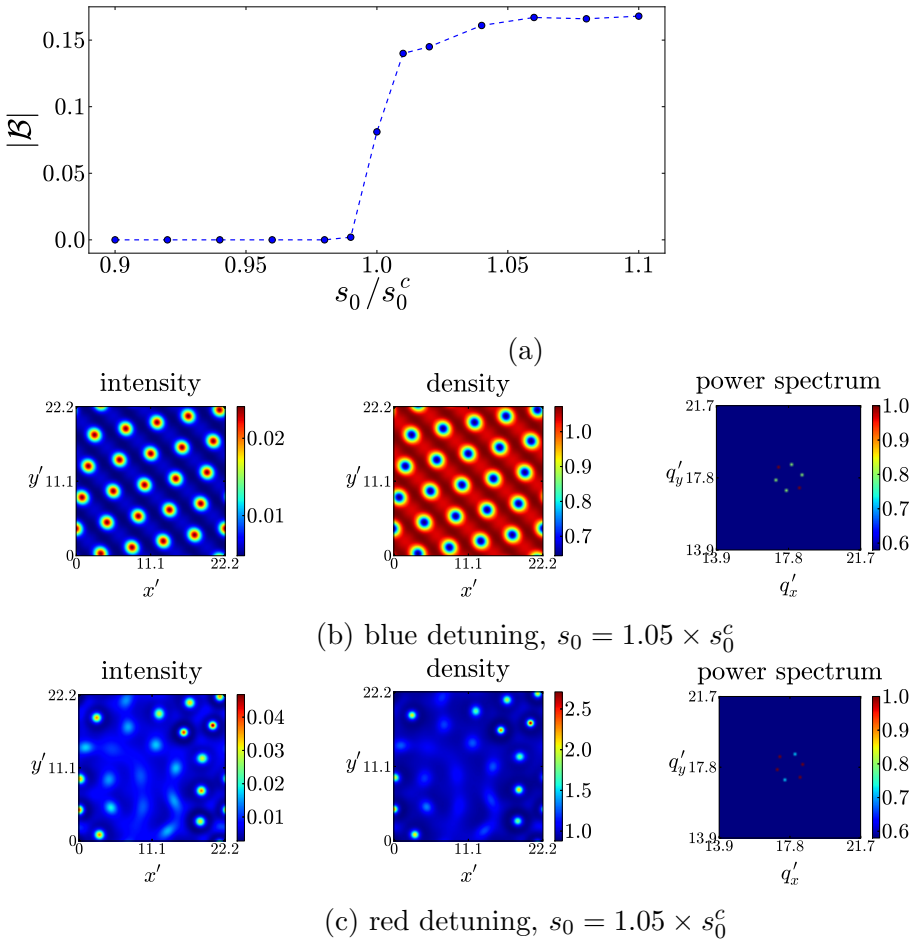

Figure 3.7: Results from the numerical simulations of the damped cavity system in the low-saturation regime, Eqs. (3.21). Above a threshold value s_0^c for the intracavity homogeneous intensity the formation of hexagons is found both on the blue (b) and red (c) side of the resonance. The top panel (a) shows the bifurcation diagram for blue detuning. Parameters are: $\hat{\theta} = -1$, $C = 5$, $\Delta = \pm 20$, and $\sigma = \pm 25$ (obtained at $b_0 = 20$, $T = 60\,\mu$K).

advantage lies in the fact that the dynamics of the atomic density is in practice eliminated from the problem, which results in a strong simplification due to the different timescales of the field and atomic dynamics (encoded in small values of $\bar{D} \sim 10^{-7}$). Moreover, care must be taken at each time step in order to correctly renormalize the density distribution, which introduces an additional nonlinearity through the normalization integral (which will depend on $|E|^2$).

In the previous Section we discussed the stability of the system,

and we found that the homogeneous state $n_0 = 1$, $E_0 = A_{\rm in}/(1 + i\hat{\theta})$ becomes unstable when the intracavity intensity s_0 exceeds the critical value

$$s_0^c = \frac{1}{\sigma \Delta C}\,.$$

As in Sec. 2.5, the emergence of spatial structures can be monitored by calculating the *field bunching factor*, i.e. the intensity of the sideband at the critical wavenumber. Note that in two dimensions an entire circle at $|\mathbf{q}'| = q_c$ is unstable. The choice operated here is to take as bunching factor the largest sideband on the 'critical circle', rescaled to the homogeneous background:

$$\mathcal{B} = \max_{|\mathbf{q}'|=q_c} \frac{\int E(\mathbf{x}') \exp(i\mathbf{q}' \cdot \mathbf{x}') d\mathbf{x}'}{\int E(\mathbf{x}') d\mathbf{x}'} \tag{3.23}$$

Another possible choice is the average intensity of the 'critical circle', which was used for the analysis of experimental data [83]. Beside the specific definition of the bunching factor, the crucial point is that $\mathcal{B}$ represents an order parameter for the system, i.e. switches from $|\mathcal{B}| = 0$ to a non-zero value at the critical point, see Fig. (3.7a). Figs. (3.7b-3.7c) show the stationary state for a control parameter 5% above threshold, for the same parameters as Fig. (3.7a) and blue/red detuning, respectively. Close to threshold hexagons are selected, a unifying feature of systems with a cubic nonlinearity (see Sec. 1.2). As it will also be stressed in Sec. (3.3), the self-structuring, opto-mechanical instabilities discussed here shares many features of spatial instabilities in Kerr, or Kerr-like, systems. The preference of the system for hexagons [81, 111] is one of these features, as is the transition from hexagons to rolls far from threshold [112], see also Fig. (3.17). However, in the low-saturation model studied here

the nonlinearity stems uniquely from density redistribution effects, and therefore spatial structures are encoded in the atomic density. Switching from blue to red detuning, thus, density structures form complementary to the optical profile, i.e. hexagons are observed for blue detuning, and honeycombs (negative hexagons) for red detuning. Hexagons for the optical intensity are formed by self-organising filaments of high refractive index via the attraction/expulsion of atoms from high intensity regions for blue/red detuning. Moreover, in the blue-detuned regime a higher saturation is obtained than in the red-detuned one, because for $\Delta > 0$ atoms are expelled from high intensity regions up to the point where no more atoms can contribute to the nonlinearity. For red detuning, instead, there is no limit (in the model) to the achievable peak density, and therefore to the peak in the refractive index of the 'filament' guiding light.

3.2 Single-mirror feedback

In this Section the analysis of the viscous regime for the single-mirror configuration is presented. Essentially the medium dynamics of Sec. 3.1 is joined with with the feedback scheme of Chap. 2, assuming optical molasses to eliminate the velocity dynamics but no cavity. As in Chap. 2, the single-mirror configuration results in a relatively simpler analysis (compared to the cavity case), as the medium and field dynamics can be separated in a 'split-step' fashion.

3.2.1 Linear analysis

Under the same set of assumptions discussed in the previous Section, the medium dynamics is governed by a continuity equation

for the atomic density $n(\mathbf{x},t)$:

$$\frac{\partial n(\mathbf{x},t)}{\partial t} = D\sigma\nabla\cdot\left[n(\mathbf{x},t)\frac{\nabla s(\mathbf{x},t)}{1+s(\mathbf{x},t)}\right] + D\nabla^2 n(\mathbf{x},t)\,, \qquad (3.24)$$

where $\sigma = \hbar\delta/2k_BT$ and the dipole potential is taken in its full form $U_{\rm dip}(\mathbf{x},t) = (\hbar\delta/2)\log(1+s(\mathbf{x},t))$ (i.e. we do not assume $s \ll 1$). The total intensity $s(\mathbf{x},t)$ is obtained by summing up the forward and backward intensities (see Fig. (3.8) and Chap. 2):

$$s(\mathbf{x},t) = |F|^2 + |B|^2 \equiv p_0 + |B(\mathbf{x},t)|^2 \qquad (3.25)$$

where $p_0 = |F|^2$ represents the injected intensity. The backward field is obtained by propagating the transmitted field to the mirror and back, for a total distance of $z = 2d$. Given a medium of thickness L and optical density b_0, the wave equation for the forward field is (see also Eq. (2.4) for the damping-free case):

$$\frac{\partial F}{\partial z} = -\alpha_0(1-i\Delta)n(\mathbf{x},t)\frac{F}{1+s(\mathbf{x},t)}\,, \qquad (3.26)$$

where

$$\alpha_0 = \frac{b_0}{2L(1+\Delta^2)} \qquad (3.27)$$

and the internal-state dynamics of the atomic two-level system was eliminated by taking the steady-state population difference $w(\mathbf{x},t) = 1/(1+s(\mathbf{x},t))$. Note that the field dynamics is identical to the one considered in Sec. 2.1, the only difference lies in the definition of the atomic density. In the damping-free case of Chap. 2 n is obtained from the atomic phase-space distribution (obeying the Boltzmann equation (2.1)), while here it is given by the continuity equation (3.24).

The linear analysis for the system can be performed by following Sec. 2.2: the atomic density and the optical intensity are

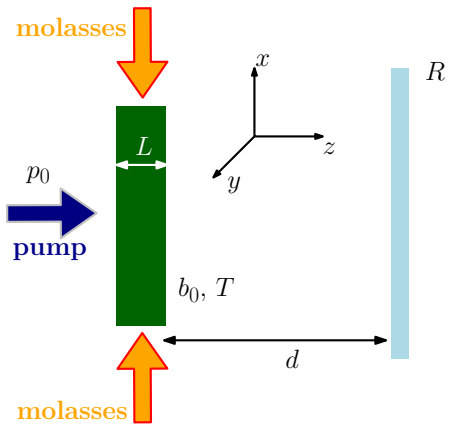

Figure 3.8: Sketch of the single-mirror 'viscous' setup. A plane wave of intensity p_0 (pump) illuminates the cloud (thickess L, optical density b_0, temperature T) from the side, is transmitted and retroreflected by the mirror (reflectivity R, distance d). Optical molasses are assumed to act on the sample during the interaction with the pump, resulting in a strong viscous damping of the atomic momenta, see Sec. 3.1.

expanded as

$$n(\mathbf{x},t) = n_0 + n_1(\mathbf{x},t) = 1 + n_1(\mathbf{x},t)$$
$$s(\mathbf{x},t) = s_0 + s_1(\mathbf{x},t) = (1+R\gamma_0)p_0 + s_1(\mathbf{x},t)$$

where $\gamma_0 = \exp\left[-2\alpha_0 L/(1+s_0)\right]$ (see Eq. (2.11)) and R is the mirror reflectivity. The transmitted field is expanded to first order in the non-homogeneous perturbations as

$$F(z=L,\mathbf{x},t) = F_0 \exp\left\{-\alpha_0 L(1-i\Delta)\frac{n(\mathbf{x},t)}{1+s(\mathbf{x},t)}\right\} \simeq$$
$$\simeq F_0 \exp\left\{-\frac{\alpha_0 L(1-i\Delta)}{1+s_0}\left[1+n_1(\mathbf{x},t)\right]\left[1-\frac{s_1(\mathbf{x},t)}{1+s_0}\right]\right\} \simeq$$
$$\simeq F_0 \exp\left\{-\frac{\alpha_0 L(1-i\Delta)}{1+s_0}\right\}\left[1-\frac{\alpha_0 L(1-i\Delta)}{1+s_0}\left(n_1(\mathbf{x},t)-\frac{s_1(\mathbf{x},t)}{1+s_0}\right)\right],$$

so that the backward field reads in Fourier space:

$$B(\mathbf{q},t) = \sqrt{R}\left\{\int F(z=L,\mathbf{x},t)\exp\left(i\mathbf{q}\cdot\mathbf{x}\right)d\mathbf{x}\right\}\exp\left(i\frac{d|\mathbf{q}|^2}{k_0}\right),$$

$\Theta = d|\mathbf{q}^2|/k_0$ being the diffractive phase slippage associated to the mode $\mathbf{q}$ in propagating for a distance $2d$. Recognising the backward field expansion $B(\mathbf{q},t) = B_0[\delta(\mathbf{q}) + b_1(\mathbf{q},t)]$ the intensity perturbation becomes

$$\begin{aligned} s_1(\mathbf{q},t) &= R\gamma_0 \left[b_1(\mathbf{q},t) + b_1^*(\mathbf{q},t)\right] = \\ &= R\gamma_0 p_0 \left[-\frac{\alpha_0 L(1-i\Delta)}{1+s_0}\left(n_1(\mathbf{q},t) - \frac{s_1(\mathbf{q},t)}{1+s_0}\right)e^{i\Theta} + c.c.\right] = \\ &= -R\gamma_0 p_0 \frac{2\alpha_0 L}{1+s_0}\left(n_1(\mathbf{q},t) - \frac{s_1(\mathbf{q},t)}{1+s_0}\right)\left[\cos\Theta + \Delta\sin\Theta\right] . \end{aligned}$$

Isolating $s_1(\mathbf{q},t)$ the following expression for the intensity perturbation is obtained:

$$s_1(\mathbf{q},t) = -\frac{\frac{2R\gamma_0 p_0}{1+s_0}\left[\cos\Theta + \Delta\sin\Theta\right]}{1 - \frac{2R\gamma_0 p_0 \alpha_0 L}{(1+s_0)^2}\left[\cos\Theta + \Delta\sin\Theta\right]} n_1(\mathbf{x},t)\,, \tag{3.28}$$

which is identical to its damping-free analogue, Eq. (2.16), upon substituting $n(\mathbf{x}) \to \int f(\mathbf{x},\mathbf{v})d\mathbf{v}$. This result can be used in linearizing the density equation (3.24): writing the perturbations in the Fourier form $n_1 \sim \exp(i\mathbf{q}\cdot\mathbf{x} + \lambda t)$, in fact, one finds

$$\begin{aligned} \lambda n_1(\mathbf{q},t) &= -\sigma D|\mathbf{q}|^2 \frac{s_1(\mathbf{q},t)}{1+s_0} - D|\mathbf{q}|^2 n_1(\mathbf{q},t) = \\ &= D|\mathbf{q}|^2\left\{\sigma\frac{K}{1-K} - 1\right\} n_1(\mathbf{q},t)\,, \end{aligned}$$

where K has been defined as (see also Eq. (2.22))

$$K = \frac{2R\gamma_0 p_0 \alpha_0 L}{(1+s_0)^2}\left[\cos\Theta + \Delta\sin\Theta\right] . \tag{3.29}$$

The dispersion relation is therefore given by

$$\lambda(\mathbf{q}) = D|\mathbf{q}|^2\left\{\sigma\frac{K}{1-K} - 1\right\}\,, \tag{3.30}$$

the threshold condition being identified by $\lambda(\mathbf{q}) = 0$:

$$1 - \sigma \frac{K}{1-K} = 0\,. \tag{3.31}$$

The threshold condition (3.31) is identical to the one found for the damping-free case, see Eq. (2.32). Hence all the considerations made in Sec. 2.2.5 apply here, and the same is true for the low saturation regime $s \ll 1$. In particular, the critical wavenumber

$$q_c = \sqrt{\frac{\pi k_0}{2d}}$$

corresponds to the maximum growth rate for purely dispersive systems; corrections due to absorption are small and will be neglected, see Sec. 2.3.3. Since the threshold condition is identical to the one obtained in the damping-free case its properties will not be discussed here, and the reader is referred to Chap. 2 for details. However, the growth rate (3.30) differs from the damping-free case, while it resembles the 'viscous' cavity case, with the $D|\mathbf{q}|^2$ term entering the growth rate but not the threshold, see Fig. (3.9b). Note that a closed expression for the growth rate λ can be derived in the single mirror case, an advantage that comes with the simpler geometry. As in the cavity 'viscous' and the single-mirror 'viscousless' cases, the instability is stationary: $\mathrm{Im}(\lambda) = 0$.

The dispersion relation (3.30) displays a feature which was already encountered in Chap. 2, namely the fact that a divergence is obtained when $K = 1$. This condition identifies the boundary in parameter space for an internal-state instability to occur, that is, a pattern-forming instability which is driven by internal-state nonlinearities. This possibility will not be discussed here (the discussion can be found in Chap. 2), but numerical results related

to internal-state driven instabilities will be discussed in the next Section.

Fig. 3.9 shows the growth rate (3.30) for blue-detuned pumps ($\Delta = 20$): as expected a transverse instability is obtained at $|\mathbf{q}| \simeq q_c = \sqrt{\pi k_0/2d}$ (absorption slightly modifies the critical wavenumber, see Sec. 2.3.3). Since the theory presented here accounts for internal-state effects, we expect the system to be asymmetric under a change in the sign of the detuning. Indeed, as shown in Fig. 3.10 the linear growth rate is smaller for $\Delta = -20$ (everything else being equal). Moreover, the threshold condition is independent on the value of the diffusion coefficient D, as already found for the cavity system (Sec. 3.1). This difference in the linear growth rate is expected because for red detuning the internal-state nonlinearity is self-defocusing, while the opto-mechanical mechanism is self-focusing. For the choice of parameters operated here the system still undergoes a self-structuring instability in the 'self-focusing' regions of the q-space, but the internal state nonlinearity competes for the instability − see Sec. 2.4.2 for a discussion of this phenomenon.

As a conclusive remark on the theoretical analysis of the 'viscous' single-mirror system,'pure' opto-mechanical instabilities due to density redistributions only are still possible. These are described by the system

$$\begin{aligned} \frac{\partial F}{\partial z} &= i\alpha_0 \Delta n \, F \\ \frac{\partial n}{\partial t} &= \sigma D \nabla \cdot [n \nabla s] + D \nabla^2 n \,, \end{aligned}$$

where as usual the approximation $\log(1+s) \simeq s$ was taken assuming low saturation, $s \ll 1$. The linear analysis is not presented for this system, as the results can be easily obtained by taking

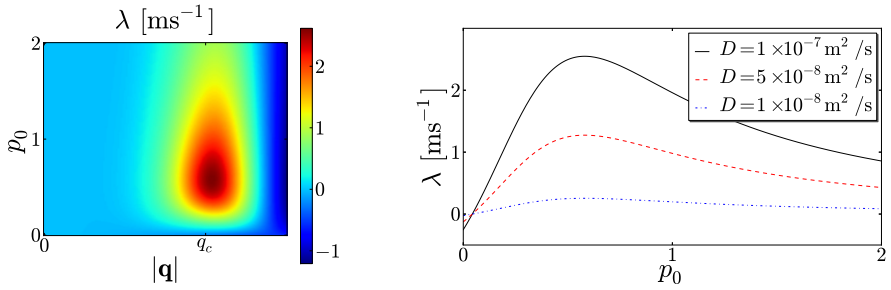

(a) (b)

Figure 3.9: On the left, the growth rate λ taken from Eq. (3.30), as a function of injected pump and transverse wavenumber with $D = 10^{-7}\,\mathrm{m}^2/\mathrm{s}$. On the right, a section at the critical wavenumber $q_c = \sqrt{\pi k_0/2d}$, showing that the threshold condition $\lambda = 0$ is unaffected by the value of the diffusion coefficient D. Other parameters are: $b_0 = 120$, $\delta = 10\Gamma$ ($\Delta = 20$), $T = 300\,\mu\mathrm{K}$, $d = 5\,\mathrm{mm}$, $L = 1\,\mathrm{cm}$.

the limit $s \ll 1$ of the results presented earlier. In particular, in the low saturation limit

$$K \simeq K' = 2Rp_0\alpha_0 L\Delta \sin\Theta$$

so that the dispersion relation and the threshold condition read:

$$\lambda'(\mathbf{q}) = D|\mathbf{q}|^2\,(\sigma K' - 1) \tag{3.32a}$$

$$1 - \sigma K' = 0 \Longrightarrow p_0^c = \frac{1}{2\sigma R\alpha_0 L\Delta} \tag{3.32b}$$

$$\sin\Theta_c = 1 \Longrightarrow |\mathbf{q}_c| \equiv q_c = \sqrt{\pi k_0/2d}\,. \tag{3.32c}$$

3.2.2 Numerical results

This Section presents the numerical results for the 'viscous' single-mirror geometry. As for the cavity case, the main advantage of the strong damping assumption consists in a reduction of the problem's dimensionality, as only two spatial coordinates + time are needed to describe the dynamics. Moreover, the single-mirror

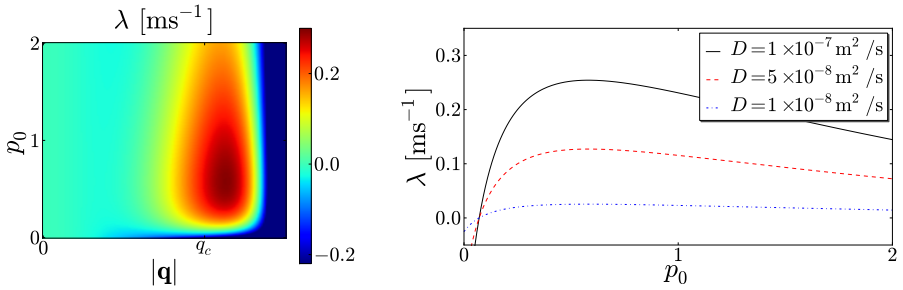

(a) (b)

Figure 3.10: Same as Fig. 3.9 but for red detuning, $\Delta = -20$. The instability is qualitatively similar, but the competition between internal-state and optomechanical nonlinearity substantially lowers the growth rate for the instability.

dynamics is made particularly attractive from the computational point of view by the fact that the light-matter interaction is completely separated from the free-space diffraction. Hence we will be able here to 'follow' the medium dynamics until a stationary state is reached without resorting to the stationary-state technique employed in Sec. 3.1.4 (see Appendix B for more details). Given the inverse atomic lifetime Γ and the diffusion coefficient D, the time and space variables are rescaled as $t \to \Gamma t$, $\mathbf{x} \to \mathbf{x}/\sqrt{D\Gamma}$, so that the medium equation becomes

$$\frac{\partial n(\mathbf{x},t)}{\partial t} = \sigma \nabla \cdot [n(\mathbf{x},t) \nabla \log(1 + s(\mathbf{x},t))] + \nabla^2 n(\mathbf{x},t)\,.$$

The field dynamics is computed by first propagating the injected field F through the cloud:

$$F_{\text{trans}} = \sqrt{p_0} \exp\left\{ -\frac{\alpha_0 L(1 - i\Delta)}{1 + |F|^2 + |B|^2} n \right\}$$

and successively obtaining the backward field as ($\mathcal{F}$ denotes the spatial Fourier transform)

$$B(\mathbf{x},t) = \sqrt{R}\mathcal{F}^{-1}\left\{ \mathcal{F}\left[F_{\text{trans}}(\mathbf{x},t) \right] e^{i\Theta} \right\} \qquad \Theta = \frac{d|\mathbf{q}|^2}{k_0}$$

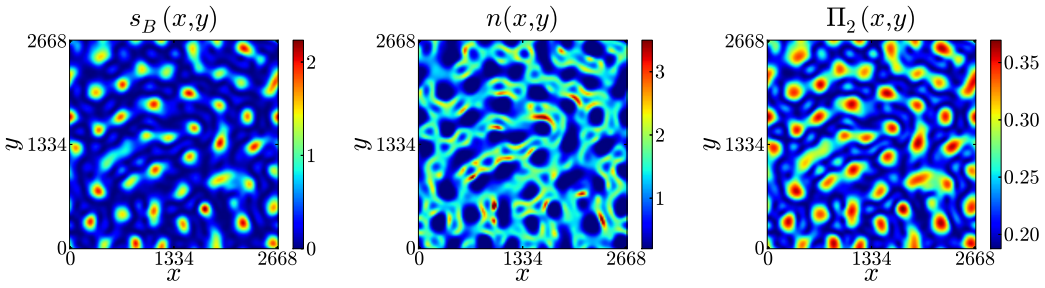

Figure 3.11: Numerical simulations for the same parameters as Fig. 3.9 (blue detuning, $\Delta = 20$), injected intensity $p_0 = 0.6$ and a final time of 2.6 ms. Spatial coordinates are rescaled so that the transverse domain accommodates 7 critical wavelengths $\Lambda_c = 2\pi/q_c$. Here $s_B = |B|^2$ denotes the intensity of the backward beam, n the atomic density and $\Pi_2 = \frac{1}{2}s/(1+s)$ the population of the excited internal state.

Defining the backward intensity as $s_B = |B|^2$ the total intensity illuminating the cloud is obtained as $s(x,y,t) = p_0 + s_B(x,y,t)$, neglecting interference effects under the assumption of a diffractively thin medium. As also stressed in Sec. 2.2, the homogeneous state requires a zero-finding routine to be evaluated. In the following the Newton-Raphson method implemented within the built-in `FindRoot` function of Mathematica [86] will be used. The low-saturation limit is obtained as usual approximating $\log(1+s) \simeq s$ and computing the transmitted field as

$$F_{\text{trans}}^{\text{low-sat}} = \sqrt{p_0}\exp\left\{i\alpha_0 L\Delta n\right\} .$$

Figs. (3.11) and (3.12) show the steady state resulting from the 'full' dynamics (including the internal state) of the system on the blue and the red sides of the resonance, respectively. As expected, atomic bunching is obtained in the minima (maxima) of the optical intensity profile. However, the internal-state steady-state population of the upper level,

$$\Pi_2 = \frac{1}{2}\frac{s}{1+s} \tag{3.33}$$

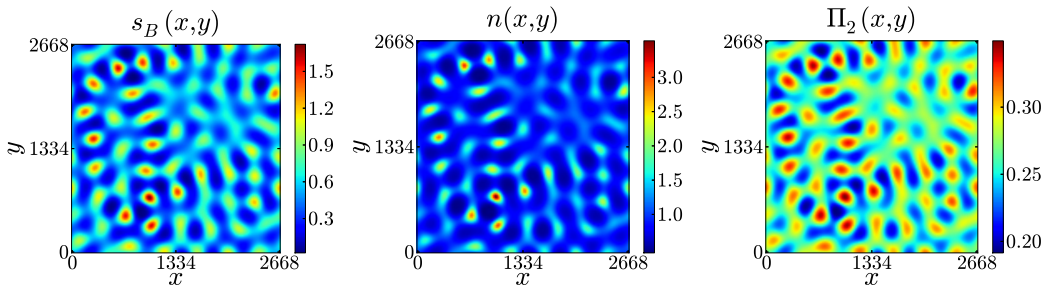

Figure 3.12: Numerical simulations for the same parameters as Fig. 3.10 (red detuning, $\Delta = -20$), injected intensity $p_0 = 0.6$ and a final time of 6.1 ms. Spatial coordinates are rescaled so that the transverse domain accomodates 7 critical wavelengths $\Lambda_c = 2\pi/q_c$. Here $s_B = |B|^2$ denotes the intensity of the backward beam, n the atomic density and $\Pi_2 = \frac{1}{2}s/(1+s)$ the population of the excited internal state.

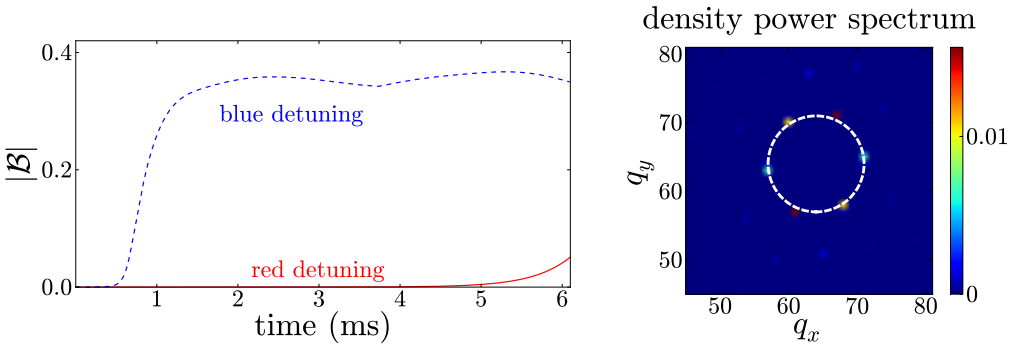

Figure 3.13: The field bunching factor $|\mathcal{B}|$ versus time for the simulations shown in Fig. 3.11 (blue detuning) and Fig. 3.12 (red detuning). As expected from our analytical results (Figs. 3.9 and 3.10), the instability is slower for red-detuned pumps. The bunching factor is calculated extracting the strongest sideband on the critical circle $|\mathbf{q}| = q_c = \sqrt{\pi k_0/2d}$, normalized to the homogeneous background at $\mathbf{q} = 0$ mode. The right panel shows the normalized far-field profile (power spectrum normalized to the background) for the blue-detuned case after 6 ms, with the $\mathbf{q} = 0$ mode removed for clarity; the white dashed circle identifies the condition $|\mathbf{q}| = q_c$.

also shows a consistent modulation. Hence the observed patterns originate from a combination of internal-state and opto-mechanical nonlinearities, as expected given the relatively high intensity ($p_0 = 0.6$); on the other hand, no internal-state-only instability is possible for the given set of parameters, since as shown in Figs. 3.9 and 3.10 there is no 'growth rate divergence'. This is confirmed by Fig. 3.13, where the field bunching factor obtained from the simulations is plotted versus time . As already found in the previous Section, the red-detuned pattern formation dynamics is considerably slower than its blue-detuned counterpart because of the 'competition' effect between internal-state and density driven nonlinearities, but it can be seen that no internal-state only instability occurs (nothing happens on the microseconds timescale). Note that the one-dimensional bunching factor introduced in Chap. 2 was generalized to the two-dimensional case simply by taking the overall largest off-axis Fourier mode rescaled to the homogeneous, $\mathbf{q} = 0$ mode. A different, slightly more elaborate definition has been used in experimental studies, see Chap. 4, but the key point is that $\mathcal{B}$ represents an order parameter for the system. Fig. 3.13 also depicts the far field profile of the steady-state intensity from Fig. 3.11, the white dashed line indicating the 'critical circle' $|\mathbf{q}| = q_c = \sqrt{\pi k_0/2d}$.

As in the viscosity-free case, internal-state-only instabilities are possible when the condition $K \geq 1$ is met in Eq. (3.30); the blue-detuned case is investigated here, in which both the internals-state and the opto-mechanical mechanisms lead to pattern formation at the same critical wavenumber. Fig. 3.14a shows the growth rate versus injected intensity for the same parameters as Fig. 3.9 but larger optical density, $b_0 = 200$, identifying a range of

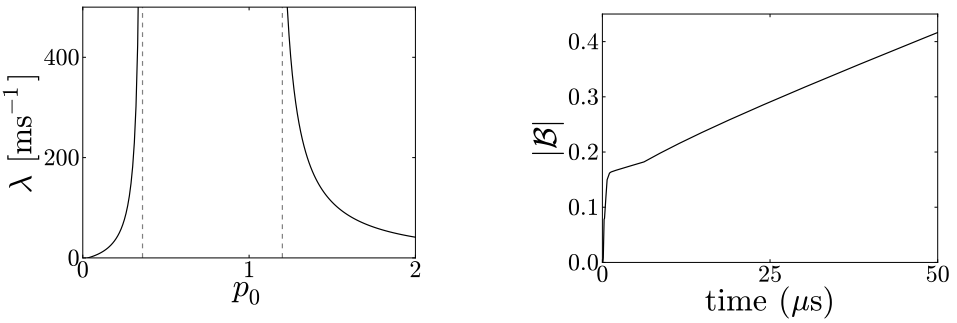

(a) (b)

Figure 3.14: Electronically-driven instability: growth rate at the critical wavenumber (left) and bunching factor evolution obtained from numerical simulations at $p_0 = 0.6$ (right, see Fig. 3.15). Parameters are: $b_0 = 200$, $\delta = 10\Gamma$ ($\Delta = 20$), $T = 300\,\mu$K, $d = 5\,$mm, $L = 1\,$cm, $D = 10^{-6}\,$m^2/s.

intensities where an internal-state instability is expected. This is confirmed by the numerical simulations, as a transition to a non-zero value of the the bunching factor $|\mathcal{B}|$ occurs already after a few microseconds, see Fg. 3.14b. Fig. 3.15 shows snapshots of the evolution after $5\,\mu$s (top row) and $50\,\mu$s (bottom row): hexagons are encoded in the internal-state population after a few μs, and the resulting optical potential causes the atoms to bunch on a longer timescale. Atomic bunching further contributes to the instability, as shown by the increase in bunching factor in Fig. 3.14b.

Numerical work also focused on the possibility of 'purely' opto-mechanical instabilities, i.e. pattern-forming processes where the only nonlinearity stems from density redistributions, see Fig. (3.16). As expected from the theoretical analysis, opto-mechanical effects lead to a self-focusing Kerr-like nonlinearity and to hexagon formation on both sides of the resonance for the light field. Correspondingly, the atomic density encodes negative hexagons (honeycombs) and positive hexagons for blue and red detuning, respectively. It is also found that red-detuned simulations are nu-

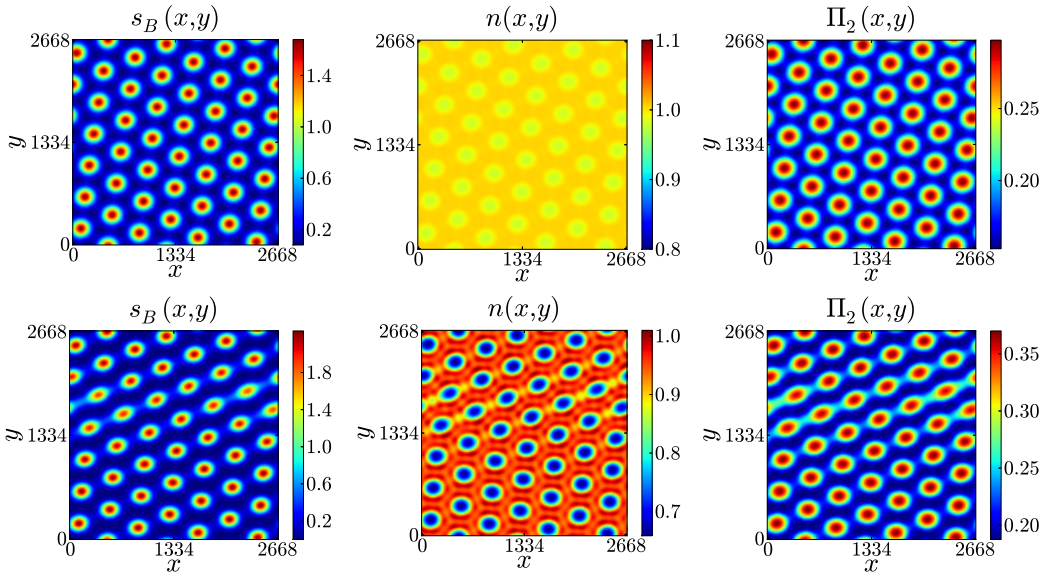

Figure 3.15: Electronically-driven instability for the same pameters as Fig. 3.14b, and for a final time of $5\,\mu$s (top row) and $50\,\mu$s (bottom row). A 'fast' instability is observed, with spatial patterns encoded in the internal-state population $\Pi_2(x, y)$, followed on a slower timescale by atomic bunching. Both processes lead to positive feedback, enhancing the modulation of the pattern and consequently the bunching factor (see Fig. 3.14b).

merically quite unstable, in the sense that no stationary state is reached, and the observed pattern depends on the time step of the simulation. On the other hand, simulations on the blue side of the resonance show high numerical stability. This is interpreted in terms of a 'super-saturation' of the opto-mechanical nonlinearity on the blue side of the resonance: as atoms are expelled from the intensity maxima, a saturation point is reached when the density is zero at some spatial point, as there are no more atoms to move. On the red-detuned side, on the other hand, atoms are attracted towards the intensity maxima and there is no limit to the peak density achievable in the model – the only constraints for $n(x, y)$ being positiveness and normalization. This can be understood in simple terms by following the work by Saffman and Wang for the counterpropagating case [92]: the 'full' (inter-

nal state+opto-mechanical) nonlinearity can be understood[1] as a saturable Kerr-like nonlinearity with a nonlinear susceptibility given by

$$\chi \sim \frac{1}{(1+s)^{1+\sigma}}\,.$$

For $\sigma = 0$ (high temperature limit) the saturable Kerr response for two-level systems is retrieved, as expected. For $\sigma > 0$ a 'super-saturating' nonlinearity is obtained, while for $\sigma < -1$ (which is typically the case in our red-detuned simulations, $|\sigma| \sim 5$) one has a nonlinear susceptibility $\chi \sim (1+s)^{|\sigma|-1}$. Non-saturating nonlinearities are known to be unstable in two-dimensional simulations. For instance, a pure Kerr medium ($\chi \sim 1+s$) is known to lead to soliton collapse (known as 'blow-up') in two dimensional systems, while it is well-behaved in one dimension [113]. The same issue is encountered in cavity simulations, for example when dealing with opto-mechanical solitons formation (Sec. 3.3).

As a closing result for this Section devoted to the numerical study of viscous single-mirror systems, hexagons to rolls transitions (already discussed in Sec. 1.2) can be observed from the simulations. Transitions from hexagonal states to rolls (or turbulent states even farther from threshold) are a common feature in systems with a cubic nonlinearity [74], and were found for instance in [82, 112] for a Kerr medium in the single-mirror feedback arrangement. Fig. 3.17 shows that the dynamics investigated in Fig. 3.15 eventually leads to roll formation, as hexagons lose stability on a timescale of a few hundreds of μs. This secondary bifurcation transforms the six-peaks far field profile corresponding to a regular hexagonal pattern (top left) into the two-peaks

[1] At least as long as the mere existence of an instability is concerned, and not the full dynamics of the system.

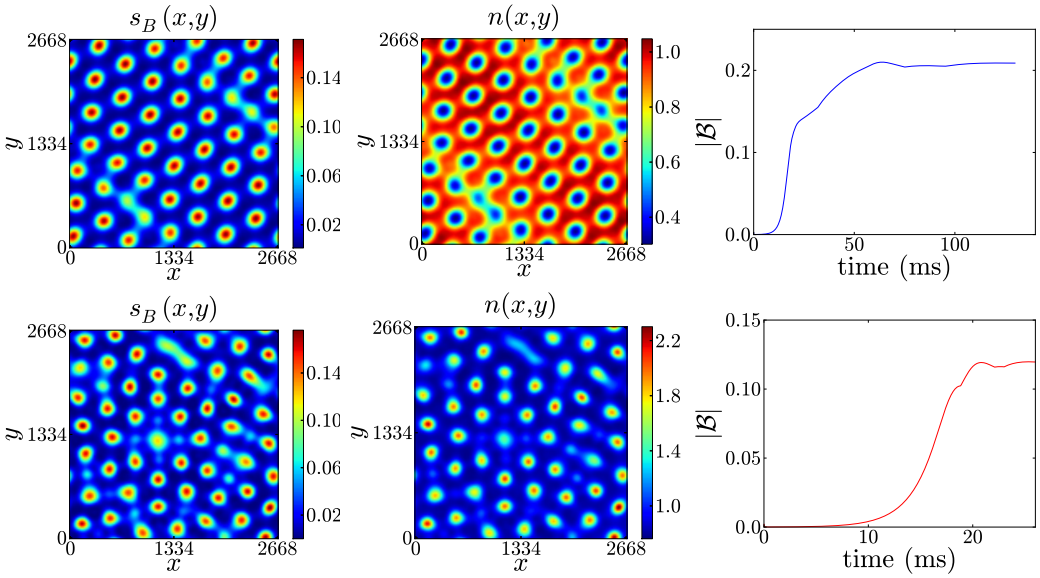

Figure 3.16: Purely opto-mechanical instability obtained at $p_0 = 0.04$ for blue detuning ($\Delta = 20$, top row) and red detuning ($\Delta = -20$, bottom row). Other parameters are: $b_0 = 120$, $T = 300\,\mu$K, $d = 5\,$mm, $L = 1\,$cm, $D = 10^{-6}\,\mathrm{m}^2/\mathrm{s}$. The pattern is found to be numerically unstable on the red side of the resonance, because there is no limit in our model to the peak density achievable. On the other hand, the expulsion of atoms from the high-intensity regions for blue detuning lead to a high saturation and the pattern is observed to be stable for very long times.

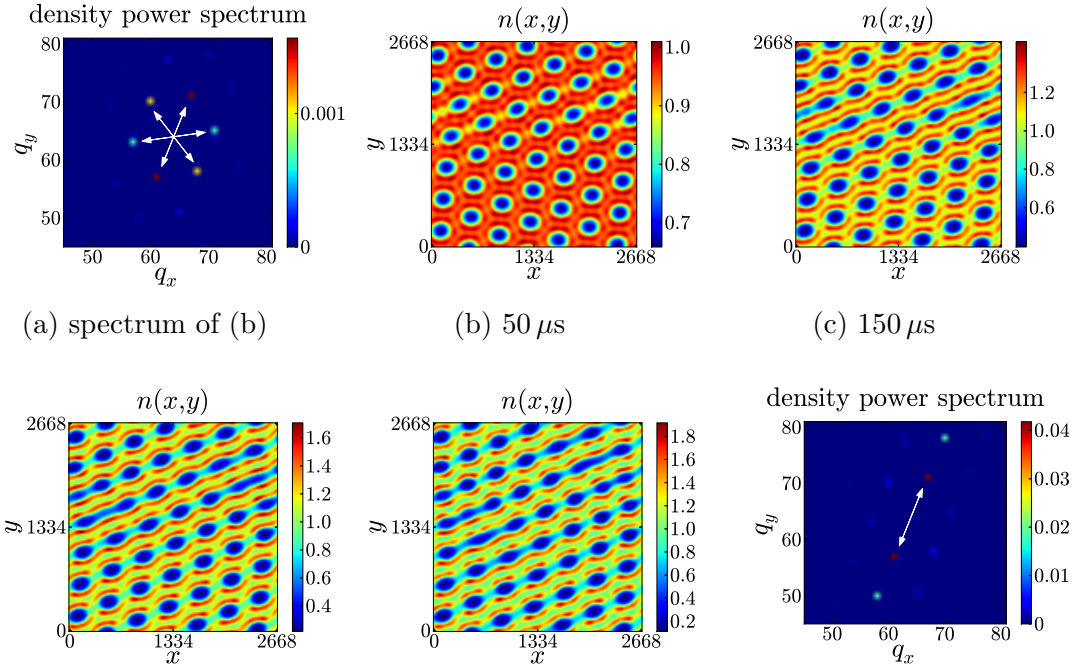

(a) spectrum of (b) (b) 50 μs (c) 150 μs

(d) 300 μs (e) 450 μs (f) spectrum of (e)

Figure 3.17: Hexagons to rolls transition, for the same parameters as Fig. 3.15. Six off-sidebands are observed in the spectrum after 50 μs (a), but hexagons lose stability against rolls and after 450 μs two off-axis peaks dominate the far-field profile (f).

profile corresponding to a roll pattern (bottom right). It should be emphasized that spontaneous symmetry breaking is observed in correspondence with hexagon formation, but the hexagonal pattern selects the symmetry of the roll pattern eventually observed: note how the strongest Fourier peaks of the hexagonal far field profile 'survive' the bifurcation and select the orientation of the roll pattern.

3.3 Opto-mechanical cavity solitons

This Section discusses the possibility of implementing opto-mechanical cavity solitons, i.e. bistable, nonlinearity-sustained localized light-matter structures. The term 'opto-mechanical' refers to the fact that the localized structure is not encoded in the internal-state properties or the excitation of a Kerr-like medium, but in the spatial distribution of the atomic density.
To demonstrate this possibility, consider the 'low saturation' cavity model of linear single-atom response introduced in Sec. 3.1.3:

$$\frac{\partial E}{\partial t'} = -(1+i\theta)E + A_{\rm in} - iC\Delta nE + i\nabla'^2 E \tag{3.34a}$$

$$\frac{\partial n}{\partial t'} = \sigma\bar{D}\nabla' \cdot \left[n\nabla'|E|^2\right] + \bar{D}\nabla'^2 E \tag{3.34b}$$

In Sec. 3.1 it was shown that the homogeneous solution given by

$$n_0 = 1$$
$$E_0 = \frac{A_{\rm in}}{1+i\hat{\theta}} \qquad \hat{\theta} = \theta + C\Delta$$

is unstable to transverse perturbations when the intracavity intensity $s_0 = |E_0|^2$ exceeds the critical value $s_0^c = (C\sigma\Delta)^{-1}$, see Eq. (3.20). Close to the critical point, hexagons are selected, see Sec. 3.1.4.

The focus of this Section consists in determining whether the emerging patterns can coexist with the homogeneous solution. If this is possible, in fact, localized 'domains' are possible, essentially given by portions of a full periodic pattern sitting on the homogeneous background. Since pattern formation is an out-of-equilibrium process occurring in driven-dissipative systems, a single localized 'spot' is termed a *dissipative soliton*. The term 'dissi-

pative' emphasizes the difference with what is commonly termed a soliton, i.e. a solitary-wave solution solution of an integrable, nonlinear system [114].

Dissipative solitons have the fundamental property of being bistable, i.e. they can be switched on and off 'at will' by means of appropriate control beams. This property fundamentally differentiates opto-mechanical soliton formation from atomic lithography [115], as here one is allowed to optically 'write' and 'erase' a given density structure which remains unaffected after the control beams have been turned off, sustained just by a homogeneous pump.

This opens up new opportunities for the shaping and control of potentially complex and reconfigurable atomic density distributions, which only need homogeneous driving to sustain after they have formed. Suppose in fact that a region of high density is created in the atomic cloud during the interaction with the pump beam. This could be achieved for instance by using additional control beams, completely incoherent with the pump. The 'slow' timescale for this process is essentially dictated by the time for atomic motion, $\tau_{\rm ext} \sim 10\,\mu$s (to move by $\sim 1\,\mu$m at $T \sim 100\,\mu$K). Light from a red-detuned (and spatially homogeneous) pump beam would then be guided towards high density regions, effectively creating a bright light spot. The 'fast' timescale for this process will be determined by the cavity lifetime, $\kappa^{-1} \ll \tau_{\rm ext}$. If localized states are stable for the system (i.e. if bistability is obtained for the 'homogeneous' and 'patterned' solutions), such a localized spot of light can sustain itself via nonlinear dipole forces. Analogously, one could create a 'hole' in the atomic cloud (on the timescale of $\tau_{\rm ext}$), which in turn would attract blue-detuned light from the spatially homogeneous pump

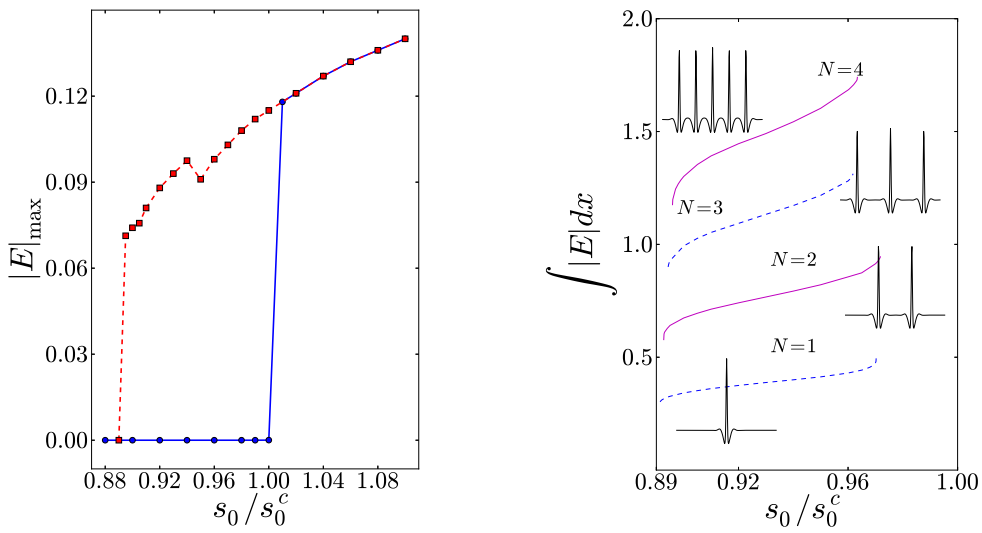

(a) (b)

Figure 3.18: On the left, subcritical bifurcation for $C|\Delta| = 4.5$, $\theta = -3.7$, $\sigma = 25$. On the right, the 'snaking' diagram showing one-dimensional intensity profiles corresponding to $N = 1, 2, 3, 4$ peaks.

(on the timescale of κ^{-1}). Such a bright localized spot of light can then sustain itself by expelling atoms from the high intensity region, again by means of dipole forces. In both cases, self-localized structures are eventually sustained just by a homogeneous driving. Additional beams can then be used to erase any given density structure present in the cloud, thus removing the entire light-matter structure.

Fig. (3.18) shows the bifurcation diagram obtained from one-dimensional simulations of the system (3.34), varying the intracavity intensity across the critical point. Note that (as in Sec. 3.1.4) all these data are related to the stationary solution of the system, as its dynamical properties are not of interest here. These simulations were performed using a split-step Fourier technique, as described in Appendix C. The domain size is set to contain seven critical wavelengths $\Lambda_c' = 2\pi/q_c'$. Fig. (3.18a) shows that the bifurcation leading to pattern formation is *subcritical*,

i.e. there is a range of intensities where both the homogeneous and the non-homogeneous solutions are stable, $0.9 < s_0/s_0^c < 1$. Increasing the pump from below threshold, in fact, a pattern appears on the whole domain at the critical point (blue circles). The 'order parameter' is here simply obtained by measuring the maximum value of the intracavity amplitude, $|E|_{\max}$. Approaching the critical point from above the 'patterned' solution survives below threshold, the system showing a hysteretic behaviour (red squares). Fig. (3.18b) presents in more detail the behaviour of the system below threshold: the upper branch of Fig. (3.18a), in fact, does not correspond necessarily to a full periodic pattern (seven periods in our simulations). A 'snaking' bifurcation diagram is obtained where N peaks are stable below threshold, and where one can switch between 'even' branches ($N = 2, 4, \ldots$, red full lines) , or 'odd' branches ($N = 1, 3, \ldots$, blue dashed lines). The stability of these branches is studied simply by imposing an initial condition which is 'close' to the stationary state, and simulating the field equation until the solution is stationary. We remark that the stable branches are connected by unstable branches, which are not studied here, as the technique used is not able to determine unstable solutions. A detailed analysis of the snaking bifurcation for a saturable absorber in a driven cavity, including the unstable branches, can be found in [111, 116]. In general, the qualitative features of cavity solitons for the case of Kerr, or Kerr-like, nonlinearities can be recovered here, as the optomechanical mechanism essentially results in a Kerr-like nonlinearity. This was made explicit in the works by M. Saffman and collaborators [92], where the stationary state for the density was approximated as

$$n_{\mathrm{eq}}(x) = \mathcal{N} \exp\left(-\sigma |E(x)|^2\right) \simeq \mathcal{N}\left(1 - \sigma |E(x)|^2\right) .$$

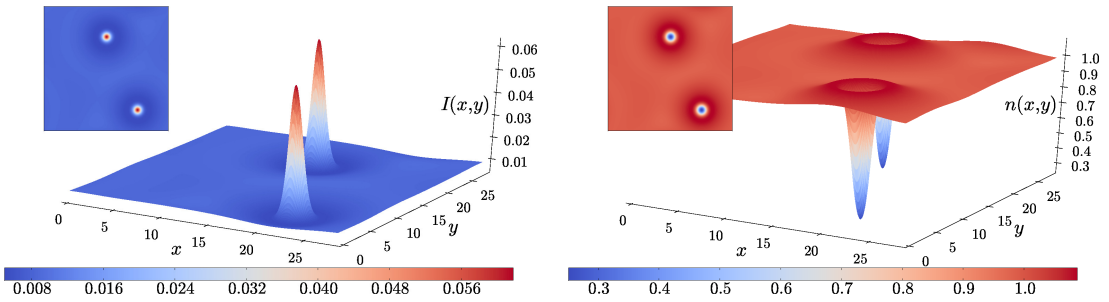

(a) blue detuning

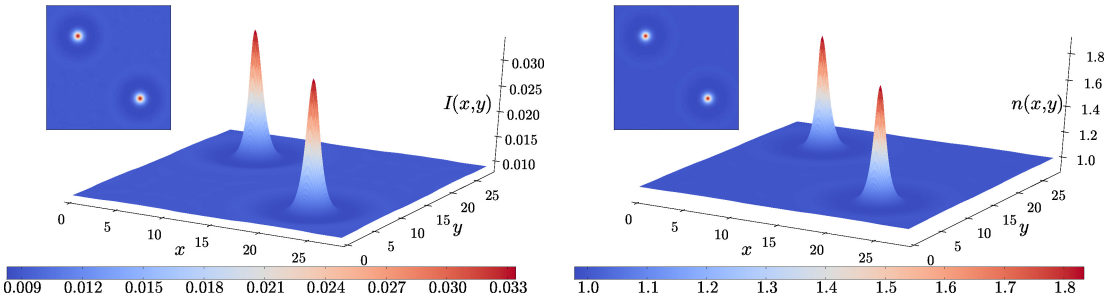

(b) red detuning

Figure 3.19: Opto-mechanical cavity solitons for blue (top panel) and red (bottom panel) detuning. Parameters are: $C|\Delta| = 4.5$, $\theta = -3.7$, $\sigma = 25$, $s_0/s_0^c = 0.93$.

However it is important to note that, in general, $n_{\rm eq}$ contains a dependence on the intensity $|E(x)|^2$ also through the normalization $\mathcal{N}$.

Fig. (3.19) shows the stationary state obtained from two-dimensional simulations of the system (3.34). Again, we start our simulations with initial conditions which are 'close' to the stationary state, and in particular with Gaussian profiles for the light intensity (and corresponding profiles for the density), the height and width of these Gaussian profiles being tailored from the stationary solution above threshold (that is, 'cutting' a soliton from a full pattern).

An important feature of the states depicted in Fig. (3.19) is the fact that multiple solitons can coexist independently – differ-

ent realizations are shown for blue and red detuning. Moreover, using a broader pump beam it is possible to excite localized domains, i.e. multi-peaked cavity solitons sitting on the homogeneous background (see Ref. [116] for the saturable absorber equivalent). The parameters used in Fig. (3.19) are within experimental reach (e.g. in cold Rb gases), as they correspond to an optical density $b_0 = 180$, a detuning of $\delta = \pm 10\Gamma$ and a temperature of $T = 60\,\mu$K. For a cavity length of $\mathcal{L} = 1\,$mm and transmittivity $\mathcal{T} = 0.1$, the pattern size is in the $0.5\,$mm range, which is well within the size of modern setups.

3.4 A sync perspective: Kuramoto model with damping and noise

In this Section a simple theoretical argument is presented, showing that the 'viscous' single-mirror self-structuring process analyzed in Section 3.2 can be reinterpreted as a synchronization transition governed by the Kuramoto model. The Kuramoto model was already found in Sec. 2.6 for the damping-free single-mirror system, where the threshold condition originates from the initial spread in the oscillators natural frequencies (i.e. the atomic initial velocities). Here it is found that, as in Sec. 3.2, the threshold is set by the strength of stochastic fluctuations, $D \sim T$. All the analysis presented in the following is concerned with the low saturation regime, that is, the word 'atoms' is used to describe any form of linearly polarizable particle. Moreover, the analysis is restricted to the one-dimensional case for simplicity. Results from Sec. 3.2 can be easily adapted in the low-saturation regime following the definitions given in Sec. 2.3 and 3.1.3. Essentially, these results extend previous work in CARL system [32, 96], where it

was already shown that CARL realizes a Kuramoto transition in the viscous regime.

The Kuramoto model is defined in the thermodynamic limit of infinitely many oscillators, $N \to \infty$, initially distributed in frequency according to some normalized function $g(\omega)$. Eq. (2.47) then becomes a continuity equation for the oscillators density $\varrho = \varrho(\theta, \omega, t)$:

$$\frac{\partial \varrho}{\partial t} = -\frac{\partial}{\partial \theta} \left\{ \varrho \left[\omega + Kr \sin(\psi - \theta) \right] \right\} + D \frac{\partial^2 \varrho}{\partial \theta^2} , \tag{3.35}$$

where the order parameter is now defined by

$$r = \int_{-\pi}^{+\pi} e^{i(\theta - \psi)} \int_{-\infty}^{+\infty} \varrho(\theta, \omega, t) g(\omega) d\omega d\theta .$$

It is easy to recognize that the form of Eq. (3.35) is formally identical to Fokker-Planck equation derived in the 'viscous' analysis, Sec. 3.1, provided that $g(\omega) = \delta(\omega)$. In this case in fact Eq. (3.35) becomes

$$\frac{\partial \varrho}{\partial t} = -K \frac{\partial}{\partial \theta} \left[\varrho \, r \sin(\psi - \theta) \right] + D \frac{\partial^2 \varrho}{\partial \theta^2} . \tag{3.36}$$

As in Sec. 2.6, assuming the critical wavenumber q to be the only mode excited in the system (i.e. working close to the critical point) a one-to-one correspondence will be found between the Kuramoto model (3.36) and Eq. (3.7). The condition $g(\omega) = \delta(\omega)$ was indeed the leading idea in the 'viscous' theory discussed in Sec. 3.1, where it was assumed that the molasses damping action is strong enough to eliminate the atomic velocities from the analysis. This essentially describes an 'overdamped' system where $\dot{v}_j = 0 \, \forall j$ and the atoms move adiabatically, continuously damped in their motion by the molasses action.

Approximating $\nabla s/(1 + s) \sim \partial s/\partial x$ and using Eq. (2.50), the

Fokker-Planck equation for the atomic density, Eq. (3.4) reads

$$\frac{\partial n(x,t)}{\partial t} = -\frac{\hbar\delta}{2}\frac{2Rp_0\chi_0 q}{\gamma}\frac{\partial}{\partial x}\left[n\, r\sin(\psi - qx)\right] + D\frac{\partial^2 n}{\partial x^2}\,.$$

In terms of the phase $\theta = qx$, the last equation is rewritten as

$$\frac{\partial n(\theta,t)}{\partial t} = -2Rp_0\sigma\chi_0 Dq^2\frac{\partial}{\partial\theta}\left[n\, r\sin(\psi - \theta)\right] + Dq^2\frac{\partial^2 n}{\partial\theta^2}\,, \quad (3.37)$$

which is formally identical to Eq. (3.36) upon identifying $n \to \varrho$, $Dq^2 \to D$, and $2Rp_0\sigma\chi_0 Dq^2 \to K$. The fact that Dq^2 appears in both terms of this equation again captures the fact that the threshold does not depend on the diffusion coefficient. Retrieving in fact the threshold for the Kuramoto model (3.37) [94],

$$K_c = 2Dq^2\,,$$

we immediately find the critical value of the pump intensity as

$$p_0^c = \frac{1}{R\sigma\chi_0}\,, \quad (3.38)$$

which was already found in Eq. (2.37). Eq. (2.37) was found in the context of the damping-free theory (Chap. 2), but as discussed in Sec. 3.2 the threshold condition is identical in the viscous and viscosity-free regimes, and therefore (3.38) is found to be the power threshold for the viscous single-mirror system in the low-saturation regime.

Chapter 4

Experimental considerations, open problems

In this final Chapter some details related to the experimental realization of single-mirror viscousless instabilities are discussed, as well as some questions left open by the previous Chapters. The experimental results are reported in Ref. [83].

4.1 Experimental observations of self-structuring

The theoretical work presented in Chap. 2 has been confirmed in a series of experiments carried on by G. Labeyrie at the Institut Non Linéaire de Nice. This led to the joint work by the INLN (G. Labeyrie, R. Kaiser) and the Strathclyde groups, published on the arXiv [83] and submitted (at the time of writing) to Nature Photonics. Indeed, the experimental observation of hexagonal pattern formation in the absence of damping was one of the main motivations to the study of viscosity-free setups, as the theoretical work focused on the 'damped' case of Chap. 3 before the realization of the experiment.

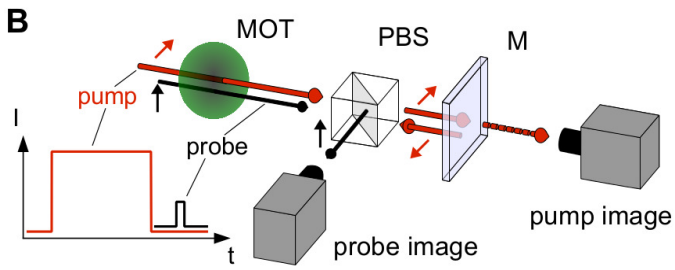

Figure 4.1: Sketch of the experimental setup (from Ref. [83]).

A schematic representation of the experimental setup is shown in Fig. 4.1: a pump beam illuminates a ^{87}Rb cloud released from the MOT, with a typical optical density of $b_0 = 120$ and a temperature $T = 290\,\mu$K. The cloud is $\sim 1\,$cm thick, and the mirror is placed at a distance d of a few mm from the cloud. The effective mirror distance can be tuned by means of a telescopic system placed between the cloud and the actual mirror – this way, also negative distances (with the mirror before the cloud) can be implemented. After the 'pump' beam is turned off, a weak 'probe' pulse illuminates the cloud. This probe is orthogonally polarized with respect to the pump, so that is selected by the polarizing beam splitter (PBS) and monitored through a CCD camera ('probe image'). The pump field instead is fed back on the medium by the mirror, with the transmitted component monitored by a second CCD camera ('pump image'). The idea behind this pump/probe experiment is to investigate (via the probe) modulations in the cloud's refractive index after the interaction with the pump. Refractive index modulations can be due to opto-mechanical redistribution effects (the main object of the investigation), but also due to internal-state effects. The internal-state dynamics of the two levels forming the D_2 line were under investigation, but care must be taken in ensuring that other internal states play little or no role in the refractive index modulations. For instance, as a 'repumper' beam is used to re-populate

the D_2 lower level, spatial structures in the Zeeman levels of the atoms may be important; the reader is referred to Ref. [83] for a more detailed discussion of these aspects.

Fig. 4.2a shows the experimental patterns resulting from a self-structuring transition for a blue-detuned pump, detected by a red-detuned probe. Since the density profile is clearly not accessible directly, in fact, the probe is used to monitor the refractive index profile of the cloud (i.e. the density, assuming there are no other gratings). Due to propagation, the detuning of the probe is important: a blue-detuned probe would result in hexagons instead of honeycombs (and resonant imaging is not an option due to the high optical density). Red-detuned probe beams are chosen in order to emphasize the complementarity of light-matter structures. The main idea is that the probe beam profile represents the atomic density, so that Fig. 4.2a is the experimental counterpart of the two-dimensional profiles shown in Chap. 3 (although for a 'viscousless' setup). To prove this, however, it must be ensured that no other 'internal-state' grating contribute to the refractive index modulation. As discussed in the previous Chapters, the main instrument to discriminate density redistribution effects from internal state ones is the relatively slow timescale of atomic motion. This instrument comes with a dark side too, as slow internal-state processes (such as Zeeman transitions) might potentially lead to a misinterpretation of the results. Making sure that no other 'slow' grating can form in the cloud, a dynamics on the timescale of tens-hundreds of μs would be a clear signature of atomic motion, while a 'fast' dynamics (few μs) would imply an internal-state instability. A first experimental corroboration that what is observed is indeed a density driven self-structuring process can be obtained from Fig. 4.2b, where the decay of the

patten 'contrast' is measured after switching the pump beam off (i.e. increasing the delay between the pump and the probe beams). The contrast is obtained by averaging the intensity of the far-field profile along 'circles' of increasing radius q, until at the critical wavenumber this quantity shows a peak. The contrast is given by this peak value divided by the homogeneous background (see Ref. [83] for details), and is therefore closely connected to what was termed *bunching factor* in the previous Chapters (maximum value on the critical circle rescaled to the background). Beside the exact definition, the key point is that the contrast represents an order parameter for the system: as the pump is switched off, the pattern decays with a timescale of $\sim 80\,\mu$s (as also shown by the insets). This slow timescale is a clear indication that the refractive index modulation is due to a modulation in the atomic density, and not in the internal state properties of the medium.
The decay of the pattern shows that atomic motion is responsible for the refractive index modulation observed by the probe beam, but it is not enough to state that an opto-mechanical, self-structuring instability occurred. As discussed in the previous Chapters, in fact, internal-state instabilities may trigger the self-organization process, so that after the pump beam is switched off a density modulation may be observed as a result of what we termed an electronically-driven instability. One of the main aims of the experiment is to observe processes as close as possible to the 'pure' opto-mechanical instability discussed in Sec. 2.3. This in turns requires low saturation levels, so that decreasing the pump power we can investigate different regimes for the instability. As Fig. 4.3 shows, decreasing the injected intensity no instability is observed before atomic motion can take place (the pump contrast is zero for curve 3 and 4 at short times). At high injected intensi-

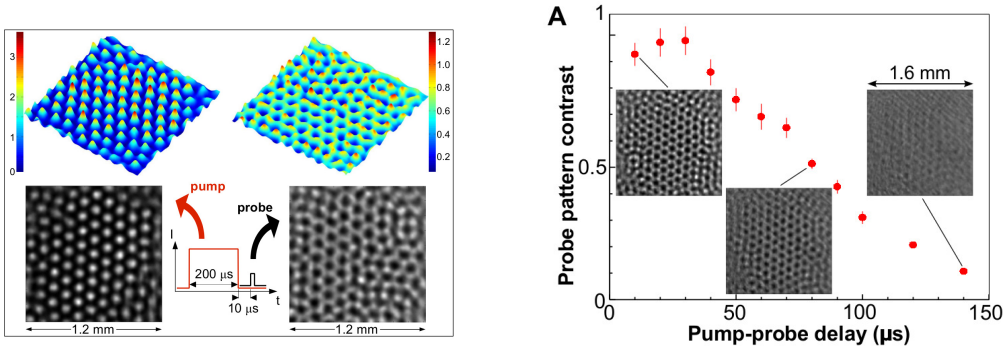

(a) (b)

Figure 4.2: On the left, experimental patterns obtained with a 200 μs pump pulse detuned by $\delta = 7\Gamma$ from the D_2 line transition, illuminating a cloud of optical thickness $b_0 = 120$ and temperature $= 290\,\mu$K. The mirror distance is $d = 5\,$mm, the cloud thickness $L = 1\,$cm. On the right, the slow decay of the pattern (with the pump off) is a signature of atomic motion. Figure taken from Ref. [83].

ties, on the other hand, an internal-state instabilities is observed, with a non-zero contrast already after a few μs. Shining a probe beam after a dark time of 10 μs, it can be seen that no structures are observed on a fast timescale, because all the internal-state gratings are washed out in a few μs. On the other hand, the opto-mechanical structures encoded in the atomic density are unaffected by this dark time. Curve 4 in Fig. 4.3 represents (to our knowledge) the closest realization of a self-structuring, symmetry breaking transition due entirely to density redistribution effects.

4.2 Wavenumber selection

An important difference between the experimental setup and the theoretical system considered in the previous Chapters is that the medium cannot be considered diffractively thin; moreover, the formation of a standing wave within the cloud is also a qualitative

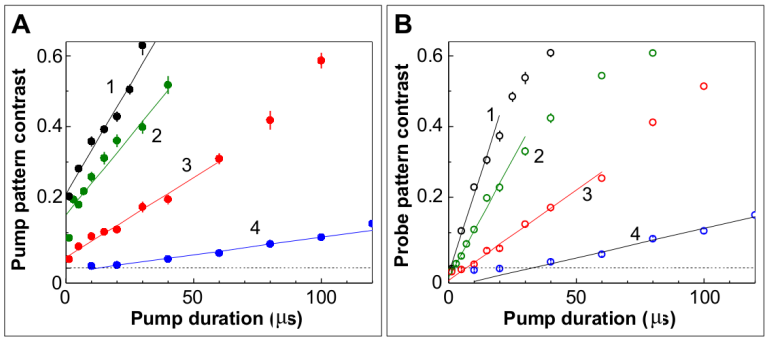

Figure 4.3: Experimentally observed dynamics of the contrast for the pump (A) and the probe (B) beams, for a pump-probe delay of 10 μs and pump intensities of = 636 mW/cm2 (curve 1), $I = 404\,\mathrm{mW/cm^2}$ (curve 2), $I = 217\,\mathrm{mW/cm^2}$ (curve 3), and $I = 91\,\mathrm{mW/cm^2}$ (curve 4) . The long timescale associated with curves 3 and 4 identifies the corresponding pattern-forming dynamics as mainly due to opto-mechanical effects. Figure taken from Ref. [83].

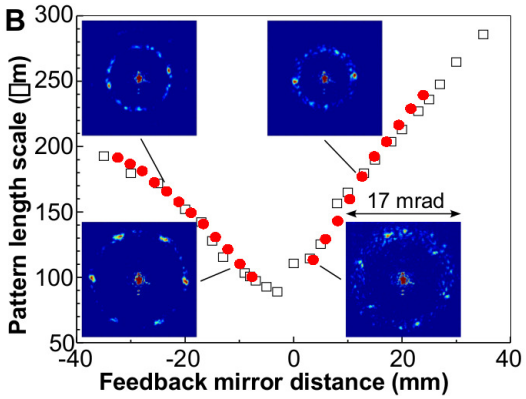

Figure 4.4: Experimental (circles) and theoretical (squares) values for the pattern length scale (in μm) as a function of the mirror distance. The theoretical values are obtained from a model consisting of a thick Kerr slab with feedback mirror (from Ref. [83]).

difference between the model (which assumes no longitudinal dependence of the field) and the experiment. The role of the medium thickness has been partially addressed in Ref. [83], by studying a thick Kerr slab with single-mirror feedback. This system extends previous studies of counterpropagating instabilities in thick Kerr media [117], accounting for the different boundary conditions due to the mirror. A remarkable improvement with respect to the thin-medium theory is found looking at the spatial scale of the emerging patterns. The lowest unstable wavenumber obtained from the thin-medium theory is in fact in qualitative agreement with the observed values, but adding the medium thickness the agreement is excellent, see Fig. 4.4.

Such thick-slab theory is also a promising candidate to solve an open problem connected to our thin-medium theoretical model: as the threshold intensity depends on the wavenumber q only via the trigonometric expressions $\sin\Theta$ (dispersion) and $\cos\Theta$ (absorption), the minimum threshold of each 'balloon' is identical, see Fig. 4.5. This is exactly the kind of situation envisaged by McDonald and coworkers [20, 19] in proposing fractal optical pattern formation: as many (in principle infinitely many) spatial scales enter the system at threshold, the resulting pattern is expected to display fractal, scaleless features. As discussed in the next Section this is indeed observed in our numerical simulations, and a low-pass filter is always employed to cut out the higher balloons (see Appendix C), which might appear to be arbitrary but is observed experimentally. Hence the opto-mechanical nonlinearity investigated in the previous Chapter for thin media realizes the 'degenerate' situation of Ref. [20, 19], with many balloons becoming unstable at the same threshold value. Whether this can be observed experimentally in thin media is an open problem:

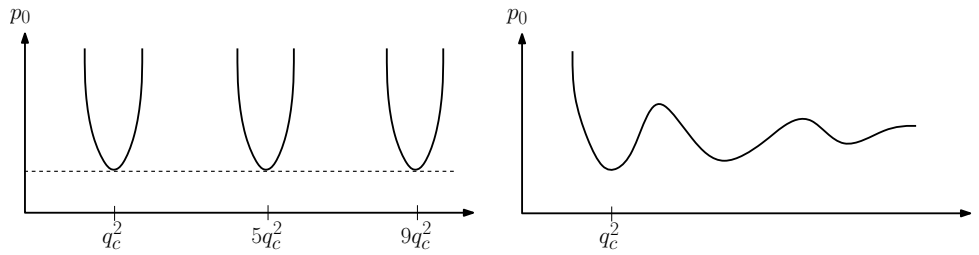

Figure 4.5: On the left, 'degeneracy' of the thin-medium single-mirror system: all the instability balloons have the same threshold in correspondence with the critical values $q_n^2 = (4n+1)q_c^2$, $n = 0, 1, 2, \ldots$. On the right, sketch of the threshold curve for a thick Kerr slab with mirror feedback: a global minimum can be identified, corresponding to the spatial scale of the emerging pattern.

opto-mechanical instabilities in cold atoms (or soft-matter systems) appear to be a viable option for the observation of such phenomenon. Since no fractal structures are observed in thick-medium experiments, however, we conclude that something is missing in the thin-medium theory which has the ability to select the critical wavenumber. In the thick-slab theory, on the other hand, the threshold is a continuous, undulating function of the wavenumber q, and depending on the values of the parameters a global minimum for the threshold can be obtained for some q. Hence the medium thickness is found to modify only 'at higher orders' the quantitative predictions for the pattern scale (see Fig. 4.4), but seems to offer a qualitatively new explanation for the problem of wavenumber selection.

4.2.1 Fractal pattern formation

In the previous Section the problem of wavenumber 'degeneracy' in single-mirror setups was discussed. Assuming to be in the low-saturation limit (without absorption), as the wavenumber q enters the linear properties of the system only through the trigonometric expressions $\sin\Theta$ all the wavenumbers satisfying $\Theta = \pi/2$ have minimum threshold. This yields the family of critical wavenum-

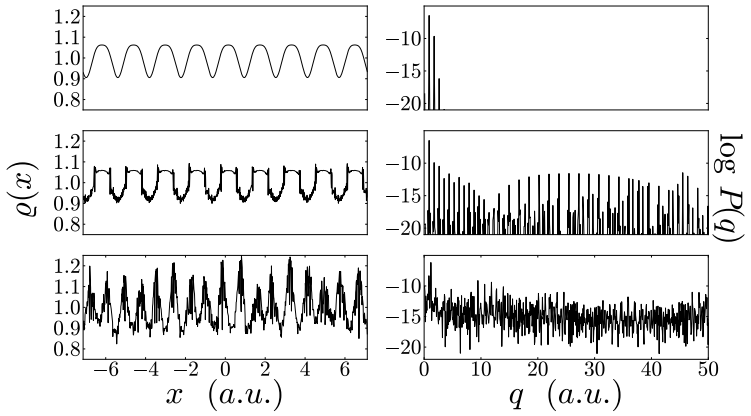

(a)

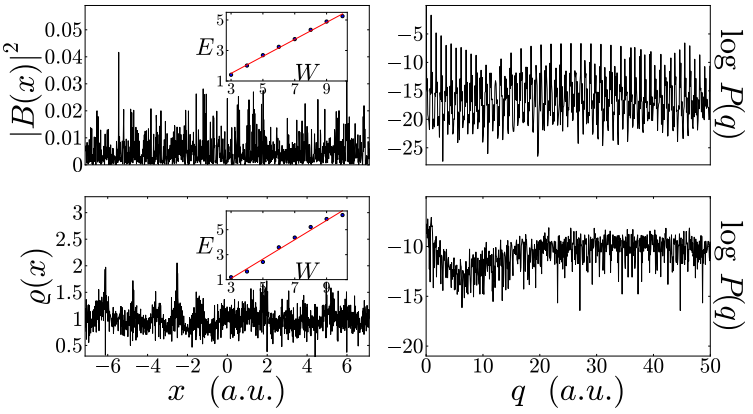

(b)

Figure 4.6: Numerical results from 1D simulations, with real-space distributions on the left and the corresponding spectra on the right. The upper panel (a) shows the evolution of the density distribution starting the dynamics with a low-pass spatial filter acting on the field. The stationary state obtained with the filter is depicted in the first row. The filter is subsequently removed and the density distribution is monitored after 0.01τ (second row) and 0.05τ (third row). The lower panel (b) shows the backward intensity (first row) and the density (second row) after τ, starting the dynamics without the filter. The insets show the evaluation of the Hurst exponent H, see text. Dots are numerical data, lines are first-order least-square fits: we find $H \simeq 0.55$ and $H \simeq 0.77$ for the intensity and density profiles, respectively ($R^2 > 0.98$). The driving intensity is 5% above threshold.

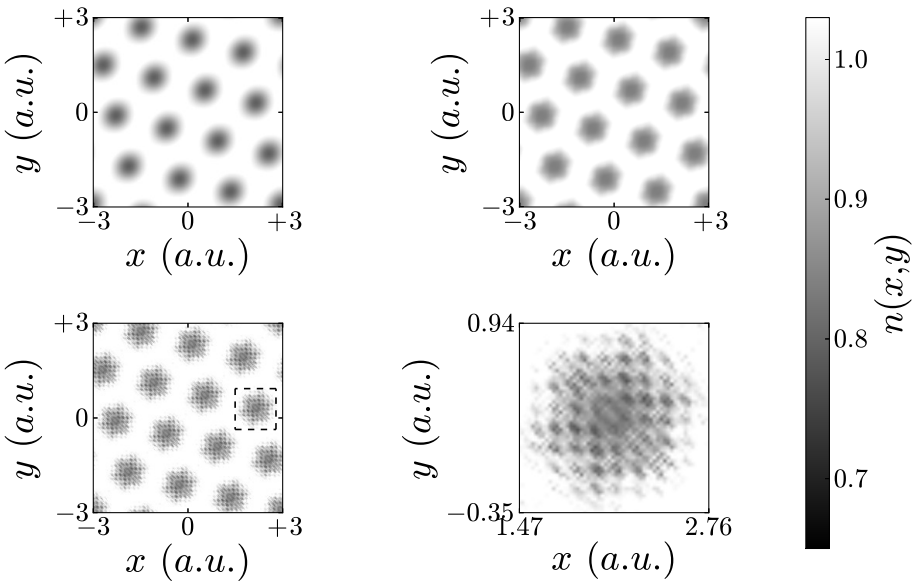

Figure 4.7: Real-space density distribution evolving in time for a system driven 5% above threshold. The stationary state obtained with the filter is shown in the upper left panel, followed by the states reached, with the filter removed, after 0.02τ (upper right) and 0.04τ (lower left). The evidenced region the lower left panel is magnified to show self-similarity (lower right).

bers

$$q_n^2 = (4n+1)q_c^2 \qquad n = 0, 1, 2, \ldots$$

where $q_c = q_0 = \sqrt{\pi k_0/2d}$, as derived in Chap. 2 and Sec. 3.2. The experimental results suggest that a wavenumber selection is actually operated by the system, which selects q_c as the most unstable wavenumber. Theoretical analysis of a thick Kerr medium indicates that the medium thickness might be the responsible for this selection, but it remains an open question whether multiple scales can be experimentally observed in thin media.

The works by McDonald and coworkers investigated the possibility of implementing 'fractal' patterns in Kerr media [20], both in multimode cavities and single-mirror setups [19]. The main idea underlying these works is to exploit the 'internal-state' Kerr non-

linearity to encode a self-similar, scaleless structure in the Kerr excitation, and complementary in a fractal profile for the optical field. The wavenumber degeneracy, however, is obtained only if the diffusion of the carriers is neglected [19]. Opto-mechanical instabilities, on the other hand, 'naturally' support fractal pattern formation, with self-similar structures encoded in the density of the medium. As usual, since this feature can be obtained for any kind of linear dielectric particles, the considerations made here are not limited to cold atoms but might be applied to any soft-matter context. To emphasize the generality of the results presented below the notation is slightly changed with respect to the rest of the thesis, and the density is denoted by $\varrho(x)$ instead of $n(x)$ (which is intended for cold-atom results). Also, writing the diffusion constant as $D = \tau^{-1} l_D^2$ the time and space coordinates can be rescaled to τ and l_D, these value being defined by the specific physical system under analysis.

All the numerical simulations shown so far use a spatial filter to cut all the spatial frequencies $q^2 > 3q_c^2$, so that only the first instability balloon is selected. Removing the filter, however, single-mode patterns evolve first in multi-mode structures, and eventually in scaleless, fractal profiles. Fig. (4.6a) shows a one-dimensional example of this kind of dynamics for the viscous single-mirror case (see Sec. 3.2). The power spectrum $P(q)$ of the density is used to monitor the emergence of multiple modes.
In order to classify these structures as fractals, one needs to evaluate some form of fractal dimension. Many definitions of such a dimension exists [118], and the so-called rescaled range analysis is used here. This consists in the following: first the dataset (1024 points in Fig (4.6a)) is divided into 2^W intervals f_k, each inter-

val containing at least 8 points. The rescaled range is defined as $RS_k = R_k/S_k$, where $R_k = \max(f_k) - \min(f_k)$ and S_k denotes the standard deviation of f_k. Given the average $\langle RS \rangle$ over all the 2^W intervals, the quantity $E = \log_2 \langle RS \rangle$ is calculated. The Hurst exponent H is defined as the slope of the $E - W$ curve shown in the insets of Fig. (4.6b): the values obtained are $H \simeq 0.56$ and $H \simeq 0.77$ for the backward intensity $|B(x)|^2$ and the density $\varrho(x)$, respectively. The Hurst exponent is connected to the fractal dimension $\mathcal{D}$ as $\mathcal{D} = 2 - H$, which gives a fractal dimension $1 < \mathcal{D} < 2$. This indicates that the structures obtained from our numerical simulations are indeed fractal self-similar objects. Remarkably, such complex dynamics is obtained with a relatively small amount of driving: the injected intensity id only 5% above threshold.

Fig. (4.7) shows the results of 2D simulations for the same driving as Fig. (4.6) (5% above threshold): here hexagons are obtained as a result of single-mode spontaneous symmetry breaking, as already found in Sec. 3.2.2. After the filter is removed, reshaping of the hexagonal pattern is observed first, followed by an increasing level of details as an increasing number of spatial modes enters the system.

4.3 Longitudinal effects

It has been stressed in Chapters 2 and 3 that the theoretical analysis presented here accounts only for the spatial dimensions $\mathbf{x} = (x, y)$ *transverse* to the propagation of the pump beam. The only relevant 'longitudinal' effect considered was diffraction, which in the paraxial limit is captured by the transverse Laplacian

$\partial_x^2 + \partial_y^2$. As already discussed above, a further assumption consisted in neglecting diffraction within the medium (thin medium approximation), but a general theory can be developed for a thick Kerr slab with feedback mirror, leading to spatial instabilities which are qualitatively similar to the thin-medium case. However, there are longitudinal effects (involving the z coordinate) which are not accounted for in the model, and it is the aim of this Section to briefly discuss them.

The first effect is the the pushing of the cloud due to the radiation pressure exerted by the pump beam. As discussed in Sec. 1.1, an optical beam illuminating the cloud from the side will result in a force (assuming the atoms at rest)

$$\mathbf{f}_{\rm rad} = \frac{\hbar\Gamma}{2}\frac{s}{1+s}\mathbf{k}_0 \qquad \mathbf{k}_0 = \frac{2\pi}{\lambda_0}\hat{z}$$

In the experimental setup discussed above, the D_2 line of ^{87}Rb at $\lambda_0 = 780.27\,\text{nm}$ is exploited, characterized by a lifetime $\Gamma^{-1} = 27\,\text{ns}$ and atom mass $M = 1.44 \times 10^{-25}\,\text{kg}$. Hence for a fairly typical saturation value $s = 0.4$ one obtains $\mathbf{f}_{\rm rad} \simeq 4.5 \times 10^{-22}\,\text{N}$ and a displacement of $\sim 0.15\,\text{cm}$ after $1\,\text{ms}$ (along $\hat{z}$). Typically, the cloud will be a cm thick or so, and this displacement is non negligible for experiments where the expected growth time for the pattern is of several milliseconds. Indeed, this is a critical point in favour of the single-mirror setup over the cavity arrangement: in the single-mirror setup, in fact, radiation pressure is balanced between the two counterpropagating beams. As the forward pump beam is partially absorbed by the cloud, the retroreflected (backward) beam will balance only partially the pressure from the pump, but this still leads to a more 'balanced' situation which can survive for longer times before pushing becomes dominant. For the typical values of the experiment ($OD = 150$,

$\delta = 7\Gamma$), the forward beam is $\sim 50\%$ absorbed by the cloud, and still the observation of self-organization processes is obtained in experimental runs lasting a few hundreds of microseconds. The obvious solution to this is to reduce absorption from the cloud, by increasing the light-atom detuning $|\delta|$ while keeping the pump intensity fixed (or better, by decreasing s). As discussed in the previous Chapters, the threshold for the saturation parameter s stays constant for large $|\delta|$, so that absorption (and radiation pressure imbalance) can be virtually eliminated from the problem if one works at low temperatures and large densities (see the threshold expression (2.37)). One basically needs to find a compromise between having a large growth rate (relatively high s) and having negligible absorption (small s); naturally electronically-driven instabilities are fast enough to overcome this issue, but the main interest of this thesis is concerned with opto-mechanically driven processes.

The ring cavity arrangement, on the other hand, seems to be much more problematic from this point of view, because there is no counterpropagating beam to balance radiation pressure. Again, the only viable option is to work at low enough saturation parameters that a 'long' experiment can be performed before 'blowing the cloud away'. A possibility to achieve this consists in building a very high-finesse cavity, which would enhance the cooperativity and allows for very low thresholds. Again, lower threshold are achieved by colder and denser clouds, as described by Eq. (3.20). The reference for this situation is given by CARL [32, 33], where millisecond-long experiments were successfully performed in extremely high-quality ring cavities. It comes as a natural question, then, whether the ring cavity setup discussed in Sec. 3.1 would display CARL sub-wavelength, longitudinal instabilities rather than

the large-size, transverse instabilities analyzed here. This possibility cannot be excluded, but the counterpropagating beam spontaneously generated by the CARL process could be suppressed by means of direction-dependent optical elements such as Faraday isolators.

The second 'longitudinal' effect is related to the formation of a standing wave within the cloud: as this is several wavelength thick, for equally polarized forward and backward beams a wavelength-scale pattern is expected for the atomic density along the z direction. Moreover, it might seem that this longitudinal bunching should be dominant over transverse effects as it occurs at smaller scales, where dipole forces are stronger and the required time for bunching is smaller. However, the formation of a standing wave inside the cloud does not seem to be necessary for the self-organization process, as hexagonal pattern formation has been observed also for orthogonally polarized forward and backward beams, with both linear and circular polarization [83]. Moreover, the heating effect due to the pump (along the z direction) is expected to destroy any bunching along the propagation axis, while only thermal dephasing occurs in the transverse direction. As the pump and retro-reflected beams are tuned on the blue side of the resonance, in fact, no cooling forces are provided along the optical axis, and the confinement in the standing wave is not favoured. The observed timescales for the pattern growth (Fig. (4.3B)) and decay (Fig. (4.2b)) indicate that transport processes take place on the transverse length scale of $\Lambda \sim 100\,\mu$m and not on the wavelength scale. The detailed investigation of these hypotheses will be the object of future studies.

Summary and outlook

This thesis presented theoretical and numerical results related to the study of symmetry-breaking, self-organizing instabilities in cold atomic gases. The spontaneous emergence of spatial structures in the coupled light-atoms dynamics has been termed self-structuring in this context, and differs from previous studies of pattern-forming instabilities in optical systems in different aspects:

- In contrast with hot-atoms pattern formation, in this work the motional degrees of freedom of the atoms is involved. The internal-state degrees of freedom has also been taken into account, but it was demonstrated that opto-mechanical self-structuring instabilities are (at least in principle) independent from internal-state-driven process.
- with respect to other spatial instabilities in cold-atoms settings (such as CARL or cavity-pump setups), here the spatial scale of the emerging structures in self-selected, and the selection of a 'critical' spatial scale breaks a continuous symmetry. In two transverse dimensions, the orientation of the pattern is also self-selected.

In Chap. 2 the situation of a cold atomic cloud left 'free' to interact with the pump beam , with the molasses beams turned off, was analysed for a single mirror feedback configuration. This resulted

in what was termed 'damping-free' or viscousless self-structuring, which was also investigated experimentally in Ref. [83] (see also Chap. 4). In Chap. 2 it was analysed under what circumstances a self-structuring instability can be observed in a sample of cold two-level atoms, and particular emphasis was put on the low-saturation limit where the atoms behave as linear dielectric particles (no internal-state nonlinearity). The low-saturation model captures the fundamental physics of opto-mechanical self-structuring, as the center-of-mass degrees of freedom are 'isolated' from the internal-state response. Analytic results for the critical quantities (growth rate, threshold power, threshold temperature, etcetera) are also available in this limit, while additional information can be obtained through numerical simulations. If the internal-state dynamics is taken into account a more realistic model is obtained, which agrees well with the experimental realisations. An important consequence of the internal-state dynamics is the possibility of realising 'electronically-driven' instabilities, where modulations in the populations and coherences of the medium drive the pattern formation process. The 'competition' or 'cooperation' of external and internal degrees of freedom depending on the value of the parameters was investigated.

Chap. 3 dealt with self-structuring in the presence of strong viscous damping, physically to be provided by optical molasses. The theoretical and numerical analysis was extended here to a ring cavity arrangement, where the possibility of realising light-density cavity solitons was investigated, see Sec. 3.3. The study of single mirror systems is strongly reminiscent of viscosity-free arrangements, and indeed all the results obtained in the linear regime are identical. However, the interpretation of the temperature is

different in this context, as it arises from stochastic noise and is not given by the kinetic temperature. In addition, numerical simulations are made less demanding by the fact that the velocity distribution needs not be taken into account, and were extended to two transverse dimensions.
In both Chap. 2 and 3 a simple theoretical argument was presented to connect single-mirror-feedback opto-mechanical self-structuring to the Kuramoto model for synchronization. Such a connection is perhaps not surprising, as the proposed setup effectively realises an all-to-all, instantaneous coupling between the atoms of the sample. Essentially the same considerations also apply to viscous CARL [96].

Chap. 4 presented the experimental results contained in Ref. [83], and discussed some 'open' questions such as that of wavenumber selection and 'fractal' pattern formation, see Sec. 4.2.1.

In the Appendices the main derivations needed in the rest of the thesis are presented, together with the discussion of the zero-temperature limit of self-structuring. The study of such a 'quantum' limit illuminates a new feature of self-structuring instabilities, connecting them with the Dicke phase transition for superradiance. In the zero-temperature limit, in fact, off-axis sidebands are spontaneously emitted in a superradiant Dicke-like transition, and since the angle of emission is self-selected by the system this Dicke-like phase transition also breaks a continuous $U(1)$ symmetry.

It is hoped that the work presented in this thesis will stimulate future research in different directions. The first one could be the

experimental observation of transverse self-organization in cold atoms using a cavity arrangement. This would open up new possibilities for engineering complex and reconfigurable light-density structures, and could be extended to other kind of dielectric particles (e.g. soft matter). Another line of work could instead extend into the quantum regime, investigating the nature of the $U(1)$ Dicke phase transition underlying the self-structuring process. A third possible line of research, which was only touched in this thesis, regards the possibility of implementing fractal, scaleless structures in optical systems. While alternative setups based on Kerr nonlinearity were already proposed, self-structuring instabilities involving the motional degrees of freedom of the medium should in fact 'natively' support this possibility, at least in the thin-medium limit.

Acknowledgements

I would like to thank all the people that supported me through the years of my PhD, and collaborated to the research presented in this thesis. These include Gordon Robb and Gian-Luca Oppo, for guiding me and teaching me more than I can probably realise, as well as Thorsten Ackemann, Willie Firth, Aidan Arnold, and Pedro Gomes for the many and fruitful discussions we had in the last years. Robin Kaiser and Guillaume Labeyrie also provided precious contributions to the projects and deserve a grateful acknowledgement − I owe many of the ideas presented in the thesis to the Stratchlyde−INLN collaboration.

Finally, I want to thank all the people in the CNQO group at

Strathclyde, Glasgow and the entire Scotland for three beautiful years.

Appendices

Appendix A: Main derivations

This Appendix presents a more detailed derivation of some fundamental equations used within the thesis, namely the field wave equation, the Maxwell-Bloch equations and the corresponding steady-state, the collisionless Boltzmann equation (viscosity-free case), and the Fokker-Planck/Smoluchowski equation (viscous case).

Field wave equation

The starting point for the study of the dynamics of the optical field is given by the Maxwell equations for a non-magnetic medium:

$$\nabla \times \mathcal{E} = -\frac{\partial \mathcal{B}}{\partial t} \tag{1a}$$

$$\nabla \times \mathcal{B} = \mu_0 \frac{\partial \mathcal{D}}{\partial t}\,, \tag{1b}$$

where $\mathcal{D} = \varepsilon_0 \mathcal{E} + \mathcal{P}$ with $\mathcal{P}$ the macroscopic polarization and $\mathcal{E}$ ($\mathcal{B}$) the electric (magnetic) field. Using the vectorial identity

$$\nabla \times \nabla \times \mathbf{f} = \nabla \left(\nabla \cdot \mathbf{f}\right) - \nabla^2 \mathbf{f}$$

the wave equation for the electric field is obtained as ($c^{-2} = \mu_0 \varepsilon_0$):

$$\nabla (\nabla \cdot \mathcal{E}) + \frac{1}{c^2} \frac{\partial^2 \mathcal{E}}{\partial t^2} - \nabla^2 \mathcal{E} = -\mu_0 \frac{\partial^2 \mathcal{P}}{\partial t^2} \,. \tag{2}$$

Since the radiation under analysis comes from a laser source (as in any nonlinear optical context), we make use of the Slowly Varying Envelope Approximation (SVEA) and expand the field and polarization as [64]

$$\mathcal{E} = \mathbf{E}(\mathbf{x}, t) e^{i(k_0 z - \omega_0 t)} + \text{c.c.} \tag{3a}$$

$$\mathcal{P} = N_0 \left[\mathbf{P}(\mathbf{x}, t) e^{i(k_0 z - \omega_0 t)} + \text{c.c.} \right] \tag{3b}$$

where N_0 is the density of the medium, $k_0 = 2\pi/\lambda_0$ the radiation wavenumber and ω_0 its frequency. This expansion essential factors out a monochromatic plane wave at frequency ω_0 and wavenumber $k_0 = \omega_0/c$, emphasizing that the laser field behaves as a slowly-changing plane wave. Mathematically, this idea is captured by the fact that the 'envelopes' $\mathbf{E}$ and $\mathbf{P}$ vary in $\mathbf{x}$ and t much more slowly than the exponential terms $\exp(i(k_0 z - \omega_0 t))$. Hence the source term in Eq. (2) reads

$$-\mu_0 \frac{\partial^2 \mathcal{P}}{\partial t} = -\mu_0 N_0 \left[\ddot{\mathbf{P}} - 2i\omega_0 \dot{\mathbf{P}} - \omega_0^2 \mathbf{P} \right] e^{i(k_0 z - \omega_0 t)} + \text{c.c} \simeq \tag{4}$$

$$\simeq \mu_0 \omega_0^2 N_0 \left[\mathbf{P} e^{i(k_0 z - \omega_0 t)} + \text{c.c.} \right] , \tag{5}$$

where the fact that $\omega_0 |\dot{\mathbf{P}}| \ll |\mathbf{P}|$ was used, which is precisely the SVEA assumption. The term

$$\nabla^2 \mathcal{E} - \frac{1}{c^2} \frac{\partial^2 \mathcal{E}}{\partial t^2} \,.$$

captures the free-space field dynamics, and again considering only SVEA-surviving terms for the temporal derivative it reads

$$\left\{ \left(\partial_x^2 + \partial_y^2 + \partial_z^2 \right) \mathbf{E} + \frac{\omega_0^2}{c^2} \right\} \mathbf{E} e^{i(k_0 z - \omega_0 t)} ,$$

while the z-derivatives give

$$\partial_z^2 \mathbf{E} e^{i(k_0 z - \omega_0 t)} = \left[\frac{\partial^2 \mathbf{E}}{\partial z^2} + 2ik_0 \frac{\partial \mathbf{E}}{\partial z} - k_0^2 \mathbf{E} \right] e^{i(k_0 z - \omega_0 t)} .$$

The k_0^2 term exactly cancels the temporal derivative ($k_0 = \omega_0/c$), so that the wave equation (including the source term) reads

$$\left(\partial_x^2 + \partial_y^2 + \partial_z^2 + 2ik_0 \partial_z \right) \mathbf{E} = \mu_0 \omega_0^2 N_0 \mathbf{P} \tag{6}$$

Making use of the *paraxial* approximation, the beam is assumed to be wide enough to have a slow variation along z:

$$\left| \frac{\partial^2 \mathbf{E}}{\partial z^2} \right| \ll k_0 \left| \frac{\partial \mathbf{E}}{\partial z} \right| . \tag{7}$$

The paraxial approximation thus requires any off-axis sideband emitted by the system not to deviate too largely from the optical axis. Laser beams typically satisfy this condition unless 'extreme' conditions are under study, such as extremely narrow solitonic beams [119]. Using the condition (7) the wave equation (6) takes the form

$$\frac{\partial \mathbf{E}}{\partial z} = \frac{i}{2k_0} \nabla_\perp^2 \mathbf{E} - i \frac{\mu_0 \omega_0^2}{2k_0} N_0 \mathbf{P} . \tag{8}$$

where $\nabla_\perp^2 = \partial_x^2 + \partial_y^2$ denotes the transverse Laplacian (note that the symbol $\perp$ is omitted in the rest of the thesis, where the only relevant coordinates for the Laplacian are the transverse ones).
The 'split-step' structure that we used in the single-mirror setup (Chap. 2 and Sec. 3.2) can be recognized in Eq. (8) : the field-medium interaction is contained in the source term ($\mathbf{P}$), while

the free-space diffraction is described by the transverse Laplacian. For purely dispersive interactions the polarization is real and the source term gives rise to a phase shift, but no absorption.

Maxwell Bloch equations for two-level atoms

The next step involves the description of the medium, i.e. the microscopic interpretation of the polarization $\mathbf{P}$. The Hamiltonian for the system is $H = H_0 + H_1$, where the interaction Hamiltonian is given by the dipole energy: $H_1 = -\mathbf{E} \cdot \mathbf{P} \equiv -e\mathbf{E} \cdot \mathbf{r}$ ($\mathbf{r}$ being the position operator). The internal state $|\psi\rangle$ of a two-level atom evolves according to

$$i\hbar \frac{\partial |\psi\rangle}{\partial t} = (H_0 + H_1) |\psi\rangle \ ,$$

and using a perturbative approach can be expanded as

$$|\psi\rangle = \sum_{j=1}^{2} a_j(t) |\psi_j\rangle \tag{9}$$

where $|\psi_j\rangle$ denotes unperturbed states, $H_0 |\psi_j\rangle = E_j |\psi_j\rangle$. The Schrödinger equation thus reads

$$i\hbar \sum_{j=1}^{2} \dot{a}_j |\psi_j\rangle = H_0 \sum_{j=1}^{2} a_j(t) |\psi_j\rangle - \mathbf{E} \cdot \mathbf{P} \sum_{j=1}^{2} a_j(t) |\psi_j\rangle \ ,$$

so that taking the expectation value with $\langle\psi_i|$ the dynamics for the amplitudes $a_i(t)$ is obtained as ($\langle\psi_i|\psi_j\rangle = \delta_{ij}$):

$$\dot{a}_i(t) = -i\omega_i a_i(t) + \frac{i}{\hbar} \mathbf{E} \cdot \sum_{j=1}^{2} \mathbf{P}_{ij} a_j(t) \, , \tag{10}$$

where $\omega_i = E_i/\hbar$ and the dipole matrix is $\mathbf{P}_{ij} = e \langle\psi_i|\mathbf{r}|\psi_j\rangle$. $\mathbf{P}_{ij}$ is symmetric and has only zeros on the diagonal (due to the parity

of the wavefunctions) [64]:

$$\mathbf{P}_{ij} = \begin{pmatrix} 0 & \vec{\mu}_{\text{dip}} \\ \vec{\mu}_{\text{dip}} & 0 \end{pmatrix}$$

Note that in this derivation the electric field was taken out of the expectation integral, an assumption that goes under the name of *dipole approximation*:

$$-e \langle \psi_i | \mathbf{E} \cdot \mathbf{r} | \psi_j \rangle = -e\mathbf{E} \cdot \langle \psi_i | \mathbf{r} | \psi_j \rangle$$

The idea behind this approximation is that the scale of spatial variation of the field is small compared to atomic size, so that $\mathbf{E}$ can effectively be considered constant. This holds as long as $\lambda_0 \ll a_0$, where a_0 is a typical atomic size [64].
Eq. (10) can be used to obtain the dynamics of the density matrix elements $\varrho_{ij} = a_i a_j^*$:

$$\dot{\varrho}_{ij} = -i(\omega_j - \omega_i)\varrho_{ij} + \frac{i}{\hbar}\sum_{l=1}^{2} \mathbf{P}_{il}\varrho_{lj} - \frac{i}{\hbar}\sum_{l=1}^{2} \mathbf{P}_{jl}^{*}\varrho_{il}\,. \tag{11}$$

Considering a linearly polarized field, say along $\hat{e}_x$ (that is, $\mathbf{E} = E\hat{e}_x$), any phase contained in the polarization vector can be dropped on the off-diagonal matrix element ϱ_{21}, so that $\vec{\mu}_{\text{dip}}$ points along $\hat{e}_x$ and can be taken real without loss of generality. Isolating again the 'plane-wave' term as $E \to Ee^{-i\omega_0 t}$ and recalling that $\varrho_{12} = \varrho_{21}^*$, the only independent equations for the density matrix elements are

$$\dot{\varrho}_{21} = -i(\omega_2 - \omega_1)\varrho_{21} + \frac{i}{\hbar}E\mu_{\text{dip}}(\varrho_{11} - \varrho_{22})e^{-i\omega_0 t} \tag{12a}$$

$$\dot{\varrho}_{11} = \frac{i}{\hbar}E\mu_{\text{dip}}(\varrho_{21} - \varrho_{12}) \tag{12b}$$

$$\dot{\varrho}_{22} = \frac{i}{\hbar}E\mu_{\text{dip}}(\varrho_{12} - \varrho_{21})\,. \tag{12c}$$

It is convenient in the following to introduce in the above equations the atomic resonance $\omega_{\rm at} = \omega_2 - \omega_1$, the light-atom detuning $\delta = \omega_0 - \omega_{\rm at}$ and the population difference $w = \varrho_{11} - \varrho_{22}$. The macroscopic polarization is given by the expectation value of the microscopic one :

$$\mathbf{P}e^{-i\omega_0 t} = \langle e\mathbf{r}\rangle = \mathrm{Tr}(e\mathbf{r}\varrho) = (\mu_{\rm dip}\varrho_{21} + \mu_{\rm dip}\varrho_{12})\hat{e}_x \,,$$

so that the 'macroscopic' polarization $\mathbf{P} = P\hat{e}_x$ (source term in the Maxwell equations) is linked to the 'microscopic' dynamics of the internal state (described by Schrödinger equation) as

$$P = \mu_{\rm dip}\varrho_{21}e^{i\omega_0 t} \tag{13}$$

Hence Eqs. (12) can be rewritten as

$$\begin{aligned}
\dot{P} &= i\delta P + i\frac{\mu_{\rm dip}^2}{\hbar}Ew \\
\dot{w} &= i\frac{2}{\hbar}\left(E^*P - EP^*\right) \,,
\end{aligned}$$

where the *rotating wave approximation* was used in keeping only terms with no $e^{\pm i\omega_0 t}$ variation. The idea behind this approximation is that rapidly oscillating terms in the Hamiltonian have zero average and do not contribute to the dynamics [64].
The last step in this analysis consists in taking into account the fact that the upper state is pumped and decays with a rate Γ (the atomic linewidth); moreover, the coherence $\varrho_{21} \propto P$ decays with a rate $\Gamma_\perp = \Gamma/2$. This last relation comes from the fact that at low temperatures collisional dephasing is negligible [58]. Hence

$$\dot{P} = -\frac{\Gamma}{2}\left(1 - i\Delta\right)P + i\frac{\mu_{\rm dip}^2}{\hbar}Ew \tag{15a}$$

$$\dot{w} = -\Gamma\left(w - 1\right) + i\frac{2}{\hbar}\left(E^*P - EP^*\right) \,, \tag{15b}$$

where as in the rest of the thesis the half-linewidth detuning has been defined as $\Delta = 2\delta/\Gamma \equiv \delta/\Gamma_\perp$. Losses and dephasing terms can be introduced in a more rigorous way by studying the Lindblad operators associated to the interaction between the two-level system and the environment [120]. This derivation will not be presented here, but the important remark is that assuming a Markovian system-environment interaction (i.e. spontaneously emitted photons are lost forever) the somewhat phenomenological argument discussed here leads to the correct result.

Eqs. (15) are commonly named the Bloch equations, and describe the dynamics of the populations (ϱ_{11}, ϱ_{22}) and coherences (ϱ_{21}, ϱ_{12}) of the two-level atomic system driven by the optical field E. The Bloch equations can be complemented by the field wave equation (8) to form what goes under the name of Maxwell-Bloch equations:

$$\frac{\partial E}{\partial z} = \frac{i}{2k_0}\nabla_\perp^2 E - i\frac{\mu_0\omega_0^2}{2k_0}N_0 P \tag{16a}$$

$$\dot{P} = -\frac{\Gamma}{2}(1 - i\Delta)\,P + i\frac{\mu_{\text{dip}}^2}{\hbar}Ew \tag{16b}$$

$$\dot{w} = -\Gamma\,(w - 1) + i\frac{2}{\hbar}\left(E^*P - EP^*\right)\,. \tag{16c}$$

Consider now the steady-state solution of the system (16). A result extensively used in the thesis, in fact, is the steady-state value of the population difference, obtained under the assumption that the internal-state dynamics is much faster than the dynamics of all the other variables. Otherwise stated, it is assumed that P and w evolve much faster than E and the atomic density. Note that in this derivation the atomic density is assumed to be constant, $n = N_0$, but obviously the dynamics of the atomic density is crucial in studying opto-mechanical instabilities. However, the

motional degrees of freedom are the slowest to evolve, so that it can be safely assumed that if P and w evolve much faster than E, they also evolve much faster than n. Alternatively, one could re-derive the wave equation by keeping derivatives $\dot{n}$, $\ddot{n}$ originating from the source term $\partial_t^2\mathbf{P}$; however, these derivatives are small and can be neglected. In conclusion, the fact that Γ is much larger that any field timescale is exploited to set $\dot{P} = \dot{w} = 0$:

$$\begin{aligned}\bar{P} &= \frac{2i\mu_{\rm dip}^2 E\bar{w}}{\hbar\Gamma(1-i\Delta)}\\ \bar{w} &= 1 + \frac{2i}{\hbar\Gamma}\left(E^*\bar{P} - E\bar{P}^*\right) =\\ &= 1 - \frac{8\mu_{\rm dip}^2}{\hbar^2\Gamma^2}\frac{\bar{w}|E|^2}{1+\Delta^2}\end{aligned}$$

which gives

$$\bar{w} = \left(1 + \frac{8\mu_{\rm dip}^2}{\hbar^2\Gamma^2}\frac{|E|^2}{1+\Delta^2}\right)^{-1} \equiv \frac{1}{1+s} \tag{17a}$$

$$\bar{P} = \frac{2i\mu_{\rm dip}^2}{\hbar\Gamma(1-i\Delta)}\frac{E}{1+s}\,. \tag{17b}$$

Here the dimensionless *saturation parameter* has been introduced as

$$s = \frac{(\varepsilon_0 c/2)|E|^2}{I_{\rm sat}(1+\Delta^2)} = \frac{8\mu_{\rm dip}^2}{\hbar^2\Gamma^2}\frac{|E|^2}{1+\Delta^2}\,, \tag{18}$$

which is extensively used in the thesis and parametrizes the effective strength of the radiation 'perceived' by the atomic system. The saturation parameter is a fundamental quantity also in describing the center-of-mass dynamics: in order to connect with the results of Sec. 1.1.1 we identify the Rabi frequency as (see Eq. (1.9))

$$g = i\frac{\mu_{\rm dip}}{\hbar}E\,,$$

so that the saturation parameter reads $s = 8|g|^2/[\Gamma^2(1+\Delta)^2]$ as in Eq. (1.12).

From the above definitions the in-resonance optical density b_0 can also be defined as follows: a weak field (inducing only linear polarization effects) of amplitude E propagates through a sample of two-level atoms of thickness L as

$$\frac{\partial E}{\partial z} = -i\frac{\mu_0\omega_0^2}{2k_0}N_0\bar{P} = -\frac{\mu_0\omega_0^2}{k_0}N_0\frac{\mu_{\rm dip}^2(1+i\Delta)}{\hbar\Gamma(1+\Delta^2)}E\,.$$

Hence the transmitted fraction of the field amplitude is

$$\left|\frac{E_{\rm out}}{E_{\rm in}}\right| = \exp\left(-\frac{\mu_0\omega_0^2}{k_0}\frac{A_\perp N_0\mu_{\rm dip}^2 L}{\hbar\Gamma(1+\Delta^2)}\right) \equiv \exp\left(-\frac{b_0}{1+\Delta^2}\right)\,.$$

where $A_\perp$ is the transverse size of the system (orthogonal to propagation), and N_0 is the density of the cloud (in m^{-3}). This identifies the susceptibility of the cloud as

$$\alpha_0 = \frac{b_0}{2L(1+\Delta^2)}\,.$$

Collisionless Boltzmann (Vlasov) equation

In Chap. 2 the atomic dynamics has been modelled in term of a collisionless Boltzmann equation for the phase-space distribution $f(\mathbf{x},\mathbf{v},t)$:

$$\frac{\partial f}{\partial t} + \mathbf{v}\cdot\frac{\partial f}{\partial \mathbf{x}} + \frac{\mathbf{f}_{\rm dip}}{M}\cdot\frac{\partial f}{\partial \mathbf{v}} = 0\,.$$

In the following two alternative ways to derive this equation are presented, and the corresponding approximations are discussed. The first approach is quite straightforward: the total variation of the phase space distribution in a small time increment dt is

written as[1]

$$f(\mathbf{x},\mathbf{v},t)d\mathbf{x}d\mathbf{v} = f\left(\mathbf{x}+\mathbf{v}dt, \mathbf{v}+\frac{\mathbf{f}_{\rm dip}}{M}dt, t+dt\right)d\mathbf{x}d\mathbf{v}\,,$$

which follows from the Liouville's theorem (phase space volumes are conserved). The phase space distribution can be Taylor-expanded to obtain

$$\begin{aligned}\frac{df}{dt} &\equiv \frac{1}{dt}\left[f\left(\mathbf{x}+\mathbf{v}dt, \mathbf{v}+\frac{\mathbf{F}}{M}dt, t+dt\right)d\mathbf{x}d\mathbf{v} - f(\mathbf{x},\mathbf{v},t)\right] = \\ &= \frac{1}{dt}\left(\frac{\partial f}{\partial t}dt + \frac{\partial f}{\partial \mathbf{x}}\cdot d\mathbf{x} + \frac{\partial f}{\partial \mathbf{v}}\cdot\mathbf{v}\right) = \\ &= \frac{\partial f}{\partial t} + \mathbf{v}\cdot\frac{\partial f}{\partial \mathbf{x}} + \frac{\mathbf{f}_{\rm dip}}{M}\cdot\frac{\partial f}{\partial \mathbf{v}} = 0\,,\end{aligned}$$

where in the last step the relations $d\mathbf{x} = \mathbf{v}dt$ and $d\mathbf{v} = \mathbf{f}_{\rm dip}/Mdt$ have been used. This last derivation assumes no variation of f due to atom-atom collisions, i.e. all the force is due to the external dipole force $\mathbf{f}_{\rm dip}$. This force contains in fact the atomic positions but only indirectly through the atom-light coupling, so that the self-organized optical potential resulting from an opto-mechanical instability essentially acts as an external one.

A second derivation of the collisionless Boltzmann equation can be given starting from a 'particle' description of the Newton dynamics:

$$\begin{aligned}\dot{\mathbf{x}}_j &= \mathbf{v}_j \\ \dot{\mathbf{v}}_j &= \mathbf{f}_{\rm dip}/M\,,\end{aligned}$$

where $\mathbf{x}_j$ and $\mathbf{v}_j$ are the positions and velocities of the atoms labelled by the index $j = 1,\ldots,N$. In the following the set of

[1] note that $\mathbf{x}$ and $\mathbf{v}$ denote transverse coordinates in the rest of the thesis, but the argument presented here is general

positions and velocities is denoted as $\mathbf{q} = \{\mathbf{x}_j, \mathbf{v}_j\}_{j=1}^N$. For large N (typically $N = 10^{10}$ in dense clouds) a numerical solutions of the Newton equations is impractical, and one is interested in the continuous probability distribution $f(\mathbf{x}, \mathbf{v}, t)$. An 'intermediate' quantity can be introduced, named the Klimontovich distribution, which allows for an exact rephrasing of the N-particle dynamics:

$$f_K(\mathbf{x}, \mathbf{v}; \mathbf{q}) = \frac{1}{N} \sum_{j=1}^{N} \delta(\mathbf{x} - \mathbf{x}_j)\delta(\mathbf{v} - \mathbf{v}_j) \tag{19}$$

The Klimontovich distribution can be used to extract 'many-body' averages of any macroscopic quantity A:

$$\langle A \rangle = \frac{1}{N} \sum_{j=1}^{N} a(\mathbf{x}_j, \mathbf{v}_j) = \int a(\mathbf{x}, \mathbf{v}) f_K((\mathbf{x}, \mathbf{v}); \mathbf{q}) d\mathbf{x} d\mathbf{v} \, .$$

In the sense of distributions, differentiating f_K with respect to time one finds (see Ref. [77])

$$\frac{\partial f_K}{\partial t} + \mathbf{v} \cdot \frac{\partial f_K}{\partial x} + \frac{\mathbf{f}_{\text{dip}}}{M} \cdot \frac{\partial f_K}{\partial \mathbf{v}} = 0 \, , \tag{20}$$

where the force should be considered as a macroscopic average in the sense discussed above.

So far $6N$ ordinary differential equations were converted into a single partial differential equation for f_K, but the same information is contained in both formulations and the task has not been made easier by introducing the Klimontovich distribution. The distribution f_K is in fact highly irregular, see the definition (19), and obtaining an exact solution for f_K is hopeless. The Boltzmann equation is retrieved if one substitutes f_K with a smooth function on the phase space: $f_K \to f$. This is intuitively correct in the limit of large number of particles, but can be proved formally [77] in the sense of the distributions, i.e. the distance

between the probability measure associated to f_K and the probability measure associated to f uniformly tends to zero as $N \to \infty$.

The Fokker-Planck/Smoluchowski equation

This Section presents the derivation of the density dynamical equation for the viscous case, which was used in Chap. 3 and reads

$$\frac{\partial n}{\partial t} = D\sigma\nabla \cdot [n\nabla \log(1+s)] + D\nabla^2 n \tag{21}$$

Here $n = n(\mathbf{x}, t)$ represents the dimensionless density variation (its uniform value is scaled to $n = 1$), $\sigma = \hbar\delta/2k_BT$ was introduced in Eq. (3.8), and $U_{\text{dip}} = (\hbar\delta/2)\log(1+s)$ is the dipole potential resulting from the optical field profile. Eq. (21) was generically termed Fokker-Planck equation in Chap. 3, as it belongs to this broad class of equations, and can be derived in all generality in statistical mechanics. The main assumption made in Chap. 3 was the particular form of the relation between the diffusion coefficient D, the viscous damping γ and the temperature T: $D\gamma = k_BT$. This constraint represents an instance of the fluctuation-dissipation relation, and can be seen as a rephrasing of the Einstein-Smoluchowski relation [121, 106]. In this context, the Fokker-Planck equation (21) is also referred to as the Smoluchowski equation.

Suppose that some potential energy U acts on the system, generating a force $\mathbf{f} = -\nabla U$. A particle (composing our atomic 'fluid') responds by moving with velocity $\mathbf{v} = \zeta\mathbf{f}$. This assumption is justified in our case because we assume strong damping, so that $M\dot{\mathbf{v}} = -\gamma\mathbf{v} + \mathbf{f} = 0$ gives $\mathbf{v} = \mathbf{f}/\gamma$. The *mobility* ζ can thus be defined as

$$\zeta = \gamma^{-1}\,. \tag{22}$$

For a large number of particles described by a continuous distribution $n(\mathbf{x}, t)$ a drift-diffusion (continuity) equation can be written in the form

$$\frac{\partial n}{\partial t} + \nabla \cdot (\mathbf{j}_{\text{drift}} + \mathbf{j}_{\text{diff}}) = 0\,,$$

where the diffusion current is given by Fick's law,

$$\mathbf{j}_{\text{diff}} = -D\frac{\partial n}{\partial \mathbf{x}}$$

and the drift current is given by

$$\mathbf{j}_{\text{drift}} = n\mathbf{v} = n\zeta\mathbf{f} = -\frac{1}{\gamma}n\frac{\partial U}{\partial x}\,.$$

At equilibrium the solution of the Smoluchowski equation is given by the Gibbs distribution:

$$n_{\text{eq}}(\mathbf{x}) = \mathcal{N}\exp\left(-\frac{U}{k_B T}\right)\,, \tag{23}$$

where $\mathcal{N}$ ensures that the distribution is normalized. This is an important point in numerical simulations, since the shape of $U(\mathbf{x})$ dynamically depends on $n(\mathbf{x})$ and the normalization condition introduces an additional nonlinearity (see Sec. 3.1.4). Deriving the equilibrium distribution (23) with respect to $\mathbf{x}$ one has that

$$\frac{\partial n_{\text{eq}}}{\partial \mathbf{x}} = -\frac{1}{k_B T}\frac{\partial U}{\partial \mathbf{x}}n_{\text{eq}}\,.$$

The mobility can found by requiring that the drift and diffusion currents balance each other at equilibrium:

$$\begin{aligned} 0 = \mathbf{j}_{\text{drift}} + \mathbf{j}_{\text{diff}} &= -n_{\text{eq}}\zeta\frac{\partial U}{\partial \mathbf{x}} - D\frac{\partial n_{\text{eq}}}{\partial \mathbf{x}} = \\ &= -n_{\text{eq}}\zeta\frac{\partial U}{\partial \mathbf{x}} + \frac{D}{k_B T}\frac{\partial U}{\partial \mathbf{x}}n_{\text{eq}} \end{aligned}$$

which imposes the Einstein-Smoluchowski condition as

$$\zeta = \frac{1}{\gamma} = \frac{D}{k_B T} \Longrightarrow D\gamma = k_B T \,. \tag{24}$$

This result justifies invoking the fluctuation-dissipation theorem in Eq. (3.6), and therefore validates using Eq. (21) through Chap. 3 of the thesis.

Appendix B: Numerical methods

This Appendix presents and discusses the numerical methods employed in the simulations of Chap. 2 (viscosity-free case) and Chap. 3 (viscous case).

Viscousless case

In Chap. 2 the collisionless Boltzmann equation was numerically solved in one dimension,

$$\frac{\partial f}{\partial t} + v\frac{\partial f}{\partial x} + \frac{f_{\mathrm{dip}}}{M}\frac{\partial f}{\partial v} = 0\,, \tag{25}$$

where $f_{\mathrm{dip}} = -(\hbar\delta/2)\partial_x \log(1+s(x))$ and $s = |F|^2 + |B|^2$ represents the total (forward+backward) intensity acting on the cloud. As discussed in Sec. 2.5 time and space can be suitably rescaled to be dimensionless, and it is assumed here that such scaling has been performed. The backward (B) field is determined by propagating the forward (F) field through the cloud according to

$$\frac{\partial F}{\partial z} = -\alpha_0(1 - i\Delta)wnF \tag{26}$$

where $w = 1/(1+s)$ is the steady-state population difference and

$$n(x,t) = \int_{-\infty}^{+\infty} dv\, f(x,v,t)$$

is the atomic density.

The numerical scheme involves the following steps:

- set the initial condition for B and w. If absorption is considered (i.e. outside the low-saturation regime) this requires a zero-finding routine, see Sec. 2.2. The initial condition for f is a spatially homogeneous Maxwell-Boltzmann distribution with a width determined by the temperature, $v_{\mathrm{th}} =$

$\sqrt{k_B T/M}$.

- propagate the forward field, simply imposing phase shift and absorption as dictated by Eq. (26)

- diffract the forward field F to the mirror and back to obtain B: this is done by moving to Fourier space (with the aid of the Fortran `libfftw` libraries [122]), phase-shifting each mode by $\Theta = \Theta(q)$ (see Eq. (2.14)) and Fourier-transforming back in the x-space. A low-pass filter is employed to cut high spatial frequencies and avoid 'fractal' pattern formation, see Sec. 4.2.1. This filter typically sets to zero all the modes with frequency $q^2 > 3q_c^2$, q_c being the critical wavenumber determined by linear analysis (in the low-saturation regime)

- calculate $s = |F|^2 + |B|^2$, its gradients and solve the Boltzmann equation (25) for a time step

- iterate steps 2 to 4

The critical point of this scheme naturally consists in solving the Boltzmann equation (25) for a time step; in this thesis the techniques introduced by Cheng and Knorr in [123] for plasma systems are adapted to our cold-atom situation. The main idea is that rather than solving Eq. (26) for a whole time step Δt the problem is split into two advection problems for a half time step each:

$$\frac{\partial f}{\partial t} + v\frac{\partial f}{\partial x} = 0 \qquad \text{('proper' advection)}$$
$$\frac{\partial f}{\partial t} + \frac{f_{\text{dip}}}{M}\frac{\partial f}{\partial v} = 0 \qquad \text{('velocity' advection)}$$

The solutions to these two equations are known, and are given by simple shifts along the x and v axes:

$$f(x, v, t + \Delta t) = f(x - v\Delta t, v, t)$$
$$f(x, v, t + \Delta t) = f(x, v - f_{\rm dip}/M\Delta t, t)$$

An important point is that the shift $x_p \to \bar{x}_p = x_p - v\Delta t$ (for any given v) will produce a spatial point which is not in the original mesh grid, and therefore one needs to interpolate the force to find $f_{\rm dip}$ at $\bar{x}_p$. Essentially this technique reduces the problem of solving the Boltzmann equation into a series of successive interpolations. To demonstrate that this indeed approximates properly the solution of our problem suppose that these interpolations can be performed to some order in Δx, Δv. Defining $A(x) = f_{\rm dip}/M$ and calling f^n the distribution function at the n-th time step, the 'double-advection' routine described above implements the following steps:

$$f^*(x, v) = f^n(x - v\Delta t/2, v) \tag{27a}$$
$$f^{**}(x, v) = f^*(x, v - A(x)\Delta t) \tag{27b}$$
$$f^{n+1}(x, v) = f^{**}(x - v\Delta t/2, v) \tag{27c}$$

These shifts are written here for generic for x and v, but are applied to the mesh points in the numerical code. Substituting the second and the first equations into the last one one finds that

$$f^{n+1}(x, v) = f^n(x - \Delta t(v - \tfrac{1}{2}A(\bar{x})\Delta t), v - A(x)\Delta t)\,,$$

where $\bar{x} = x - v\Delta t$. On the other hand, expanding this result the corresponding characteristics (curves of constant f) are given

by [123]

$$x(t) = x(t+\Delta t) - \Delta t \left[v(t+\Delta t) - \tfrac{1}{2} A(\bar{x}, t+\Delta t/2)\Delta t \right]$$
$$v(t) = v(t+\Delta t) - \Delta t A(\bar{x}, t+\Delta t/2)$$

which in the continuous limit simply read

$$\dot{x} = v \tag{28a}$$
$$\dot{v} = A(x(t), t)\,, \tag{28b}$$

A being calculated after the first shift along x (i.e. from f^*). Since the shift along the v axis leaves the density (and therefore A) unaffected, $A(\bar{x}, t+\Delta t/2)$ can be approximated by $A(x - v\Delta t/2, t+\Delta t/2)$. The point is that as the characteristic equations for the approximated system reproduce the 'correct' characteristic equations (28), and therefore to the Boltzmann dynamics (25), the scheme (27) correctly approximates the Boltzmann solution[2]. With a view to the practical implementation of this routine, note that a half-shift in x is followed by another half-shift along x, so that effectively whole-step shifts along x and v alternate in a split-step fashion.

So far it was demonstrated that the scheme (27) correctly approximates the Boltzmann equation, because it generates the same characteristics. However, one needs to interpolate the force term $A(\bar{x})$ in points $\bar{x} = x - v\Delta t$ which not necessarily fall on the mesh grid. It is convenient (but not necessary) that $v_{\max}\Delta t \leq \Delta x$, where $v_{\max}$ is the maximum value of the velocity on the grid, $-v_{\max} \leq v_j \leq v_{\max}$. Typically the maximum velocity is set to $v_{\max} = 6v_{\text{th}}$ in the simulations, see Sec. 2.5.

[2] i.e. this scheme is *consistent*

A spline interpolation method [123, 85] has been implemented in the simulations, which has the advantage of a computational time which scales linearly in the number of grid points. The numerical code uses 4 processors in parallel using the `openmp` libraries [124] to further reduce computational time. Any interpolated value $f(x_p + \Delta)$, where x_p is a grid point and $\Delta = \delta \Delta x$ with $0 \leq \delta \leq 1$ can be expressed by a combination of the grid values f_p and its derivatives g_i as [123]

$$\begin{aligned} \bar{f_p} = f(x_p + \Delta) = \left[g_p \delta (1-\delta)^2 - g_{p+1}(1-\delta)\delta^2 \right] \Delta x + \\ + f_p (1-\delta)^2 (1+2\delta) + f_{p+1}\delta^2 \left[1 + 2(1-\delta) \right] , \end{aligned}$$

where

$$g_{p-1} + 4g_p + g_{p+1} = \frac{3}{\Delta x} \left(f_{p+1} - f_{p-1} \right) .$$

This last equation identifies a tridiagonal linear system; since periodic boundary conditions are used this is supplemented by extra elements at the top-right and bottom-left of the system matrix . A Sherman-Morrison routine [85] has been implemented to solve this linear problem, together with the `DGTSV` (real, double precision) tridiagonal solver provided by the Fortran `lapack` libraries [125]. Periodic boundary conditions are then implemented also for f_p, i.e. $f_{N+1} = f_1$ and $f_0 = f_N$.

In calculating the field phase shift one needs to use the density $n(x)$, obtained integrating $f(x, v)$ over the entire velocity space. This integral is calculated over the range $(-v_{\max}, v_{\max})$ via the Simpson method [85]. Moreover, the Simpson method is also used to normalize the density distribution at each time step. We also verified that increasing the number of grid points and/or increasing the time step, the results are unchanged if the condition

$v_{\max}\Delta t \leq \Delta x$ is not fulfilled, but very large values of Δt typically lead to blow-ups and numerical instabilities. For 'purely opto-mechanical' simulations (no internal state involved), a time step in the microsecond range for a millisecond long simulation amply ensures the stability of the routine.

Viscous case

This Section discusses the numerical methods employed for the viscous simulations of Chap. 3. Different methods are used for the cavity system, Sec. 3.1 and Sec. 3.3, and the damped single-mirror system, Sec. 3.2.
For the cavity simulations the problem consists in solving the coupled equations (in two dimensions and dimensionless units)

$$\frac{\partial E}{\partial t} = -(1+i\theta)E + A_{\text{in}} - iC\Delta n\, E + i\nabla^2 E \tag{29a}$$

$$\frac{\partial n}{\partial t} = \bar{D}\sigma\nabla\cdot[n\nabla s] + \bar{D}\nabla^2 n\,, \tag{29b}$$

where $s = |E|^2$ denotes the intracavity intensity. As discussed in Sec. 3.1.4 only the low-saturation limit is considered here, with the goal of finding the stationary state of the system. The equilibrium density is given by the Gibbs distribution (see Eq. (3.22))

$$n_{\text{eq}} = \frac{\exp\{-\sigma s(\mathbf{x})\}}{\int \exp\{-\sigma s(\mathbf{x})\}\, d\mathbf{x}}\,,$$

which can be plugged into the dynamics of E to have a Lugiato-Lefever-like [6] nonlinear equation of the field. This is solved using a finite-difference Crank Nicholson method [85], which has the advantage of being accurate to second order but asks only for first-order time differences (and hence for only two values of the function to be kept in memory at each step). The basic principles

of the Crank Nicholson is the following: given an equation in the form

$$\frac{\partial f}{\partial t} = F[f]\,,$$

for a one-dimensional function $f(x,t)$, limiting to the mesh points $f_i^n = f(x_i, t_n)$ the system is written as

$$\begin{aligned}\frac{f_i^{n+1} - f_i^n}{\Delta t} &= \frac{1}{2} F\left[f_i^{n+1}\right] + \\ &+ \frac{1}{2} F\left[f_i^n\right]\,.\end{aligned}$$

Note that this essentially accounts for a weighted average (with weights 1/2) of the forward and backward Euler methods. The Crank Nicholson comes with the advantage in terms of stability of the backward Euler method [85], but also with the disadvantage of having an implicit nonlinear system for f_i^{n+1}. However, one can proceed by approximating the nonlinear term coming from the $n_{\rm eq}^{n+1} \propto \exp(-\sigma|E^{n+1}|^2) \simeq \exp(-\sigma|E^n|^2)$, so that a linear system for E^{n+1} is obtained. Since the spatial gradients are given by the transverse Laplacian associated to diffraction, up to second order in Δx the system is in tridiagonal form. Adding the extra top-right and bottom-left values due to periodic boundary conditions the problem can be solved using the Sherman-Morrison routine [85], with the help of the tridiagonal solver `ZGTSV` (complex, double precision) implemented in the Fortran `lapack` libraries [125]. This solves the one-dimensional problem, and can be extended to two transverse dimensions by updating for half a time step taking the gradient along the x direction, and using this intermediate solution to update for another half time step along the y direction. This is correct to order Δx^2, Δy^2, as the one-dimensional Crank Nicholson scheme.

An alternative approach to the problem which has been used for the simulations regarding opto-mechanical cavity solitons, Sec. 3.3, consists in a standard split-step routine. In this case the field equation (with the nonlinear term $n_{\rm eq}$) is split in two parts:

$$\frac{\partial E}{\partial t} = -(1+i\theta)E + A_{\rm in} - iC\Delta n_{\rm eq}E + \\ + i\nabla^2 E\,.$$

The first line (which has no spatial operators, and hence is a standard o.d.e.) is solved by a second-order Runge Kutta routine [85], while the second line is simple diffraction and can be solved exactly in Fourier space. Numerical simulations rely on the `libfftw` libraries [122] for the Fourier transform. This was found to give similar results as the Crank Nicholson method, both in terms of speed and stationary states.

A Crank Nicholson approach has been followed for the simulations of the damped single-mirror system, Sec. 3.2. As discussed in Sec. 3.2.2, in fact, here the dynamics of the density is followed in time, without resorting to the Gibbs state 'trick' to obtain the stationary state. This allows, for instance, to distinguish between density driven instabilities and electronically-driven ones.
In this case a Crank Nicholson routine with periodic boundary conditions was implemented for the real-valued array n_i, solving the resulting tridiagonal system (diffusion again gives only second-neighbour finite-difference gradients) with periodic boundary conditions via a Sherman-Morrison routine [85]. The tridiagonal solver `DGTSV` (real, double precision) from the `lapack` libraries [125] was used. The field is then phase-shifted and diffracted as in the viscousless case discussed in the previous Sec-

tion. As in the viscousless single-mirror simulations one needs to normalize the density distribution at each time step: the normalization integral is calculated by a Simpson integration method [85].

Appendix C: The zero-temperature limit. Self-structuring as a phase transition

Self-organizing transitions due to cavity-mediated interactions [26] received a notable attention in recent years, partly because a simple and insightful interpretation can be given in terms of phase transitions in Condensed Matter models. In the limit of ultracold gases, the self-organizing instability obtained in transversely pumped cavities [39, 41, 42] can in fact be interpreted in term of a Dicke model [126]. The breaking of a discrete Z_2 symmetry in the Dicke phase transition is obtained as initial fluctuations select whether the atoms will bunch in the 'even' or 'odd' potential wells. These experiments are reviewed in Ref. [26], and provided an important advancement in a fascinating field of modern research, namely the study of Condensed Matter models in highly tunable and controllable atom-optical systems. In term of dynamical instabilities, the same qualitative features are found for a thermal cloud [127] (and indeed the original treatment [38] dealt with thermal atoms), but the Dicke dynamics is found in the limit of ultracold atoms, $T \to 0$ [43].

It appears therefore quite natural to ask whether a 'Condensed Matter' description can be given of the self-structuring instabilities analyzed in this thesis. Indeed, the answer is that such an interpretation can be given, and that the Dicke model again captures the fundamental physics of the transition − at least at zero temperature. However, since a continuous symmetry breaking is obtained in correspondence with transverse self-structuring instabilities a $U(1)$ symmetry is broken, and the corresponding phase transition is referred to as a $U(1)$ Dicke phase transition. The analysis presented here will focus on the physically simplest and

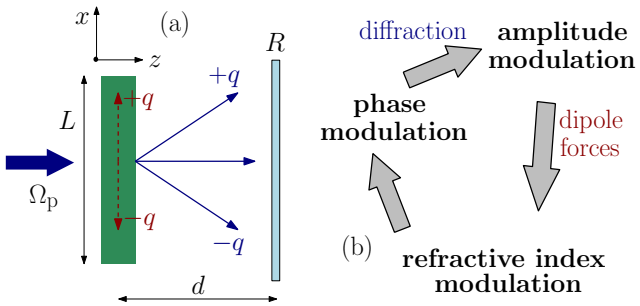

Figure 8: Sketch of the single-mirror scheme. A plane-wave beam of Rabi frequency $\Omega_{\rm p}$ illuminates an elongated BEC from the side, is transmitted and retroreflected by a mirror placed at distance d. The critical wavenumber $|q|$ is selected by the mirror distance, as phase modulations with period $2\pi/|q|$ are fully converted into amplitude modulations. A continuous symmetry is broken in correspondence with the spontaneous self-organization of the gas, which scatters off-axis sideband at wavenumber $k = \pm q$.

most insightful case, that of a single-mirror setup in the low-saturation regime (see Sec. 2.3). The single-mirror setup is chosen also because it is of immediate interest, as experimental realizations are available [83].

The following analysis closely follows the original work by Nagy *et al.* [43] for the transversely pumped cavity case, the important differences lying in the different conservation laws. An ultracold gas at $T = 0$ is considered, which is physically obtained with Bose-Einstein condensates (BECs). However, it is important to note that Bose-Einstein condensation is not a 'requirement' for the theory presented here: the Dicke and the BEC transitions are of different nature, and a Dicke transition can be obtained above the condensation point. The reader is referred to Ref. [128] for a field-theoretical analysis of the interplay between the two transitions.

Consider a zero-temperature Bose-Einstein condensate formed by N atoms of mass M. The gas is elongated along the $\hat{x}$ axis (L being its transverse size), and interacts with a monochromatic

plane-wave pump beam of Rabi frequency $\Omega_{\rm p}$ travelling along $\hat{z}$. The pump beam is transmitted by the condensate, and then retro-reflected by a mirror of reflectivity $R = 1$ placed at a distance d (see Fig. 8a). The pump frequency ω_0 is considered to be largely detuned from the optical resonance $\omega_{\rm at}$, so that the atomic excited state can be adiabatically eliminated. The Hamiltonian describing the interaction is ($\hbar = 1$):

$$H = \sum_{i=1}^{N} \frac{p_i^2}{2m} + \omega_0 \sum_k a_k^\dagger a_k + U_0 \sum_{i=1}^{N} E^*(x_i) E(x_i)\,, \qquad (30)$$

where $E(x)$ represents the amplitude of the (adimensional) electric field and the last term accounts for dispersive dipole forces. The strength of atom-light interaction is parametrized by $U_0 = g_0^2/\delta$, where g_0 is the single-photon Rabi frequency and $\delta = \omega_0 - \omega_{\rm at}$. The bosonic operators $a_k^\dagger$ (a_k) describe creation (annihilation) of a photon at transverse wavenumber k, $k = 0$ identifying the spatially homogeneous (on-axis) mode. Note also that we neglect atomic motion along the $\hat{z}$ axis, and atom-atom interactions in the condensate.

Transverse self-structuring is triggered by the spontaneous generation of optical off-axis sidebands at $k \neq 0$. The resulting density grating (period $\Lambda = 2\pi/q$) then scatters the off-axis sidebands at wavenumber q. The critical (most unstable) wavenumber is here denoted by q, and for purely dispersive interactions is given by $q^2 = \pi k_0/2d$, where k_0 is the radiation wavenumber, see [5] and Sec. 2.3.

The analysis presented in Chap. 2 dealt with thermal gases with a continuous velocity distribution, its spread determining the temperature of the gas. On the other hand, in the ultracold limit analyzed here the discrete motional states of the gas can be resolved.

Assuming to be close to the critical point, thus, the Fourier expansion of the field can be truncated to only two modes (plus the contribution from the homogeneous pump),

$$E(x) = \eta + a_0 + a_q \exp(iqx)\,.$$

Correspondingly, the atomic wave $\psi(x)$ will be in the form

$$\psi(x) = L^{-1/2}\left(b_0 + b_q \exp(iqx)\right] \,,,$$

the two momentum states identified by $k = 0$ and $k = q$ forming a closed two-level system: $b_0^\dagger b_0 + b_q^\dagger b_q = N$. The many-particles Hamiltonian then reads

$$\begin{aligned} H &= \omega_0 \sum_k a_k^\dagger a_k + \int_{-L/2}^{L/2} dx\, \psi^\dagger(x) \left[-\frac{1}{2m}\frac{\partial^2}{\partial x^2} + U_0 E^* E\right] \psi(x) = \\ &= \bar{\omega} a_0^\dagger a_0 + \sqrt{N} y (a_0^\dagger + a_0) + \\ &+ \bar{\omega} a_q^\dagger a_q + \omega_{\mathrm{R}} b_q^\dagger b_q + y\left(a_q^\dagger b_0^\dagger b_q + a_q b_q^\dagger b_0\right)/\sqrt{N} + \\ &+ u_0\left(a_0^\dagger a_q b_q^\dagger b_0 + a_q^\dagger a_0 b_0^\dagger b_q\right)/N \end{aligned} \tag{31}$$

where the recoil frequency has been defined as $\omega_{\mathrm{R}} = q^2/2m$, and as in Ref. [43] the quantities $u_0 = NU_0$, $y = \sqrt{N}\Omega_{\mathrm{p}} g_0/\delta$ and $\bar{\omega} = \omega_0 + u_0$ have been introduced. Importantly, these quantities are kept constant in the thermodynamic limit $N \to \infty$, $V \to \infty$, $N/V = \text{const}$. It is important to remark that the modal expansion has been truncated here to only two modes, but at the critical point also perturbations at $k = -q$ are unstable. This point will be reconsidered in the following, for the moment it suffices to say that this simple two-modes theory is already able to capture the essential features of the transition.

Before proceeding in the analysis of the Hamiltonian (31), con-

sider first the $k = 0$ mode. Since this mode is pumped by the classical amplitude y, the mode a_0 is described by a coherent state of amplitude α_0, and can be formally substituted as $a_0 \to \sqrt{N}\alpha_0$ (the $\sqrt{N}$ ensuring that the classical Hamiltonian is extensive in the number of particles). A representation of the angular momentum can be given by introducing the raising, lowering and population difference operators as:

$$\begin{aligned} S^+ &= b_q^\dagger b_0 \\ S^- &= b_0^\dagger b_q \\ S_z &= (b_q^\dagger b_q - b_0^\dagger b_0)/2\,. \end{aligned}$$

The Hamiltonian (31) then reads:

$$H = \bar{\omega} a_q^\dagger a_q + \omega_{\mathrm{R}} S_z + y\,[1 + u_0\alpha_0]\,\frac{a_q^\dagger S^- + a_q S^+}{\sqrt{N}} \qquad (32)$$

The last step consists in invoking the Holstein-Primakoff transformation to define bosonic operators γ, $\gamma^\dagger$ such that

$$\begin{aligned} S^+ &= \gamma^\dagger\sqrt{N - \gamma^\dagger\gamma} \simeq \sqrt{N}\gamma^\dagger \\ S^- &= \sqrt{N - \gamma^\dagger\gamma}\gamma \simeq \sqrt{N}\gamma \\ S^z &= \gamma^\dagger\gamma - N/2\,. \end{aligned}$$

The approximations taken above hold in the thermodynamic limit and for small excitations, $\gamma^\dagger\gamma \ll N$. The Hamiltonian (32) then transforms as

$$H = \bar{\omega} a_q^\dagger a_q + \omega_{\mathrm{R}}\gamma^\dagger\gamma + y\,[1 + u_0\alpha_0]\left(a_q^\dagger\gamma + a_q\gamma^\dagger\right)\,, \qquad (33)$$

which is a $U(1)$ Dicke Hamiltonian describing the interaction of the field 'sideband' mode with the atomic motional two-level system. The Hamiltonian (33) presents a phase transition at the

critical point $y_{\text{eff}} = \sqrt{\bar{\omega}\omega_{\text{R}}}$. The effective coupling is given by $y_{\text{eff}} = y + u_0\alpha_0$, where in general α_0 depends from y. In correspondence with the critical point, a mean-field analysis (detailed below) shows that $\alpha_0 = -y/\bar{\omega}$. Substituting this value into the expression for the critical point, thus, the critical point is found as $y_{\text{c}} = [\omega_{\text{R}}\bar{\omega}/(1 - u_0/\omega_c)^2]^{1/2}$. Below the critical point, $y \leq y_{\text{c}}$, the ground state of (33) is characterized by $\langle a_q^\dagger a_q\rangle = \langle\gamma^\dagger\gamma\rangle = 0$. This physically corresponds to a homogeneous optical profile $E(x) = E_0$ and a spatially homogeneous condensate. Above the critical point, the ground state is characterized by a non-zero number of photons being emitted into the sideband, $\langle a_q^\dagger a_q\rangle \sim (y - y_{\text{c}})^{1/2}$, and correspondingly by a non-zero occupation of the higher momentum state, $\langle\gamma^\dagger\gamma\rangle \sim 1 - (y_c/y)^2$ [129]. In the x-space, this zero-temperature transition thus corresponds to the self-amplification (from quantum fluctuations) of cosine-modulated optical fields and atomic profiles, essentially realizing the one-dimensional analogue of the observations presented in [83].

With respect to the well-known Dicke phase transition in cavity-pump setups, an important difference of the single-mirror transition is encoded in the conservation laws of the system. The presence of a standing-wave cavity, in fact, breaks the translational symmetry and creates an ambiguity in the sign of the momentum. On the other hand, no symmetry is explicitly broken (below the critical point) for the single-mirror scheme, so that a non-zero homogeneous field represents a valid solution for the system. The phase transition breaks a continuous symmetry, selecting one of the infinitely many transverse modes available. In this sense, the single-mirror phase transition discussed here is closer in spirit to the multi-mode proposal of Refs. [130, 131], where atomic internal degrees of freedom are involved. Moreover, translational

invariance implies that momentum must be conserved, so that counter-rotating terms $a_q^\dagger \gamma^\dagger + a_q \gamma$ do not enter the interaction term of Eq. (33). In other words, the Hamiltonian possesses a conserved quantity, namely the total excitation $a_q^\dagger a_q + S_z$. Given N excitations at disposal for the system, they can be stored as $\langle a_q^\dagger a_q \rangle = s$, $\langle S_z \rangle = r$ for any choice of r, s such that $r + s = N$. The phase transition thus corresponds to the transition from a state with $s = 0$, $r = N$ to a state with $s \neq 0$, $r = N - s$.

So far the interaction of a single field mode at $k = q$ with the atomic momentum states at $k = 0, q$ was discussed. This simple treatment revealed the basic nature of the interaction, encoded in the $U(1)$ excitation-conserving Dicke Hamiltonian. However, since the selection of the critical wavenumber is operated by diffraction, and the diffractive phase shift of each mode is proportional to $|k|^2$, modes at $k = -q$ should also be taken into account. Indeed, there are processes which conserve the total excitation and should therefore be considered, such as the emission of a photon at $k = q$ accompanied by the creation of an atom at momentum $k = -q$ and the annihilation of an atom at $k = 0$. In order to account for such processes, the field and atomic wave are expanded as

$$\begin{aligned} E(x) &= a_0 + \eta + a_q \exp(iqx) + a_{-q} \exp(-iqx) \\ \psi(x) &= L^{-1/2} \left[b_0 + b_q \exp(iqx) + b_{-q} \exp(-iqx) \right] . \end{aligned}$$

Repeating the procedure which led to Eq. (31) the following Hamiltonian is obtained:

$$\begin{aligned} H = & \tfrac{1}{2}\left[\bar{\omega}a_0^\dagger a_0 + y(a_0^\dagger + a_0)\sqrt{N}\right] + \bar{\omega}a_q^\dagger a_q + \omega_{\mathrm{R}} b_q^\dagger b_q + \\ & + yN^{-1/2}\left[a_q^\dagger\left(b_0^\dagger b_q + b_{-q}^\dagger b_0\right) + a_q\left(b_0^\dagger b_{-q} + b_q^\dagger b_0\right)\right] + \\ & + u_0 N^{-1}\left[a_q^\dagger a_0\left(b_0^\dagger b_q + b_{-q}^\dagger b_0\right) + a_0^\dagger a_q\left(b_0^\dagger b_{-q} + b_q^\dagger b_0\right)\right] + \\ & + u_0 N^{-1} a_{-q}^\dagger a_q b_q^\dagger b_{-q} + \{q \leftrightarrow -q\} \end{aligned} \tag{34}$$

where the last part is obtained by swapping the mode labels. To investigate the phase transitions of (34) the following mean-field technique can be used, as discussed in Ref. [43]. First the bosonic operators are expanded as $a_j = \sqrt{N}\alpha_j + \tilde{a}_j$ and $b_j = \sqrt{N}\beta_j + \tilde{b}_j$. Successively the Hamiltonian is expanded up to the first order in the operators $\tilde{a}_j$, $\tilde{b}_j$. Setting the linear terms in the displaced Hamiltonian to zero a set of six equations is obtained, one for each mode. The problem can be further reduced by imposing that the classical amplitudes satisfy $\alpha_q = \alpha_{-q}^*$ and $\beta_q = \beta_{-q}^*$, reaching the following system of equations:

$$\begin{aligned} & \bar{\omega}\alpha_0 + y + u_0\left[\alpha_q\beta_q^*\beta_0 + \alpha_q^*\beta_0^*\beta_q + \right. \\ & \qquad \left. + \alpha_q\beta_0^*\beta_q^* + \alpha_q^*\beta_0\beta_q\right] = 0 \\ & \bar{\omega}\alpha_q + u_0\alpha_q\left(\beta_q\beta_0 + \beta_0^*\beta_q\right) + y\beta_0^*\beta_q + u_0\alpha_q^*\beta_q^2 = 0 \\ & \omega_{\mathrm{R}}\beta_q + u_0\beta_0\left(\alpha_0^*\alpha_q + \alpha_q\alpha_0\right) + y\alpha_q\beta_0 + u_0\beta_q^*\alpha_q^2 = 0 \end{aligned} \tag{35}$$

The homogeneous solution for the system corresponds to $\alpha_q = \beta_q = 0$, which identifies the on-axis amplitude (up to the critical point) as $\alpha_0 = -y/\bar{\omega}$. This result is unchanged in the two-modes theory described above, and was used in determining the critical point − see the discussion after Eq. (33). This homogeneous solution becomes unstable when the coupling exceeds the critical

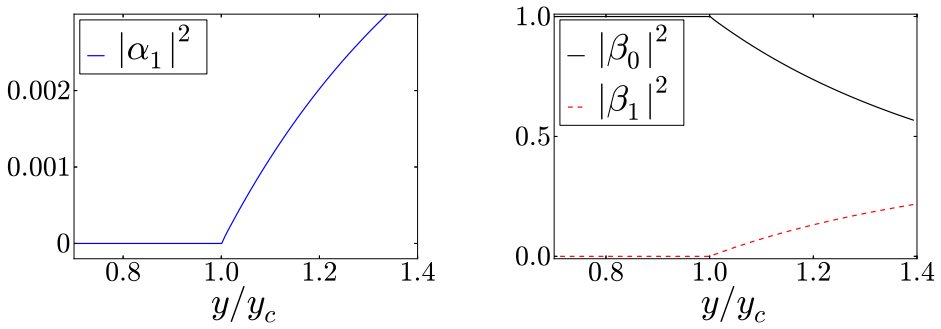

Figure 9: On the left, mean-field amplitude of the sideband at $k = +q$. On the right, mean-field occupations of the ground state (mode at $k = 0$) and the higher momentum state (mode at $k = q$) of the atomic wave. The total excitation is given by $2|\beta_q|^2$. Parameters are: $\omega_R = 1$, $u_0 = 20$, $\omega_0 = 100$.

value $y_c = [\omega_R\bar{\omega}/(1 - 2u_0/\bar{\omega})^2]^{1/2}$. Note that the critical point is identical to the one obtained from the two-modes Hamiltonian (33), apart from a numerical prefactor of 2 which appears because there are now two 'channels' for the transition.

Fig. (9) shows the mean-field amplitudes $|\alpha_q|^2$ and $|\beta_q|^2$ obtained from the system (35), varying the coupling strength y across the critical point. These represent respectively the intensity of the off-axis sideband and the population of the motional excited state (divided by the number of atoms N). At the critical point the system emits a 'macroscopic' sideband mode of amplitude $|\alpha_q| \neq 0$, self-amplified from quantum fluctuations (left panel of Fig. (9)). The corresponding dipole forces impose a modulation in the gas density, populating the excited motional state (right panel of Fig. (9)).

The three-modes theory described by the Hamiltonian (34) leads only to a different threshold compared to the simple, two-modes theory of (33). As long as momentum is conserved, in fact, creating an atom/photon at momentum $+q$ ($b_q^\dagger/a_q^\dagger$) or destroying an atom/photon at $k = -q$ (b_{-q}/a_{-q}) is equivalent. Essentially, thus, the transition shown by the two-modes Hamiltonian is repli-

cated in the three-modes theory. The denomination 'Dicke-model Hamiltonian' is here generalized to what is effectively a three-level system interacting with two bosonic modes.

A natural question is now whether this theoretical framework can be extended to a non-zero temperature, and used to describe the experiments presented in Ref. [83]. As a matter of fact, the Dicke phase transition (with or without counter-rotating terms) is a classical one, occurring at a non-zero critical temperature [132, 133]. In Ref. [128] the interplay between the Dicke phase transition and the BEC transition at $T \neq 0$ was investigated, and this work may be extended also to the single-mirror case. As the temperature is increased to the point where $\omega_{\mathrm{R}} \ll k_B T$ (as it is the case in Ref. [83]), however, the approximation of discrete momentum states breaks down. Although we would expect a thermal gas to reproduce the phenomenology of the quantum phase transition described here, the dynamics would not be captured by the Hamiltonian (34). The same holds, for instance, in the transversely pumped cavity setup − Ref. [127] realizing the thermal transition and Ref. [39] the quantum one.
As a final remark, the analysis presented here shares a common trait with other studies of self-organization in quantum systems, e.g. cavity-pump studies [43] or quantum CARL works [134]. While the threshold for self-organization derived from a classical theory (high T) vanishes if $T \to 0$, a non-zero threshold is found if the full many-body nature of the problem is taken into account at zero temperature. When analyzing the results from our classical theory (and particularly the temperature dependence of the threshold, see Fig. (2.2c)), it should be kept in mind that these results do not extend to the $T \to 0$ limit: even if thermal fluctu-

ations vanish, in fact, quantum fluctuations still yield a non-zero threshold for the transition.

Bibliography

[1] A. M. Turing. The chemical basis of morphogenesis. *Philosophical Transactions of the Royal Society of London*, 237:37, 1952.

[2] I. Prigogine. *Introduction to the thermodynamics of irreversible processes*. New York: Interscience, 1961.

[3] H. Haken. *The science of structure: Synergetics*. Van Nostrand Reinhold, 1984.

[4] M. C. Cross and P. C. Hohenberg. Pattern formation outside of equilibrium. *Rev. Mod. Phys.*, 65:851, 1993.

[5] W. J. Firth. Spatial instabilities in a kerr medium with single feedback mirror. *J. Mod. Opt.*, 37:151–153, 1990.

[6] L. A. Lugiato and R. Lefever. Spatial dissipative structures in passive optical systems. *Phys. Rev. Lett.*, 58:2209, 1987.

[7] G.L. Lippi, T. Ackemann, L.M. Hoffer, and W. Lange. Transverse structures in a sodium-filled fabry-prot resonator. *Chaos, Solitons & Fractals*, 4:1409, 1994.

[8] T. Ackemann and W. Lange. Optical pattern formation in alkali metal vapors: Mechanisms, phenomena and use. *Appl. Phys. B*, 72:21, 2001.

[9] G. Grynberg, E. Le Bihan, P. Verkerk, P. Simoneau, J. R. R. Leite, D. Bloch, S. Le Boiteux, and M. Ducloy. Observation

of instabilities due to mirrorless four-wave mixing oscillation in sodium. *Opt. Comm.*, 67:363, 1988.

[10] W. J. Firth and C. Paré. Transverse modulational instabilities for counterpropagating beams in kerr media. *Opt. Lett.*, 13:1096–1098, 1988.

[11] T. Ackemann and W. Lange. Non- and nearly hexagonal patterns in sodium vapor generated by single-mirror feedback. *Phys. Rev. A*, 50:4468(R), 1994.

[12] R. Neubecker, G.-L. Oppo, B. Thuering, and T. Tschudi. Pattern formation in a liquid-crystal light valve with feedback, including polarization, saturation, and internal threshold effects. *Phys. Rev. A*, 52:791, 1995.

[13] S. Fernández-Vidal, G. De Chiara, J. Larson, and Giovanna Morigi. Quantum ground state of self-organized atomic crystals in optical resonators. *Phys. Rev. A*, 81:043407, 2010.

[14] C. Denz, M. Shwab, and C. Weilnau. *Transverse Pattern Formation in Photorefractive Optics.* Springer, 2003.

[15] L. A. Lugiato. Transverse nonlinear optics: introduction and review. *Chaos, Solitons & Fractals*, 4:12511258, 1994.

[16] F. T. Arecchi, S. Boccaletti, and P. L. Ramazza. Pattern formation and competition in nonlinear optics. *Phys. Rep.*, 318:1–83, 1999.

[17] N. B. Abraham and W. J. Firth. Overview of transverse effects in nonlinear-optical systems. *J. Opt. Am. Soc. B*, 7:951–962, 1990.

[18] E. Pampaloni, P. L. Ramazza, S. Residori, and F. T. Arecchi. Two-dimensional crystals and quasicrystals in nonlinear optics. *Phys. Rev. Lett.*, 74:258–261, 1995.

[19] J. G. Huang and G. S. McDonald. Spontaneous optical fractal pattern formation. *Phys. Rev. Lett.*, 94:174101, 2005.

[20] J. G. Huang, J. M. Christian, and G. S. McDonald. Spontaneous spatial fractal pattern formation in absorptive systems. *J. Nonlinear Optic. Phys. Mat.*, 21:1250018, 2012.

[21] R. Barboza, U. Bortolozzo, G. Assanto, E. Vidal-Henriquez, M. G. Clerc, and S. Residori. Harnessing optical vortex lattices in nematic liquid crystals. *Phys. Rev. Lett.*, 111:093902, 1993.

[22] D. Wineland, R. E. Drullinger, and F. L. Walls. Radiation-pressure cooling of bound resonant absorbers. *Phys. Rev. Lett.*, 40(25):1639, 1978.

[23] W. Neuhauser, M. Hohenstatt, P. Toschek, and H. Dehmelt. Optical-sideband cooling of visible atom cloud confined in parabolic wall. *Phys. Rev. Lett.*, 41(4):233, 1978.

[24] W. Ketterle. When atoms behave as waves: Bose-Einstein condensation and the atom laser. *Rev. Mod. Phys.*, 74:1131–1151, 20012.

[25] I. Bloch. Ultracold quantum gases in optical lattices. *Nat. Phys.*, 1:23–30, 2005.

[26] H. Ritsch, P. Domokos, F. Brennecke, and T. Esslinger. Cold atoms in cavity-generated dynamical optical potentials. *Rev. Mod. Phys.*, 85:553–601, 2013.

[27] J. J. García-Ripoll, P. Zoller, and P. Cirac. Quantum information processing with cold atoms and trapped ions. *J. Phys. B: At. Mol. Opt. Phys.*, 38:S567, 2005.

[28] O. Morsch and M. Oberthaler. Dynamics of Bose-Einstein condensates in optical lattices. *Rev. Mod. Phys.*, 78:179–215, 2006.

[29] J.-Y. Courtois, G. Grynberg, B. Lounis, and P. Verkerk. Recoil-induced resonances in cesium: An atomic analogto the free-electron laser. *Phys. Rev. Lett.*, 72:3017, 1994.

[30] R. Bonifacio and L. De Salvo. Collective atomic recoil laser (carl) optical gain without inversion by collective atomic recoil and self-bunching of two-level atoms. *Nucl. Instrum. Methods Phys. Res. A*, 341:360, 1994.

[31] R. Bonifacio, L. De Salvo, L. M. Narducci, and E. J. D'Angelo. Exponential gain and self-bunching in a collective atomic recoil laser. *Phys. Rev. A*, 50:1716–1724, 1994.

[32] C. von Cube, S. Slama, D. Kruse, C. Zimmermann, Ph. W. Courteille, G. R. M. Robb, N. Piovella, and R. Bonifacio. Self-synchronization and dissipation-induced threshold in collective atomic recoil lasing. *Phys. Rev. Lett.*, 93:083601, 2004.

[33] S. Slama, S. Bux, G. Krenz, C. Zimmermann, and Ph. W. Courteille. Superradiant rayleigh scattering and collective atomic recoil lasing in a ring cavity. *Phys. Rev. Lett.*, 98:053603, 2007.

[34] S. Inouye, A. P. Chikkatur, D. M. Stamper-Kurn, J. Stenger, D. E. Pritchard, and W. Ketterle. Superradi-

ant Rayleigh scattering from a Bose-Binstein condensate. *Science*, 285:571–574, 1999.

[35] S. Gopalakrishnan, B. L. Lev, and P. Goldbart. Emergent crystallinity and frustration with Bose-Einstein condensates in multimode cavities. *Nat. Phys.*, 5:845–850, 2009.

[36] S. Gopalakrishnan, B. L. Lev, and P. Goldbart. Atom-light crystallization of becs in multimode cavities: Nonequilibrium classical and quantum phase transitions, emergent lattices, supersolidity, and frustration. *Phys. Rev. A*, 82:043612, 2012.

[37] B. W. J. McNeil and N. R. Thompson. X-ray free-electron lasers. *Nat. Phot.*, 4:814–821, 2010.

[38] P. Domokos and H. Ritsch. Collective cooling and self-organization of atoms in a cavity. *Phys. Rev. Lett.*, 89:253003, 2002.

[39] K. Baumann, C. Guerlin, F. Brenneke, and T. Esslinger. Dicke quantum phase transition with a superfluid gas in an optical cavity. *Nature (London)*, 464:1301–1306, 2010.

[40] K. Baumann, R. Mottl, F. Brennecke, and T. Esslinger. Exploring symmetry breaking at the Dicke quantum phase transition. *Phys. Rev. Lett.*, 107:140402, 2011.

[41] R. Mottl, F. Brennecke, K. Baumann, R. Landig, T. Donner, and T. Esslinger. Roton-type mode softening in a quantum gas with cavity-mediated long-range interactions. *Science*, 336:1570–1573, 2012.

[42] F. Brennecke, R. Mottl, K. Baumann, R. Landig, T. Donner, and T. Esslinger. Real-time observation of fluctuations

at the driven-dissipative Dicke phase transition. *Proceedings of the National Academy of Science*, 110:11763–11767, 2013.

[43] D. Nagy, G. Konya, G. Szirmai, and P. Domokos. The Dicke model phase transition in the uantum motion of a Bose-Einstein condensate in an optical cavity. *Phys. Rev. Lett.*, 104:130401, 2010.

[44] J. K. Asbóth, P. Domokos, H. Ritsch, and A. Vukics. Self-organization of atoms in a cavity field: threshold, bistability and scaling laws. *Phys. Rev. A*, 72:053417, 2005.

[45] J. A. Greenberg and D. J. Gauthier. Steady-state, cavityless, multimode superradiance. *Phys. Rev. A.*, 86:013823, 2012.

[46] J. A. Greenberg and D. J. Gauthier. High-order optical nonlinearity at low light levels. *Eur. Phys. Lett.*, 98:24001, 2012.

[47] J. A. Greenberg, B. L. Schmittberger, and D. J. Gauthier. Bunching-induced optical nonlinearity and instability in cold atoms. *Opt. Express*, 19:22535, 2011.

[48] J. C. Maxwell. A tratise on electricity and magnetism.

[49] R. Frisch. Experimenteller nachweis des eintenschen strahlungrückstosses. *Z. Phys.*, 86:42, 1933.

[50] P. Lebedev. Untersuchungen über die druckkräfte des lichtes. *Ann. Phys.*, 6:433, 1901.

[51] E. F. Nichols and G. F. Hull. The pressure due to radiation. *Phys. Rev.*, 17:26, 1903.

[52] A. Ashkin. Atomic-beam deflection by resonance-radiation pressure. *Phys. Rev. Lett.*, 25(19):1321, 1970.

[53] T. W. Hänsch and A. L. Schawlow. Cooling of gases by laser radiation. *Opt. Comm.*, 13(1):68, 1975.

[54] D. Wineland and H. Dehmelt. Proposed $10^{14}\Delta\nu < \nu$ laser fluorescence spectroscopy on Ti^+ mono-ion oscillator III. *Bull. Am. Phys. Soc.*, 20:637, 1975.

[55] A. Ashkin. Trapping of atoms by resonant radiation pressure. *Phys. Rev. Lett.*, 40(12):729, 1978.

[56] J. P. Gordon and A. Ashkin. Motions of atoms in a radiation trap. *Phys. Rev. A*, 21:1606, 1980.

[57] C. S. Adams and E. Riis. Laser cooling and trapping of neutral atoms. *Progress in Quantum. Electronics*, 21:1–79, 1997.

[58] H. J. Metcalf and P. Van Der Straten. *Laser cooling and trapping*. Springer-Verlag, 2001.

[59] W. D. Phillips. Laser cooling and trapping of neutral atoms. *Rev. Mod. Phys.*, 70(3):721, 1998.

[60] J. Dalibard and C. Cohen-Tannoudji. Dressed-atom approach to atomic motion in laser light: the dipole force revisited. *J. Opt. Am. Soc. B*, 2(11):1707, 1985.

[61] G. A. Askar'yan. Radiation pressure on an object with varying polarizability changes. Deformation absorption of a wave by variable inhomogeneities. *Zh. Eksper. i Teor. Fiz. − Pis'ma Redakt.*, 9:404, 1969.

[62] A. Ashkin. Acceleration and trapping of particles by radiation pressure. *Phys. Rev. Lett.*, 24(4):156, 1970.

[63] C. Cohen-Tannoudji, J. Dupont-Roc, and G. Grynberg. *Atom-photon interactions: basic processes and applications.* John Wiley and Sons, 1992.

[64] R. W. Boyd. *Nonlinear Optics.* Academic Press, 3 edition, 2008.

[65] P. D. Lett, R. N. Watts, C. I. Westbrook, W. D. Phillips, P. L. Gould, and H. J. Metcalf. Observation of atoms laser cooled below the Doppler Limit. *Phys. Rev. Lett.*, 61:169–172, 1988.

[66] J. Dalibard and C. Cohen-Tannoudji. Laser cooling below the doppler limit by polarization gradients - simple theoretical models. *J. Opt. Soc. Am. B*, 6:2023–2045, 1989.

[67] P. J. Ungar, D. S. Weiss, S. Chu, and E. Riis. Optical molasses and multilevel atoms - theory. *J. Opt. Am. Soc. B*, 6:2058–2071, 1989.

[68] M. Cross and H. Greenside. *Pattern formation and dynamics in nonequilibrium systems.* Cambridge University Press, 2009.

[69] S. H. Strogatz. *Nonlinear Dynamics And Chaos: With Applications To Physics, Biology, Chemistry, And Engineering.* Perseus, 1994.

[70] J. Guckenheimer and P. Holmes. *Nonlinear oscillations, dynamical systems and bifurcations of vector fields.* Springer-Verlag, 1983.

[71] V. I. Krinsky. *Self-organization autowaves and structures far from equilibrium.* Springer-Verlag, 1984.

[72] J. Swift and P.C. Hohenberg. Hydrodynamic fluctuations at the convective instability. *Phys. Rev. A*, 15:319–332, 1977.

[73] L. D. Landau and E. L. Lifshitz. *Statistical mechanics.* Addison Wesley, 1958.

[74] S. Ciliberto, P. Coullet, J. Lega, E. Pampolini, and C. Perez-Garcia. Defects in roll-hexagon competition. *Phys. Rev. Lett.*, 65:2370, 1990.

[75] G.-L. Oppo. Formation and control of Turing patterns and phase fronts in photonics and chemistry. *J. Math. Chem.*, 45:95–112, 2009.

[76] F. Chen. *Introduction to Plasma Physics.* Springer, 1995.

[77] T. Grießer, H. Ritsch, M. Hemmerling, and G. R. M. Robb. A Vlasov approach to bunching and selfordering of particles in optical resonators. *Eur. Phys. J. D*, 58:349–368, 2000.

[78] R. Bachelard, T. Dauxois, G. De Ninno, S. Ruffo, and F. Staniscia. Vlasov equation for long-range interactions on a lattice. *Phys. Rev. E*, 83:061132, 2011.

[79] S. Gupta, A. Campa, and S. Ruffo. Nonequilibrium first-order transition in coupled oscillator systems with inertia and noise. arXiv:1309.0035.

[80] S. Gupta, M. Potters, and S. Ruffo. One-dimensional lattice of oscillators coupled through power-law interactions: Continuum limit and dynamics of spatial fourier modes. *Phys. Rev. E*, 85:066201, 2012.

[81] G. D'Alessandro and W. J. Firth. Spontaneous hexagon formation in a nonlinear optical medium with feedback mirror. *Phys. Rev. Lett.*, 66:2597, 1991.

[82] G. D'Alessandro and W. J. Firth. Hexagonal spatial patterns for a kerr slice with a feedback mirror. *Phys. Rev. A*, pages 537–548, 1992.

[83] G. Labeyrie, E. Tesio, P.M. Gomes, G.-L. Oppo, W.J. Firth, G.R.M. Robb, A.S. Arnold, R. Kaiser, and T. Ackemann. Optomechanical self-structuring in cold atomic gases. Accepted for publication on Nat. Phot. (2014).

[84] K. Huang. *Statistical Mechanics*. Wiley, 2 edition, 1987.

[85] W. H. Press, B. P. Flannery, S. A. Teukolsky, and W. T. Vetterling. *Numerical Recipes in Fortran: The Art of Scientific Computing*. Cambridge University Press, 2 edition, 1992.

[86] Wolfram Research, Inc., Mathematica, Version 8.0, Champaign, IL (2010).

[87] L. Landau. On the vibration of the electronic plasma. *JETP*, 16:574, 1946.

[88] H. J. Lee and M. Y. Song. Causality and collisionless damping in plasma. *J. Mod. Phys.*, 4:555, 2013.

[89] H. F. Talbot. Facts related to optical science. *Philos. Mag.*, 9, 1836.

[90] R. El-Ganainy, D. N. Christodoulides, Z. H. Musslimani, , C. Rotschild, and M. Segev. Optical beam instabilities in nonlinear nanosuspensions. *Opt. Lett.*, 32:3185 – 3187, 2007.

[91] R. El-Ganainy, D. N. Christodoulides, C. Rotschild, and M. Segev. Soliton dynamics and self-induced transparency in nonlinear nanosuspensions. *Opt. Expr.*, 15:10207 – 10218, 2007.

[92] M. Saffman and Y. Wang. Collective focusing and modulational instability of light and cold atoms. *Lect. Notes Phys.*, 751:361, 2008.

[93] M. A. Muradyan, Y. Wang, W. Williams, and M. Saffman. in *Trends in Optics and Photonics (TOPS)*, vol. **80**, Nonlinear Applications, OSA Technical Digest (OSA, Washington, D.C., 2005), paper ThB29.

[94] J. A. Acebrón, C. J. Pérez Vicente, and R. Spigler. The Kuramoto model: a simple paradigm for synchronization phenomena. *Rev. Mod. Phys.*, 77:137–185, 2005.

[95] S. H. Strogatz. *Sync: the emerging sience of spontaneous order*. Hyperion, 1 edition, 2003.

[96] J. Javaloyes, M. Perrin, and A. Politi. Collective atomic recoil laser as a synchronization transition. *Phys. Rev. E*, 78:011108, 2008.

[97] P. W. Smith, P. J. Maloney, and A. Ashkin. Use of a liquid suspension of dielectric spheres as an artificial kerr medium. *Opt. Lett.*, 7:347–349, 1982.

[98] A. Ashkin, J. M. Dziedzic, and P. W. Smith. Continuous-wave self-focusing and self-trapping of light in artificial kerr media. *Opt. Lett.*, 7:276–278, 1982.

[99] P. J. Reece, E. M. Wright, and K. Dholakia. Experimental observation of modulation instability and optical spatial

soliton arrays in soft condensed matter. *Phys. Rev. Lett.*, 98:203902, 2007.

[100] C. Conti, N. Ghofraniha, G. Ruocco, and S. Trillo. Laser beam filamentation in fractal aggregates. *Phys. Rev. Lett.*, 97:123903, 2006.

[101] C. Conti, G. Ruocco, and S. Trillo. Optical spatial solitons in soft matter. *Phys. Rev. Lett.*, 95:183902, 2005.

[102] Michal Matuszewski, Wieslaw Krolikowski, and Y. S. Kivshar. Spatial solitons and light-induced instabilities in colloidal media. *Opt. Expr.*, 16:1371 – 1376, 2008.

[103] L. P. Kadanoff. *Statistical Physics: statics, dynamics and renormalization*. World Scientific, 2000.

[104] A. N. Kolmogorov. On analytical methods in probability theory. in Mathematics and its applications (Soviet series), vol. 26, edited by A. N. Shiryayev, 1992.

[105] S. Chandrasekhar. Stochastic problems in physics and astronomy. *Rev. Mod. Phys.*, 15:1–89, 1943.

[106] U. M. B. Marconi, A. Puglisi, L. Rondoni, and A. Vulpiani. Fluctuation-dissipation: response theory in statistical physics. *Phys. Rep.*, 461:111–195, 2008.

[107] L. A. Lugiato and C. Oldano. Stationary spatial patterns in passive optical systems: Two-level atoms. *Phys. Rev. A*, 37:3896–3908, 1988.

[108] R. Bonifacio and L. A. Lugiato. Optical bistability and cooperative effects in resonance fluorescence. *Phys. Rev. A*, 18:1129–1144, 1978.

[109] L.A. Lugiato. Theory of optical bistability. *Progress in optics*, 21:69–216, 1984.

[110] T. W. Hodapp, C. Gerz, C. Furtlehner, C. I. Westbrook, W. D. Phillips, and J. Dalibard. Three-dimensional spatial diffusion in optical molasses. *Appl. Phys. B*, 60:135–143, 1995.

[111] J. M. McSloy, W. J. Firth, G. K. Harkness, and G.-L. Oppo. Computationally determined existence and stability of transverse structures. I. Periodic optical patterns. *Phys. Rev. E*, 66:046606, 2002.

[112] E. Pampaloni, S. Residori, and F. T. Arecchi. Roll-Hexagon transition in a Kerr-like experiment. *Eur. Phys. Lett.*, 24:647, 1993.

[113] J. J. Rasmussen and K. Rypdal. Blow-up in Nonlinear Schroedinger Equations-i: A general review. *Phys. Scr.*, 33:481, 1986.

[114] N. Akhmediev and A. Ankiewicz. *Dissipative Solitons.* Springer Verlag, 2005.

[115] M.K. Oberthaler and T. Pfau. One-, two- and three-dimensional nanostructures with atom lithography. *J. Phys.: Conden. Matter*, 15:R223, 2003.

[116] J. M. McSloy, W. J. Firth, G. K. Harkness, and G.-L. Oppo. Computationally determined existence and stability of transverse structures. II. Multipeaked cavity solitons. *Phys. Rev. E*, 66:046606, 2002.

[117] J. B. Geddes, R. A. Indik, J. V. Moloney, and W. J. Firth. Hexagons and squares in a passive nonlinear optical system. *Phys. Rev. A*, 54:3471–3485, 1994.

[118] Brian Klinkenberg. A review of methods used to determine the fractal dimension of linear features. *Math. Geol.*, 26:23–46, 1994.

[119] P. Chamorro-Posada, G. S. MacDonald, and G. H. C. New. Non-paraxial solitons. *J. Mod. Opt.*, 45:1111–1121, 1998.

[120] H. Carmichael. *An Open Systems Approach to Quantum Optics*. Springer Verlag, 1991.

[121] R. Kubo. The fluctuation-dissipation theorem. *Rep. Prog. Phys.*, 29:255, 1966.

[122] `http://www.fftw.org`.

[123] C. Z. Cheng and G. Knorr. The integration of the vlasov equation in configuration space. *J. Comp. Phys.*, 22:330–351, 1976.

[124] `http://openmp.org/wp`.

[125] `http://www.netlib.org/lapack/`.

[126] R.H. Dicke. Coherence in spontaneous radiation processes. *Phys. Rev.*, 93:99, 1954.

[127] A. T. Black, H. W. Chan, and V. Vuletić. Observation of collective friction forces due to spatial self-organization of atoms: from Rayleigh to Bragg scattering. *Phys. Rev. Lett.*, 91:203001, 2003.

[128] F. Piazza, P. Strack, and W. Zwerger. Bose-Einstein condensation versus Dicke-Hepp-Lieb transition in an optical cavity. *Ann. Phys.*, 339:135–159, 2013.

[129] C. Emary and T. Brandes. Quantum chaos triggered by precursors of a quantum phase transition: the Dicke model. *Phys. Rev. Lett.*, 90:044101, 2003.

[130] S. Gopalakrishnan, B.L. Lev, and P. Goldbart. Emergent crystallinity and frustration with Bose-Einstein condensates in multimode cavities. *Nat. Phys.*, 5:845–850, 2009.

[131] S. Gopalakrishnan, B.L. Lev, and P. Goldbart. Frustration and glassiness in spin models with cavity-mediated interactions. *Phys. Rev. Lett.*, 107:277201, 2011.

[132] K. Hepp and E. Lieb. On the superradiant phase transition for molecules in a quantized radiation field: The Dicke maser model. *Ann. Phys.*, 76:360–404, 1973.

[133] Y. K. Wang and F. T. Hioe. Phase transition in the Dicke model of superradiance. *Phys. Rev. A*, 7:831–836, 1973.

[134] N. Piovella, M. Cola, and R. Bonifacio. Classical and quantum regimes in the collective atomic recoil laser from a Bose-Einstein condensate. *J. Mod. Opt.*, 51:1019–1023, 2004.